UAB

Universitat Autònoma de Barcelona

UAB
Universitat Autònoma
de Barcelona

Clip-off Chemistry in Three-Dimensional Metal-Organic Frameworks

Yunhui Yang

Doctoral Thesis
PhD in Chemistry

Supervisors

Prof. Dr. Daniel Maspoch

Dr. Inhar Imaz

Catalan Institute of Nanoscience and Nanotechnology (ICN2)
Department of Chemistry – Faculty of Sciences

2023

Memòria presentada per aspirar al Grau de Doctor per Yunhui Yang

Yunhui Yang

vist-i-plau

Prof. Dr. Daniel Maspoch

ICREA Research Professor & Group Leader
Supramolecular NanoChemistry & Materials Group
Catalan Institute of Nanoscience and Nanotechnology

Dr. Inhar Imaz

CSIC Research Scientist
Supramolecular NanoChemistry & Materials Group
Catalan Institute of Nanoscience and Nanotechnology

Bellaterra, 10 de Setembre de 2023

Table of Contents

Abstract

The present PhD dissertation has been dedicated to establishing the foundation for Clip-off Chemistry within three-dimensional metal-organic frameworks (3-D MOFs). We aim to introduce and develop a new synthetic approach based on bond cleavage, termed as Clip-off Chemistry, to achieve the targeted synthesis of new molecules and materials, and to discover new phenomena in MOFs.

Chapter 1 provides readers with a brief overview of the journey of MOFs, from their rise as porous coordination polymers to their successful practical real-world applications. This chapter showcases the cutting-edge synthetic approaches for constructing targeted functional MOFs, which focuses on two key aspects: the bond-forming process by the guidance of reticular chemistry and bond-breaking process leading to the formation of deconstructed MOFs. A particular emphasis is placed on addressing the current state and challenges associated with the bond-breaking process.

Chapter 2 describes the general and specific objectives of the dissertation.

Chapter 3 aims to develop a new enzyme-powered micromotor based on a hierarchically porous MOF. In particular, this MOF is generated by subjecting a presynthesized microporous MOF to an ozonolysis reaction, effectively breaking and removing randomly distributed olefin-containing linkers. This process facilitates the fusion of micropores to mesopores within the MOF structure. By making use of the hierarchical porosity, we validate that the enzyme catalase can be successfully adsorbed inside the mesopores. This encapsulation enables the resulting MOF (or MOFtor) to exhibit the jet-like bubble propulsion in the presence of H_2O_2. The study further explores the control of MOFtor speed through varying enzyme incubation times and H_2O_2 concentrations. Additionally, thanks to the remaining empty pores inside the MOFtor, we show its potential capability to capture rhodamine B in water during its self-propulsion.

Chapter 4 extends the concept of the covalent bond breaking into well-defined reticular materials where all cleavable bonds are spatially arranged in an ordered fashion. By programmed disassembly of reticular materials through bond breaking, we are able to achieve remarkable molecules and materials that are unattainable by direct syhthesis. This innovative approach that we call Clip-off Chemistry can revolutionize the design and targeted synthesis of desired structures. Based on this, we validate Clip-off Chemistry by synthesizing two topologically distinct 3-D MOFs (Zr-**pcu**-MOF and Sc-**pcu**-MOF, respectively) from two other well-established 3-D MOF precursors (Zr-**scu**-MOF and Sc-**soc**-MOF). Through these illustrative examples, we demonstrate the periodic, quantitative, and selective nature of bond breaking within these structures. Notably, this process corroborates that this cleavage is effective in both solid and liquid phases, while also exhibiting the ability to occur in a single-crystal-to-single-crystal fashion throughout the entire bulk precursor sample.

Chapter 5 applies the principle of Clip-off Chemistry within a more intricate system. In this case, our focus is on multicomponent MOFs based on the MIL-142 family, which consist of both cleavable and noncleavable organic linkers. Through a solid-gas phase ozonolysis reaction, we are able to selectively and quantitatively break all the cleavable linkers within these frameworks into two fragments. Subsequently, by incubating these ozonated MOFs into certain solvent, we observe an unusual phenomenon: spontaneous self-rearrangement leading to the formation of contracted isoreticular MOFs. This transformation involves various dynamic chemical and structural processes taking place within the frameworks. Remarkably, the single-crystal nature of the parent MOF is retained throughout the entire transformation, enabling us to monitor the contraction using single-crystal X-ray diffraction.

Finally, Chapter 6 presents the key findings and main conclusions. Additionally, it also offers valuable insights into future perspectives toward covalent bond-breaking in reticular materials.

Resum

La present tesi doctoral s'ha dedicat a establir les bases de Clip-off Chemistry utilitzant xarxes metal·lorgàniques tridimensionals (3-D MOFs). El nostre objectiu és introduir i desenvolupar un nou mètode sintètic, anomenat Clip-off Chemistry, per aconseguir la síntesi de noves molècules i materials, i descobrir nous fenòmens en MOFs, utilitzant el trencament d'enllaços.

El capítol 1 proporciona als lectors una breu visió general dels MOFs, des del seu inici com a polímers de coordinació porosos fins a les seves exitoses aplicacions en el món real. Aquest capítol mostra els mètodes sintètics prèviament desenvolupats per a la construcció de MOFs funcionals, que se centren en dos aspectes clau: el procés de formació d'enllaços guiat per la química reticular i el procés de ruptura d'enllaços que condueix a la formació de MOFs deconstruits. Es fa especial èmfasi en abordar l'estat actual i els reptes associats amb el procés de ruptura d'enllaços.

El capítol 2 descriu els objectius generals i específics de la tesi doctoral.

El Capítol 3 té com a objectiu desenvolupar un nou micromotor accionat per enzims basat en un MOF jeràrquicament porós. En particular, aquest MOF es genera sotmetent un MOF microporós a una reacció d'ozonòlisi, trencant i eliminant eficaçment els lligands que contenen enllaços olefínics i que estan distribuïts aleatòriament. Aquest procés facilita la fusió de micropors a mesopors dins l'estructura del MOF. Aprofitant la porositat jeràrquica, es valida que l'enzim catalasa pot ser absorbit amb èxit dins els mesopors. Aquesta encapsulació permet que el MOF resultant (o MOFtor) mostri una propulsió de bombolles similar a un jet en presència de H_2O_2. L'estudi també explora el control de la velocitat del MOFtor mitjançant la variació del temps d'incubació de l'enzim i les concentracions de H_2O_2. A més, gràcies als pors buits restants dins del MOFtor, es mostra la seva capacitat per capturar la rodamina B en aigua durant la seva autopropulsió.

El capítol 4 exté el concepte de trencament d'enllaços covalents en materials reticulars on tots els enllaços que es poden trencar estan ordenats espacialment dins l'estructura. Mitjançant el desmuntatge programat de materials reticulars a través del trencament d'enllaços som capaços d'aconseguir molècules i materials que abans no són accessibles per la síntesis directa. Aquest mètode sintètic innovador, que anomenem Clip-off Chemistry, pot revolucionar el disseny i la síntesis selectiva d'estructures desitjades. Basant-nos en això, en aquest capítol es valida la Clip-off Chemistry mitjançant la síntesi de dos nous MOFs 3-D topològicament diferents (Zr-**pcu**-MOF i Sc-**pcu**-MOF) utilitzant dos MOF 3-D precursors (Zr-**scu**-MOF i Sc-**soc**-MOF). A través d'aquests exemples il·lustratius, es demostra la naturalesa periòdica, quantitativa i selectiva dels enllaços que es trenquen dins d'aquestes estructures. Cal destacar que aquest procés corrobora que aquesta escissió és efectiva tant en fase sòlida

com líquida, mentre que també demostra la possibilitat de tenir lloc de cristall-a-cristall al llarg de tota la mostra precursora.

El capítol 5 aplica el principi de Clip-off Chemistry dins d'un sistema més complex. En aquest cas, el nostre focus està en MOFs multicomponents basats en la família del MIL-142, que estan formats per en lligands orgànics que es poedn i no es poden trencar. Mitjançant una reacció d'ozonòlisi sòlid-gas, som capaços de trencar selectivament i quantitativament tots els lligands que es poden trencar en dos fragments. Posteriorment, l'incubació d'aquests MOFs ozonats en un cert dissolvent provoca d'un fenomen inusual: una autoreordenació espontània que condueix a la formació de nous MOFs isoreticulars contrets. Aquesta transformació implica diversos processos dinàmics i estructurals que tenen lloc dins de les xarxes metal·lorganiques. Cal remarcar que la naturalesa de monocristall es manté durant tota la transformació, permetent-nos monitoritzar la contracció mitjançant difracció de raigs X de monocristall.

Finalment, el capítol 6 presenta les troballes clau i les conclusions principals. A més, també ofereix valuoses idees sobre perspectives futures cap a la ruptura d'enllaços covalents en materials reticulars.

Acknowledgements

When I began writing this section, a flood of memories and thoughts filled my mind. During my five years stay as a PhD student in this group, I've witnessed numerous colleagues come and go. As I approach the end of my PhD journey, I am filled with immense gratitude for all those who have made my experience truly special, unforgettable, and wonderful.

First and foremost, I would like to express my sincere gratitude to my supervisor, Prof. Daniel Maspoch. Without your initial permission, I would never have the chance to start to do such incredible chemistry in my life. Your dedication, intelligence and the attitude toward science have a profound impact on me. I always looked forward to our meetings, during which I not only received valuable guidance but also was inspired by your passion for science. Thanks to your guidance, I've acquired certain skills in scientific research and gained the confidence to move forward into the next stage of my academic journey.

I would also like to thank another supervisor, Dr. Inhar Imaz, who played a crucial role in shaping my scientific mindset. Before, I was someone who would easily give up when faced with overwhelming project challenges, and you taught me that persistence and perseverance could sometimes work miracles. Meanwhile, I deeply cherish and appreciate the numerous brainstorming we've had together. I would like to give special recognition to Dr. Vincent Guillerm, who provided invaluable guidance during the first year of my PhD. Your profound expertise in the field of reticular chemistry has left an impression on me.

During my five years in NanoUP, I've been incredibly fortunate to collaborate with numerous amazing colleagues. I want to express my gratitude to our initial CLIPOFF-CHEM team, Borja and Anna. We started this project together and dedicated all our efforts to achieving the goal. I am deeply thankful to my bro, Borja, for the invaluable five years we've spent working side by side. We shared work, engaged in numerous discussions, and your continuous support during challenging times meant a great deal to me. Your intelligence and expertise have inspired me a lot, and I've learned a wealth of knowledge from you. I'd also like to extend my appreciation to the colleagues who joined the CLIPOFF-CHEM project later: Michele, Sofía, Marcel, Jorge, Roberto, Partha, Dongsik, and Juan Pablo. Jorge is such a clever guy and can often provide valuable suggestions. Roberto and Juan Pablo are quite good at making jokes. I am impressed by Partha's efficient management of various projects. I also feel fortunate to have the opportunity to get to know Dongsik. Although we only had a short time working together, your kindness, intelligence, diligence and passion for science has served as an extraordinary model for me. I enjoyed our discussions, not only about science but also about our shared culture. I truly believe that you will shine as an outstanding researcher with a promising future. I am also lucky

to have worked alongside Marcel for a year. Your warmth and kind-hearted nature added significance to each day we worked together. Michele's sweetness and his cherished "lucky ducks" will forever hold a special place in my heart.

Throughout these years away from my home country, I've never felt alone, thanks to the wonderful friendships I've made here. These friendships have been more than just connections--they've been profound bonds that have enriched my life. I cherish the moments we've shared, whether it was at Gerard's house for a barbecue or playing board games. Thais has always been a ray of positivity, and I appreciate her kindness. Xulián's humor has consistently brightened our office with laughter and enlightened our daily life. Xiang is a warm-hearted person, and I've enjoyed our conversations in our own dialect. I extend special thanks to my four lovely friends, Laura, Alba, Sara and Pilar, who make my PhD life vivid. Laura's kindness has always been a source of comfort. I love those tortillas she made and delightful dishes prepared by her mom. Alba "minion" has the most adorable smile and I've always enjoyed sharing a wide range of experiences with her, whether they be happy or sad. Sara's boundless energy and optimism have been contagious, and I especially love the conversations when both of us got drunk. Pilar is very mature and diligent, and I believe she will have a bright future. To all the members in NanoUP I have met during these five years—Mary, Sonia, Asier, Javier Fonseca, Mateo, Lingxin, Amir, Gerard Pena, Funda, Mateusz, Ceren, Xu, Civan, Najmeh, Yang, Jordi Martínez, Javier Pérez, Marta Ruiz, Heng, Jiemin, Farnoosh, Hosein, Susana, Arnau, Cornelia, Akim, Javier Troyano, Marta Sanmartí, Maria Àngels, and José— I treasure the memories of our beer celebrations each time someone had a publication. Besides, the group activities and Christmas dinners we enjoyed together made me feel like we are one big, united family.

I would also like to extend my gratitude to the collaborators who played an integral role in my PhD research: Prof. Felipe Gándara, Dr. Judith Juanhuix, Dr. Xavier Arqué, and Prof. Samuel Sánchez. Your contributions were instrumental in advancing our work.

I would like to express my special and heartfelt gratitude to my parents. Although I haven't seen you for years, I've missed you tremendously, especially during these past five years when many unexpected things happened around us. I am deeply sorry for not being able to be there with you. Your continuous support and endless love mean the whole world to me, and all I want to say is 爸爸妈妈，我爱你们！！

Finally, I want to express my heartfelt appreciation to my Chinese friends. In particular, I'd like to thank Junjie. We started this journey together, shared travels, and experienced the ups and downs of everyday life. Your support and help have been invaluable, and I hope our friendship endures for a lifetime. I'd also like to extend my thanks to Liming, Sen, Ze, Chen, and Yakun for all the support and

encouragement you've provided. Each of you holds a special place in my life, and I consider you all to be true treasures.

Chapter 1

Introduction

1.1 Metal-organic frameworks

Metal-organic frameworks (MOFs), a class of crystalline porous materials, have aroused considerable interest over the past few decades. According to the International Union of Pure and Applied Chemistry (IUPAC), MOFs are defined as coordination networks consisting of organic ligands with potential voids.[1] This definition highlights two key characteristics of MOFs. First, as coordination networks, MOFs can be considered as the self-assembly outcome of inorganic and organic moieties. By this means, different combinations of these two moieties can bring out a multitude of structures and functionalities of MOFs. Notably, the number of MOF structures deposited in the Cambridge Structural Database (CSD) has steadily grown, reaching to over 100000 in 2020 (Figure 1.1).[2,3] And second, MOFs exhibit confined voids, such as pores, which can range in size from micropores (< 2 nm) to mesopores (≤ 50 nm and ≥ 2 nm). It is worth mentioning that MOFs hold the experimental record for the highest Brunauer-Emmett-Teller (BET) surface areas among all reported porous materials, reaching a milestone of 7800 m²/g.[4]
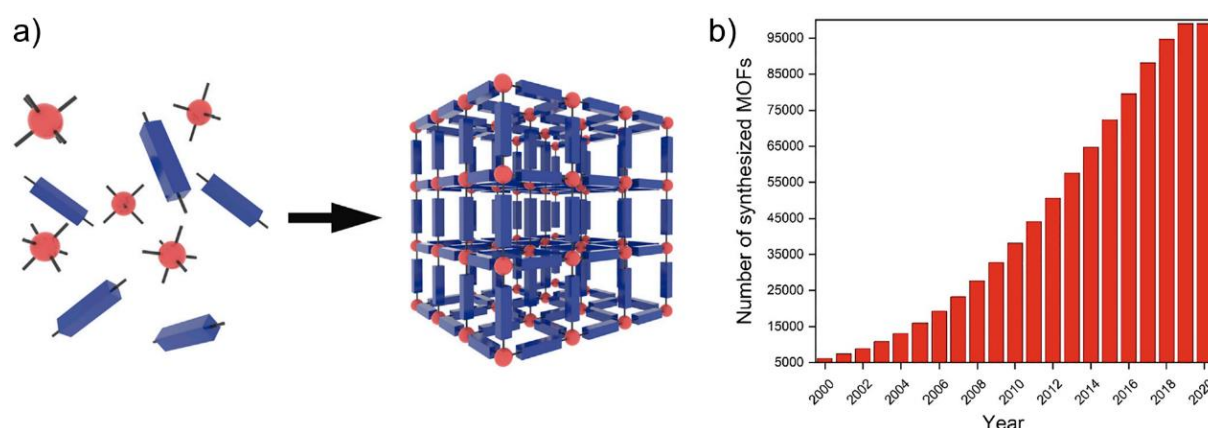
Figure 1.1 a) Scheme of the MOF formation.[5] b) The number of MOFs reported in the CSD from 2000 to 2020.[6]

1.2 Historical perspective

The development of MOFs, recognized as the coordination networks, can be dated back to the year of 1959 when Prof. Saito and co-workers reported a series of bis(alkylnitrilo)copper(I) structures by single-crystal X-ray diffraction.[7-9] Those structures were all built from tetrahedral $Cu(CN)_4$ building units. Due to different lengths and conformations of organic moieties, those building units could be further assembled into various dimensionalities: one dimensional (1D) chains, and 2D and 3D coordination networks.

In 1989, pioneering work was made by Prof. Hoskins and Prof. Robson who presented the synthesis of what they called "*infinite polymeric frameworks*".[10] They obtained the first 3D framework assembled from tetrahedral Cu(I) building units and tetratopic 4,4',4'',4'''-tetracyanotetraphenylmethane (TCTPM) organic ligands. The resultant framework with the formula [Cu(TCTPM)](BF$_4$) showed a non-interpenetrated and diamond-like lattice (**dia**). This framework was cationic and the counter ions BF$_4^-$ were charge-balanced and located inside the pores. Interestingly, upon exchanging between BF$_4^-$ and PF$_6^-$, the integrity of the framework could still be maintained. In the following year, they expanded their syntheses for obtaining "*scaffolding like materials*", analogous 3D diamond-like structures from different combinations of single metal ions and polytopic nitrogen-donor ligands.[11] More importantly, in this work, they envisioned that the final structure of the framework could be predicted and achieved based on node and spacer approach, which was proposed by Prof. A. F. Wells in 1977.[12] The neutral N-donor ligands used here can be regarded as spacers, whereas the single metal ions can be considered to be nodes. Later, lots of 3D networks have been greatly synthesized following this geometric design principle.[13-16]

The term metal-organic frameworks or MOFs was first proposed by Prof. Yaghi and co-workers in 1995.[17] It was initially utilized for the description and simplification of coordination networks from two aspects: the chemical composition (metal-organic) and the unique feature of the structure (frameworks). In their work, they synthesized a diamond-like 3D framework (**dia**) built up from a single metal ion, Cu(I), in trigonal planar geometry, and the linear ligand 4,4'-bipyridine (4,4'-bpy). The overall structure with the formula [Cu(4,4'-bpy)$_{1.5}$](NO$_3$) showed a cationic interpenetrated 3D framework with an underlying ThSi$_2$ (**ths**) topology, where counter NO$_3^-$ ions were situated inside the channels and could be readily exchanged with BF$_4^-$ or SO$_4^{2-}$, without interference of the whole framework integrity. Significantly, different from conventional diffusion method, this MOF was synthesized under hydrothermal conditions adapted from zeolite chemistry. Afterwards, hydrothermal or solvothermal synthesis has become very common for the synthesis of MOFs.

However, these early coordination networks displayed a major drawback. Because of the flexible and weak nature of the monodentate metal-nitrogen bond, the resultant materials did not show permanent porosity and their long-range order periodic structures were totally lost upon complete or partial removal of the guest solvent molecules inside the pores. This is also known as the "*first generation of MOFs*".[18,19] Based on this, Prof. Yaghi and coworkers reported the first MOF composed of a charged chelating ligand in 1995.[20] Instead of using neutral N-donor ligands, they synthesized a MOF with Co(II) and BTC ligands (BTC = 1,3,5-benzenetricarboxylate). In the structure, each single Co(II) center was six-coordinated by two pyridine and three carboxylates from three different tritopic BTC ligands. Among these three BTC ligands around the Co(II) center, only one BTC was fully deprotonated and coordinated in a bidentate fashion, while the other two BTC remain monodentate.

Because of the strong coordination bond formed by charged chelating ligands, this MOF showed extraordinary thermal and chemical stability. The integrity of the structure still remained after removing the pyridine molecules and only collapse at a temperature above 350 °C. Two years later, Prof. Kitagawa and coworkers reported a 3D MOF that was able to adsorb various gases (CH_4, N_2, CO_2) at 298 K under high pressure (1-36 atm), also confirming the porosity nature of MOFs.[21]

One of the greatest discoveries that has exerted a far-reaching influence on MOF chemistry is MOF-2 reported by Prof. Yaghi and co-workers in 1998.[22] Instead of monotonous single metal ion-based MOFs, they introduced polynuclear metal-based clusters into the MOF structure, which could ultimately enhance the rigidity and stability of the framework. In the MOF-2 structure, each bimetallic Zn(II) cluster forms a 4-connected paddle wheel $Zn_2(COO)_4$, which is linked by BDC ligands (BDC = 1,4-benzenedicarboxylate) to give a stacked 2-periodic crystalline framework with a square grid (**sql**) topology (Figure 1.2). The incorporation of the paddle-wheel building block in the structure provides MOF-2 with permanent microporosity, as confirmed by N_2 and CO_2 gas adsorption at 77 K and 195 K, respectively. Right after the publication of MOF-2, Prof. Williams and co-workers used the same concept to construct HKUST-1 through the assembly of dinuclear $Cu_2(COO)_4$ paddle wheel clusters and BTC linkers (Figure 1.2).[23] This 3D MOF exhibited high adsorption of N_2 molecules.
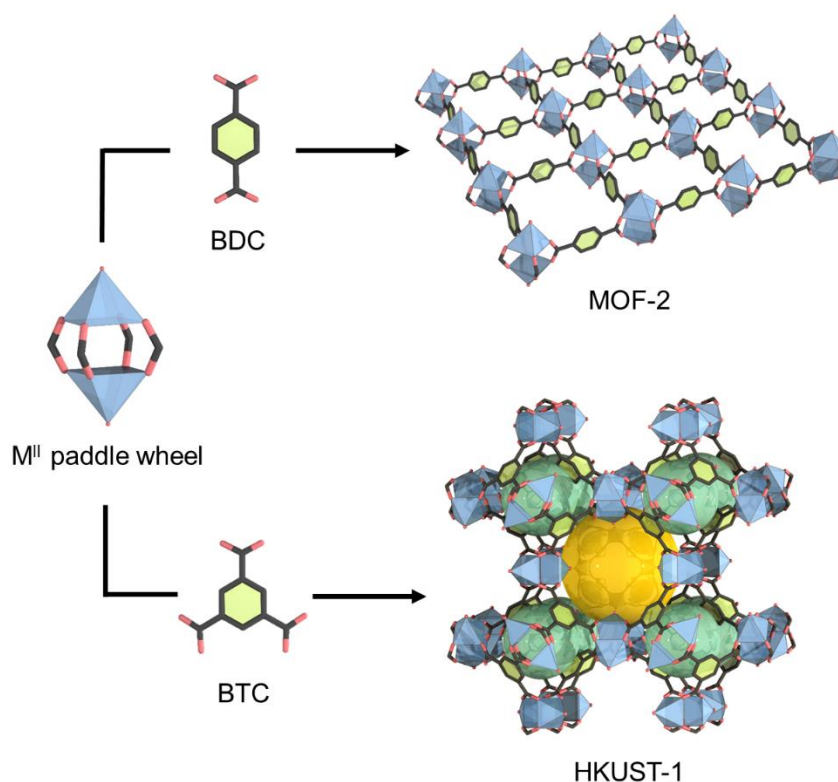
Figure 1.2 Assembly of a paddle wheel cluster with BDC or BTC forms the structure of 2-periodic MOF-2 or 3-periodic HKUST-1.

Since then, increasing the complexity of both polynuclear clusters and gas adsorption performance has become the main goal of this field. In 1999, Prof. Yaghi and co-workers synthesized MOF-5, which represents an iconic milestone in the development of MOFs.[24] In this work, they first introduced the concept of "*secondary building units*" (SBUs) for the description of well-defined polynuclear clusters. In this case, MOF-5 was constructed from octahedral $Zn_4O(COO)_6$ clusters and ditopic BDC ligands, forming a 3D framework with the underlying **pcu** topology (Figure 1.3). These inorganic clusters, in which each Zn(II) was adapted in a tetrahedral ZnO_4 fashion through a central oxygen atom, can greatly constrain the orientation of BDC ligands perpendicularly to one another, giving the resultant MOF-5 an exceptional architecture stability. The permanent porosity of MOF-5 was tested by N_2 adsorption at 77 K upon the evacuation of chloroform as guest molecules. The adsorption isotherm revealed its microporosity nature with a Langmuir surface area of 2900 $m^2 \cdot g^{-1}$ and a pore volume of 0.61 cm^3/cm^3. Remarkably, these two values were far beyond any reported records in zeolites and amorphous carbon materials.[25]
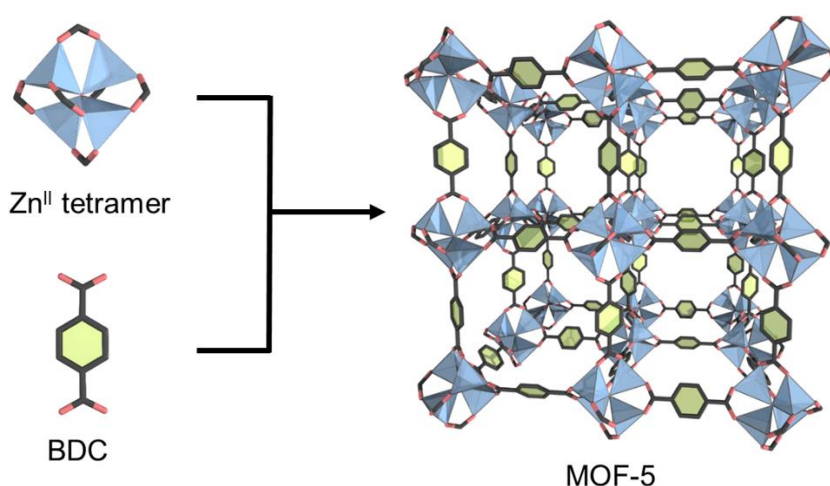
Figure 1.3 Assembly of octahedral Zn tetranuclear clusters with BDC forms the structure of 3-periodic MOF-5.

After that, there has been an explosive surge in research focused on MOFs, utilizing a wide range of building units. For example, Prof. Férey and co-workers reported the synthesis of MIL-series MOFs (MIL stands for Material Institut Lavoisier) based on trimeric SBUs, including the well-established MIL-53[26], MIL-100[27] and MIL-101[28]. In 2005, Prof. Yaghi and co-workers, as well as Prof. Dietzel and co-workers, independently synthesized MOF-74 (also known as CPO-27) based on infinite rod-shaped metal oxide building blocks.[29,30] Prof. Lillerud and co-workers first obtained UiO-66 (UiO stands for University of Oslo) in 2008.[31] This latter MOF is based on hexanuclear Zr(IV) clusters and it has attracted numerous attentions because of the extra high stability under water and acidic conditions (Figure 1.4).
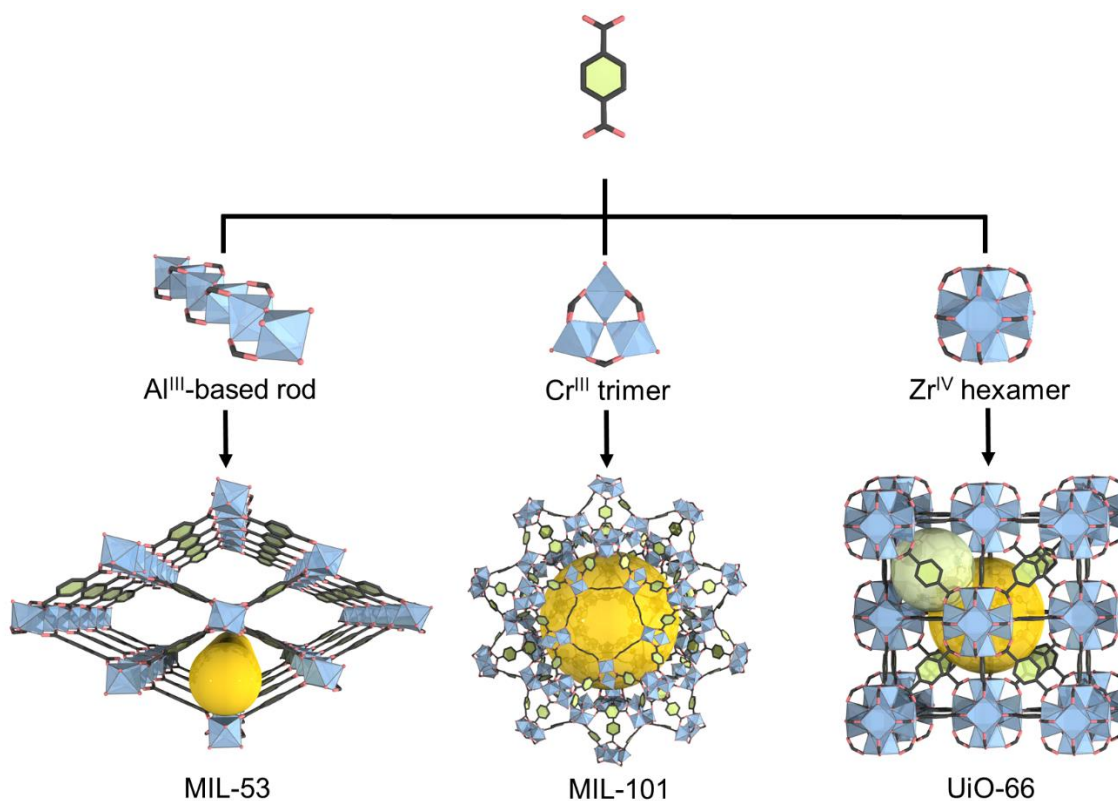
Figure 1.4 Assembly of different molecular building blocks with BDC forms various MOF structures.

1.3 Applications of MOFs

MOFs possessing high surface areas, structural diversity as well as tailorable pore sizes have been considered as the ideal candidates in various applications. In this section, some applications of MOFs will be briefly explained.

1.3.1 Gas adsorption

Gas adsorption including gas storage and sequestration has become a very important issue in industry. On one hand, developing a suitable technology will allow the ideal adsorbents to store fuel gases efficiently, such as methane, propane and hydrogen. On the other hand, it is crucial for adsorbents to sequester toxic gases, such as carbon monoxide, hydrogen sulfide and nitrogen dioxide, in a more energy-saving and eco-friendly way. Since the gas adsorption behavior will occur when the surface of the adsorbent poses a strong affinity to the certain gas, rational design and selection of the adsorbent has turned into a critical point. Nowadays, various types of porous materials like zeolites, activated carbon and silica have been widely studied and explored, but most of them failed to be designated or functionalized for a special need.[32,33] In this context, MOFs can be considered as potential candidates for gas adsorption owing to their high surface area, tailorable pore sizes and operative surface

functionalization. In this section, some of the representative examples toward certain gas adsorption in MOFs are discussed.

1.3.1.1 Methane storage

The increasing demand for crude oil has drawn tremendous attention to the sustainability of natural resources and environmental issues. The significant emission of carbon dioxide (CO_2) during the combustion of fossil fuels in power plants and vehicles has made it essential for humans to be aware of the severity of the global warming. Methane (CH_4), the major component of natural gas, is considered as a promising and alternative fuel to replace the crude oil due to the following two aspects: first, methane is affordable and environmentally sustainable in comparison to conventional liquid fossil fuels; and second, the combustion of methane is releasing small amounts of CO_2 per unit of heat owing to its high hydrogen to carbon ratio.[34-36] However, methane has a low volumetric energy density of 0.12 % (*i.e.* the amount of the energy released per unit volume of methane during the combustion) in comparison to that of the liquid fossil fuels, which severely constrains its widespread use.[36] Therefore, it is desirable to find ways to store high amounts of methane in a compressed manner. One possible solution is to use porous materials to adsorb methane, as these materials can maximally confine and store high densities of methane molecules. Furthermore, compared to conventional technologies such as compression at high pressure (*e.g.* 200-250 bar) or liquefaction at low temperature (*e.g.* 112 K)[37-39], keeping methane molecules in porous materials allows for packing the same or greater amount per unit volume under feasible pressure and temperature conditions. This approach potentially avoids safety risks and reduces costs.

To promote the widespread commercialization of alternative fuels, U.S. Department of Energy (DOE) standardized metrics for the development of methane onboard storage.[40] The targeted gravimetric storage capacity is 0.5 $g \cdot g^{-1}$ (meaning 0.5 g of methane in 1 g of adsorbents), and the volumetric target is 263 cm^3 (standard temperature and pressure, STP)$\cdot cm^{-3}$. In 2020, Prof. Farha and co-workers synthesized a record-breaking MOF material, NU-1501-Al, which is based on the Al_3O trimer cluster and hexatopic linker.[41] This MOF has shown the highest gravimetric CH_4 uptake at 100 bar, both at 296 K (0.54 $g \cdot g^{-1}$) and 270 K (0.66 $g \cdot g^{-1}$), among all reported MOFs, surpassing the standard recommended by the DOE (Figure 1.5).
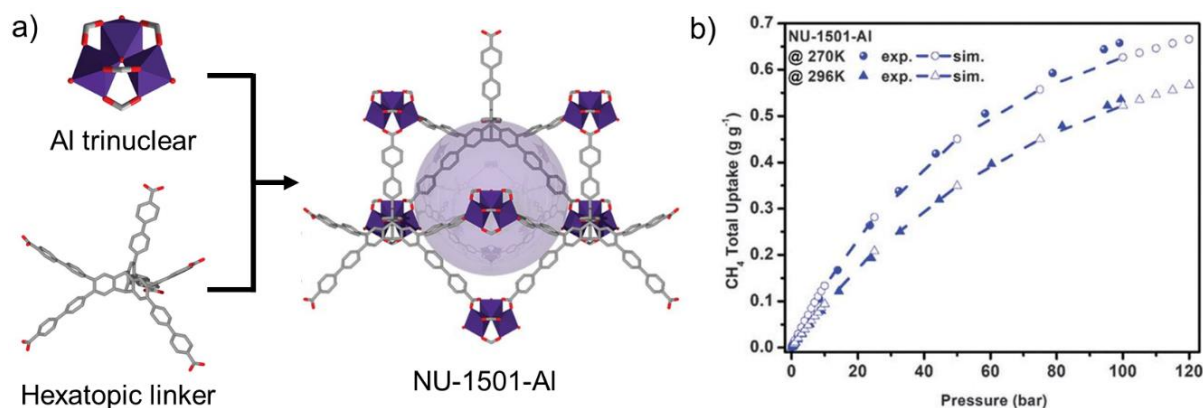
Figure 1.5 a) Schematic representation of the crystal structure of NU-1501-Al. b) Methane uptake of NU-1501-Al at 270 K and 298K.[41]

1.3.1.2 Carbon dioxide capture

Carbon dioxide (CO_2) is the major contributor to the rise in global temperatures. Since the early 1800s, overall CO_2 emissions have dramatically increased to nearly 2 times higher than before.[42] It is urgent to limit the CO_2 emissions, particularly from anthropogenic sources. Currently, a significant amount of CO_2 emissions comes from the combustion of fossil fuels in power plants. While developing alternative, cleaner, carbon-free fuels such as solar and wind power can radically transform the energy infrastructure and reduce reliance on natural resources, the use of fossil fuels is still dominant.[43] Therefore, it is essential and highly valuable to explore strategies that can effectively capture and store CO_2 before its release. Considering that flue gas from stationary power plants contains only 15-16% CO_2, potential candidates for CO_2 capture should be capable of operating under low pressure and even humid conditions.[44-47]

MOFs, due to their unique structural diversity, have shown their potential use for CO_2 capture. So far, there are two main strategies to enhance CO_2 capture in MOFs: utilizing unsaturated metal sites and chemical functionalization inside the pores. Unsaturated metal sites can be considered as Lewis acid, allowing CO_2 molecules to bind to these metal centers through dipole-dipole interactions.[48-53] MOF-74, which possesses high-density unsaturated metal sites, is a promising candidate. Prof. Matzger and co-workers reported that Mg-MOF-74 has a record-high CO_2 uptake value, providing an uptake of 23.6 wt % at 0.1 atm (Figure 1.6).[54] Subsequently, Prof. Queen and co-workers studied how different types of unsaturated metal sites can affect CO_2 adsorption capacity in MOF-74.[55] They synthesized a series of MOF-74 structures based on various metals types and observed that the CO_2 uptake increased with changes in the metal source at low pressure, following the order of Mg^{2+}, Ni^{2+}, Co^{2+}, Fe^{2+}, Mn^{2+}, Zn^{2+}, and Cu^{2+}. However, when the MOF was exposed to more realistic conditions where water vapor was

present in the flue gas, water molecules would compete with CO_2 for binding to the unsaturated metal sites, resulting in the reduced CO_2 adsorption capacity.[56-60] To address this challenge, chemical functionalization of MOFs has become a prevalent strategy. This functionalization can be achieved through ligand decoration or post-synthetic appending of amine groups. In the latter approach, a common design involves the use of alkyldiamine-appended MOFs, where diamines bind to unsaturated metal sites. In this context, CO_2 can selectively react with diamines and be inserted into metal-amine bonds, leading to the formation of ammonium carbamate chains.[61-68] A very recent study by Prof. Long and co-workers showed that a MOF-74 analogue, $Mg_2(olz)$, could be functionalized with nine different $1°,1°$-, or $1°,2°$-, or $1°,3°$-diamines. A specific MOF, denoted as ee-2–$Mg_2(olz)$, functionalized with N,N-diethylethylenediamine, was chosen for detailed CO_2 adsorption studies (Figure 1.6).[69] In a simulated coal flue gas stream containing 15% humidified CO_2 in N_2, ee-2–$Mg_2(olz)$ was able to capture 90% of the CO_2. Exposure and cycling tests were conducted to demonstrate the stability and reusability of this MOF, showing that ee-2–$Mg_2(olz)$ maintained excellent CO_2 adsorption capacity of 15.5 g/100 g and the long-term stability over 1000 adsorption-desorption cycles under simulated humid flue gas conditions.
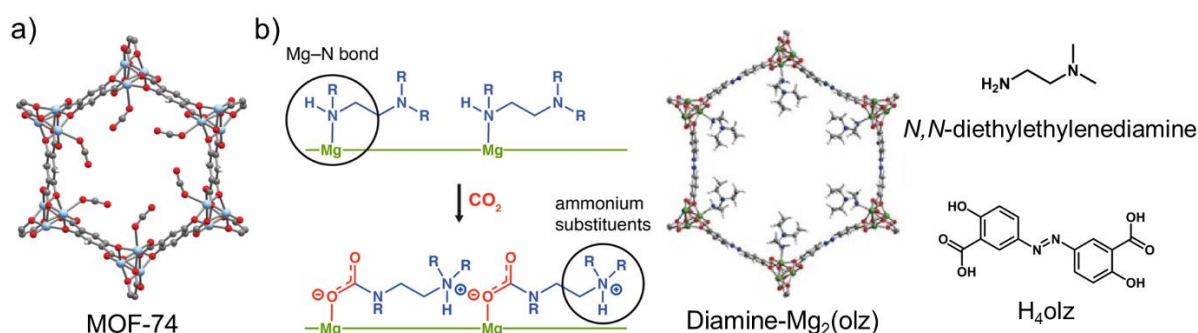
Figure 1.6 a) Crystallographic structures of MOF-74, $Mg_2(dobdc)$, showing the interaction between CO_2 and activated magnesium(II) sites.[55] b) Schematic illustration of CO_2 insertion into diamine-$Mg_2(olz)$ to form ammonium carbamate.[69]

1.3.1.3 Water harvesting

Water is indispensable for human life. However, only 2.5% of the Earth's water is freshwater, and nearly four billion of the population are living in water-stressed regions. This global challenge calls for increased efforts to find solutions.[70-72] The majority of water on Earth, about 96.5%, is found in oceans, but purifying seawater through processes like desalination is complex and energy-intensive.[73,74] One alternative strategy is to extract water from the atmosphere, which requires the use of water adsorbents

that meet specific criteria: they should be stable enough in water during repeated cycles, capture water at low relative humidity (RH), and maximumly release water in an energy-saving manner.[71,75,76]

In 2017, Prof. Yaghi and co-workers developed the first water harvesting device to test its viability. The device consisted of an enclosure with a lid containing activated MOF-801 and a condenser (Figure 1.8). The water harvesting experiment was conducted on a building´s roof and later in the Arizona desert.[77,78] The MOF-801 adsorbent (1.8 g) began capturing water from the ambient air at night. Once saturated, the enclosure was sealed to create a closed system. The desorption process occurred when the device was exposed to natural sunlight during midday, causing the water to be released and condensed on the cooled condenser. However, the device only yielded water droplets, and no significant water collection was achieved. Inspired by these results, the same group optimized the apparatus by loading kilograms of MOF-801 to collect a considerable amount of water.[79] The improved apparatus consisted of two boxes, with the smaller one fitted inside (Figure 1.8). The smaller box, open and loaded with MOF-801, was placed within the outer box, which had a lid that could be opened at night and closed during the day. In this configuration, the inner wall of the outer box acted as the condenser, and part of the device was covered with soil to maximize the temperature difference between the inside and outside of the outer box. Remarkably, using 0.825 kg of MOF-801, they were able to collect 55 mL of liquid water in the Arizona desert. However, there are still some issues that need to be addressed to optimize the efficiency of water harvesting. The inner box used in this setup did not provide full accessibility of the MOF to the air, which may have resulted in a lower water productivity than expected. Additionally, the low heat conductivity of MOF-801 affected the kinetics of water release.

The discovery of MOF-303 has enabled MOFs to fully realize their potential as water adsorbents in practical applications. MOF-303 is constructed from an infinite 1D Al-oxo chain and HPDC (1H-pyrazole-3,5-dicarboxylate). This MOF possesses unique features: the strong Al-O bonds can prevent the hydrolysis, ensuring exceptional stability in water over multiple cycles; the pyrazole-based linkers can create hydrophilic sites inside the 1D channel for rapid water adsorption; and the use of inexpensive Al(III) sources allows for large-scale preparation of MOFs.[76,80,81] In 2019, Prof. Yaghi and co-workers tested MOF-303 for water harvesting in the Mojave Desert, the most arid area in North America. Instead of using the abovementioned passive devices, they invented a new one powered by solar panels that utilized fans to facilitate airflow through the MOF-303 cartridge (Figure 1.8).[82] Surprisingly, this device was capable of delivering 0.7 L water/kg of MOF per day, representing an improvement of nealy one order of magnitude compared to previous water harvesting devices. In 2023, Yaghi and co-workers designed a new passive device for water harvesting.[83] This device has two separated compartments: a cylinder-shaped MOF cartridge and a condenser (Figure 1.8). The MOF cartridge contains a pellet made of MOF-303 mixed with graphite to enhance thermal conductivity and mechanical properties. The pellet is loaded into the cartridge along with porous Ni foams to maximize airflow diffusion and heat

conduction. Water harvesting experiments were conducted in Death Valley under extremely dry and hot conditions. As a result, the device containing MOF-303 achieved a water productivity of 210 g water/kg of MOF per day, showing the highest water productivity among reported passive devices.
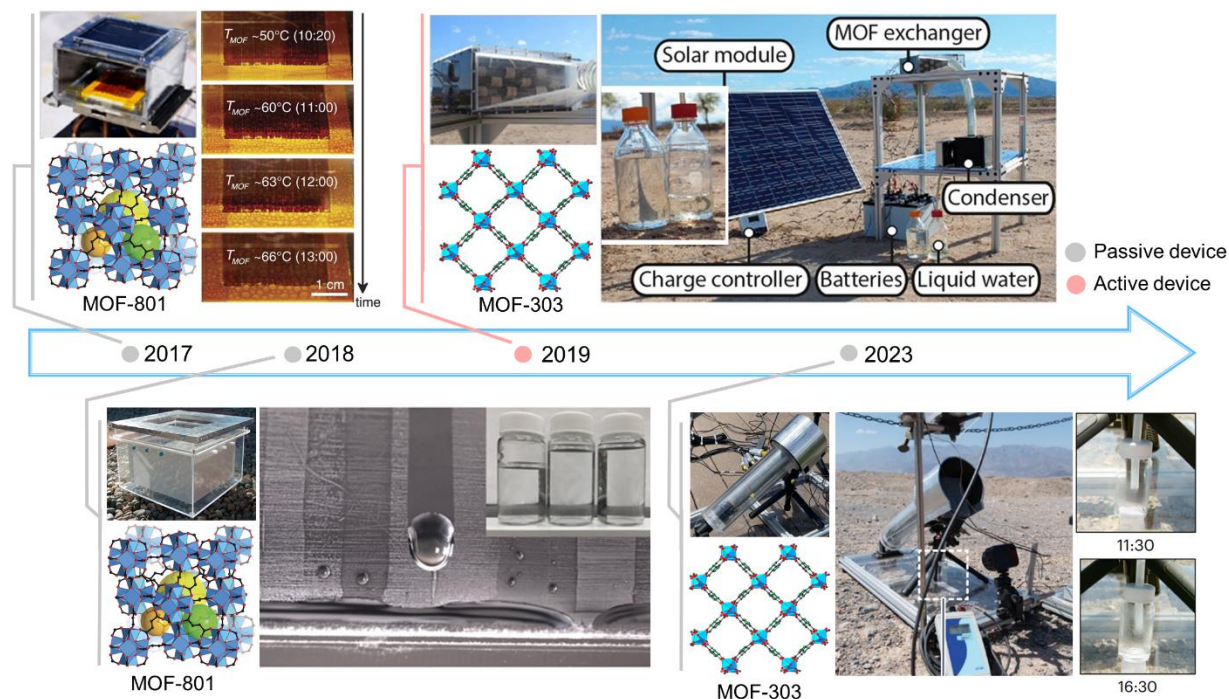
Figure 1.8 Evolution of the used MOFs and related devices for water harvesting.

1.3.2 MOF-based swimmers

The development of miniaturization from macroscopic swimmers to micro/nanoscale replicas is indispensable in multidisciplinary fields.[84] These tiny self-propelled machines, inspired by biomolecular machines found in animals, individual cells or micro-organisms, are capable of swimming in certain fluids through interfacial reactions with the surrounding environment or external forces such as light,[85,86] magnetic fields[87] and electric fields[88]. Due to their capability of autonomous locomotion, these artificial swimmers have garnered interest in a myriad of applications including sensors[89,90], therapeutic mobile carriers[91] and environmental remediation[92].

MOFs, owing to their ordered structures, high accessible surface area and tailorable pore sizes, have become attractive candidates and have shown promise as autonomous swimmers. During the synthesis of MOFs, many guest molecules with a wide range of sizes, such as drugs and active biomolecules, can be incorporated, offering a promising loading capacity.[93-97] In addition, these molecules can engage in specific interactions within the pre-existing structure of the MOF, either through pore or surface chemistry. This provides an additional opportunity for incorporating external complexes into the

MOFs.[98-102] This section will place special emphasis on catalytically-driven MOFs-based micro/nano swimmers.

1.3.2.1 Catalytically-driven MOF-based swimmers

Catalytically-driven swimmers, also known as micro/nanomotors, are mainly based on converting chemical energy into mechanical motion.[103,104] It involves introducing an additional fuel supply into the swimming environment, initiating a certain catalytic reaction within the MOF particle. This reaction generates products that, in turn, propel the micro/nanomotors into autonomous motion.

One method to achieve the locomotion of the motor is to create the bubble ejection.[105,106] In this case, hydrogen peroxide (H_2O_2) is widely used as the fuel for catalysis. The decomposition of H_2O_2 generates and expels oxygen bubbles in the swimming environment around the motor, resulting in the propulsion of the MOF particle.

One strategy for catalyzing H_2O_2 is to use metals, alloys or metal oxides. Prof. Chin and co-workers reported the first catalytic propulsion in MOFs based on Janus particles.[107] They first partially embedded ZIF-8 crystals with a poly(methyl methacrylate) (PMMA) film, allowing the exposed surface of ZIF-8 to be further covered with a ZIF-67 layer through epitaxial growth. Subsequently, the PMMA film was washed away with ethyl acetate, resulting in the formation of ZIF-67/ZIF-8 Janus particles. The motion of Janus particles was propelled by O_2 bubbles, where Co(II) nodes from ZIF-67 prompted the decomposition of H_2O_2. In 2016, Prof. Maspoch and co-workers prepared a monolayer of MOFs (ZIF-8, UiO-66) on a substrate through drop casting.[108] This monolayer was then sputtered with one or more layers of various metals (Co, Au, or Pt), resulting in the formation of Janus particles. Among them, ZIF-8 covered with asymmetric Pt layer, denoted as Pt@ZIF-8, showed good motion ability upon the addition of H_2O_2 through bubble propulsion (Figure 1.11). Instead of MOF-based Janus motors, in 2017, Prof. Cohen and co-workers proposed a different approach to incorporate metals.[109] They synthesized UiO-67 using mixed ligands, dcbpy (2,2'-bipyridine-dicarboxylate) and bpdc (biphenyldicarboxylate). By post-synthetical metalation of bipyridine sites with catalytically active metal centers (cobalt or manganese), the resulting MOF could achieve catalytic motion through bubble propulsion upon the addition of H_2O_2. The speed of the motor could be adjusted by choosing the metal centers (Figure 1.11). Furthermore, the motor was able to brake chemically by introducing acidic chelators, iminodiacetic acid (IDA) or ethylenediaminetetraacetic acid (EDTA). These acids were used to completely remove the metals from the MOF, resulting in the loss of motor propulsion.
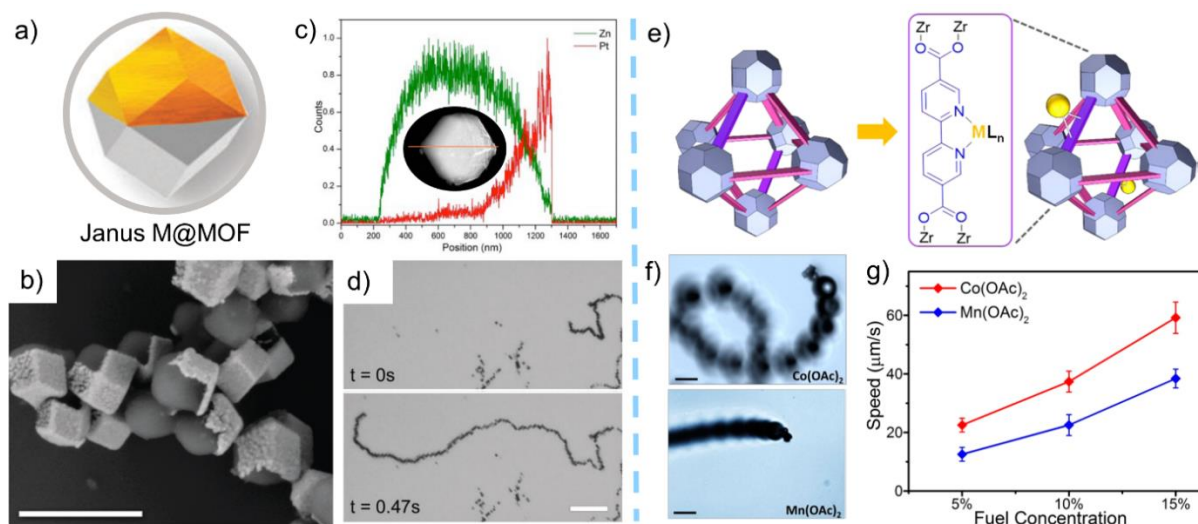
Figure 1.11 MOF motion driven by the catalytic reaction. a) Scheme of Janus metal@MOF particle. b) SEM image of Janus Au@MOF particles showing the asymmetric Au layer on ZIF-8 particle. c) EDX mapping of Janus Pt@MOF particle showing the elementals (Zn and Pt) distribution. d) Optical microscopy images of motorized Pt@ZIF-8 particle at different catalysis time.[108] e) Scheme of the metalation process in Zr-MOF. f) Optical microscopy images of motorized Zr-MOF with different metal sources. g) Tuning the speed of motorized Zr-MOF with different metal sources.[109]

Another strategy to catalyze H_2O_2 is by using enzymes. Prof. Ma and co-workers reported dual enzyme-functionalized ZIF-8 encapsulated with upconversion nanoparticles (UCNPs) and photosensitizers (PSs) for cancer treatment.[110] Two types of enzymes, glucose and catalase, were bounded onto the surface of ZIF-8, triggering two enzymatic cascade reactions for both motor motion and therapeutic effects. In particular, glucose was decomposed into H_2O_2 by glucose oxidase as the catalyst. The generated H_2O_2, when encountered with catalase, further converted into H_2O and O_2. The O_2 molecules not only created bubbles for the propulsion of the motor motion, but also converted into the singlet oxygen state for photodynamic therapy (PDT) process (Figure 1.12).
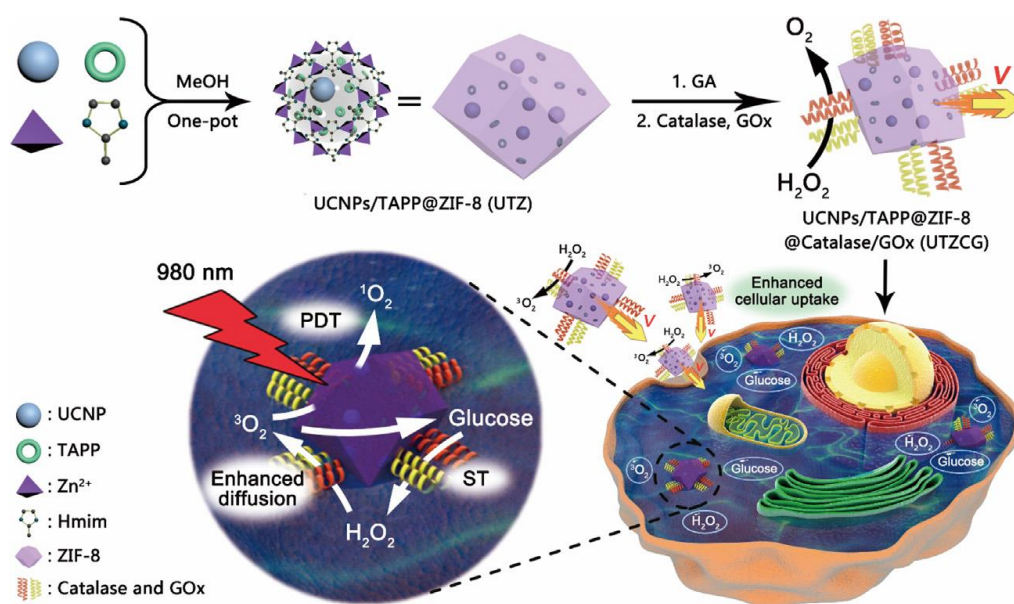
Figure 1.12 Schematic illustration showing the motor motion based on ZIF-8 particle triggered by two enzymatic cascade reactions.[110]

1.4 Bond forming process: MOF synthesis and reticular chemistry

One of the most fascinating aspects in MOFs is that their crystalline structures can be designed based on the specific knowledge of their chemical compositions. In particular, the emergence of reticular chemistry has facilitated the synthesis of a growing number of novel MOF structures with unique pore shapes, sizes and functionalities.

Reticular chemistry refers to *the chemistry of linking molecular building blocks by strong bonds to make crystalline open frameworks*.[111,112] In this context, strong bonds in reticular chemistry indicate not only covalent bonds but also metal-charged ligand bonds, which significantly differentiates from the early discovery of coordination networks and expands its scope to other reticular materials such as covalent-organic frameworks (COFs) and metal-organic polyhedra (MOPs).[113-115] Reticular chemistry enables the predesign of a suitable net as a blueprint, and the molecular building blocks encoded with desired constrains in geometry, directionality and rigidity can be implemented to achieve the final targeted framework. While synthesis may sometimes encounter challenges in practice, the knowledge gained can further enhance the delicate design under the guidance of reticular chemistry.

In the following sections, a general introduction to topology will be provided to describe the underlying nets and design principles through reticular chemistry.

1.4.1 Topology of MOFs

MOFs, owing to their long-range order periodic structures, can be abstracted and simplified into their network topology, known as underlying nets. The analysis of the underlying nets of MOFs allows scientists to identify and classify numerous MOF structures from databases, and these underlying nets can serve as blueprints for the judicious design of new frameworks.

The topology analysis of MOFs is typically conducted through the calculation of coordination sequences and vertex symbols.[116,117] Various software tools are available for determining the underlying nets. One commonly used software is TOPOS[118], which is based on a comprehesive database. Another tool is Systre[116,119], which is associated with RCSR (Reticular Chemistry Structure Resource) database and capable of identifying new nets not included in the RCSR.

The RCSR database, developed by Prof. O'Keeffe and co-workers[119], is a collection of existing nets. It contains a multitude of underlying nets in the field of reticular materials, and the related topology for each net is described using a bold lowercase three-letter code. The terminology of these codes or symbols inside the database can be considered as derivatives from several sources: (1) the known solids, such as diamond (**dia**), fluorite (**flu**), Nb_2O_5 (**nbo**); (2) the intrinsic connectivity or geometrical building units of a given net, such as face-centered cubic (**fcu**), square and cube (**scu**), square and octahedron (**soc**); (3) zeolite database, such as MTN (**mtn**), SOD (**sod**), RHO (**rho**); and (4) author's name or choice, such as Zhiyong Guo (**zyg**), Nottingham (**ntt**), Queen of MOFs (**qom**).

1.4.2 Molecular building blocks and secondary building units

To describe each organic or inorganic node for the targeted design and synthesis of MOFs, it is essential to introduce molecular building blocks (MBBs) and secondary building units (SBUs). MBBs stand for chemical entities, including their detailed composition, while SBUs represent the geometrical entities by connecting their points of extension (*e.g.* carbon atoms from carboxylates are the points which link to the organic moiety) from a given MBBs.[120-122] For instance, a 12-c hexanuclear cluster can be considered as an MBB, and by connecting its points of extension, a SBU with cuboctahedral shape is formed (Figure 1.13).
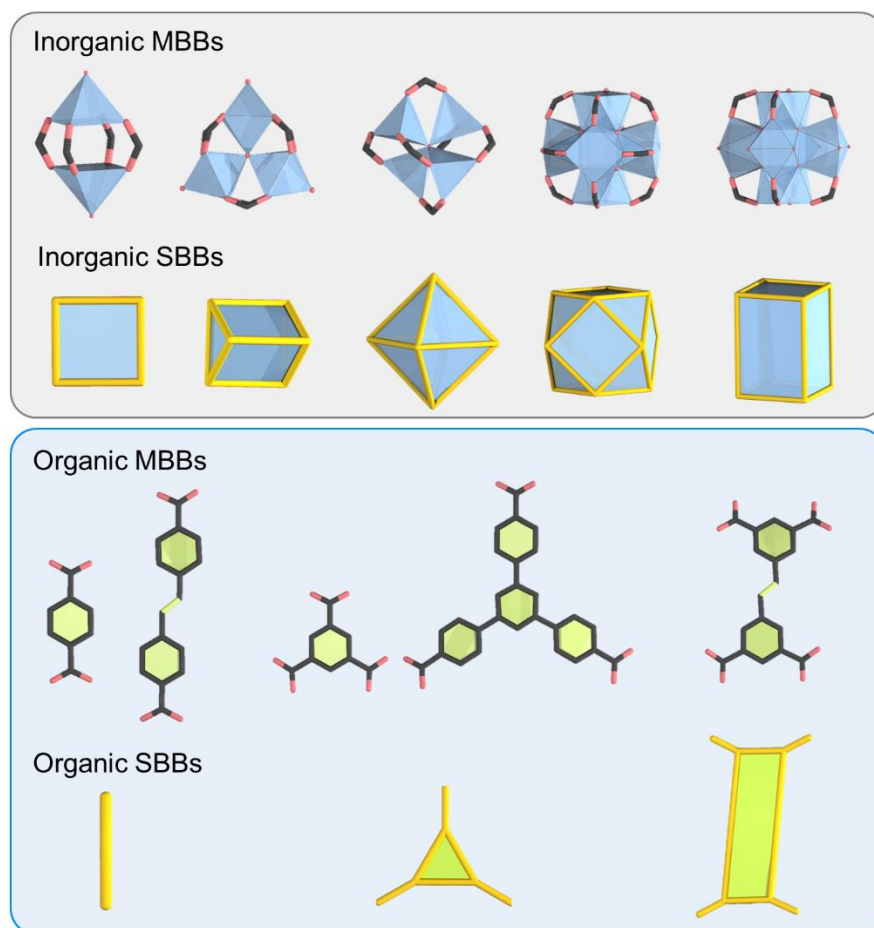
Figure 1.13 Representation of some common MBBs and their corresponding SBBs.

1.4.3 Reticular design principle

Based on the above mentioned, an entire network topology can be regarded as the combination of different sets of organic and inorganic SBUs encoded with special geometrical constrains. Thus, for the synthesis of targeted MOF structures, predetermining an ideal net as a blueprint and rational design of these related building blocks are highly valuable. Based on this, various design routes are discussed in this section.

1.4.3.1 Molecular building block (MBB) approach

The MBB approach has become a prevailing and dominant strategy for the synthesis of novel MOFs. Briefly, it started with the careful analysis of the organic and inorganic SBUs from the targeted underlying net. Then, any MBBs of interest, including organic linkers and inorganic clusters, that represent the same directionality and connectivity as those SBUs can be judiciously designed prior to

the assembly process. In this way, MOFs with desired topology are possible to be synthesized (Figure 1.14).

In general, there are two ways to implement MBBs, particularly inorganic MBBs, into the desired structure. One is to synthesize the requisite inorganic MBBs in-situ, which requires the appropriate synthetic condition. Another way is to use pre-assembled inorganic MBBs with designed connectivity and geometry.[123,124] In this case, the solubility of the inorganic cluster is the key point.
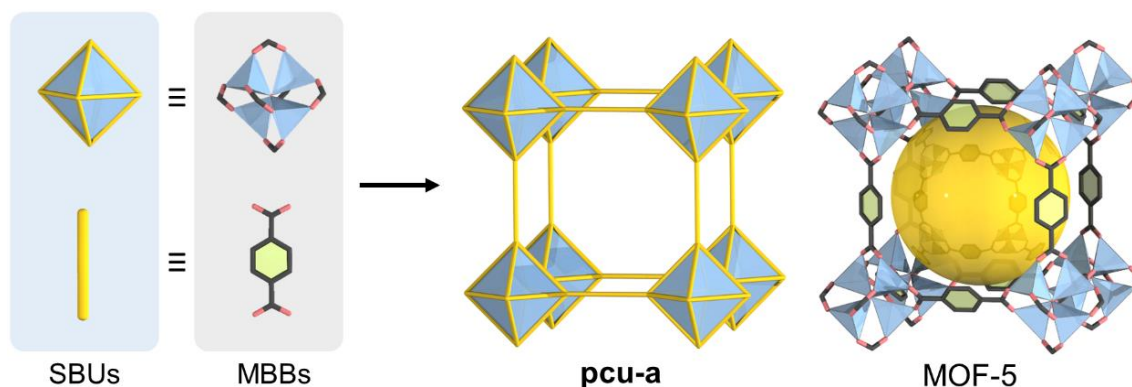
Figure 1.14 Representation of the synthesis of MOF-5 by using the MBB approach.

1.4.3.2 Supermolecular building block (SBB) approach

SBB approach refers to the assembly of externally functionalized metal-organic polyhedra (MOPs) into targeted MOFs, giving the final structure with a highly connected net.[125-127]

Similar to the mentioned above, the formation of MOPs as SBBs can be formed in-situ or pre-assembled prior to the synthesis. For example, MOFs with **rht** topology was first discovered to describe this concept.[128-133] This **rht**-MOF has its unique binodal (3,24)-connected net which is composed of 24-connected rhombicuboctahedra (**rco**) and 3-connected triangles. Here, 3-connected (3-c) triangles can be viewed as the central core of organic ligands, whereas the 24-c **rco** is considered as the combination of 12 4-c Cu(II) paddle wheels and 24 isophthalates ligands when 5-position of the isophthalates are acting as the functionalized vertices. This polyhedron has been recognized as the well-known MOP-1 (Figure 1.15).[134] It is noteworthy that the geometry of the MOP as a SBB can differ a lot depending on the decorated vertices of the linkage. That is to say, MOP-1 can also be seen as the 12-c cuboctahedron (**cuo**) when axial positions of the paddle wheels are counting as vertices. When this 12-c cuboctahedron is further linked by a 4-c square, a highly connected MOF with **ftw** topology is formed (Figure 1.15).[135]
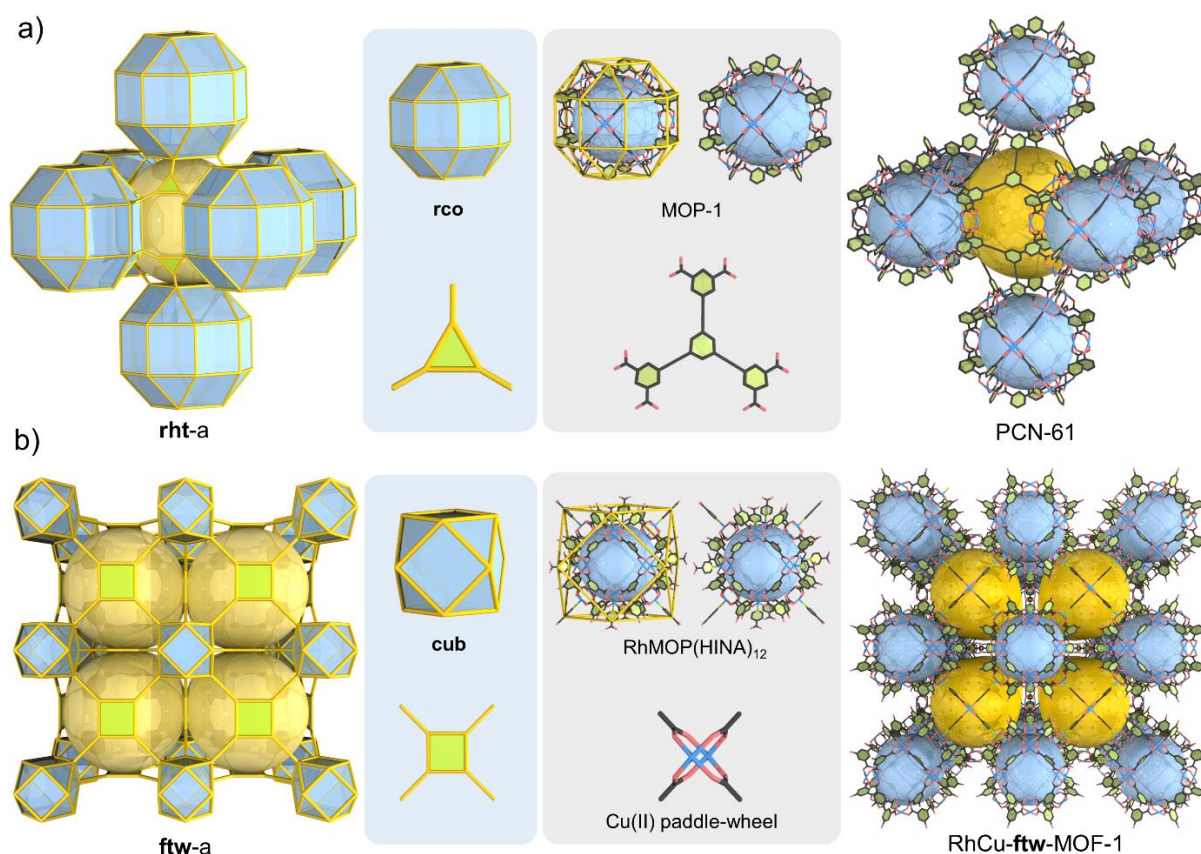
Figure 1.15 Representation of the syntheses of a **rht**-MOF and a **ftw**-MOF by the SBB approach.

Besides MOP-1, other types of polyhedra as SBBs can also be implemented into the structure, promoting the formation of targeted MOFs with desired topologies. For example, octahedron (**oct**) and elongated triangular orthobicupola (**ebc**) MOPs allow to give their related MOFs with 6-c **pcu**[136,137] and (3, 18)-c **gea**[138] nets, respectively.

1.4.3.3 Supermolecular building layer (SBL) approach

SBL approach is introduced to describe 3-periodic pillared MOFs by linking 2-periodic layers.[139] Actually, many 3-periodic MOFs with their underlying nets can be destructed into this type. The isolated metal-organic 2D layers, considered as the building block, are able to construct a series of MOFs with unlimited confined spaces (pores or cavities). Here, the critical point is to design organic linkers for pillaring those layers.

One successful example for implementing this SBL approach is the well-known HKUST-1 with **tbo** topology.[139] This structure can be destructed into 2-periodic square lattice (**sql**) layers linked by the pillars, 4-c Cu(II) paddle wheels as the central cores. Further by substituting paddle wheel structures

with various organic linkers having the same geometry, a series of **tbo**-MOFs with different pore sizes were successfully synthesized.

1.4.3.4 Isoreticular principle

Isoreticular principle is widely used for the synthesis of novel MOFs through rational design. The main objective of this strategy is to tune the ligands or metal clusters inside the framework without affecting their underlying nets. So far, there are three existing ways to achieve this goal.

1.4.3.4.1 Substitution or modification of the building blocks

The modification of the building blocks here refers to the ligand functionalization. The common way is to introduce specific functional groups inside organic linkers toward certain property or application. An interesting example is to synthesize MOF-5 analogues functionalized by BDC linker with long alkyl side chains so that a certain degree of the frustrated flexibility appears inside MOF-5 upon desolvation.[140] Substitution of the building blocks mainly focuses on the replacement of the metal clusters and organic linkers. Replacing metal clusters by using different metal sources requires the formed clusters have the same connectivity and geometry. For example, Zr hexanuclear clusters in UiO-66 can be replaced by Hf and Ce analogues.[141,142] The replacement of the organic linkers, involving the post-synthetic modification and bond-breaking process, will be discussed in the next subchapter of this dissertation.

1.4.3.4.2 Expansion or contraction of building blocks

Expansion or contraction of building blocks is only limited to the organic linkers. The length between the central core and chelating moieties of the organic linker can be designed and implemented into the framework, resulting in the change of the whole lattice or pore sizes. The best example is the isoreticular synthesis of MOF-5 from a series of organic linkers with different lengths. In this family of MOF-5 analogues, the pore sizes are in the range of 3.8 to 28.8 Å (Figure 1.16).[143]

1.4.3.4.3 The multivariate approach (MTV)

The multivariate approach aims to employ more than one types of metal clusters or organic linkers into the framework for increasing the whole complexity. It should be noted that a multivariate MOF means that various chemical species (multiple metals or ligands) have the same equivalent positions in the framework but they are not periodically occupying in the crystal structure. Thus different combinations of those species should be observed in the multivariate MOF. So far, up to 10 different

types of metals could be incorporated into the rod building block of MOF-74,[144] and up to 8 different ligands were simultaneously incorporated in the structure of MOF-5.[145]
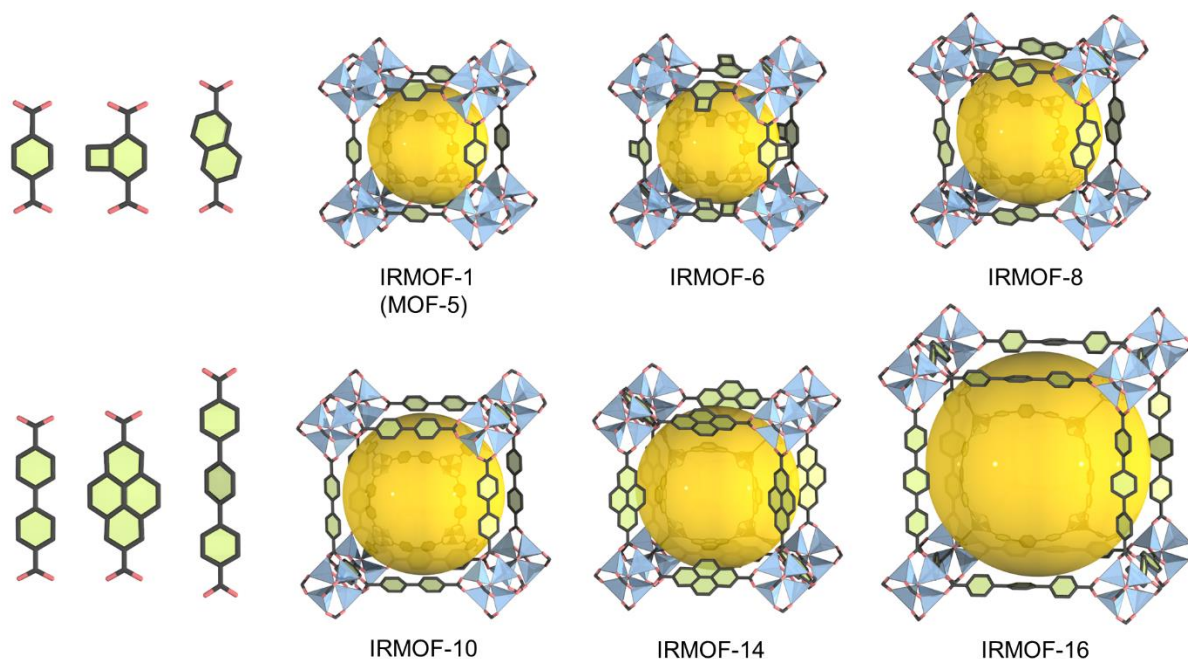
Figure 1.16 Ligands used for the syntheses of isoreticular IRMOFs and their corresponding crystal structures.

1.5 Bond breaking process: post-synthetic MOF deconstruction

The implementation of reticular chemistry into MOFs has successfully expanded the structural diversity and potential applications of MOFs. However, the formation of various chemical bonds during synthesis introduces uncertainties in achieving the desired products. For example, while 2D layered MOFs can be obtained directly, the synthesis of ultrathin (multilayer or even single-layer) MOF nanosheets is still highly demanding. This is because the bulk 2D MOF crystal has a strong bonding within the plane, whereas the interlayer is often connected by weak interactions. Thus, the formation of weak interactions during synthesis may hinder their broad use in the field of electronic devices, separation and sensing.[146,147] Another example is the design of hierarchical pores in MOFs. Hierarchically porous MOFs (HP MOFs), which contain multiple ranges of porosities, exhibit the unique characteristic of integrating micropores and mesopores/macropores, potentially solving mass transfer issues when used as catalysts.[148,149] Currently, a major challenge is to synthesize HP MOFs. By simply elongating the ligand through the isoreticular principle, the resulting framework may lead to self-dual interpenetration such as in well-known IRMOF-15[143], UiO-69[150]. An alternative approach is to introduce monodentate modulators to create defects during synthesis, but only a few reported systems

have limited their widespread utilization.[151-153] Therefore, finding a feasible and general strategy to overcome these difficulties is of great importance.

Contrary to the bond forming process (bottom-up), bond breaking from an existing MOF (top-down) has gained increasing research interest.[154,155] This approach allows to break certain type(s) of bonds selectively inside an already made MOF and the ultimate modified structure can still maintain its crystallinity. In this case, bond breaking inside the MOF can be considered as the post-synthetic deconstruction process in which MOF served as the precursor is able to moderately tailor its constituents and consequently transform into a new material with distinct characteristics. Based on this, an ultrathin layer is possible to be obtained from the bulk 2D MOF materials through breaking weak interactions between layers. Similarly, breaking coordination or covalent bonds in a microporous MOF and removing the corresponding fragments can lead to the synthesis of HP MOFs.

Overall, the deconstruction of MOFs through bond breaking allows for the creation of daughter MOFs with new functionalities, including the generation of defects, hierarchical pores and novel morphologies. It is important to note that both the parent and daughter MOFs should maintain their crystallinity throughout the post-synthetic modification (PSM) process. Any attempts to create amorphous daughter MOFs are not considered in this dissertation.

In the following Table 1.1, we summarize the most representative examples of PSM in MOFs using different types of bond breaking.

Table 1.1 Representative examples of different bond-breaking types in MOFs.

MOFs	Bond-breaking type	Stimuli	Resultant MOFs	Mechanism	*ref.*
MIL-100 (Fe)	Coordination	$HClO_4$ or CF_3COOH	Defective MOFs	Partial ligand replacement	[156]
MOF-5 @ UiO-66	Coordination	HCl	HP UiO-66	The dissociation of MOF-5	[157]
CuBDC	Coordination	L-ascorbic acid	Cu_2BDC	Ligand removal and Cu^{2+} reduction	[158]
Ni-MOFNA	Coordination	ultraviolet/ozone	Defective MOFs	Partial ligand decomposition	[159]
Zn-MOF	Coordination	H_2O	MOFs with partial rearrangement	Partial ligand replacement	[160]
POST-66 (Y)	Coordination	H_2O	HP MOFs	Leaching of yttrium ions	[161]
Zn/Cu-UMOM-10	Coordination	DMSO	HP MOFs	Leaching of weak coordinating molecule	[162]
Zn-MOF	Coordination	H_2O, DMF or MeOH + grinding	New Zn-MOF	Structural rearrangement	[163]
3D Co-MOF	Coordination	MeOH, $CHCl_3$ or sc CO_2	2D Co-MOF	Ligand decoordination and recoordination	[164]

HKUST-1	Coordination	CH_3OH vapor	HP MOFs	Ligand removal and Cu^{2+} reduction	[165]
hcp UiO-67	Coordination	Grinding or ultrasonication	Nanosheets	Breaking hafnium-carboxylate bonds	[166]
ZIF-8, ZIF-67	Coordination	Acidified/basified xylenol orange	Diverse crystal morphologies	Leaching of metal ions and ligand removal	[167]
MIL-101 (Cr)	Coordination	Acetic acid	Hollow MOF	Leaching of Cr^{3+} and ligand replacement	[168]
MCF-13	Coordination	Electrochemical exfoliation	Nanosheets	Breaking and removing interlayer ligands	[169]
HKUST-1	Coordination	H_2O vapor	Stacked nanosheets	Ligand replacement	[170]
$Zn_2(bim)_4$	Weak interactions	Ball-milling and ultrasonication	Nanosheets	Breaking van der Waals forces	[171]
Ca-MOF	Weak interactions	Grinding or ultrasonication	Nanosheets	Breaking van der Waals forces	[172]
Cd-MOF, Zn-MOF	Weak interactions	Ultrasonication	Nanosheets	Breaking van der Waals forces	[173]
ZIF-9(III)	Weak interactions	Ultrasonication	Nanosheets	Breaking van der Waals forces	[174]
$[Cu_2Br(IN)_2]_n$	Weak interactions	Ultrasonication	Nanosheets	Breaking π-π interaction	[175]
$Zn_2(bim)_3$	Weak interactions	Ball-milling and ultrasonication	Nanosheets	Breaking van der Waals forces	[176]
$[Co(CNS)_2(pyz)_2]_n$	Weak interactions	Ultrasonication	Nanosheets	Breaking van der Waals forces	[177]
$[Cu(\mu-pym_2S_2)(\mu-Cl)]_n$	Weak interactions	Ultrasonication	Nanosheets	Breaking van der Waals forces	[178]
MOF-2	Weak interactions	Ultrasonication	Nanosheets	Breaking hydrogen-bonding	[179]
$[Hphen]_2[(UO_2)_2(ox)_3]$	Weak interactions	UV irradiation	Nanosheets	Breaking π-π interaction	[180]
MIL-121	Covalent	Heating	HP MIL-121	Decarboxylation	[181]
PCN-250	Covalent	Heating	HP PCN-250	Decarboxylation	[182, 183]
CPM-33	Covalent	Heating	HP CPM-33	Decarboxylation	[184]
UiO-66(Zr), UiO-66(Zr)-NO_2, MIL101 (Fe), MIL125(Ti)-NH_2, MIL-101(Cr)	Covalent	UV/Vis irradiation	HP MOFs	Photodecarboxylation	[185]
Zn-MOF	Covalent	UV irradiation	MOFs with enhanced gas adsorption	Photodecarboxylation	[186]
Co, Cu, Mn-MOF	Covalent	Electrolyte ion (Li^+) intercalation	MOF-based batteries with enhanced capacities	Dynamic formation and cleavage of disulfide bond	[187]
ZIF-8 with crosslinked imine moiety	Covalent	Heating	ZIF-8 functionalized with aldehyde groups	Cleavage of imine bond	[188]

PCN-160 with partial labile ligands	Covalent	Acidic DMF solution	PCN-160 implemented with different metals	Cleavage of imine bond	[189]
MOF-on-MOF heterostructure	Covalent	Singlet oxygen ($^1O_2$)	Exfoliated nanosheets	Cleavage of olefinic bond	[190]

In the following section, various types of bond breaking and how this cleavage can affect the formation of new MOFs will be discussed.

1.5.1 Coordination bond cleavage

Coordination bond cleavage usually occurs between the metal-based node and organic linker when external forces (*e.g.* solvents, acids, pressure) are applied, resulting in the formation of defective MOF with missing clusters or/and missing linkers.

One representative example of coordination bond cleavage in MOFs is the use of acid as an etching reagent. The acidic etching can be considered as the ligand exchange by replacing existing coordinated ligands. Prof. Kim and co-worker reported size-dependent acid etching in MOFs, resulting in the generation of mesopores from the microporous MOFs (Figure 1.17).[191] In particular, the structure of the selected water-stable MIL-100(Fe), which is constructed from Fe^{3+}- trimer clusters and BTC linkers, exhibits two types of cages: large cages with hexagonal windows ($d = 0.89$ nm) and small cages with pentagonal windows ($d = 0.49$ nm). Phosphoric acid was chosen as the etching agent due to its exclusive size ($d = 0.61$ nm), which allowed diffusion only into the large cages of the MOF. By incubating MIL-100(Fe) in various concentrations of acid in a DMF solution (0 to 80 mM) under 70 °C, a gradual change in the N_2 adsorption isotherms was observed, from a microporous type I to a mesoporous type IV. The pore size distribution also showed a gradual increase in mesopore size from 2.4 to 18.4 nm. This whole acidic etching process involved the stepwise destruction of the large cage, enabling further merging with adjacent small cages to form larger mesopores.
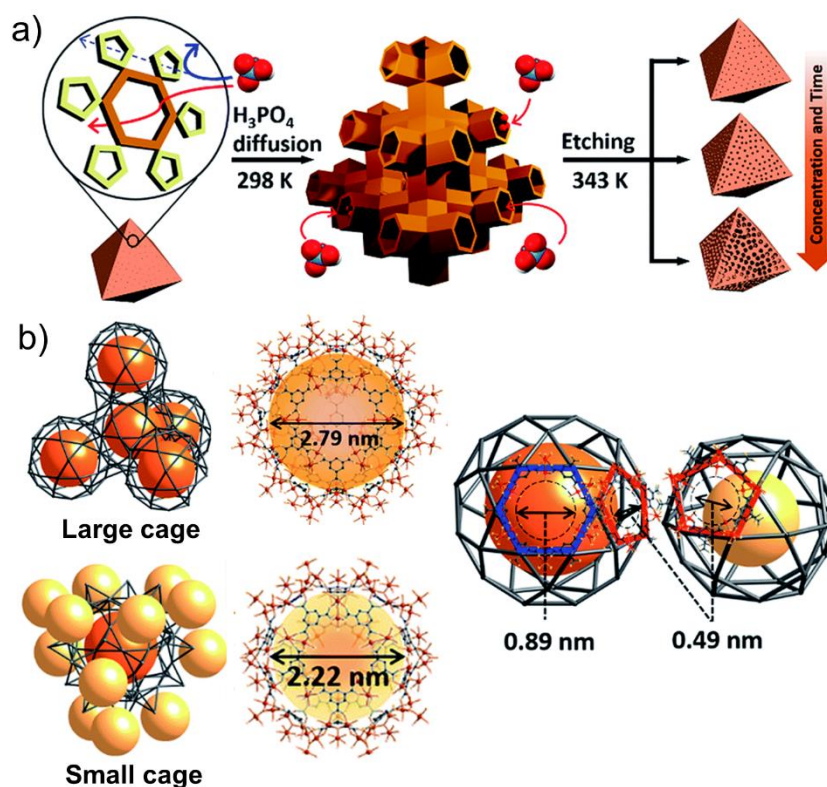
Figure 1.17 a) Illustration of the etching process for MIL-100(Fe) by using phosphoric acid. b) Representation of the two types of cages existing inside MIL-100(Fe).[191]

Introducing external acids for the partial destruction of MOFs is a very useful strategy, but how to control the amount of acids is a critical point as it may lead to the generation of either hierarchical pores or amorphization of MOFs. An interesting example reported by Prof. Wu and co-workers showed that an excess amount of introduced acid can not only fully dissociate MOFs but also trigger an unusual structure arrangement, from MOF-5 into ZIF-8 through the incorporation of 2-methylimidazole (Hmim).[192] In particular, the introduction of an Hmim solution creates a weakly acidic environment (Hmim $\rightleftharpoons$ (1-x)H$^+$ + (1-x)mim$^-$ + xHmim), enabling the disassociation of less stable Zn-O tetrahedral coordination in MOF-5. The dissociated free Zn^{2+} is able to coordinate with deprotonated mim$^-$ in the solution, forming a more stable Zn-N tetrahedral coordination. This etching mechanism reveals that the transformation from MOF-5 to ZIF-8 occurs through a diffusion-controlled exchange process. Initially, ZIF-8 started to nucleate and grow on the surface of MOF-5 crystal. Due to the fact that the dissociation rate of MOF-5 was much faster than the crystallization rate of ZIF-8, a hollow nanotube-shaped pure ZIF-8 particle was eventually obtained. Interestingly, the dissociation rate of MOF-5 could be adjusted by controlling the etching time and temperature so that ZIF-8 with different nanoarchitectures was able to be observed: yolk-shell MOF-5@ZIF-8, single-shell ZIF-8, double-shell ZIF-8, ball-in-box ZIF-8, *et al*. (Figure 1.18)
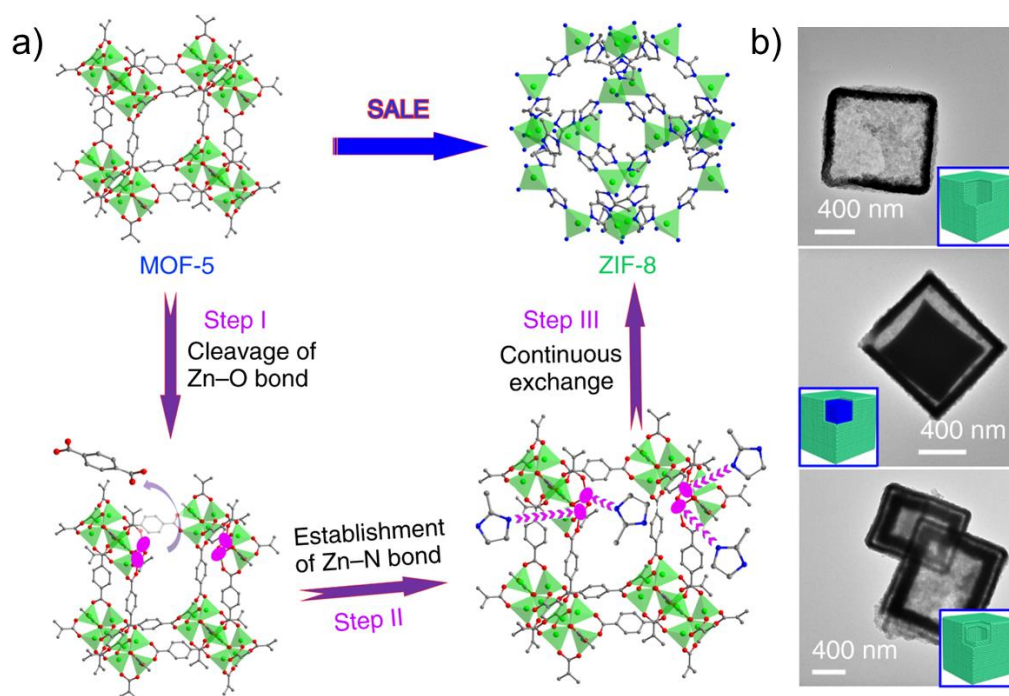
Figure 1.18 a) Phase transformation from MOF-5 to ZIF-8 triggered by solvent-assisted ligand exchange (SALE) process. b) TEM images of single-shell ZIF-8 nanotube (top), yolk-shell MOF-5@ZIF-8 nanotube (middle), double-shell ZIF-8 nanotube (bottom).[192]

Instead of using acids, the solvent itself can also trigger the cleavage of coordination bonds between the metal-based node and ligand, resulting in the porosity and topology changes in MOFs. Prof. Zhou and co-workers reported a fascinating example of the structural rearrangement in MOFs through the desolvation and resolvation process (Figure 1.19).[193] They synthesized Al-based MOF, AlTz-53, which consists of 1D Al-oxo chains linked by TzDB ligands (4,4'-(1,2,4,5-tetrazine-3,6-diyl)dibenzoate) and coordinating DEF solvents (*N,N*-diethylformamide), with **sql** topology. By exchanging the solvent from DEF to toluene and then subjecting it to thermal desolvation, AlTz-53 could be transformed into a new MOF, AlTz-68, with **kgm** topology. AlTz-68 showed a dramatic increase in BET surface area from 725 to 2749 m^2/g and enhanced crystallinity in PXRD. Interestingly, AlTz-68 can also convert back to AlTz-53 by incubating it in polar solvents such as DMF, H_2O and DMSO. This desolvation-resolvation cycle was achieved twice without any loss of the crystallinity. Further mechanistic studies revealed that the desolvated MOF, upon the loss of the coordinating solvents, entered a metastable state, triggering the decoordination and recoordination of ligands to different metal centers. Thus, this self-arrangement of the lattice led to the formation of a more stable AlTz-68 MOF.
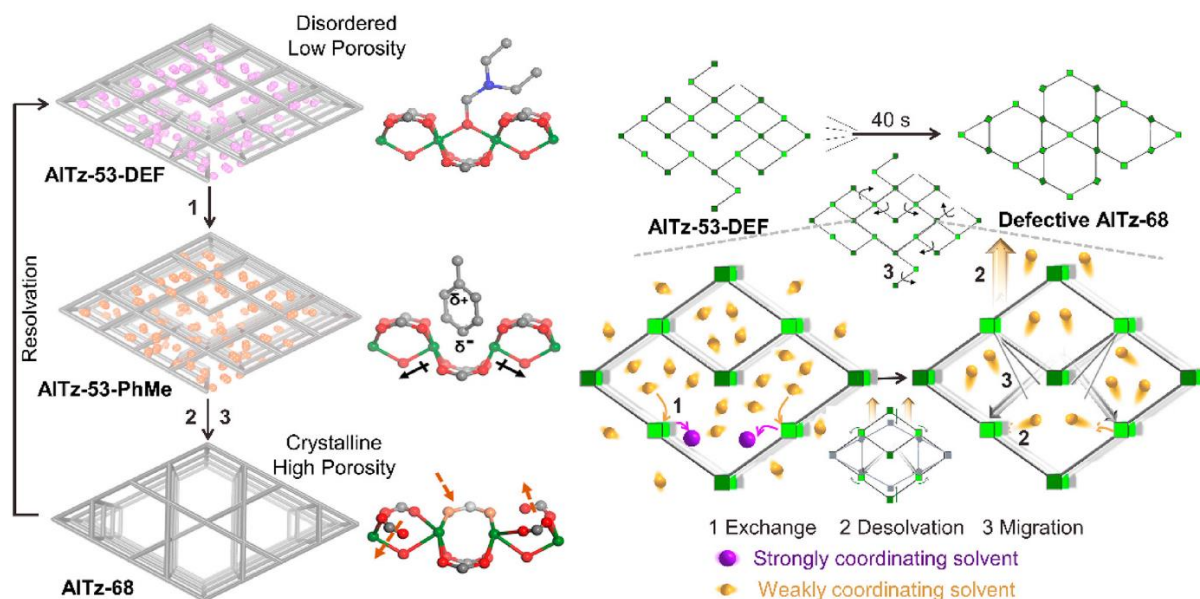
Figure 1.19 Lattice rearrangement from AlTz-53 to AlTz-68 triggered by desolvation process.[193]

1.5.2 Weak interactions cleavage

Weak interactions refers to intermolecular forces such as van der Waals forces, π-π interactions, hydrogen bonding, which are generally fragile when external forces are employed.[147,194] Cleavage of weak interactions usually occurs in 2D layered MOFs, resulting in single-layer or multi-layer structures suitable for applications such as molecular sieving, catalysis and sensing.[195] This is classified as a top-down strategy which focuses on the disintegration of starting bulk materials. So far, there are two ways to break weak interactions: mechanical forces (pressure, grinding and sonication) or increasing the distance between layers through the intercalation of external molecules. [147,196]

One representative example is the use of mechanical exfoliation (*e.g.* ultrasonication) to obtain crystalline metal-organic nanosheets from bulk materials. Prof. Moorthy and co-workers reported that a 2D Cd-MOF constructed from Cd^{2+} single ions and H_4BPDP linker (biphenyl dipyrrole tetracarboxylic acid) exhibited a 2-fold interpenetrated framework linked by weak hydrogen bonds.[197] Each framework consisted of two interwoven 2D layers (Figure 1.20). By sonicating this Cd-MOF in methanol for 60 min, a few layered 2D nanosheets could be successfully delaminated from the bulk precursors. Several techniques were then applied to confirm this result, including Tyndall light scattering, atomic force microscopy (AFM) and scanning electron microscopy (SEM). The crystallinity nature of 2D nanosheets was verified by selected area electron diffraction (SAED). Additionally, they demonstrated that mechanical grinding for 30 min could also achieve the synthesis of few-layered 2D nanosheets.
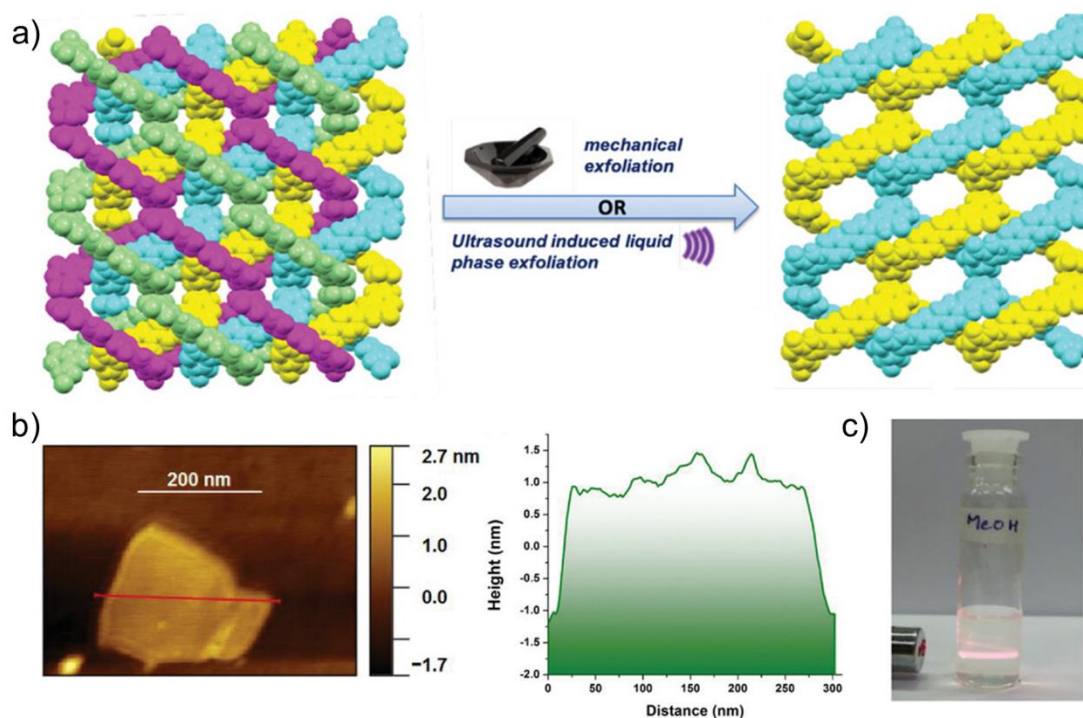
Figure 1.20 a) Exfoliation of bulk precursors into 2D nanosheets by ultrasound sonication or mechanical grinding. b) AFM image (left) and the height-profile diagram (right) of nanosheets. c) Tyndall light scattering effect of nanosheets.[197]

Interestingly, instead of using mechanical forces to exfoliate interlayers of MOFs, the solvent itself can play a significant role in delaminating 2D MOFs. In this case, the solvent can not only break the weak interactions of MOFs but also stabilize the obtained nanosheets. The key factor here is to choose the proper solvent, because the surface tension between certain solvents and bulk MOFs can tremendously reduce the energy and enhance the efficiency of exfoliation. Prof. Aida and co-workers first synthesized the layered Cu-MOF, **kgm^{SMe}**, which is constructed from Cu(II)-paddlewheel units and SMe-H$_2$ip linker (5-methylthioisophthalic acid).[198] This MOF showed an infinite 2D kagomé lattice where each interlayer was connected by hydrogen bonds, and the relative distance was 6.8 Å. When this MOF was exposed to THF vapor at 20 °C for 5 min, the interlayer expansion of **kgm^{SMe}** rapidly occurred, forming the bilayer-expanded state (state II). Upon exposure of this MOF for 1 day, the bilayer of state II crystals could further evolve into monolayer-expanded state (state III). AFM characterization confirmed the existence of state II and III, showing the successful preparation of bilayer and monolayer nanosheets (Figure 1.21). A similar study has been reported by Prof. Zhao and co-workers, showing that homogeneous bilayered nanosheets could be successfully obtained and separated from the bulk Ni-MOF by shear forces from hexane after 10-cycle freeze-thaw treatments.[199]
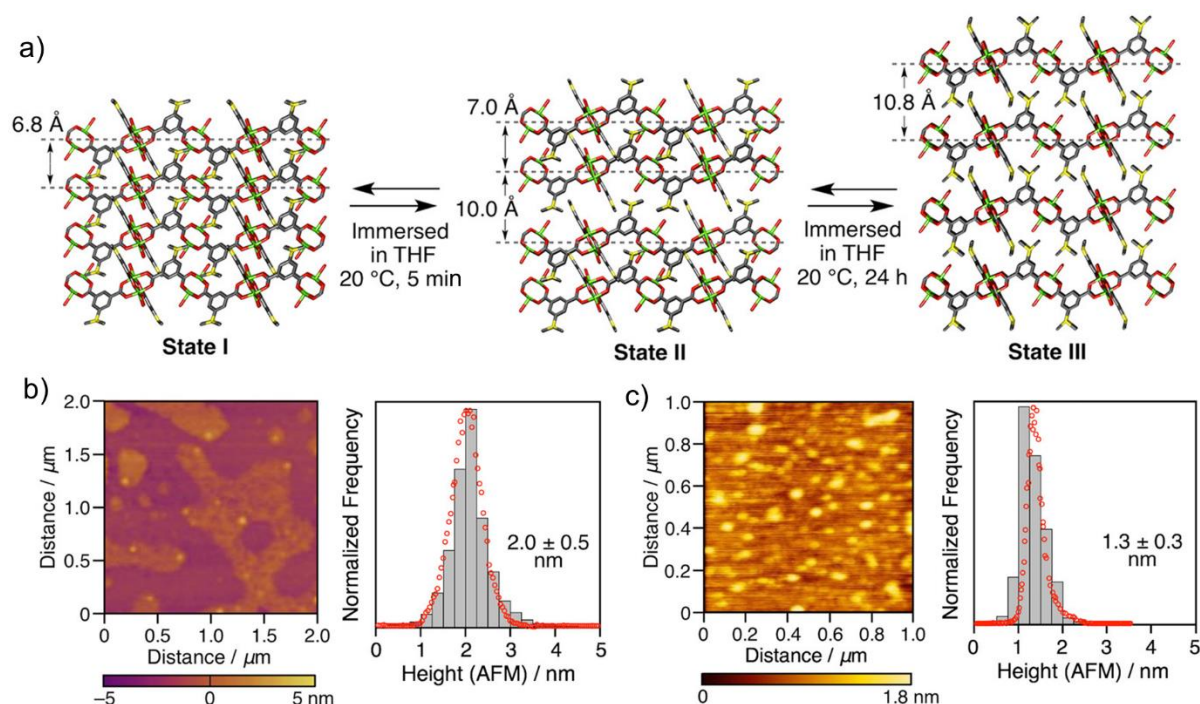
Figure 1.21 a) Structural changes from as-synthesized (state I) **kgm^SMe** to bilayer-expanded state (state II) and monolayer-expanded state (state III) induced by THF. b) AFM image (left) and the height-profile diagram (right) of state II. c) AFM image (left) and the height-profile diagram (right) of state III.[198]

1.5.3 Covalent bond cleavage

The abovementioned two types of cleavage can endow daughter MOFs with distinct properties compared to their parent MOFs, but they still have some inevitable drawbacks. For example, it is challenging to control the limit for breaking coordination bonds inside MOFs as the structure can be easily collapsed by simple removal of metal-based nodes or organic linkers, or only limited structures like 2D layered MOFs can be applied to certain means of exfoliation. Unlike these two kinds of cleavage, covalent bond cleavage has recently aroused great interest due to the fact that breaking covalent bonds inside the MOF structure shows promising prospects, and the cleavage selectively takes place inside the organic linker without interfering with metal-based nodes.

In coordination chemistry, a prevailing viewpoint toward bond breaking is that the coordination bond is more fragile than the covalent bond.[200,201] If the covalent bond is cleaved inside coordination solids, the coordination bond is likely to be cleaved simultaneously or prior to the covalent bond cleavage, which ultimately leads to amorphization. However, recent developments in the MOF field have revealed that MOFs can be considered as ideal chemical substrates for covalent modifications.[202,203] In this section, we will show recent advancements and progress in MOFs toward breaking covalent bonds while maintaining the integrity of the whole framework.

So far, the common strategy for MOF deconstruction is to incorporate labile covalent bonds into the backbone of the MOF structure. By breaking these labile bonds, some metal-based nodes or clusters in the local structure may undergo changes in connectivity, resulting in the emergence of new characteristics in the material. Based on this, we will discuss different types of covalent bond cleavage and how this cleavage can directly affect certain properties of MOFs.

1.5.3.1 Disulfide bond cleavage

The disulfide bond, referring to the functional group R-S-S-R', is an important and commonly observed structural moiety, especially in the structure of proteins.[204] Disulfide bonds are strong and can be cleaved through reduction. Several reductants can be used for this purpose. For example, in biochemistry, the cleavage of disulfide bonds can be triggered by thios or phosphines such as tris(2-carboxyethyl)phosphine (TCEP), β-mercaptoethanol (β-ME) and dithiothreitol (DTT).[205] In organic chemistry, this cleavage can occur through the introduction of alkali or alkaline earth metal complexes such as sodium chloride.[206] The cleavage of disulfide bond can be represented as follows (Figure 1.22):
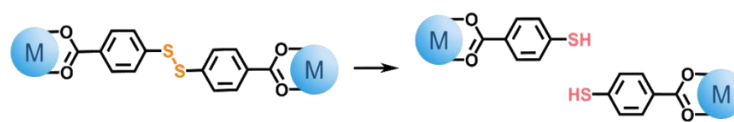
Figure 1.22 Scheme of disulfide bond cleavage.

Prof. Zhou and co-workers reported that untrathin 2D MOF nanosheets can be produced by the chemical cleavage of disulfide bonds.[207] They synthesized a 2D layered Zn_2(PdTCPP) MOF (TCPP = tetrakis(4-carboxyphenyl)porphyrin). By further intercalating the labile ligand DPDS (4,4'-dipyridyl disulfide) into the interlayer, the resulting intercalated Zn-MOF showed a dramatic increase in interlayer distance from 9.8 to 22.6 Å. Since the length of the labile ligand DPDS is only around 10 Å, the single crystal structure revealed that only one pyridinic N from DPDS ligand is able to coordinate with Zn^{2+}, while the other remains free. Further chemical reduction of sulfide groups using trimethylphosphine (TMP) as a reductant in ethanol for 10 h under N_2 atmosphere resulted in partial cleavage of the labile DPDS, generating ultrathin 2D MOF nanosheets (Figure 1.23). These obtained nanosheets were further characterized by HRTEM and AFM, confirming their crystalline nature and single-layer features with a uniform thickness of ~ 1 nm. Three years later, Prof. Lei and coworkers used the same MOF but with Cu^{2+} for the cleavage of S-S bonds when glutathione (GSH) was used as a reducing agent.
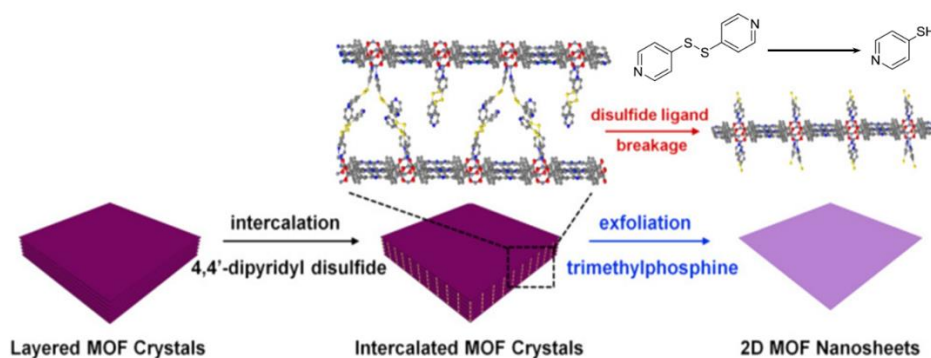
Figure 1.23 Illustrated creation of 2D MOF nanosheets through intercalation and chemical exfoliation.[207]

1.5.3.2 Ester bond cleavage

The ester bond is considered to be more chemically stable than the disulfide bond, which can favor the direct synthesis of MOFs under mild conditions. The structure of the ester complex plays an important role in ester bond cleavage. Primary esters can undergo bond cleavage under basic conditions, while tertiary esters are more labile under acidic environments and are subjected to thermal decomposition at elevated temperatures.[208] The cleavage of the ester bond, forming carboxylic acid and hydroxyl groups, can be seen as follows (Figure 1.24):
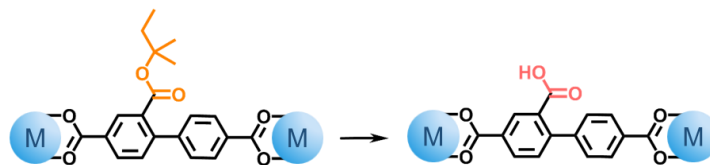
Figure 1.24 Scheme of ester bond cleavage.

Prof. Xiao and co-workers reported the first case of ester bond cleavage in MOFs.[208] In their work, they chose the mixed linker system, H_4dotpc (4,4"-dioxido-[1,1':4',1"-terphenyl]-3,3"-dicarboxylic acid) and pentyl cross-linker H_8-TE-L5 containing tertiary esters, for the construction of a MOF-74 analogue. In this isoreticular MOF-704 structure, these two types of ligands were randomly distributed in a certain ratio, containing 23% TE-L5^{8-} or 50% TE-L5^{8-}. Geometry optimization of this cross-linker TE-L5^{8-} through density functional calculations revealed that this cross-linker could only adopt and be located down the pore channels of MOF-74. Subsequently, under microwave heating at 230 °C for 10 min, tertiary ester groups from this linker could be completely cleaved and converted into free carboxylic acids. Interestingly, after this thermolysis treatment, MOF-74 containing 23% TE-L5^{8-} showed a dramatic increase in BET surface area (2510 m^2/g) compared to that of MOF containing 50% TE-L5^{8-}

(2190 m^2/g) due to the lower density of free carboxylic acids within MOF pores (Figure 1.25). However, this study also showed that in order to obtain better crystallinity for the MOF-74 analogues, increasing the reaction time might induce the uncontrollable decomposition of H$_8$-TE-L5, which limits a broad application for the direct synthesis of other MOFs containing tertiary ester bonds.
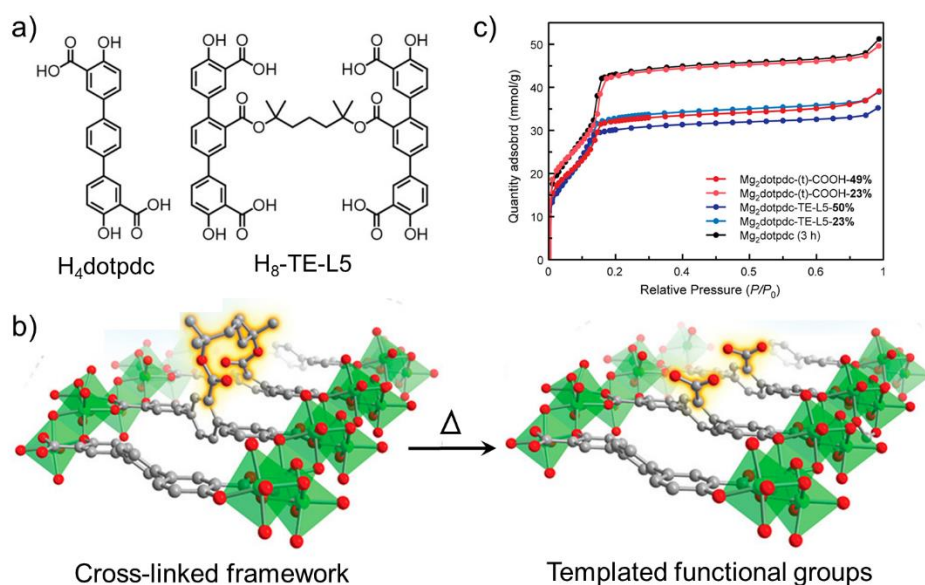
Figure 1.25 a) Representation of the used mixed linkers. b) Illustration of cross-linker changes inside the MOF structure before and after thermolysis. c) Surface area of initial MOFs and thermo-treated MOFs.[208]

1.5.3.3 Imine bond cleavage

The imine bond, recognized as a dynamic covalent bond, has been widely used in the synthesis of covalent-organic frameworks (COFs) and organic cages.[209,210] The imine bond can be selectively broken through hydrolysis under acidic conditions. The cleavage of the imine bond, forming amino and aldehyde groups, can be seen as follows (Figure 1.26):
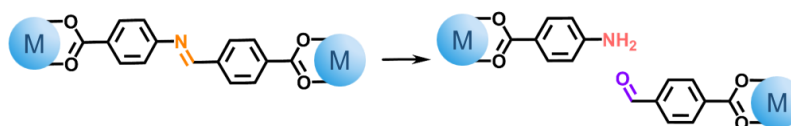
Figure 1.26 Scheme of imine bond cleavage.

In 2017, Prof. Zhou and co-workers first reported the cleavage of the imine bond in MOFs.[211] They focused on a Zr-MOF, which is built from 12-connected Zr$_6$ clusters and azo linkers (azo = azobenzene-

4,4'-dicarboxylate). Later, different amounts of the labile linker CBAB (4-carboxybenzylidene-4-aminobenzate) containing the imine bond were introduced into Zr-MOF by ligand exchange, and the exchange ratio of the CBAB linker varied from 5 to 65 %. These two types of linkers are randomly distributed inside the structure, forming a multivariate Zr-MOF. By adjusting the concentration of acetic acid in a DMF solution from 0.5 M to 2 M, these labile linkers could be partially dissociated and removed, resulting in the formation of mesoporosity in the microporous MOF with pore sizes ranging from 2.5 nm to 13.6 nm (Figure 1.27). Further investigation into the formation of hierarchical pores revealed that the labile CBAB linkers could be initially cleaved and removed by acetic acid, generating missing linker defects inside the Zr-MOF. As the remaining less connected Zr-clusters became "weak" compared to defect-free ones, acid washing could further remove some parts of these weak points, forming missing-cluster defects. As a result, the mesopore size got enlarged while the crystallinity of the Zr-MOF was not affected. This study perfectly showed that the porosity inside the MOF structure can be finely tuned through the cleavage of covalent imine bonds, but how to cleave labile covalent bonds in a quantitative, controllable way is still a challenging issue.
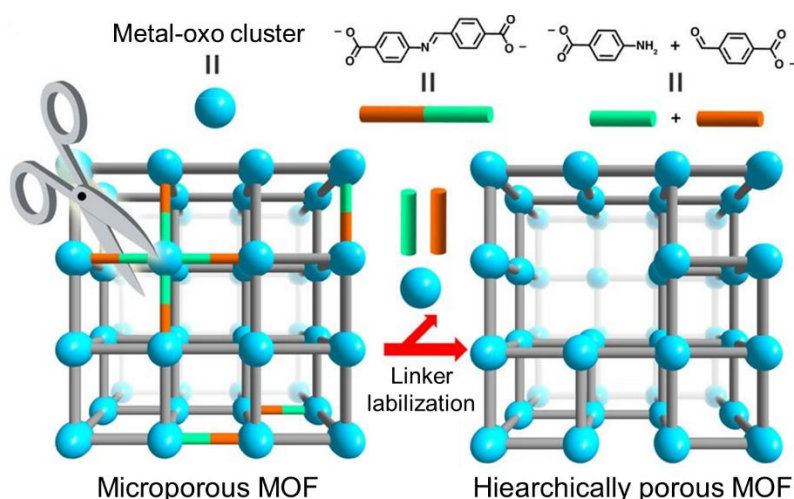
Figure 1.27 Illustrated creation of hierarchically porous MOF by the cleavage of imine bond.[211]

Later, the same group reported that the level of interpenetration in Zr-MOFs can be controlled by imine bond cleavage and new linker reinstallation.[212] In their study, the organic linker azo used for the synthesis of Zr-MOF could be totally exchanged to the labile CBAB linker post-synthetically. This Zr-MOF made by CBAB linkers can be recognized as a metastable intermediate. Subsequently, introducing H_2TPDC (terphenyl-4,4''-dicarboxylic acid) into this Zr-MOF could generate a weak acidic environment, which enables the partial dissociation of the CBAB linker. As a result, the metastable MOF became destabilized, and with continuous etching of H_2TPDC, a complete linker exchange from CBAB to TPDC could be realized. In this case, the MOF structure comprised of 12-connected Zr(IV)

hexanuclear clusters and TPDC linkers was identified as the non-interpenetrated UiO-68 (Figure 1.28). Compared to the traditional one-pot synthesis, which inevitably involves the formation of 2-fold interpenetrated UiO-68, this strategy, through linker cleavage and reinstallation, provides a new way to obtain a dynamically kinetic product. In addition, this work also showed that using Zr-MOF with labile linkers as a template, a series of secondary organic linkers with different lengths could be sequentially reinstalled, resulting in the contraction or expansion of their lattices.
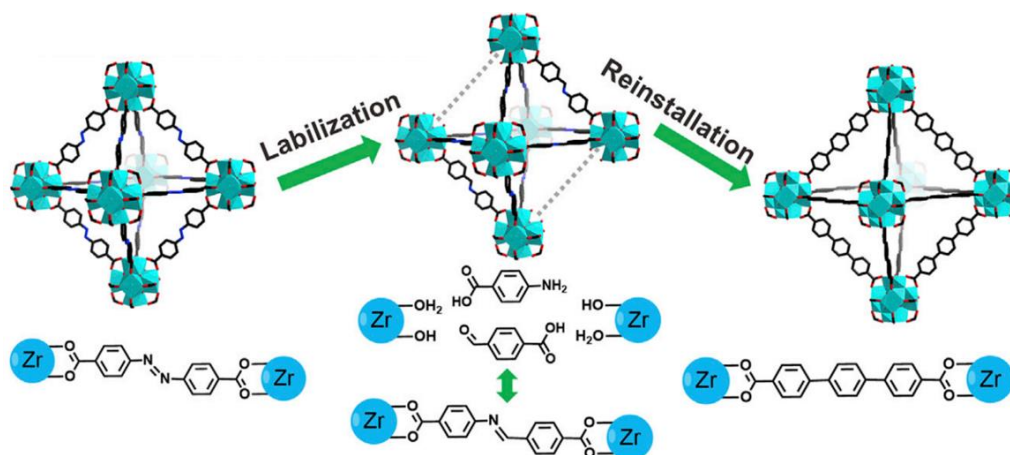
Figure 1.28 Illustration of linker labilization and reinstallation in Zr-MOF.[212]

In addition to that, the topology of MOFs can also be tuned by cleaving the labile imine bond inside the organic linker. Prof. Zhou and co-workers first synthesized Zr-MOF, PCN-160-imine, with fully labile CBAB linkers.[213] By using the abovementioned strategy, introducing the Co-isonicotinate moiety (Co-INA$_2$) could induce a complete linker exchange, resulting in the generation of a new Zr-MOF, PCN-160-CoCl$_2$. In this structure, Co-INA$_2$ moiety, in which the metal center Co(II) was coordinated with two INA linkers, two Cl$^-$ and two solvent molecules, showed in a *trans* orientation. Due to the lability of these two coordinated solvent molecules, another pair of INA ligands could be further incorporated and replace them, forming the square planar-shaped metaloligand (Co-INA$_4$) with two free carboxylic acids. Interestingly, these free carboxylic acids were able to further coordinate with new Zr hexanuclear clusters by the extra addition of Zr(IV) salts. Consequently, the resulting MOF, PCN-161-CoCl$_2$, showed a topology transformation from **fcu** to **ftw** (Figure 1.29). In addition, different metals (Fe^{2+}) and counterions (OH$^-$, Cl$^-$, Br$^-$, I$^-$, NCS$^-$ or NCSe$^-$) could also be introduced into this metaloligand, endowing the Zr-MOF with its potential to exhibit single-ion magnetic behavior.
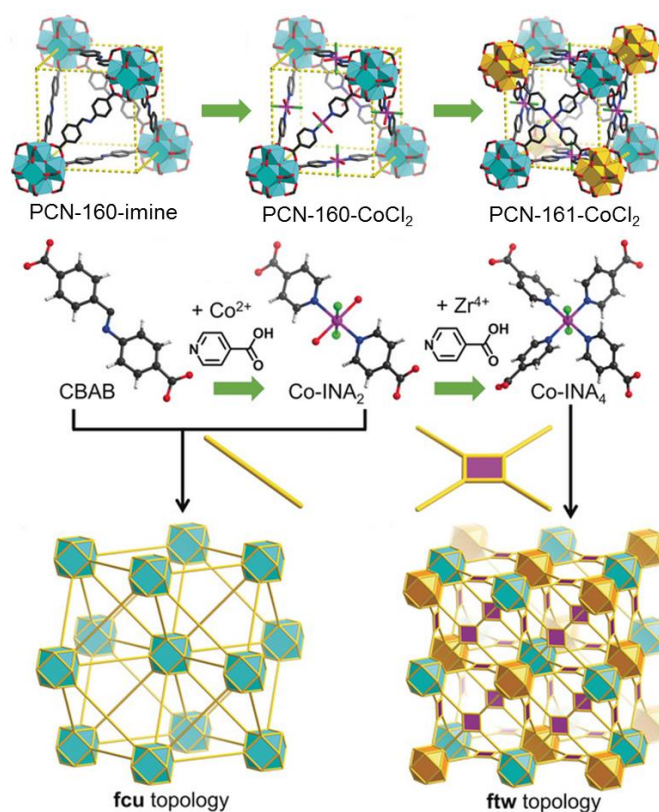
Figure 1.29 Single-crystal structures of PCN-160-imine, PCN-160-CoCl₂, PCN-161-CoCl₂ and their relative topology transformation.[213]

1.5.3.4 C-carboxylate bond cleavage

The C-carboxylate bond cleavage in MOF chemistry refers to the decarboxylation process. Decarboxylation is a chemical reaction that breaks C-C bonds to release CO_2 from carboxylic acids. This reaction can be triggered by light or elevated temperatures.[214] The decarboxylation process can be seen as follows (Figure 1.30):
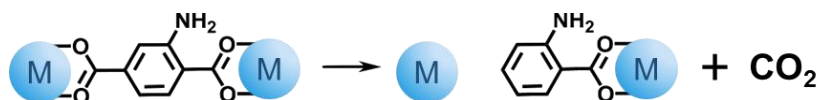
Figure 1.30 Scheme of C-carboxylate bond cleavage.

Prof. Zhou and co-workers reported that hierarchical pores could be created in MOFs by linker thermolysis.[215] In this work, mixed linkers, thermostable terephthalate (BDC) and thermolabile 2-amino-1,4-benzenedicarboxylate (BDC-NH₂) were randomly incorporated into UiO-66 type MOFs. Upon heating to 350 °C for 3.5 h, thermolabile BDC-NH₂ linkers were selectively decomposed and

underwent the decarboxylation process by the removal of CO_2. The complete decarboxylation reaction was confirmed and characterized by TGA-MS, FTIR and ^{1}H NMR, respectively. As a result, the resulting framework showed hierarchical porosity, and the mesopore size gradually increased from 5.5 nm to 13 nm with the programed temperature up to 375 °C (Figure 1.31). Further investigation revealed that the decarboxylation reaction was facilitated by certain functional groups (*e.g.* -NH$_2$, -NO$_2$) inside the organic linker. These functional groups could weaken the strength of the C-C bonds between carboxylates and phenylene rings, ultimately leading to the cleavage of the C-C bonds. However, in this case, unexpected ultrasmall ZrO_2 nanoparticles were formed inside the pores of MOFs during the decarboxylation process. In the same year, Prof. De Vos and co-workers also reported similar work in which thermolabile linkers, *trans*-1,4-cyclohexane-dicarboxylates, were selectively cleaved inside UiO-66 to create missing linker defects.[216]
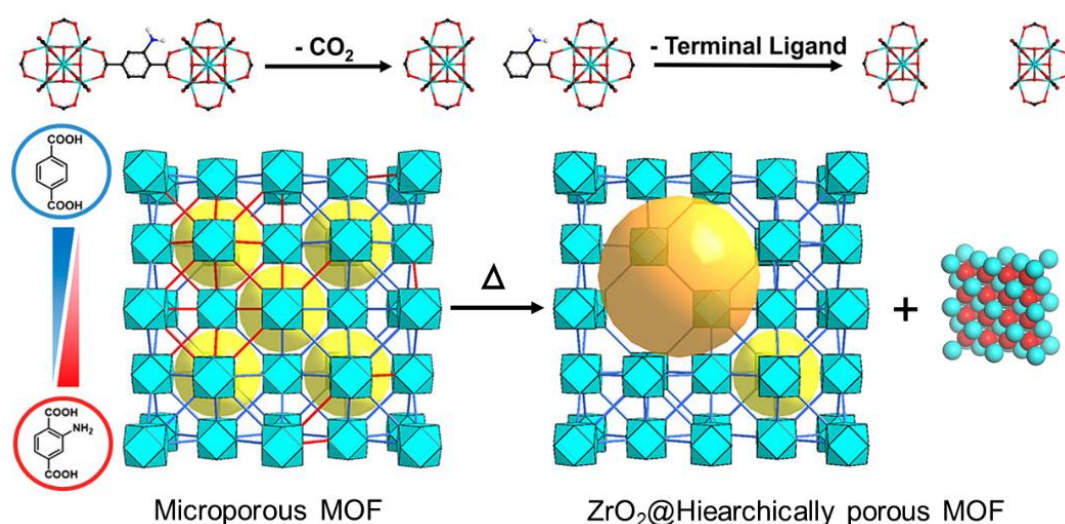
Figure 1.31 Illustration of the decarboxylation of thermolabile linker (top) and the resulting porosity changes in MOFs (bottom).[215]

Besides using the thermolysis strategy for decarboxylation, Prof. Kim and co-workers reported that the discriminative etching chemistry, known as silver-catalyzed decarboxylation, can also achieve efficient elimination of carboxylic groups in MOFs under mild conditions.[217] In their study, a series of representative MOFs with highly structural stability were chosen, including HKUST-1 (Cu), UiO-66 (Zr), Eu-MOF, MIL-100 (Al or Fe), MIL-100 (Al), MIL-53 (Al) and MIL-101 (Cr). By mixing these MOFs with $AgNO_3$ and $K_2S_2O_8$ in acetonitrile under solvothermal conditions at 120 °C, MOFs would undergo the decarboxylation process and as a result, different pore sizes ranging from mesopores to macropores could be observed depending on the reaction time. For example, when the reaction time was 20 min or 40 min, mesopores were generated in microporous HKUST-1 (Cu), as evidenced by the

N$_2$ sorption isotherm where the typical mesoporous hysteresis loop appeared. Furthermore, when the reaction time was increased to 60 min, macropores started to grow from 50 nm to 100 nm in size (Figure 1.32). Further mechanistic studies revealed that the decarboxylation occurred through two aspects: the change of the chemical state from Ag(I) to Ag(III) and the presence of a radical sulfate ion (SO$_4^{\cdot-}$) from potassium persulfate.
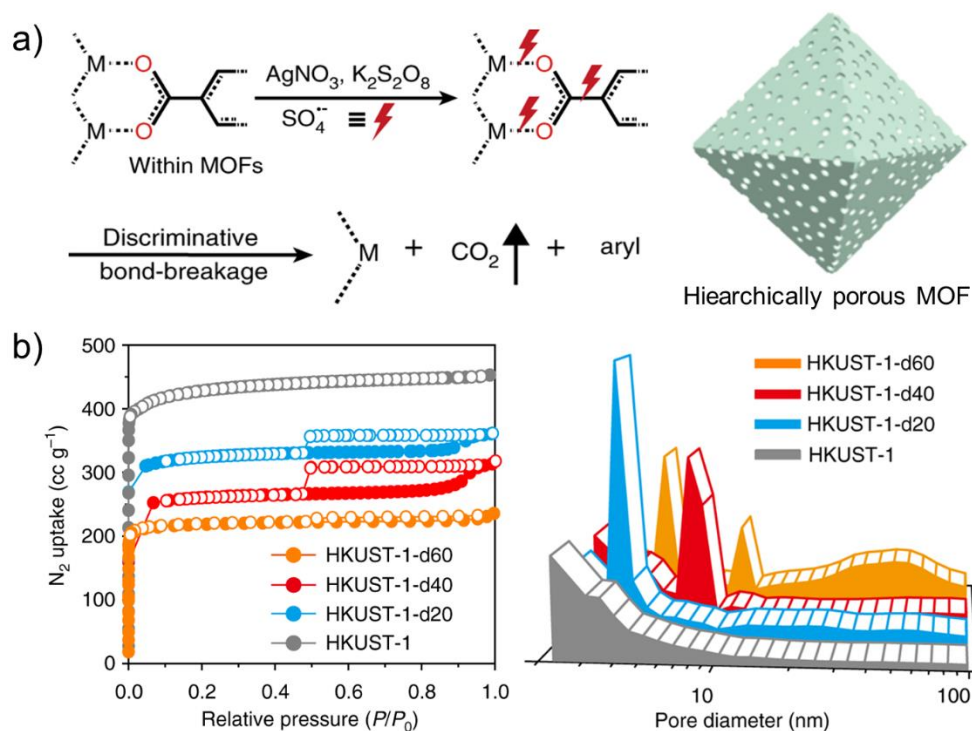
Figure 1.32 a) Illustrated creation of hierarchically porous HKUST-1 through silver-catalyzed decarboxylation. b) N$_2$ adsorption isotherms (left) and the relative pore-size distribution of HKUST-1 before and after decarboxylation under different reaction time (right).[217]

Another interesting way to create hierarchically porous MOFs is through photolysis. Prof. Zhou and co-workers partially incorporated the photolabile porphyrin-based ligand TCPP (tetrakis(4-carboxyphenyl)porphyrin) into UiO-66, resulting in the formation of a MTV MOF.[218] The used porphyrin ligand has a strong ability to absorb light in the UV-vis region. When the sample was irradiated by an ultraviolet laser (7×10^7 W/m^2) for different exposure times (20 ms, 40 ms, 80 ms), the TCPP ligand could be selectively and gradually eliminated. Consequently, an increasing number of defects occurred inside UiO-66 with longer exposure times. After washing the sample with acidic DMF solution, the defective UiO-66 showed a significant increase in BET surface area and the number of mesopores (Figure 1.33). Further analysis revealed that the decomposition of TCPP was initiated by decarboxylation and oxidation destruction reactions once the ligand had absorbed the energy of laser. This led to the formation of a large number of missing-cluster defects in MOFs. By removing all

residues, including free metal-based clusters and decomposed ligand fragments, through acidic DMF solution washing, MOFs with hierarchical porosity could be obtained. Additionally, the researchers attempted to increase the complexity of this MTV Zr-MOFs by incorporating another photolabile BDC-NH$_2$ ligand, resulting in the generation of more mesopores under the UV laser.
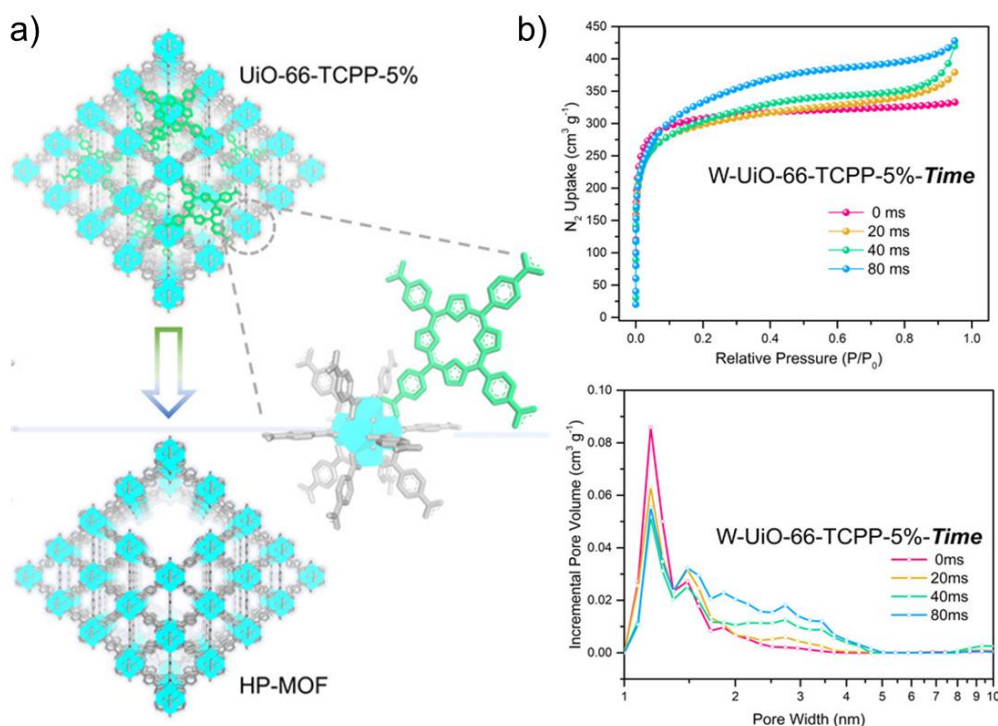
Figure 1.33 a) Illustrated creation of hierarchically porous Zr-MOF through linker photolysis. b) N$_2$ adsorption isotherms (top) and the relative pore-size distribution before and after photolysis with various exposure time under laser (bottom).[218]

1.5.3.5 Olefinic bond cleavage

Despite their usefulness, the aforementioned covalent bond cleavage methods have some drawbacks:

- The labile linker can only be incorporated into the framework post-synthetically, and the extent to which the labile linker can be exchanged remains uncertain.

- While some labile ligands are possible to be used directly for one-pot synthesis, most of them are acid-sensitive and can only survive under mild conditions. The introduction of an acidic modulator in the synthesis or the acidic nature of the ligand itself can greatly hinder the synthesis of MOFs.

- Achieving quantitative cleavage of the labile linker inside the MOF is still a challenging and critical issue.

To address these challenges, olefinic bond cleavage has been recently developed and has shown great control over the cleavage. In this case, ozone gas has been demonstrated as the most efficient method for breaking the olefinic bond.

Ozone is a powerful oxidizing reagent widely used in various fields of the chemical industry. It is commonly employed in the production of azelaic acid and pelargonic acid through the ozonolysis of oleic acid in the industry.[219] Recently, there has been increasing attention towards maximizing the potential of ozone for multiple applications, such as water and wastewater purification, as well as sewage and industrial waste treatment.[220]

In ozone chemistry, several terms are frequently used, but their definitions may not be clear to readers. Therefore, we would like to highlight and provide clear definitions for these terms based on numerous reported papers. The term *ozonator* refers to an apparatus used for the ozone generation. Both *ozonization* or *ozonation* indicate the action of ozone on any substance in a broad sense. And the term *ozonolysis* has a narrow and specific meaning, which only denotes to designate the cleavage of covalent bonds comprised of sp^2 or sp carbon atoms.

Ozonolysis reactions are targeted towards the oxidative cleavage of unsaturated compounds. It can be applied to the cleavage of olefinic bonds, acetylenic bonds, aromatic rings (both carbocylic rings and heterocyclic rings), carbonyl groups and alkanes.[221] When multiple unsaturated groups exist in the same system, ozone can react with some groups much faster than others or react with some groups exclusively. The relative relationship between ozone and the reactivity of corresponding groups can be summarized as follows (Figure 1.34):
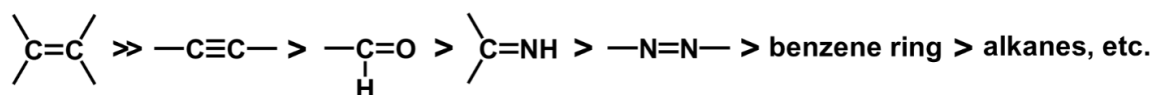
Figure 1.34 Scheme of the reactivity of unsaturated bonds toward ozone.

This mean that, for example, alcohols or even alkanes can be used as solvents during the ozonolysis of olefins due to the significant difference between these two groups.

The use of the ozone-reactive olefinic bond in MOFs can offer several unprecedented advantages in terms of the covalent bond cleavage:

- The ligand containing olefinic bonds is stable enough to resist any acidic and basic conditions, which means it can be easily characterized by NMR spectroscopy, mass spectrometry, *etc*.

Using aggressive conditions such as HF or NaOH aqueous solution for MOF digestion will not result in the loss of the olefinic bond signal.

- The ligand containing olefinic bonds can be directly used for the direct synthesis of MOFs, even under harsh conditions.

- The ozonolysis reaction for olefinic bond cleavage can be performed in the solid-gas phase, which has several benefits: first, solid-gas phase reactions are considered time-saving, energy-efficient and environmentally friendly; second, the use of a reactive gas can overcome the limitation of diffusion into porous materials, which is a challenge in conventional solid-liquid phase reactions.

The cleavage of the olefinic bond through ozonolysis can generate a mixture of carboxylic and aldehyde groups. By further oxidative or reductive workup, only one type of product containing either one of these two groups can be formed. The relative cleavage process can be seen as follows (Figure 1.35):
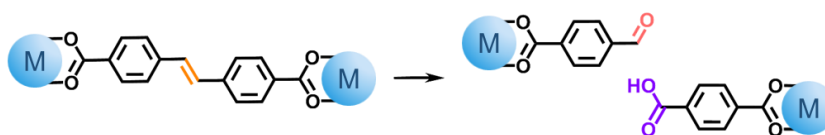
Figure 1.35 Scheme of olefinic bond cleavage.

Prof. Maspoch and co-workers reported the first case of ozonolysis reaction in MOFs with an olefinic bond-containing ligand.[222] In this study, they used H_2EBDC (2-ethenylbenzene-1,4-dicarboxylic acid) ligand to construct isoreticular UiO-66, named as ZrEBDC, where the olefinic groups have been regarded as the dangling groups pointing to the pore of the framework (Figure 1.36). The cleavage of the olefinic bond was achieved by ozonolysis treatment under solid-gas phase reaction conditions. In particular, the activated ZrEBDC sample loaded in a U-shaped Pyrex tube was ozonized under a dry ice/acetone bath at -78 °C for 30 min. Further characterization of this ozonized sample, ozo-ZrBDC, by single crystal X-ray diffraction and NMR spectroscopy revealed that the olefinic bond had been completely converted into a 1,2,4-trioxolane group. This cyclic ring, 1,2,4-trioxolane, recognized as the ozonide intermediate during the ozonolysis reaction, could be further transformed into either partial aldehyde groups under an acidic solution of dimethyl sulfide (reductive workup) or full carboxylic groups in the presence of an aqueous hydrogen peroxide (H_2O_2) solution (oxidative workup).
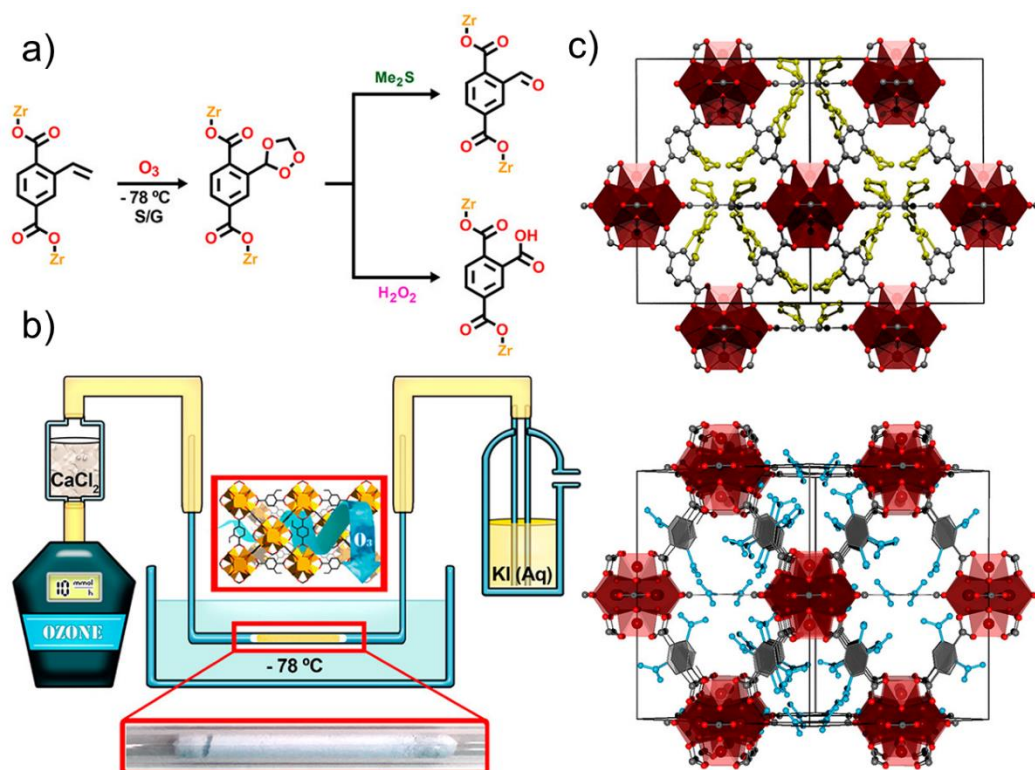
Figure 1.36 a) Cleavage of olefinic bond and the following two pathways: oxidative and reductive workup. b) Set-up used for ozonolysis reaction. c) Single crystal structures of ozo-ZrBDC (top) and full carboxylate-functionalized Zr-MOF after oxidative workup.[222]

Later, the same group reported that the cleavable olefinic bond could be incorporated into the backbone of the framework, resulting in changes in the porosity of MOFs after bond cleavage.[223] They synthesized multivariate Zr-MOFs by mixing two types of carboxylate ligands with similar shape and length: the ozone-inert H_2azo (4,4'-azobenzene dicarboxylic acid) and the ozone-active H_2sti (4,4'-stilbene dicarboxylic acid). These two types of ligands were randomly distributed inside the MOF structure. Interestingly, the ratio of azo/sti (ranging from 90:10 to 40:60) could be directly adjusted during the synthesis, forming the corresponding MOFs, denoted as Zr-**fcu**-azo/sti-*X*% ($X \approx$ 10, 20, 30, 40, 50, 60 sti molar percentage). The solid-gas phase ozonolysis reaction was carried out at room temperature for 30 min. After the quantitative cleavage of olefinic bonds and being washed in acidic DMF solution, those ozonated MOFs showed a gradual increase in the number of mesopores from N_2 sorption isotherms. From ozonated Zr-**fcu**-azo/sti-10% to ozonated Zr-**fcu**-azo/sti-50%, the ratio of mesopores to micropores increased by nearly 40 %. Likewise, the fusion of micropores to mesopores could also be achieved in a similar system, Zr-MOF constructed from the ozone-inert H_2bpdc ligand (4,4'-biphenyldicarboxylic acid) and the ozone-active H_2pdac ligand (1,4-phenylenediacrylic acid), by the sublimation of terephthaldehyde (Figure 1.37).
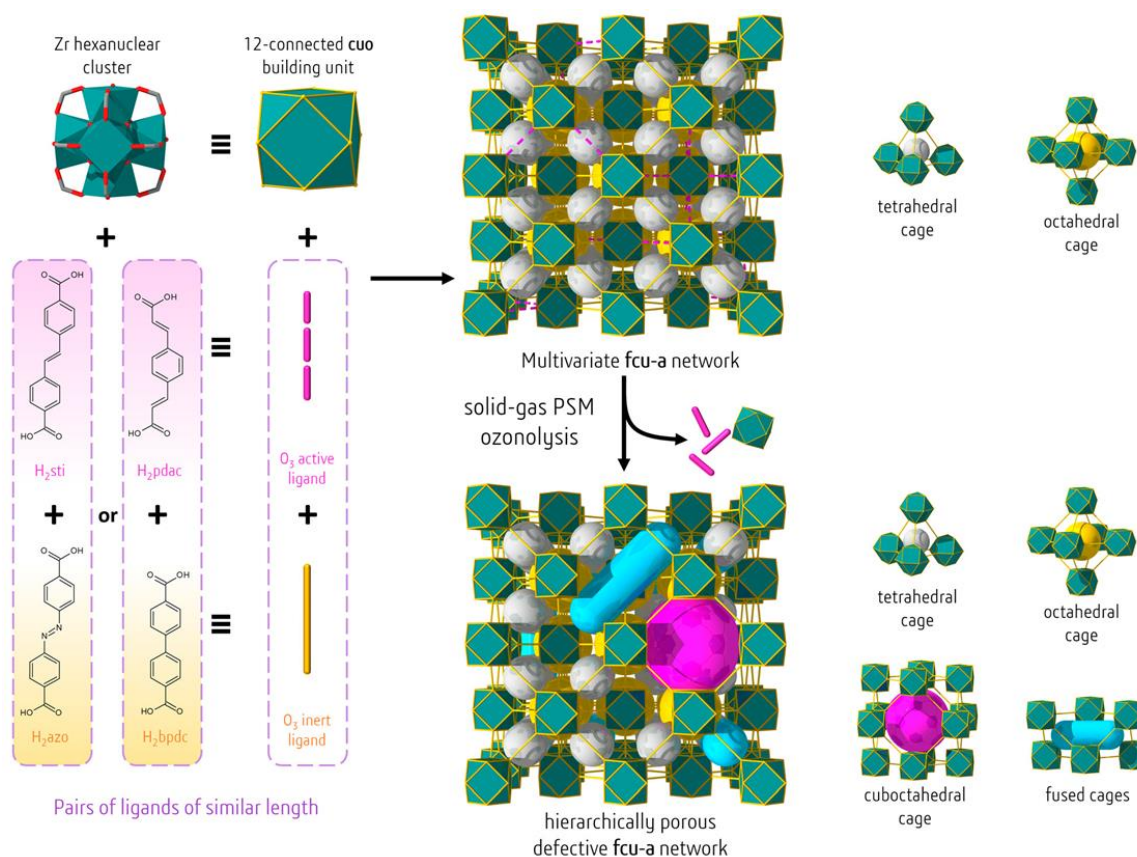
Figure 1.37 Illustration of mixed ligands used for constructing Zr-MOF and the formed hierarchically porous framework after solid-gas ozonolysis reaction.[223]

In addition to that, breaking the olefinic bond can create open metal sites for installing other catalytically active metals, which endows MOF with the potential for certain applications such as catalysis. Prof. Lin and co-workers synthesized a multivariate Al-MOF, isoreticular to MIL-53, which consists of a rod-like $(Al-OH)_n$ chain and a ligand pair: the ozone-inert H_2dcbpy (2,2'-bipyridine-5,5'-dicarboxylic acid) and the ozone-active H_2pdac.[224] Through ozonolysis treatment and acidic DMF washing, the pdac ligand could be completely cleaved and eliminated, forming open metal sites along the Al-based chain. These generated open metal sites were able to accommodate a strong Lewis acidic center, trimethylsilyl triflate (Me_3SiOTf). By subsequent metalation of dcbpy ligands with Pd nanoparticles (NPs), this Al-MOF, acting as a synergistic catalyst, showed excellent performance in the tandem dehydroalkoxylation-hydrogenation reaction of C-O bonds (Figure 1.38). Later, the same group installed $[Ir(ppy)_2(Cl)]_2$ instead of Pd into the dcpby ligand to effectively catalyze new reactions in a bioinspired fashion.[225]
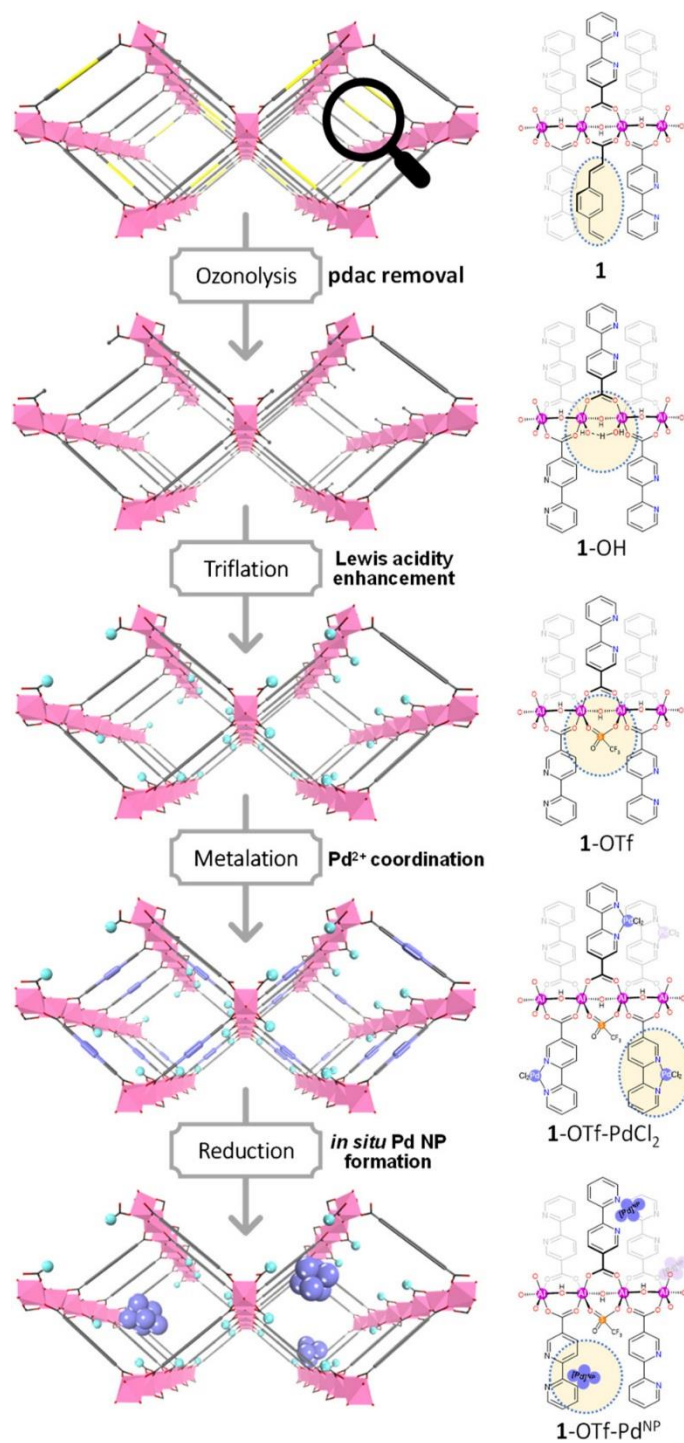
Figure 1.38 Illustration of stepwise incorporation of Lewis acid and Pd NP inside the MOF.[224]

1.6 References

(1) Batten, S. R.; Champness, N. R.; Chen, X.-M.; Garcia-Martinez, J.; Kitagawa, S.; Öhrström, L.; O'Keeffe, M.; Suh, M. P.; Reedijk, J. *Pure Appl. Chem.* **2013**, *85* (8), 1715-1724.

(2) Li, A.; Bueno-Perez, R.; Wiggin, S.; Fairen-Jimenez, D. *CrystEngComm* **2020**, *22* (43), 7152-7161.

(3) Li, A.; Bueno-Perez, R.; Madden, D.; Fairen-Jimenez, D. *Chem. Sci.* **2022**, *13* (27), 7990-8002.

(4) Hönicke, I. M.; Senkovska, I.; Bon, V.; Baburin, I. A.; Bönisch, N.; Raschke, S.; Evans, J. D.; Kaskel, S. *Angew. Chem. Int. Ed.* **2018**, *57* (42), 13780-13783.

(5) Li, A.; Perez, R. B.; Wiggin, S.; Ward, S. C.; Wood, P. A.; Fairen-Jimenez, D. *Matter* **2021**, *4* (4), 1105-1106.

(6) Daglar, H.; Keskin, S. *Coord. Chem. Rev.* **2020**, *422*, 213470.

(7) Yukio, K.; Ikuo, M.; Yoshihiko, S. *Bull. Chem. Soc. Jpn.* **1959**, *32* (7), 741-747.

(8) Yukio, K.; Ikuo, M.; Yoshihiko, S. *Bull. Chem. Soc. Jpn.* **1959**, *32* (11), 1216-1221.

(9) Yukio, K.; Ikuo, M.; Taiichi, H.; Yoshihiko, S. *Bull. Chem. Soc. Jpn.* **1959**, *32* (11), 1221-1226.

(10) Hoskins, B. F.; Robson, R. *J. Am. Chem. Soc.* **1989**, *111* (15), 5962-5964.

(11) Hoskins, B. F.; Robson, R. *J. Am. Chem. Soc.* **1990**, *112* (4), 1546-1554.

(12) Wells, A. F. *Three-Dimensional Nets and Polyhedra*; Wiley, 1977.

(13) Robinson, F.; Zaworotko, M. J. *J. Chem. Soc., Chem. Commun.* **1995**, (23), 2413-2414.

(14) Fujita, M.; Kwon, Y. J.; Washizu, S.; Ogura, K. *J. Am. Chem. Soc.* **1994**, *116* (3), 1151-1152.

(15) Abrahams, B. F.; Hoskins, B. F.; Michail, D. M.; Robson, R. *Nature* **1994**, *369* (6483), 727-729.

(16) Fujita, M.; Yazaki, J.; Ogura, K. *J. Am. Chem. Soc.* **1990**, *112* (14), 5645-5647.

(17) Yaghi, O. M.; Li, H. *J. Am. Chem. Soc.* **1995**, *117* (41), 10401-10402.

(18) Susumu, K.; Mitsuru, K. *Bull. Chem. Soc. Jpn.* **1998**, *71* (8), 1739-1753.

(19) Kitagawa, S.; Kitaura, R.; Noro, S.-i. *Angew. Chem. Int. Ed.* **2004**, *43* (18), 2334-2375.

(20) Yaghi, O. M.; Li, G.; Li, H. *Nature* **1995**, *378* (6558), 703-706.

(21) Kondo, M.; Yoshitomi, T.; Matsuzaka, H.; Kitagawa, S.; Seki, K. *Angew. Chem. Int. Ed.* **1997**, *36* (16), 1725-1727.

(22) Li, H.; Eddaoudi, M.; Groy, T. L.; Yaghi, O. M. *J. Am. Chem. Soc.* **1998**, *120* (33), 8571-8572.

(23) Chui, S. S. Y.; Lo, S. M. F.; Charmant, J. P. H.; Orpen, A. G.; Williams, I. D. *Science* **1999**, *283* (5405), 1148-1150.

(24) Li, H.; Eddaoudi, M.; O'Keeffe, M.; Yaghi, O. M. *Nature* **1999**, *402* (6759), 276-279.

(25) Yaghi, O. M. *Mol. Front. J.* **2019**, *03* (01), 66-83.

(26) Millange, F.; Serre, C.; Férey, G. *Chem. Commun.* **2002**, (8), 822-823.

(27) Férey, G.; Serre, C.; Mellot-Draznieks, C.; Millange, F.; Surblé, S.; Dutour, J.; Margiolaki, I. *Angew. Chem. Int. Ed.* **2004**, *43* (46), 6296-6301.

(28) Férey, G.; Mellot-Draznieks, C.; Serre, C.; Millange, F.; Dutour, J.; Surblé, S.; Margiolaki, I. *Science* **2005**, *309* (5743), 2040-2042.

(29) Rosi, N. L.; Kim, J.; Eddaoudi, M.; Chen, B.; O'Keeffe, M.; Yaghi, O. M. *J. Am. Chem. Soc.* **2005**, *127* (5), 1504-1518.

(30) Dietzel, P. D. C.; Morita, Y.; Blom, R.; Fjellvåg, H. *Angew. Chem. Int. Ed.* **2005**, *44* (39), 6354-6358.

(31) Cavka, J. H.; Jakobsen, S.; Olsbye, U.; Guillou, N.; Lamberti, C.; Bordiga, S.; Lillerud, K. P. *J. Am. Chem. Soc.* **2008**, *130* (42), 13850-13851.

(32) Petit, C. *Curr. Opin. Chem. Eng.* **2018**, *20*, 132-142.

(33) Li, J.-R.; Kuppler, R. J.; Zhou, H.-C. *Chem. Soc. Rev.* **2009**, *38* (5), 1477-1504.

(34) Li, B.; Wen, H.-M.; Zhou, W.; Xu, Jeff Q.; Chen, B. *Chem* **2016**, *1* (4), 557-580.

(35) Peng, Y.; Krungleviciute, V.; Eryazici, I.; Hupp, J. T.; Farha, O. K.; Yildirim, T. *J. Am. Chem. Soc.* **2013**, *135* (32), 11887-11894.

(36) He, Y.; Zhou, W.; Qian, G.; Chen, B. *Chem. Soc. Rev.* **2014**, *43* (16), 5657-5678.

(37) Lozano-Castelló, D.; Alcañiz-Monge, J.; de la Casa-Lillo, M. A.; Cazorla-Amorós, D.; Linares-Solano, A. *Fuel* **2002**, *81* (14), 1777-1803.

(38) Semin; Bakar, R. A.; Ismail, A. R. *Am. J. Environ. Sci.* **2009**, *5* (1), 1-11.

(39) Saha, D.; Grappe, H. A.; Chakraborty, A.; Orkoulas, G. *Chem. Rev.* **2016**, *116* (19), 11436-11499.

(40) *MOVE Program Overview (ARPA-E, 2012). https://arpa-e.energy.gov/?q=arpa-e-programs/move.* (accessed).

(41) Chen, Z.; Li, P.; Anderson, R.; Wang, X.; Zhang, X.; Robison, L.; Redfern, L. R.; Moribe, S.; Islamoglu, T.; Gómez-Gualdrón, D. A.; Yildirim, T.; Stoddart, J. F.; Farha, O. K. *Science* **2020**, *368* (6488), 297-303.

(42) Jia, T.; Gu, Y.; Li, F. *J. Environ. Chem. Eng.* **2022**, *10* (5), 108300.

(43) Sumida, K.; Rogow, D. L.; Mason, J. A.; McDonald, T. M.; Bloch, E. D.; Herm, Z. R.; Bae, T.-H.; Long, J. R. *Chem. Rev.* **2012**, *112* (2), 724-781.

(44) Liang, L.; Liu, C.; Jiang, F.; Chen, Q.; Zhang, L.; Xue, H.; Jiang, H.-L.; Qian, J.; Yuan, D.; Hong, M. *Nat. Commun.* **2017**, *8* (1), 1233.

(45) Xiang, S.; He, Y.; Zhang, Z.; Wu, H.; Zhou, W.; Krishna, R.; Chen, B. *Nat. Commun.* **2012**, *3* (1), 954.

(46) Lee, K. B.; Sircar, S. *AlChE J.* **2008**, *54* (9), 2293-2302.

(47) Granite, E. J.; Pennline, H. W. *Ind. Eng. Chem. Res.* **2002**, *41* (22), 5470-5476.

(48) Easun, T. L.; Moreau, F.; Yan, Y.; Yang, S.; Schröder, M. *Chem. Soc. Rev.* **2017**, *46* (1), 239-274.

(49) Kong, X.; Scott, E.; Ding, W.; Mason, J. A.; Long, J. R.; Reimer, J. A. *J. Am. Chem. Soc.* **2012**, *134* (35), 14341-14344.

(50) Lin, L.-C.; Kim, J.; Kong, X.; Scott, E.; McDonald, T. M.; Long, J. R.; Reimer, J. A.; Smit, B. *Angew. Chem. Int. Ed.* **2013**, *52* (16), 4410-4413.

(51) Britt, D.; Furukawa, H.; Wang, B.; Glover, T. G.; Yaghi, O. M. *Proc. Natl. Acad. Sci. U.S.A.* **2009**, *106* (49), 20637-20640.

(52) Queen, W. L.; Brown, C. M.; Britt, D. K.; Zajdel, P.; Hudson, M. R.; Yaghi, O. M. *J. Phys. Chem. C* **2011**, *115* (50), 24915-24919.

(53) García, E. J.; Mowat, J. P. S.; Wright, P. A.; Pérez-Pellitero, J.; Jallut, C.; Pirngruber, G. D. *J. Phys. Chem. C* **2012**, *116* (50), 26636-26648.

(54) Caskey, S. R.; Wong-Foy, A. G.; Matzger, A. J. *J. Am. Chem. Soc.* **2008**, *130* (33), 10870-10871.

(55) Queen, W. L.; Hudson, M. R.; Bloch, E. D.; Mason, J. A.; Gonzalez, M. I.; Lee, J. S.; Gygi, D.; Howe, J. D.; Lee, K.; Darwish, T. A.; James, M.; Peterson, V. K.; Teat, S. J.; Smit, B.; Neaton, J. B.; Long, J. R.; Brown, C. M. *Chem. Sci.* **2014**, *5* (12), 4569-4581.

(56) Haldoupis, E.; Borycz, J.; Shi, H.; Vogiatzis, K. D.; Bai, P.; Queen, W. L.; Gagliardi, L.; Siepmann, J. I. *J. Phys. Chem. C* **2015**, *119* (28), 16058-16071.

(57) Tan, K.; Zuluaga, S.; Gong, Q.; Gao, Y.; Nijem, N.; Li, J.; Thonhauser, T.; Chabal, Y. J. *Chem. Mater.* **2015**, *27* (6), 2203-2217.

(58) Maia, R. A.; Louis, B.; Gao, W.; Wang, Q. *React. Chem. Eng.* **2021**, *6* (7), 1118-1133.

(59) Kizzie, A. C.; Wong-Foy, A. G.; Matzger, A. J. *Langmuir* **2011**, *27* (10), 6368-6373.

(60) Liu, J.; Tian, J.; Thallapally, P. K.; McGrail, B. P. *J. Phys. Chem. C* **2012**, *116* (17), 9575-9581.

(61) McDonald, T. M.; Lee, W. R.; Mason, J. A.; Wiers, B. M.; Hong, C. S.; Long, J. R. *J. Am. Chem. Soc.* **2012**, *134* (16), 7056-7065.

(62) Milner, P. J.; Siegelman, R. L.; Forse, A. C.; Gonzalez, M. I.; Runčevski, T.; Martell, J. D.; Reimer, J. A.; Long, J. R. *J. Am. Chem. Soc.* **2017**, *139* (38), 13541-13553.

(63) Yeon, J. S.; Lee, W. R.; Kim, N. W.; Jo, H.; Lee, H.; Song, J. H.; Lim, K. S.; Kang, D. W.; Seo, J. G.; Moon, D.; Wiers, B.; Hong, C. S. *J. Mater. Chem. A* **2015**, *3* (37), 19177-19185.

(64) Dinakar, B.; Forse, A. C.; Jiang, H. Z. H.; Zhu, Z.; Lee, J.-H.; Kim, E. J.; Parker, S. T.; Pollak, C. J.; Siegelman, R. L.; Milner, P. J.; Reimer, J. A.; Long, J. R. *J. Am. Chem. Soc.* **2021**, *143* (37), 15258-15270.

(65) Babaei, H.; Lee, J.-H.; Dods, M. N.; Wilmer, C. E.; Long, J. R. *ACS Appl. Mater. Interfaces* **2020**, *12* (40), 44617-44621.

(66) Siegelman, R. L.; Milner, P. J.; Forse, A. C.; Lee, J.-H.; Colwell, K. A.; Neaton, J. B.; Reimer, J. A.; Weston, S. C.; Long, J. R. *J. Am. Chem. Soc.* **2019**, *141* (33), 13171-13186.

(67) Lee, W. R.; Hwang, S. Y.; Ryu, D. W.; Lim, K. S.; Han, S. S.; Moon, D.; Choi, J.; Hong, C. S. *Energy Environ. Sci.* **2014**, *7* (2), 744-751.

(68) Forse, A. C.; Milner, P. J.; Lee, J.-H.; Redfearn, H. N.; Oktawiec, J.; Siegelman, R. L.; Martell, J. D.; Dinakar, B.; Zasada, L. B.; Gonzalez, M. I.; Neaton, J. B.; Long, J. R.; Reimer, J. A. *J. Am. Chem. Soc.* **2018**, *140* (51), 18016-18031.

(69) Zhu, Z.; Parker, S. T.; Forse, A. C.; Lee, J.-H.; Siegelman, R. L.; Milner, P. J.; Tsai, H.; Ye, M.; Xiong, S.; Paley, M. V.; Uliana, A. A.; Oktawiec, J.; Dinakar, B.; Didas, S. A.; Meihaus, K. R.; Reimer, J. A.; Neaton, J. B.; Long, J. R. *J. Am. Chem. Soc.* **2023**, *145* (31), 17151-17163.

(70) Gleick, P. H. *Water in Crisis: A Guide to the Worlds Fresh Water Resources*; Oxford University Press, New York, 1993.

(71) Hanikel, N.; Prévot, M. S.; Yaghi, O. M. *Nat. Nanotechnol.* **2020**, *15* (5), 348-355.

(72) Liu, C.-H.; Nguyen, H. L.; Yaghi, O. M. *ACM.* **2020**, *1* (1), 18-25.

(73) Van der Bruggen, B.; Vandecasteele, C. *Desalination* **2002**, *143* (3), 207-218.

(74) Kalmutzki, M. J.; Diercks, C. S.; Yaghi, O. M. *Adv. Mater.* **2018**, *30* (37), 1704304.

(75) Xu, W.; Yaghi, O. M. *ACS Cent. Sci.* **2020**, *6* (8), 1348-1354.

(76) Yang, P.; Clark, D. S.; Yaghi, O. M. *Mol. Front. J.* **2021**, *05* (01n02), 30-37.

(77) Kim, H.; Yang, S.; Rao, S. R.; Narayanan, S.; Kapustin, E. A.; Furukawa, H.; Umans, A. S.; Yaghi, O. M.; Wang, E. N. *Science* **2017**, *356* (6336), 430-434.

(78) Kim, H.; Rao, S. R.; Kapustin, E. A.; Zhao, L.; Yang, S.; Yaghi, O. M.; Wang, E. N. *Nat. Commun.* **2018**, *9* (1), 1191.

(79) Fathieh, F.; Kalmutzki, M. J.; Kapustin, E. A.; Waller, P. J.; Yang, J.; Yaghi, O. M. *Sci. Adv.* **2018**, *4* (6), eaat3198.

(80) Hanikel, N.; Pei, X.; Chheda, S.; Lyu, H.; Jeong, W.; Sauer, J.; Gagliardi, L.; Yaghi, O. M. *Science* **2021**, *374* (6566), 454-459.

(81) Zheng, Z.; Hanikel, N.; Lyu, H.; Yaghi, O. M. *J. Am. Chem. Soc.* **2022**, *144* (49), 22669-22675.

(82) Hanikel, N.; Prévot, M. S.; Fathieh, F.; Kapustin, E. A.; Lyu, H.; Wang, H.; Diercks, N. J.; Glover, T. G.; Yaghi, O. M. *ACS Cent. Sci.* **2019**, *5* (10), 1699-1706.

(83) Song, W.; Zheng, Z.; Alawadhi, A. H.; Yaghi, O. M. *Nat. Water* **2023**, *1* (7), 626-634.

(84) Liu, X.; Sun, X.; Peng, Y.; Wang, Y.; Xu, D.; Chen, W.; Wang, W.; Yan, X.; Ma, X. *ACS Nano* **2022**, *16* (9), 14666-14678.

(85) Palagi, S.; Singh, D. P.; Fischer, P. *Adv. Opt. Mater.* **2019**, *7* (16), 1900370.

(86) Šípová-Jungová, H.; Andrén, D.; Jones, S.; Käll, M. *Chem. Rev.* **2020**, *120* (1), 269-287.

(87) Chen, X.-Z.; Hoop, M.; Mushtaq, F.; Siringil, E.; Hu, C.; Nelson, B. J.; Pané, S. *Appl. Mater. Today* **2017**, *9*, 37-48.

(88) Loget, G.; Kuhn, A. *Nat. Commun.* **2011**, *2* (1), 535.

(89) Kagan, D.; Calvo-Marzal, P.; Balasubramanian, S.; Sattayasamitsathit, S.; Manesh, K. M.; Flechsig, G.-U.; Wang, J. *J. Am. Chem. Soc.* **2009**, *131* (34), 12082-12083.

(90) Kong, L.; Guan, J.; Pumera, M. *Curr. Opin. Electrochem.* **2018**, *10*, 174-182.

(91) Wang, J.; Dong, R.; Wu, H.; Cai, Y.; Ren, B. *Nano-Micro Lett.* **2019**, *12* (1), 11.

(92) Parmar, J.; Vilela, D.; Villa, K.; Wang, J.; Sánchez, S. *J. Am. Chem. Soc.* **2018**, *140* (30), 9317-9331.

(93) Lyu, F.; Zhang, Y.; Zare, R. N.; Ge, J.; Liu, Z. *Nano Lett.* **2014**, *14* (10), 5761-5765.

(94) Cui, J.; Feng, Y.; Lin, T.; Tan, Z.; Zhong, C.; Jia, S. *ACS Appl. Mater. Interfaces* **2017**, *9* (12), 10587-10594.

(95) Li, Z.; Xia, H.; Li, S.; Pang, J.; Zhu, W.; Jiang, Y. *Nanoscale* **2017**, *9* (40), 15298-15302.

(96) Shieh, F.-K.; Wang, S.-C.; Yen, C.-I.; Wu, C.-C.; Dutta, S.; Chou, L.-Y.; Morabito, J. V.; Hu, P.; Hsu, M.-H.; Wu, K. C. W.; Tsung, C.-K. *J. Am. Chem. Soc.* **2015**, *137* (13), 4276-4279.

(97) Gao, S.; Hou, J.; Zeng, J.; Richardson, J. J.; Gu, Z.; Gao, X.; Li, D.; Gao, M.; Wang, D.-W.; Chen, P.; Chen, V.; Liang, K.; Zhao, D.; Kong, B. *Adv. Funct. Mater.* **2019**, *29* (18), 1808900.

(98) Li, P.; Moon, S.-Y.; Guelta, M. A.; Harvey, S. P.; Hupp, J. T.; Farha, O. K. *J. Am. Chem. Soc.* **2016**, *138* (26), 8052-8055.

(99) Lian, X.; Huang, Y.; Zhu, Y.; Fang, Y.; Zhao, R.; Joseph, E.; Li, J.; Pellois, J.-P.; Zhou, H.-C. *Angew. Chem. Int. Ed.* **2018**, *57* (20), 5725-5730.

(100) Li, P.; Chen, Q.; Wang, T. C.; Vermeulen, N. A.; Mehdi, B. L.; Dohnalkova, A.; Browning, N. D.; Shen, D.; Anderson, R.; Gómez-Gualdrón, D. A.; Cetin, F. M.; Jagiello, J.; Asiri, A. M.; Stoddart, J. F.; Farha, O. K. *Chem* **2018**, *4* (5), 1022-1034.

(101) Xu, M.; Yuan, S.; Chen, X.-Y.; Chang, Y.-J.; Day, G.; Gu, Z.-Y.; Zhou, H.-C. *J. Am. Chem. Soc.* **2017**, *139* (24), 8312-8319.

(102) Doherty, C. M.; Grenci, G.; Riccò, R.; Mardel, J. I.; Reboul, J.; Furukawa, S.; Kitagawa, S.; Hill, A. J.; Falcaro, P. *Adv. Mater.* **2013**, *25* (34), 4701-4705.

(103) Terzopoulou, A.; Nicholas, J. D.; Chen, X.-Z.; Nelson, B. J.; Pané, S.; Puigmartí-Luis, J. *Chem. Rev.* **2020**, *120* (20), 11175-11193.

(104) Khezri, B.; Pumera, M. *Adv. Mater.* **2019**, *31* (14), 1806530.

(105) Mirkovic, T.; Zacharia, N. S.; Scholes, G. D.; Ozin, G. A. *Small* **2010**, *6* (2), 159-167.

(106) Li, L.; Wang, J.; Li, T.; Song, W.; Zhang, G. *Soft Matter* **2014**, *10* (38), 7511-7518.

(107) Tan, T. T. Y.; Cham, J. T. M.; Reithofer, M. R.; Andy Hor, T. S.; Chin, J. M. *Chem. Commun.* **2014**, *50* (96), 15175-15178.

(108) Ayala, A.; Carbonell, C.; Imaz, I.; Maspoch, D. *Chem. Commun.* **2016**, *52* (29), 5096-5099.

(109) Li, J.; Yu, X.; Xu, M.; Liu, W.; Sandraz, E.; Lan, H.; Wang, J.; Cohen, S. M. *J. Am. Chem. Soc.* **2017**, *139* (2), 611-614.

(110) You, Y.; Xu, D.; Pan, X.; Ma, X. *Appl. Mater. Today* **2019**, *16*, 508-517.

(111) Yaghi, O. M. *J. Am. Chem. Soc.* **2016**, *138* (48), 15507-15509.

(112) Omar M. Yaghi, M. J. K., Christian S. Diercks. *Introduction to Reticular Chemistry: Metal-Organic Frameworks and Covalent Organic Frameworks*; Wiley-VCH: Weinheim, 2019.

(113) Gropp, C.; Canossa, S.; Wuttke, S.; Gándara, F.; Li, Q.; Gagliardi, L.; Yaghi, O. M. *ACS Cent. Sci.* **2020**, *6* (8), 1255-1273.

(114) O'Keeffe, M. *Chem. Soc. Rev.* **2009**, *38* (5), 1215-1217.

(115) Jiang, J.; Zhao, Y.; Yaghi, O. M. *J. Am. Chem. Soc.* **2016**, *138* (10), 3255-3265.

(116) Delgado-Friedrichs, O.; O'Keeffe, M. *Acta Crystallogr. A.* **2003**, *59* (4), 351-360.

(117) Bonneau, C.; Delgado-Friedrichs, O.; O'Keeffe, M.; Yaghi, O. M. *Acta Crystallogr. A.* **2004**, *60* (6), 517-520.

(118) Alexandrov, E. V.; Blatov, V. A.; Kochetkov, A. V.; Proserpio, D. M. *CrystEngComm* **2011**, *13* (12), 3947-3958.

(119) O'Keeffe, M.; Peskov, M. A.; Ramsden, S. J.; Yaghi, O. M. *Acc. Chem. Res.* **2008**, *41* (12), 1782-1789.

(120) Jiang, H.; Alezi, D.; Eddaoudi, M. *Nat. Rev. Mater.* **2021**, *6* (6), 466-487.

(121) Tranchemontagne, D. J.; Mendoza-Cortés, J. L.; O'Keeffe, M.; Yaghi, O. M. *Chem. Soc. Rev.* **2009**, *38* (5), 1257-1283.

(122) Schoedel, A.; Li, M.; Li, D.; O'Keeffe, M.; Yaghi, O. M. *Chem. Rev.* **2016**, *116* (19), 12466-12535.

(123) Guillerm, V.; Gross, S.; Serre, C.; Devic, T.; Bauer, M.; Férey, G. *Chem. Commun.* **2010**, *46* (5), 767-769.

(124) Dai, S.; Simms, C.; Dovgaliuk, I.; Patriarche, G.; Tissot, A.; Parac-Vogt, T. N.; Serre, C. *Chem. Mater.* **2021**, *33* (17), 7057-7066.

(125) Guillerm, V.; Kim, D.; Eubank, J. F.; Luebke, R.; Liu, X.; Adil, K.; Lah, M. S.; Eddaoudi, M. *Chem. Soc. Rev.* **2014**, *43* (16), 6141-6172.

(126) Guillerm, V.; Eddaoudi, M. *Acc. Chem. Res.* **2021**, *54* (17), 3298-3312.

(127) Perry Iv, J. J.; Perman, J. A.; Zaworotko, M. J. *Chem. Soc. Rev.* **2009**, *38* (5), 1400-1417.

(128) Zou, Y.; Park, M.; Hong, S.; Lah, M. S. *Chem. Commun.* **2008**, (20), 2340-2342.

(129) Zhao, D.; Yuan, D.; Sun, D.; Zhou, H.-C. *J. Am. Chem. Soc.* **2009**, *131* (26), 9186-9188.

(130) Zheng, B.; Bai, J.; Duan, J.; Wojtas, L.; Zaworotko, M. J. *J. Am. Chem. Soc.* **2011**, *133* (4), 748-751.

(131) Li, B.; Zhang, Z.; Li, Y.; Yao, K.; Zhu, Y.; Deng, Z.; Yang, F.; Zhou, X.; Li, G.; Wu, H.; Nijem, N.; Chabal, Y. J.; Lai, Z.; Han, Y.; Shi, Z.; Feng, S.; Li, J. *Angew. Chem. Int. Ed.* **2012**, *51* (6), 1412-1415.

(132) Hong, S.; Oh, M.; Park, M.; Yoon, J. W.; Chang, J.-S.; Lah, M. S. *Chem. Commun.* **2009**, (36), 5397-5399.

(133) Nouar, F.; Eubank, J. F.; Bousquet, T.; Wojtas, L.; Zaworotko, M. J.; Eddaoudi, M. *J. Am. Chem. Soc.* **2008**, *130* (6), 1833-1835.

(134) Eddaoudi, M.; Kim, J.; Wachter, J. B.; Chae, H. K.; O'Keeffe, M.; Yaghi, O. M. *J. Am. Chem. Soc.* **2001**, *123* (18), 4368-4369.

(135) Grancha, T.; Carné-Sánchez, A.; Zarekarizi, F.; Hernández-López, L.; Albalad, J.; Khobotov, A.; Guillerm, V.; Morsali, A.; Juanhuix, J.; Gándara, F.; Imaz, I.; Maspoch, D. *Angew. Chem. Int. Ed.* **2021**, *60* (11), 5729-5733.

(136) Park, J.; Hong, S.; Moon, D.; Park, M.; Lee, K.; Kang, S.; Zou, Y.; John, R. P.; Kim, G. H.; Lah, M. S. *Inorg. Chem.* **2007**, *46* (24), 10208-10213.

(137) Li, J.-R.; Timmons, D. J.; Zhou, H.-C. *J. Am. Chem. Soc.* **2009**, *131* (18), 6368-6369.

(138) Guillerm, V.; Weseliński, Ł. J.; Belmabkhout, Y.; Cairns, A. J.; D'Elia, V.; Wojtas, Ł.; Adil, K.; Eddaoudi, M. *Nat. Chem.* **2014**, *6* (8), 673-680.

(139) Eubank, J. F.; Wojtas, L.; Hight, M. R.; Bousquet, T.; Kravtsov, V. C.; Eddaoudi, M. *J. Am. Chem. Soc.* **2011**, *133* (44), 17532-17535.

(140) Pallach, R.; Keupp, J.; Terlinden, K.; Frentzel-Beyme, L.; Kloß, M.; Machalica, A.; Kotschy, J.; Vasa, S. K.; Chater, P. A.; Sternemann, C.; Wharmby, M. T.; Linser, R.; Schmid, R.; Henke, S. *Nat. Commun.* **2021**, *12* (1), 4097.

(141) Hu, Z.; Nalaparaju, A.; Peng, Y.; Jiang, J.; Zhao, D. *Inorg. Chem.* **2016**, *55* (3), 1134-1141.

(142) Lammert, M.; Wharmby, M. T.; Smolders, S.; Bueken, B.; Lieb, A.; Lomachenko, K. A.; Vos, D. D.; Stock, N. *Chem. Commun.* **2015**, *51* (63), 12578-12581.

(143) Eddaoudi, M.; Kim, J.; Rosi, N.; Vodak, D.; Wachter, J.; O'Keeffe, M.; Yaghi, O. M. *Science* **2002**, *295* (5554), 469-472.

(144) Wang, L. J.; Deng, H.; Furukawa, H.; Gándara, F.; Cordova, K. E.; Peri, D.; Yaghi, O. M. *Inorg. Chem.* **2014**, *53* (12), 5881-5883.

(145) Deng, H.; Doonan, C. J.; Furukawa, H.; Ferreira, R. B.; Towne, J.; Knobler, C. B.; Wang, B.; Yaghi, O. M. *Science* **2010**, *327* (5967), 846-850.

(146) Zhao, M.; Lu, Q.; Ma, Q.; Zhang, H. *Small Methods* **2017**, *1* (1-2), 1600030.

(147) Wang, J.; Li, N.; Xu, Y.; Pang, H. *Chem. Eur. J.* **2020**, *26* (29), 6402-6422.

(148) Cai, G.; Yan, P.; Zhang, L.; Zhou, H.-C.; Jiang, H.-L. *Chem. Rev.* **2021**, *121* (20), 12278-12326.

(149) Feng, L.; Wang, K.-Y.; Lv, X.-L.; Yan, T.-H.; Zhou, H.-C. *Natl. Sci. Rev.* **2019**, *7* (11), 1743-1758.

(150) Manna, K.; Ji, P.; Greene, F. X.; Lin, W. *J. Am. Chem. Soc.* **2016**, *138* (24), 7488-7491.

(151) Øien, S.; Wragg, D.; Reinsch, H.; Svelle, S.; Bordiga, S.; Lamberti, C.; Lillerud, K. P. *Cryst. Growth Des.* **2014**, *14* (11), 5370-5372.

(152) Trickett, C. A.; Gagnon, K. J.; Lee, S.; Gándara, F.; Bürgi, H.-B.; Yaghi, O. M. *Angew. Chem. Int. Ed.* **2015**, *54* (38), 11162-11167.

(153) Gutov, O. V.; Molina, S.; Escudero-Adán, E. C.; Shafir, A. *Chem. Eur. J.* **2016**, *22* (38), 13582-13587.

(154) Feng, L.; Wang, K.-Y.; Day, G. S.; Ryder, M. R.; Zhou, H.-C. *Chem. Rev.* **2020**, *120* (23), 13087-13133.

(155) Zhou, X.; Jin, H.; Xia, B. Y.; Davey, K.; Zheng, Y.; Qiao, S.-Z. *Adv. Mater.* **2021**, *33* (51), 2104341.

(156) Vermoortele, F.; Ameloot, R.; Alaerts, L.; Matthessen, R.; Carlier, B.; Fernandez, E. V. R.; Gascon, J.; Kapteijn, F.; De Vos, D. E. *J. Mater. Chem.* **2012**, *22* (20), 10313-10321.

(157) Huang, H.; Li, J.-R.; Wang, K.; Han, T.; Tong, M.; Li, L.; Xie, Y.; Yang, Q.; Liu, D.; Zhong, C. *Nat. Commun.* **2015**, *6* (1), 8847.

(158) Zhou, X.; Dong, J.; Zhu, Y.; Liu, L.; Jiao, Y.; Li, H.; Han, Y.; Davey, K.; Xu, Q.; Zheng, Y.; Qiao, S.-Z. *J. Am. Chem. Soc.* **2021**, *143* (17), 6681-6690.

(159) Ni, C.; Zheng, H.; Liu, W.; Wu, L.; Li, R.; Zhou, K.; Zhang, W. *Adv. Funct. Mater.* **2023**, *33* (25), 2301075.

(160) Burtch, N. C.; Walton, I. M.; Hungerford, J. T.; Morelock, C. R.; Jiao, Y.; Heinen, J.; Chen, Y.-S.; Yakovenko, A. A.; Xu, W.; Dubbeldam, D.; Walton, K. S. *Nat. Chem.* **2020**, *12* (2), 186-192.

(161) Kim, Y.; Yang, T.; Yun, G.; Ghasemian, M. B.; Koo, J.; Lee, E.; Cho, S. J.; Kim, K. *Angew. Chem. Int. Ed.* **2015**, *54* (45), 13273-13278.

(162) Lee, J.; Choi, J. S.; Jeong, N. C.; Choe, W. *Chem. Sci.* **2019**, *10* (24), 6157-6161.

(163) Yuan, W.; Friščić, T.; Apperley, D.; James, S. L. *Angew. Chem. Int. Ed.* **2010**, *49* (23), 3916-3919.

(164) Tan, F.; López-Periago, A.; Light, M. E.; Cirera, J.; Ruiz, E.; Borrás, A.; Teixidor, F.; Viñas, C.; Domingo, C.; Planas, J. G. *Adv. Mater.* **2018**, *30* (29), 1800726.

(165) Qi, S.-C.; Qian, X.-Y.; He, Q.-X.; Miao, K.-J.; Jiang, Y.; Tan, P.; Liu, X.-Q.; Sun, L.-B. *Angew. Chem. Int. Ed.* **2019**, *58* (30), 10104-10109.

(166) Cliffe, M. J.; Castillo-Martínez, E.; Wu, Y.; Lee, J.; Forse, A. C.; Firth, F. C. N.; Moghadam, P. Z.; Fairen-Jimenez, D.; Gaultois, M. W.; Hill, J. A.; Magdysyuk, O. V.; Slater, B.; Goodwin, A. L.; Grey, C. P. *J. Am. Chem. Soc.* **2017**, *139* (15), 5397-5404.

(167) Avci, C.; Ariñez-Soriano, J.; Carné-Sánchez, A.; Guillerm, V.; Carbonell, C.; Imaz, I.; Maspoch, D. *Angew. Chem., Int. Ed.* **2015**, *127* (48), 14625-14629.

(168) Liu, W.; Huang, J.; Yang, Q.; Wang, S.; Sun, X.; Zhang, W.; Liu, J.; Huo, F. *Angew. Chem. Int. Ed.* **2017**, *56* (20), 5512-5516.

(169) Huang, J.; Li, Y.; Huang, R.-K.; He, C.-T.; Gong, L.; Hu, Q.; Wang, L.; Xu, Y.-T.; Tian, X.-Y.; Liu, S.-Y.; Ye, Z.-M.; Wang, F.; Zhou, D.-D.; Zhang, W.-X.; Zhang, J.-P. *Angew. Chem. Int. Ed.* **2018**, *57* (17), 4632-4636.

(170) Huang, C.; Dong, J.; Sun, W.; Xue, Z.; Ma, J.; Zheng, L.; Liu, C.; Li, X.; Zhou, K.; Qiao, X.; Song, Q.; Ma, W.; Zhang, L.; Lin, Z.; Wang, T. *Nat. Commun.* **2019**, *10* (1), 2779.

(171) Peng, Y.; Li, Y.; Ban, Y.; Jin, H.; Jiao, W.; Liu, X.; Yang, W. *Science* **2014**, *346* (6215), 1356-1359.

(172) Liao, W.-M.; Zhang, J.-H.; Yin, S.-Y.; Lin, H.; Zhang, X.; Wang, J.; Wang, H.-P.; Wu, K.; Wang, Z.; Fan, Y.-N.; Pan, M.; Su, C.-Y. *Nat. Commun.* **2018**, *9* (1), 2401.

(173) Mukhopadhyay, A.; Maka, V. K.; Savitha, G.; Moorthy, J. N. *Chem* **2018**, *4* (5), 1059-1079.

(174) Jayaramulu, K.; Masa, J.; Morales, D. M.; Tomanec, O.; Ranc, V.; Petr, M.; Wilde, P.; Chen, Y.-T.; Zboril, R.; Schuhmann, W.; Fischer, R. A. *Adv. Sci.* **2018**, *5* (11), 1801029.

(175) Amo-Ochoa, P.; Welte, L.; González-Prieto, R.; Sanz Miguel, P. J.; Gómez-García, C. J.; Mateo-Martí, E.; Delgado, S.; Gómez-Herrero, J.; Zamora, F. *Chem. Commun.* **2010**, *46* (19), 3262-3264.

(176) Peng, Y.; Li, Y.; Ban, Y.; Yang, W. *Angew. Chem. Int. Ed.* **2017**, *56* (33), 9757-9761.

(177) Luo, Y.-H.; Chen, C.; He, C.; Zhu, Y.-Y.; Hong, D.-L.; He, X.-T.; An, P.-J.; Wu, H.-S.; Sun, B.-W. *ACS Appl. Mater. Interfaces* **2018**, *10* (34), 28860-28867.

(178) Hermosa, C.; Horrocks, B. R.; Martínez, J. I.; Liscio, F.; Gómez-Herrero, J.; Zamora, F. *Chem. Sci.* **2015**, *6* (4), 2553-2558.

(179) Li, P.-Z.; Maeda, Y.; Xu, Q. *Chem. Commun.* **2011**, *47* (29), 8436-8438.

(180) Xie, J.; Wang, Y.; Zhang, D.; Liang, C.; Liu, W.; Chong, Y.; Yin, X.; Zhang, Y.; Gui, D.; Chen, L.; Tong, W.; Liu, Z.; Diwu, J.; Chai, Z.; Wang, S. *Chem. Commun.* **2019**, *55* (78), 11715-11718.

(181) Chen, S.; Mukherjee, S.; Lucier, B. E. G.; Guo, Y.; Wong, Y. T. A.; Terskikh, V. V.; Zaworotko, M. J.; Huang, Y. *J. Am. Chem. Soc.* **2019**, *141* (36), 14257-14271.

(182) Drake, H. F.; Day, G. S.; Vali, S. W.; Xiao, Z.; Banerjee, S.; Li, J.; Joseph, E. A.; Kuszynski, J. E.; Perry, Z. T.; Kirchon, A.; Ozdemir, O. K.; Lindahl, P. A.; Zhou, H.-C. *Chem. Commun.* **2019**, *55* (85), 12769-12772.

(183) Drake, H. F.; Xiao, Z.; Day, G. S.; Vali, S. W.; Chen, W.; Wang, Q.; Huang, Y.; Yan, T.-H.; Kuszynski, J. E.; Lindahl, P. A.; Ryder, M. R.; Zhou, H.-C. *Mater. Adv.* **2021**, *2* (16), 5487-5493.

(184) Lin, Q.-Y.; Ding, H.-J.; Liu, M.; Liu, X.-Y.; Nie, H.-X.; Fu, Z.-X.; Zhang, S.-M.; Yu, M.-H.; Chang, Z. *Inorg. Chem.* **2022**, *61* (15), 5800-5812.

(185) Mateo, D.; Santiago-Portillo, A.; Albero, J.; Navalón, S.; Alvaro, M.; García, H. *Angew. Chem. Int. Ed.* **2019**, *58* (49), 17843-17848.

(186) Han, X.; Cheng, Q.; Meng, X.; Shao, Z.; Ma, K.; Wei, D.; Ding, J.; Hou, H. *Chem. Commun.* **2017**, *53* (74), 10314-10317.

(187) Shimizu, T.; Wang, H.; Matsumura, D.; Mitsuhara, K.; Ohta, T.; Yoshikawa, H. *ChemSusChem* **2020**, *13* (9), 2256-2263.

(188) Feng, L.; Wang, K.-Y.; Lv, X.-L.; Powell, J. A.; Yan, T.-H.; Willman, J.; Zhou, H.-C. *J. Am. Chem. Soc.* **2019**, *141* (37), 14524-14529.

(189) Yuan, S.; Zhang, P.; Zhang, L.; Garcia-Esparza, A. T.; Sokaras, D.; Qin, J.-S.; Feng, L.; Day, G. S.; Chen, W.; Drake, H. F.; Elumalai, P.; Madrahimov, S. T.; Sun, D.; Zhou, H.-C. *J. Am. Chem. Soc.* **2018**, *140* (34), 10814-10819.

(190) Liu, X.; Mazel, A.; Marschner, S.; Fu, Z.; Muth, M.; Kirschhöfer, F.; Brenner-Weiss, G.; Bräse, S.; Diring, S.; Odobel, F.; Haldar, R.; Wöll, C. *ACS Appl. Mater. Interfaces* **2021**, *13* (48), 57768-57773.

(191) Koo, J.; Hwang, I.-C.; Yu, X.; Saha, S.; Kim, Y.; Kim, K. *Chem. Sci.* **2017**, *8* (10), 6799-6803.

(192) Yu, D.; Shao, Q.; Song, Q.; Cui, J.; Zhang, Y.; Wu, B.; Ge, L.; Wang, Y.; Zhang, Y.; Qin, Y.; Vajtai, R.; Ajayan, P. M.; Wang, H.; Xu, T.; Wu, Y. *Nat. Commun.* **2020**, *11* (1), 927.

(193) Lo, S.-H.; Feng, L.; Tan, K.; Huang, Z.; Yuan, S.; Wang, K.-Y.; Li, B.-H.; Liu, W.-L.; Day, G. S.; Tao, S.; Yang, C.-C.; Luo, T.-T.; Lin, C.-H.; Wang, S.-L.; Billinge, S. J. L.; Lu, K.-L.; Chabal, Y. J.; Zou, X.; Zhou, H.-C. *Nat. Chem.* **2020**, *12* (1), 90-97.

(194) Xiao, L.; Wang, Z.; Guan, J. *Coord. Chem. Rev.* **2022**, *472*, 214777.

(195) Zhao, M.; Huang, Y.; Peng, Y.; Huang, Z.; Ma, Q.; Zhang, H. *Chem. Soc. Rev.* **2018**, *47* (16), 6267-6295.

(196) Chen, J. E.; Yang, Z.-J.; Koh, H. U.; Shen, J.; Cai, Y.; Yamauchi, Y.; Yeh, L.-H.; Tung, V.; Wu, K. C.-W. *Adv.Mater. Interfaces* **2022**, *9* (13), 2102560.

(197) Tamuly, P.; Sama, F.; Moorthy, J. N. *Adv. Mater. Interfaces* **2022**, *9* (16), 2200337.

(198) Au, V. K.-M.; Nakayashiki, K.; Huang, H.; Suginome, S.; Sato, H.; Aida, T. *J. Am. Chem. Soc.* **2019**, *141* (1), 53-57.

(199) Wang, X.; Chi, C.; Zhang, K.; Qian, Y.; Gupta, K. M.; Kang, Z.; Jiang, J.; Zhao, D. *Nat. Commun.* **2017**, *8* (1), 14460.

(200) Wang, Z.; Cohen, S. M. *Chem. Soc. Rev.* **2009**, *38* (5), 1315-1329.

(201) Liu, X.-M.; Xie, L.-H.; Wu, Y. *Inorg. Chem. Front.* **2020**, *7* (15), 2840-2866.

(202) Cohen, S. M. *Chem. Rev.* **2012**, *112* (2), 970-1000.

(203) Tanabe, K. K.; Cohen, S. M. *Chem. Soc. Rev.* **2011**, *40* (2), 498-519.

(204) Bardwell, J. C. A.; McGovern, K.; Beckwith, J. *Cell* **1991**, *67* (3), 581-589.

(205) Mthembu, S. N.; Sharma, A.; Albericio, F.; de la Torre, B. G. *ChemBioChem* **2020**, *21* (14), 1947-1954.

(206) Kim, H. I.; Beauchamp, J. L. *J. Am. Chem. Soc.* **2008**, *130* (4), 1245-1257.

(207) Ding, Y.; Chen, Y.-P.; Zhang, X.; Chen, L.; Dong, Z.; Jiang, H.-L.; Xu, H.; Zhou, H.-C. *J. Am. Chem. Soc.* **2017**, *139* (27), 9136-9139.

(208) Geary, J.; Wong, A. H.; Xiao, D. J. *J. Am. Chem. Soc.* **2021**, *143* (27), 10317-10323.

(209) Qian, C.; Feng, L.; Teo, W. L.; Liu, J.; Zhou, W.; Wang, D.; Zhao, Y. *Nat. Rev. Chem.* **2022**, *6* (12), 881-898.

(210) Belowich, M. E.; Stoddart, J. F. *Chem. Soc. Rev.* **2012**, *41* (6), 2003-2024.

(211) Yuan, S.; Zou, L.; Qin, J.-S.; Li, J.; Huang, L.; Feng, L.; Wang, X.; Bosch, M.; Alsalme, A.; Cagin, T.; Zhou, H.-C. *Nat. Commun.* **2017**, *8* (1), 15356.

(212) Feng, L.; Yuan, S.; Qin, J.-S.; Wang, Y.; Kirchon, A.; Qiu, D.; Cheng, L.; Madrahimov, S. T.; Zhou, H.-C. *Matter* **2019**, *1* (1), 156-167.

(213) Yuan, S.; Qin, J.-S.; Su, J.; Li, B.; Li, J.; Chen, W.; Drake, H. F.; Zhang, P.; Yuan, D.; Zuo, J.; Zhou, H.-C. *Angew. Chem. Int. Ed.* **2018**, *57* (38), 12578-12583.

(214) March, J. *J. Chem. Educ.* **1963**, *40* (4), 212.

(215) Feng, L.; Yuan, S.; Zhang, L.-L.; Tan, K.; Li, J.-L.; Kirchon, A.; Liu, L.-M.; Zhang, P.; Han, Y.; Chabal, Y. J.; Zhou, H.-C. *J. Am. Chem. Soc.* **2018**, *140* (6), 2363-2372.

(216) Bueken, B.; Van Velthoven, N.; Krajnc, A.; Smolders, S.; Taulelle, F.; Mellot-Draznieks, C.; Mali, G.; Bennett, T. D.; De Vos, D. *Chem. Mater.* **2017**, *29* (24), 10478-10486.

(217) Jeong, G.-Y.; Singh, A. K.; Kim, M.-G.; Gyak, K.-W.; Ryu, U.; Choi, K. M.; Kim, D.-P. *Nat. Commun.* **2018**, *9* (1), 3968.

(218) Wang, K.-Y.; Feng, L.; Yan, T.-H.; Wu, S.; Joseph, E. A.; Zhou, H.-C. *Angew. Chem. Int. Ed.* **2020**, *59* (28), 11349-11354.

(219) Klein, H.-P. *J. Am. Oil Chem. Soc.* **1984**, *61* (2), 306.

(220) Christiane Gottschalk, J. A. L., Adrian Saupe. *Ozonation of water and wastewater*; Wiley, VCH: Weinheim, Germany, 2010.

(221) Bailey, P. S. *Ozonation in Organic Chemistry*; Academic Press, N. Y. Vol. 2, 1982.

(222) Albalad, J.; Xu, H.; Gándara, F.; Haouas, M.; Martineau-Corcos, C.; Mas-Ballesté, R.; Barnett, S. A.; Juanhuix, J.; Imaz, I.; Maspoch, D. *J. Am. Chem. Soc.* **2018**, *140* (6), 2028-2031.

(223) Guillerm, V.; Xu, H.; Albalad, J.; Imaz, I.; Maspoch, D. *J. Am. Chem. Soc.* **2018**, *140* (44), 15022-15030.

(224) Song, Y.; Feng, X.; Chen, J. S.; Brzezinski, C.; Xu, Z.; Lin, W. *J. Am. Chem. Soc.* **2020**, *142* (10), 4872-4882.

(225) Quan, Y.; Song, Y.; Shi, W.; Xu, Z.; Chen, J. S.; Jiang, X.; Wang, C.; Lin, W. *J. Am. Chem. Soc.* **2020**, *142* (19), 8602-8607.

Chapter 2

Objectives

As shown in the previous chapter, the practice of breaking bonds, particularly covalent bonds within organic linkers in MOFs, holds the potential to enable the synthesis of archetypical MOFs that are generally unattainable by direct synthesis. As observed in many reported cases, the presence of cleavable covalent bonds, randomly distributed within the framework, results in the formation of hierarchically porous MOFs after the bond cleavage. However, there is no such a research concerning the precise positioning of cleavable covalent bonds within the framework. In the latter, the cleavage of said bonds within MOFs will allow for the prediction of outcomes, thus enabling the generation of desired new molecules and materials.

Based on the mentioned above, the aim of this dissertation is to push the boundaries of the bond breaking, with a particular emphasis on the covalent bond breaking, for the synthesis of new molecules and materials. This innovative synthetic approach, which we have coined "Clip-off Chemistry", has the potential to synthesize a diverse array of molecules and materials with a wide range of compositions (*e.g.*, metal-organic clusters, MOPs) and dimensionalities (*e.g.*, 3-D to 0-D, 3-D to 2-D, 3-D to 3-D). The successful implementation of Clip-off Chemistry requires several key principles:

- Encoding cleavable covalent bonds inside organic linkers.
- Positioning cleavable bonds precisely inside the crystal structure.
- The targeted and selective cleavage of specific covalent bonds.
- The quantitative cleavage of the said bonds.

In this dissertation, we will show the evolution of bond-breaking process, transitioning from random cleavage to precise cleavage of covalent bonds in 3-D MOFs. Our main aim is thus demonstrating the feasibility of the above-mentioned key principles, opening new avenues for the Clip-off Chemsitry. Regarding the choice of covalent bond breaking, our target is the cleavage of olefinic bonds using ozonolysis reactions. To be more precise, the dissertation aims to achieve the following specific objectives:

➢ Make use of the hierarchically porous MOF for the generation of a porous motor. Our previous work showed that microporous MTV Zr-MOFs built up from randomly-positioned alkene-containing (*i.e.* cleavable) ligands were able to generate larger pores at the mesoscale by selectively breaking those alkene bonds. To this end, we would like to take advantage of those hierarchical pores (both micropores and mesopores) for encapsulation of a bigger molecule, enzyme such as catalase (size: 6×10 nm). Those encapsulated catalase will be characterized by various techniques to identify the amount and location inside the framework. We will then study the feasibility of using these encapsulated catalase enzymes to create an enzyme-powered porous MOF motor.

➢ Expand the scope of bond-breaking regime and develop a new synthetic methodology, Clip-off Chemistry. In this case, we aim to locate the cleavable bonds at precise positions inside a MOF structure and study their topology transformation from a 3-D MOF precursor to a new 3-D MOF. To do so, we will first focus on the synthesis of MOFs with only one type of polytopic ligands containing alkene bonds. The used polytopic linker should have different circuits of connections where at least one contains the cleavable bond. By carefully selecting the MOF precursor, a series of MOFs with this polytopic linker can be potentially synthesized. In addition, we will study the bond breaking behavior of these MOFs toward the ozonolysis reaction and follow the process of structural evolution by the use of the single-crystal X-ray diffraction.

➢ Explore the first-time ozonolysis reaction in a multicomponent 3-D MOF. Based on the previous MOFs built from only one type of polytopic ligands, we intend to increase the whole complexity by selecting two types of linkers. These two types of linkers, of which one contains cleavable alkene bond while another does not, have distinct geometries and are able to occupy at specific positions in the framework. To this end, we will study the isoreticular contraction of this multicomponent MOFs by cleaving the olefinic bond.

Chapter 3

Enzyme-Powered Porous Micromotors Built from a Hierarchical Micro- and Mesoporous UiO-Type Metal–Organic Framework

3.1 Introduction

The field of bioinspired micro- and nanomotors has evolved extensively over the past decade.[1] From the various ways these tiny motors can be powered, self-propulsion via chemical reactions is one of the most widely used. Among them, the use of natural catalysts, such as enzymes, is a promising alternative to achieve efficient and biocompatible systems. Several milestones toward real-world applications of such motors have been achieved, primarily in the fields of biomedicine[2-7] and environmental applications.[8-11] In those applications, porosity of the motor chassis is crucial, as it enables adsorption, transport, and/or release of cargo (*e.g.* drugs or pollutants).[8,12,13] Its performance is then being dictated mainly by its sorption capacity and its cargo transport versatility.[14-17]

Among the alternatives available for developing enzyme-powered porous motors, metal–organic frameworks (MOFs) are an attractive choice.[18-19] MOFs exhibit very high surface areas, tunable pore sizes and shapes, and adjustable pore-surface functionality, suggesting their potential for myriad applications, including gas storage, separation, catalysis, contaminant removal, and drug delivery.[20,21] In fact, researchers have used MOFs to build a stable and adaptable chassis for micro- and nanomotors,[18,22] in which motion is based on Marangoni effects,[23-26] magnetically driven corkscrew locomotion,[27,28] or bubble propulsion.[29-35] In parallel, researchers have demonstrated that biomolecules, particularly enzymes, can be encapsulated within MOFs for protection and to confer the MOFs with new functionalities, mainly in catalysis. For instance, Falcaro, Doonan, and co-workers explored biomimetic mineralization and controlled co-precipitation to encapsulate several enzymes in ZIF-8.[36] Another challenging approach has required custom-made linkers to assemble MOFs with pores large enough (mesopores) to adsorb and host enzymes. For instance, the groups of Farha,[37] Zhou,[38] and Ma[39] exploited MOF mesopores to encapsulate various enzymes. Importantly, for a MOF to be used as the chassis of an enzyme-powered porous motor, it must combine mesopores sufficiently large to host the enzyme used for propulsion, with micropores of an appropriate size to adsorb and release additional guest species.

In this chapter, the aim is to design an enzyme-powered, porous, MOF-based micromotor via compartmentalized encapsulation of the enzyme catalase within a hierarchical micro- and mesoporous MOF (Figure 3.1). Catalase is selected as a model enzyme, as it has been extensively used to induce ballistic propulsion through bubble propulsion via decomposition of H_2O_2.[40-43] Moreover, a UiO-type Zr-MOF is chosen as the chassis because of its well-known water stability,[44] a condition that should fulfill any MOF intended to be used for the fabrication of motors powered by enzymatic reactions. In this design, another essential condition was the use of a UiO-type MOF with mesopores sufficiently large to host catalase (size: 6–10 nm) and micropores that preserve the ability to adsorb and/or release additional guest species. To achieve a rational design for this MOF, an approach that had been previously developed by our group was utilized. In this approach, presynthesized microporous MOFs

functionalized with a mixture of linkers, some containing olefins and others not, were subjected to ozonolysis, which selectively oxidized the olefins, resulting in the generation of new mesopores.[45,46] To achieve this, a presynthesized UiO-type MOF was subjected to the ozonolysis process, and the newly formed mesopores were then utilized to host the catalase molecules.
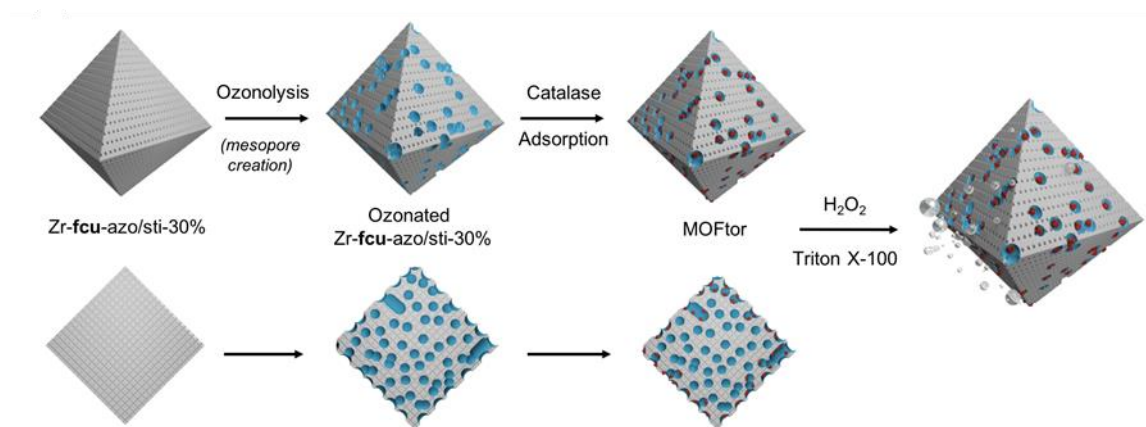

Figure 3.1 Schematic representation of the multistep process used to synthesize the MOFtors. Cross sections of the crystals at bottom.

3.2 Results and discussion

3.2.1 Synthesis and characterization of Zr-fcu-MOF

The synthesis of a UiO-type Zr-**fcu**-MOF (hereafter called *Zr*-**fcu**-azo/sti-30%) was achieved by mixing 4,4′-azobenzenedicarboxylic acid (H$_2$azo) with olefin-containing 4,4′-stilbenedicarboxylic acid (H$_2$sti) linkers at a molar ratio of 7:3, respectively (Figure 3.2). These two dicarboxylic acids are similar in shape and length, and randomly-positioned inside multivariate *Zr*-**fcu**-azo/sti-30%. However, the reactivity of this ligand pair to ozone is diametrically opposite. Olefin-containing H$_2$sti linkers are prone to be cleaved via ozonolysis whereas H$_2$azo linkers are ozone-inert.

A series of characterizations were carried out for this multivariate *Zr*-**fcu**-azo/sti-30%. Field-emission scanning electron microscopy (FESEM) revealed the formation of octahedral microcrystals (size: 2–15 μm) characteristic of Zr-**fcu**-MOFs (Figure 3.3a), and powder X-ray diffraction (PXRD: Figure 3.3b) confirmed the phase purity. ^{1}H NMR of digested crystals confirmed the formation of Zr-**fcu**-azo/sti-30% in an azo/sti molar ratio of 7:3 (Figure 3.3c). Moreover, N$_2$ sorption analysis (77 K) confirmed the microporosity of Zr-**fcu**-azo/sti-30%, with a Brunauer–Emmett–Teller surface area (S_{BET}) of 2830 m^2/g (Figure 3.3d).
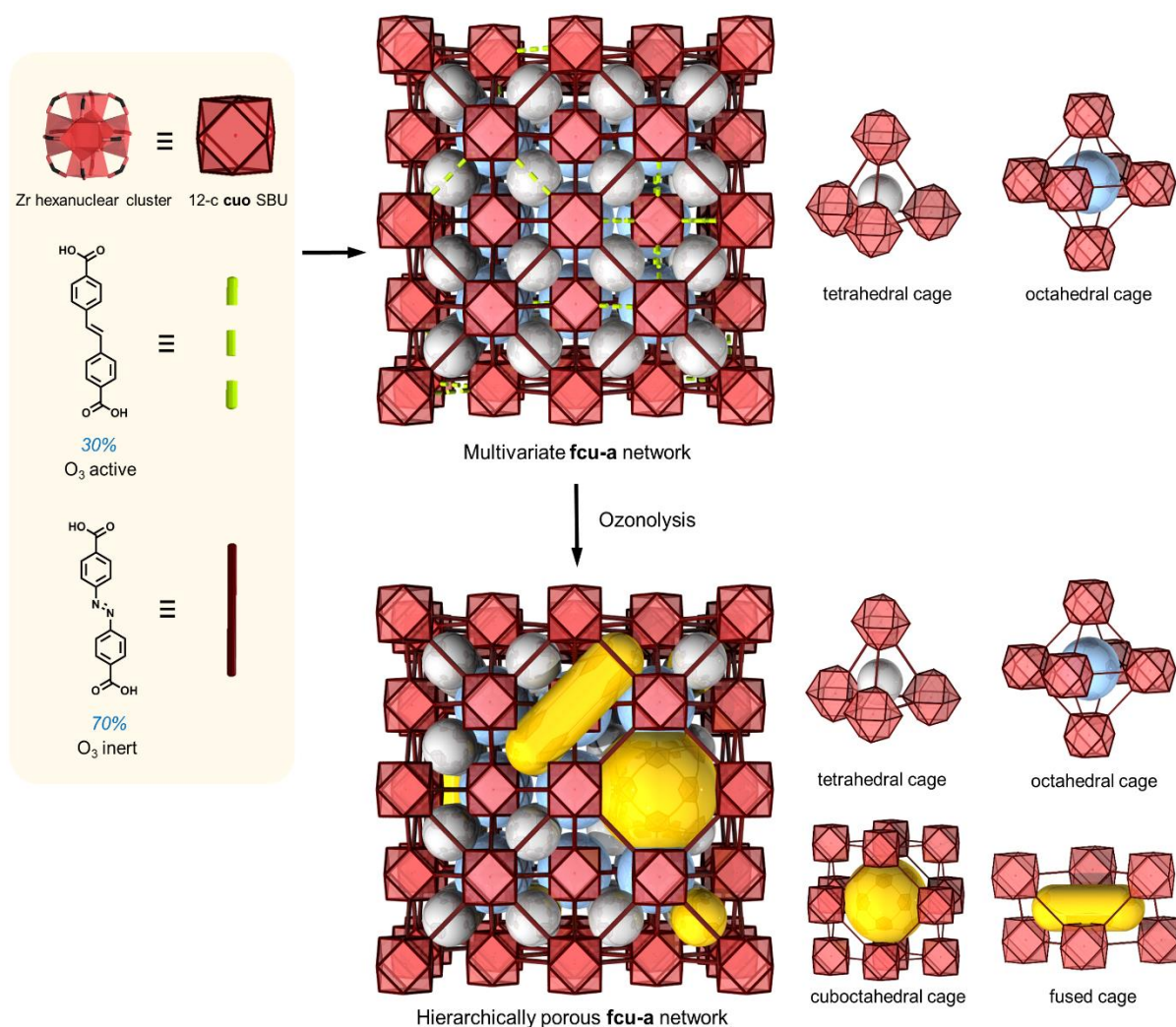
Figure 3.2 Scheme of the formation of hierarchically porous MOF from a multivariate microporous Zr-**fcu**-MOF via solid-gas phase ozonolysis.

3.2.2 Ozonolysis of Zr-fcu-MOF

After the successful synthesis of Zr-**fcu**-azo/sti-30%, ozonolysis reaction was carried out based on our reported protocol.[45,46] In order to selectively cleave the sti linkers, ~30 mg of Zr-**fcu**-azo/sti-30% was packed in a plastic tube and connected to the ozonator setup. A continuous flow of ozone passed through the desiccator loaded with anhydrous $CaCl_2$ prior to the sample. The reaction was run under vacuum for 30 min at room temperature (ozonolysis procedure see section 3.4.2). Afterwards, the ozonated sample was directly collected and washed with 0.5 M solution of acetic acid in DMF to remove residual organic and Zr(IV) fragments trapped in the pores of the ozonated Zr-**fcu**-azo/sti-30%.

In this case, the obtained particles did not exhibit any marked difference in their octahedral shape and crystallinity compared to the initial nonozonated samples (Figure 3.4a,b and Figure 3.3a,b). The

ozonated Zr-**fcu**-azo/sti-30% was analyzed by ^{1}H NMR, which revealed that these linkers had been completely removed from the crystals (Figure 3.4c). As expected, the remaining signal from ^{1}H NMR were found to be the sole azo ligand, confirming its high resistance to ozone. The creation of mesopores was confirmed by N_2 sorption tests at 77 K (Figure 3.3d). The isotherm did not show the type-I shape of the isotherm of the corresponding starting MOF: instead, it exhibited a small hysteresis between the adsorption and desorption branch, characteristic of mesoporosity. As expected, ozonolysis reduced the apparent S_{BET} down to 2470 m^2/g. However, this decrease was offset by the creation of mesopores, at a proportion of 24%.[47] The mesoporosity was also confirmed by studying the pore size distribution (PSD). Compared to the starting material, ozonated Zr-**fcu**-azo/sti-10% showed a major decrease in the initial pore size of microporosity (~ 18 Å) along with a noticeable increase of the second population at ~ 22 Å (Figure 3.4c). The pores were significantly spread over a wide range up to 50 Å, confirming that the micropores are fused and merged into wider pores. The appearance of the mesopores with the size around 22 Å could be ascribed to the presence of nonordered **reo** motifs caused by missing clusters defects, as indicated by our previous study.[46]
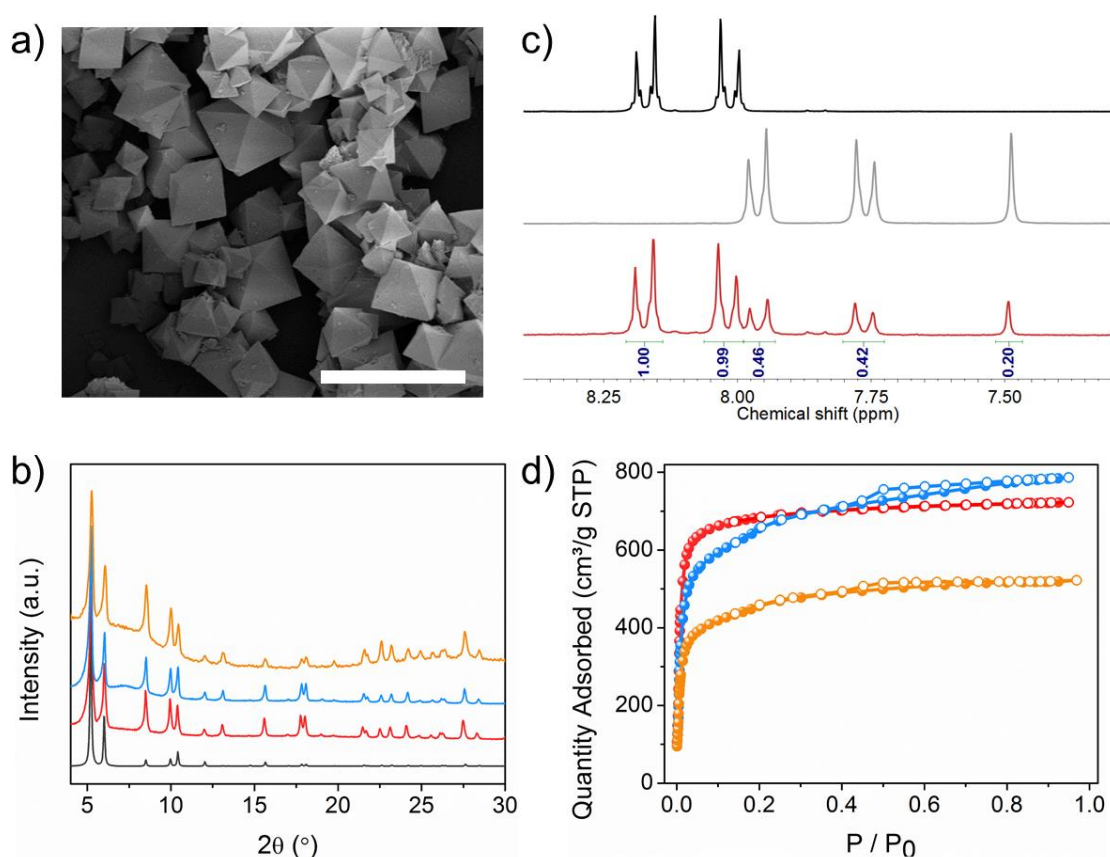
Figure 3.3 (a) FESEM image of Zr-**fcu**-azo/sti-30%. Scale bar: 20 μm. (b,d) PXRD and N_2 isotherms of Zr-**fcu**-azo/sti-30% before (red) and after (blue) ozonolysis and after catalase encapsulation (orange). In (b), simulated pattern for Zr-**fcu**-azo (black). (c) ^{1}H NMR spectra (250 MHz, DMSO-d_6) of digested H$_2$azo (black), H$_2$sti (gray), Zr-**fcu**-azo/sti-30% (red).
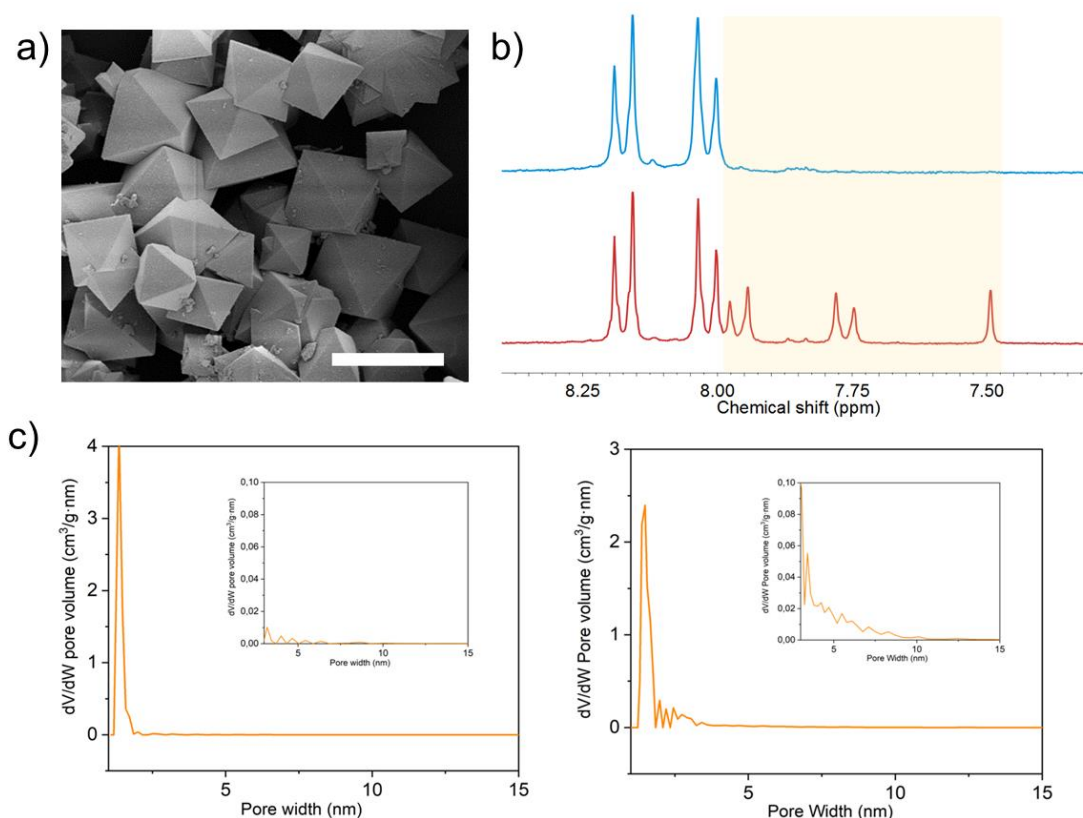
Figure 3.4 (a) FESEM image of ozonated Zr-**fcu**-azo/sti-30%. Scale bar: 10 µm. (b) ^{1}H NMR spectra (250 MHz, DMSO-d_6) of digested Zr-**fcu**-azo/sti-30% (red) and ozonated Zr-**fcu**-azo/sti-30% (blue). The sti ligand was highlighted in yellow. (c) Pore size distribution estimated by DFT for Zr-**fcu**-azo/sti-30% (left) and ozonated Zr-**fcu**-azo/sti-30% (right).

3.2.3 Catalase encapsulation

Once the formation of Zr-**fcu**-MOF containing hierarchical porosity was confirmed, the study on the adsorption of catalase into the latter was conducted. For this, 5 mg of ozonated Zr-**fcu**-azo/sti-30% was incubated in 1 mL of an aqueous solution of catalase (3 mg/mL) for different periods of time. After each period, the particle shape was characterized by FESEM and the amount of encapsulated catalase was quantified by the standard Bradford protein assay. From FESEM, the catalase-encapsulated Zr-**fcu**-MOF did not show any change in their octahedral shape under different incubation time (Figure 3.5c). The amount of catalase confined in the ozonated Zr-**fcu**-azo/sti-30% was gradually increased from 1 h (0.14 ± 0.01 mg catalase/mg MOF) to 8 h (0.21 ± 0.01 mg catalase/mg MOF (Figure 3.5a and Table 3.1).

To further demonstrate the encapsulation of catalase into the mesopores, the spatial distribution of catalase within the Zr-**fcu**-azo/sti-30% crystals was studied using confocal laser scanning microscopy (CLSM). For this, the encapsulation process was repeated over 8 hours, using a catalase tagged with

the green dye fluorescein isothiocyanate (FITC). For comparison, the encapsulation process was also repeated using a non-ozonated Zr-**fcu**-azo/sti-30% that does not contain mesopores. Micrographs of the ozonated and the non-ozonated Zr-**fcu**-azo/sti-30% demonstrated that catalase is encapsulated only within the crystals of the former, where it is predominantly compartmentalized at the subsurface (Figure 3.5b). The preferential localization of catalase at the subsurface of each MOF crystal was attributed to the initial random distribution of azo- and sti- linkers that, following removal of the latter via ozonolysis, produce crystals in which the meso- and micropores are randomly localized. This makes the external mesoscale cavities more accessible for catalase than the internal ones, as the diffusion of catalase into the internal large cavities is highly restricted by the probability of encountering pores smaller than the size of catalase.
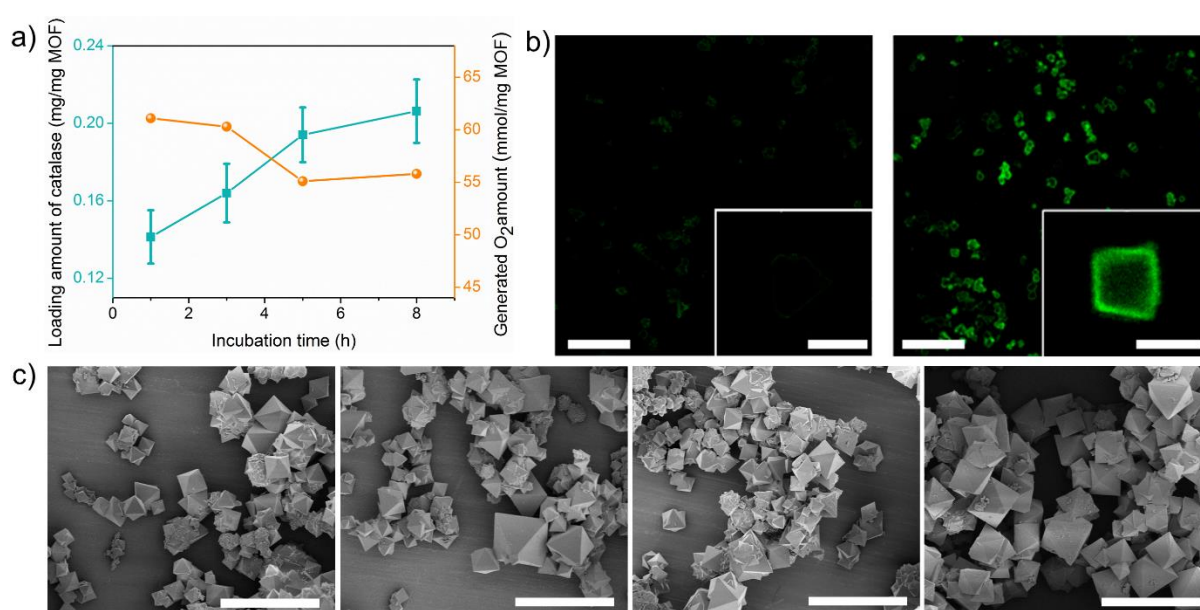
Figure 3.5 (a) Encapsulation efficiency (cyan) and oxygen generated (orange) vs time. (b) CLSM micrographs of (left) as-synthesized and (right) ozonated Zr-**fcu**-azo/sti-30% crystals after incubation with FITC-tagged catalase (green) for 8 h. Scale bars: 50 μm; 5 μm (inset, left) and 3 μm (inset, right). (c) FESEM images of ozonated Zr-**fcu**-azo/sti-30% after being incubated with catalase for different incubation time (from left to right): 1 h, 3 h, 5 h and 8 h. Scale bars = 20 μm.

Table 3.1 Catalase loading amount in ozonated Zr-**fcu**-azo/sti-30%.

Incubation time (h)	1	3	5	8
Loading amount (mg/mg MOF)	0.14 ± 0.01	0.16 ± 0.01	0.19 ± 0.01	0.21 ± 0.02

After the catalase encapsulation, the ozonated Zr-**fcu**-azo/sti-30% materials maintained their high crystallinity, as confirmed by PXRD (Figure 3.6a). Notably, the encapsulated catalase induced a partial loss of the porosity in ozonated Zr-**fcu**-azo/sti-30%, as demonstrated by a dramatically decrease in the apparent S_{BET} down to 1715 cm^3/g (Figure 3.3d and section 3.4.7). The proportion of pores with mesoscale dimensions derived from the Dubinin–Radushkevich (DR) equation reduced slightly, with a contribution of ~20% to the total porosity (Figure 3.6b).
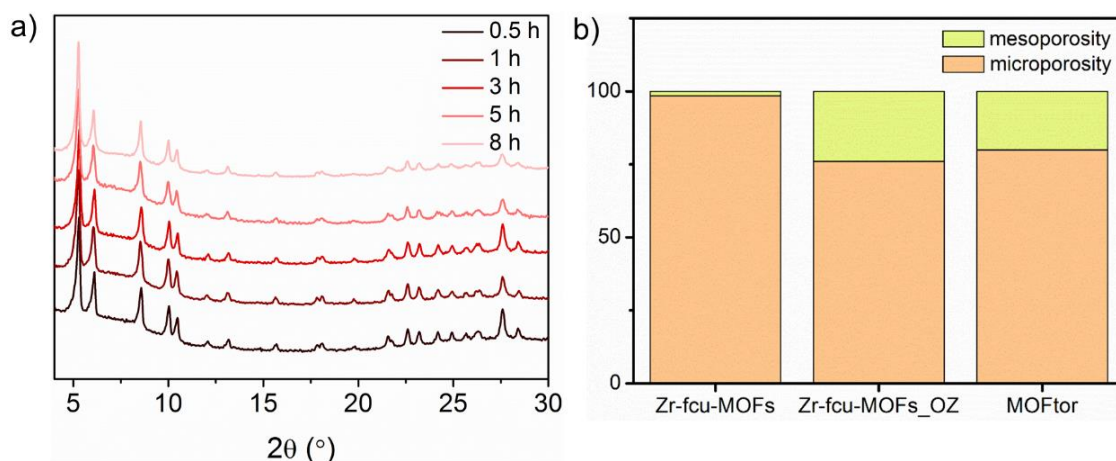
Figure 3.6 (a) PXRD patterns for catalase-encapsulated Zr-**fcu**-azo/sti-30% (denoted as MOFtor) at different incubation time. (b) Change in total pore volume and in the relative contribution of microporosity and mesoporosity to total uptake in Zr-**fcu**-azo/sti-30%, ozonated Zr-**fcu**-azo/sti-30% and MOFtor calculated using the DR equation.

3.2.4 Self-propulsion of MOF-based motors (in collaboration with Prof. Dr. Samuel Sánchez)

The self-propulsion of Zr-**fcu**-azo/sti-30% crystals, into which catalase has been incorporated (hereafter called MOFtors), was studied for 1, 3, 5, or 8 h. For these experiments, it was considered that bubble propulsion is improved by the addition of surfactants to the media;[48-52] thus, the MOFtor crystals were recorded in an aqueous solution containing 0.5% H$_2$O$_2$ and Triton X-100 at a 0.25% (v/v) concentration. Remarkably, all four samples showed bubble generation and motion capability (Figure 3.7a), propelling themselves by a thrust of oxygen bubbles released asymmetrically from a point of nucleation. In this regard, researchers have reported that any cavity in a micromotor structure, in this case in the MOF crystal, due to porosity, surface defects, or crystal aggregation, can enable accumulation of oxygen bubbles for jet-like propulsion.[53,54]
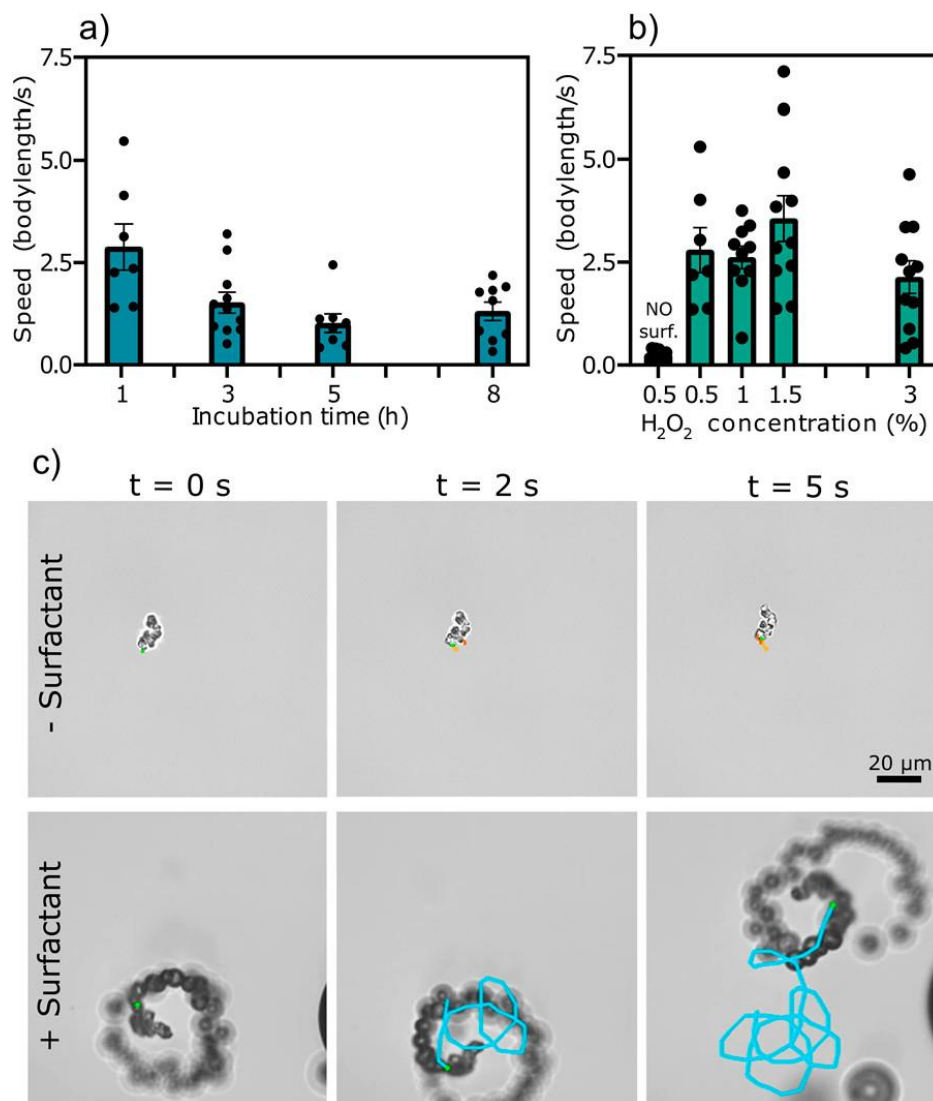
Figure 3.7 (a) Speed of MOFtors obtained at different incubation times. (b) Speed of the MOFtors at different H_2O_2 concentrations. (c) Snapshots of the trajectories of MOFtors at different times in the presence (bottom) or absence (top) of 0.25% Triton X-100.

Among the MOFtors generated at different incubation times, the one corresponding to 1 h incubation reached the highest maximum speed (2.79 ± 0.55 body-lengths/s). Interestingly, incubation time was indirectly proportional to speed (Figure 3.7a). To explore this trend, the enzymatic activity (O_2 production) of the catalase confined inside the MOFtors was quantified by using the displacement method (experimental details see section 3.4.3). For all samples, the amount of generated O_2 increased during the first 2 min and then gradually plateaued at a saturation value (Figure 3.8). The MOFtor from 1 h of incubation generated the greatest amount of O_2 (61.1 μmol/mg$_{MOFtor}$) and highest speed of O_2 generation ([49 μmol O_2/min]/mg$_{MOFtor}$) (Figure 3.5a). These results are consistent with those of the aforementioned motion experiments. This slight decrease in activity and motion could be tentatively

attributed to either a certain degree of inactivation of catalase inside the MOF crystals or to the fact that the catalase molecules diffuse into the interior of MOF crystals more at longer incubation times, thereby complicating both arrival of the H_2O_2 molecules to the enzymes and the release of the O_2 bubbles produced by the enzymatic reaction.
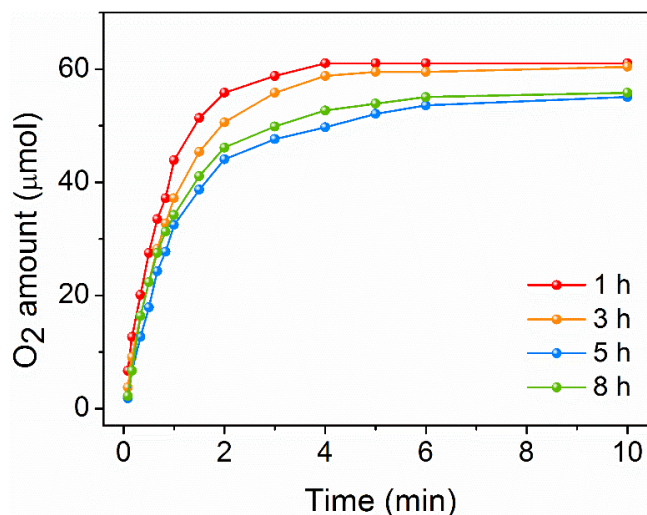
**Figure 3.8** Generated O_2 amount versus time in the MOFtors produced with different incubation times after adding H_2O_2.

Once the optimum incubation time of 1 h had been confirmed, the motion capabilities of the corresponding MOFtor were further investigated. Initially, the influence of the surfactant was studied by reproducing the recording of MOFtors in an aqueous solution containing 0.5% H_2O_2 in the presence and absence of Triton X-100 (Figure 3.7b,c). Figure 3.7c shows different snapshots from the video recordings with their corresponding trajectories where MOFtors in a Triton X-100 dilution displayed high bubble production, leading to propulsion. However, in the absence of surfactant (Figure 3.7c), no bubbles or self-propulsion were observed. It was reasoned that the surfactant in the medium reduced the surface tension of the liquid, which in turn promoted formation of and stabilized the bubbles.[40,55] The self-propulsion of the MOFtor was also assessed as a function of H_2O_2 concentration (Figure 3.7b). Self-propulsion was observed at low surfactant and fuel concentrations[56] compared to those in other studies, in which 3% to 5% H_2O_2 was utilized.[53] Given its toxicity, minimizing the concentration of the H_2O_2 is important for biological and environmental applications. When the H_2O_2 concentration was increased to 1.5%, the self-propulsion increased, reaching a maximum speed of 3.56 ± 0.56 body-lengths/s and propelling for 7.0 ± 0.4 min. Yet, motion can be resumed after the addition of fresh fuel.

3.2.5 MOFtors for pollutant removal

Given that our MOFtor combines both meso- and micropores and that the catalase enzymes are encapsulated mainly in the mesopores located at the crystal subsurface, using the remaining empty pores to adsorb other guest molecules was highly possible. Considering that MOFtors has accessible porosity ($S_{BET} = 1715$ m^2/g) and that their mesopore proportion is 20%, the capacity of MOFtors to capture rhodamine B, a common water pollutant from the textile, plastic, and dye industries, was also studied during self-propulsion in water. To this end, catalase-powered MOFtors (5 mg) were dispersed in an aqueous solution (1 mL) of 0.5 mg/mL rhodamine B and 1.5% H_2O_2/0.25% Triton X-100 at room temperature. After 5 min of incubation, the rhodamine B content adsorbed by the MOFtors was determined by UV–vis spectrometry. It turned out that MOFtors was able to capture $51.0 \pm 2.7\%$ % of rhodamine B from the solution. For comparison, without using H_2O_2/Triton X-100, non-powered MOFtors adsorbed only $14.6 \pm 6.4\%$ of rhodamine B, thus confirming the positive effect of self-propulsion in the performance of MOFtors. The adsorption of rhodamine B in the catalase-powered MOFtors was also confirmed by CLSM (Figure 3.9). Indeed, the CLSM image shows that, while catalase remains localized at the subsurface of the crystals, rhodamine B molecules are adsorbed throughout the entire crystal.
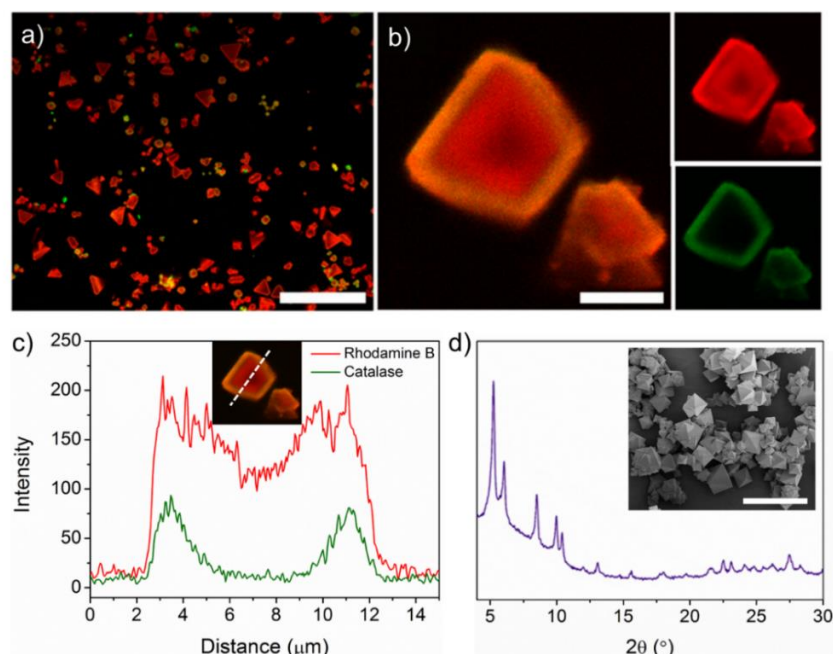
Figure 3.9 (a) CLSM micrographs of MOFtors after adsorption of rhodamine B (red). (b) Enlarged CLSM micrographs. The left image is the superposition of both right images showing adsorbed rhodamine B (red, top) and compartmentalized FITC-tagged catalase (green, bottom). Scale bars: 50 μm (a) and 5 μm (b). (c) Line-scan profile of fluorescence intensity of FTIC-catalase and rhodamine B in a MOFtor particle. The optic image was inserted. (d) PXRD pattern for rhodamine B@MOFtor. FESEM image of rhodamine B@MOFtor was inserted (scale bars = 20 μm).

3.3 Conclusions

In conclusion, we have reported the multistep synthesis of enzyme-powered MOF-based porous motors, which involves generating new mesopores in a microporous UiO-66-type MOF, via ozonolysis. We exploited the newly generated mesopores to adsorb and host the enzyme catalase, which were compartmentalized at the subsurface of each MOF crystal. This encapsulation enabled jet-like bubble propulsion of the MOF crystals using H_2O_2 as fuel, even at very low concentrations. Moreover, the remaining unoccupied micro- and mesopores in these MOFtors can be used for adsorbing additional species, as we demonstrated with capture of rhodamine B in water. Our work demonstrates the versatility of MOFs as the structural basis of enzyme-powered porous motors for delivery, sorption, and catalytic applications.

3.4 Experimental section

3.4.1 Chemicals and characterization

Zirconium(IV) chloride, *L*-proline, (3-aminopropyl)triethoxysilane (APTES), acetone, catalase from bovine liver (≥10,000 units/mg protein), rhodamine B, hydrogen peroxide solution (30 wt. % in H_2O), fluorescein isothiocyanate (FITC), Bradford reagent were purchased from Sigma-Aldrich. 4,4'-stilbenedicarboxylic acid and azobenzene-4,4'-dicarboxylic acid were purchased from TCI Chemicals. *N,N*-dimethylformamide (DMF), toluene, conc. HCl, glacial acetic acid were purchased from Fisher Chemical. All the reagents and solvents were used as received without further purification. The deionized water from all the aqueous solutions in the article was obtained from a Milli-Q® system (18.2 MΩ·cm). The ozone generator (model N1668A, 500 mg/h O_3 at room temperature) was purchased from Ozonotec. Triton X-100 was purchased from Alfa Aesar.

Powder X-ray diffraction (PXRD) data were collected on an X'Pert PRO MPD analytical diffractometer (Panalytical) at 45 KV, 40 mA using Cu-Kα radiation ($\lambda = 0.15406$ nm). The diffraction patterns were collected between the 2θ range of 4°-30°. Field Emission Scanning Electron Microscopy (FESEM) images were collected on a FEI Magellan 400L scanning electron microscope at an acceleration voltage of 1.0 KV, using aluminum as support. UV-vis spectra were recorded in Shimadzu UV-1900 UV-VIS spectrophotometer at room temperature. Proton Nuclear Magnetic Resonance (^{1}H NMR) spectra were acquired in Bruker Avance DPX of 250 MHz NMR Spectrometer. All the digested samples were dissolved in DMSO-*d_6*. Nitrogen adsorption/desorption isotherms were collected using an ASAP 2460 (Micromeritics). Temperature was controlled by using a liquid nitrogen bath. Micro- and meso-pore ratio was obtained by the existing mesopore volume which was calculated at $P/P_0 = 0.95$, and the microporous volume was calculated using the Dubinin-Radushkevich equation. Pore size distribution was estimated using a density functional theory (DFT) model (N_2–cylindrical pores–oxide

surface) implemented in the Microactive 4.00 software with a regularization factor of 0.01. Prior to sorption measurements, all the samples were activated at 120 °C overnight to obtain at a high vacuum. Confocal laser scanning microscopy images were collected on a Leica TCS SP5 microscope.

3.4.2 Synthetic procedures

Synthesis of Zr-fcu-azo/sti-30%. Zr-**fcu**-azo/sti-30% was synthesized according to the previously reported method with slight modifications.[46] Briefly, ZrCl$_4$ (105 mg, 0.45 mmol), 4,4′-stilbenedicarboxylic acid (H$_2$sti, 36 mg, 0.14 mmol), azobenzene-4,4′-dicarboxylic acid (H$_2$azo, 84 mg, 0.3 mmol) and L-proline (250 mg, 2.17 mmol) were dissolved in 15 mL of DMF. Then, 45 µL of conc. HCl was transferred. After sonicating for 30 min, the mixture was heated at 120 °C for 24 h. The resulting orange solid was washed three times with fresh DMF every 8 h and then, exchanged with fresh toluene for three times every 8 h. The final solid sample was obtained by vacuum filtration.

Ozonolysis of Zr-fcu-azo/sti-30% and acetic acid washing. Ozonolysis procedure was based on our previously reported method.[1] To this end, 50 mg of Zr-**fcu**-azo/sti-30% was added into a L-shaped glass tube which contained a cotton stopper. Then, the tube was connected to the ozone generator and to the colorimetric indicator (aqueous potassium iodine solution). The solid-gas ozonolysis reaction was held for 1 h and the resulting solid was directly harvested from the tube. Next, the solid was soaked in 20 mL of acetic acid solution (0.5 M in DMF) and held at room temperature for 12 h. After that, the supernatant was decanted, and ozonated Zr-**fcu**-azo/sti-30% was washed three times with toluene every 8 h and collected under vacuum filtration.

Encapsulation of catalase into ozonated Zr-fcu-azo/sti-30%. The different samples of catalase@Zr-**fcu**-azo/sti-30% (hereafter called MOFtors) were prepared by incubating 5 mg of ozonated Zr-**fcu**-azo/sti-30% into a 1 mL of catalase aqueous solution (3 mg/mL) under continuous stirring at the speed of 40 rpm for 1 h, 3 h, 5 h and 8 h. The final solids were collected by centrifugation and washed three times with water.

Catalase labeled with FITC. Catalase (15 mg) was dissolved in 1 mL of PBS (pH 7.4) and then, 2 mL of borate buffer (pH 8.5) was added. FITC (10.5 mg) was dissolved in DMSO anhydride (3.5 mL) to form a clear solution. After that, 0.5 mL of FITC solution was added into 3 mL of the catalase-containing solution. The mixture was incubated at 37 °C for 90 min. The unreacted FITC was removed by PD-10 column.

3.4.3 Determination of the amount of catalase encapsulated into MOFtors

Bradford protein assay (Sigma-Aldrich) was used to quantify the amount of the catalase encapsulated into the MOFtors at different incubation times. For this, 10 µL of each supernatant that

results from the centrifugation processes (see above) were taken out and mixed with 2.99 mL of water. Afterwards, 1 mL of each one of these solutions was added to 1 mL of the Bradford solution. The resulting mixtures were blended by vortex for 30 s and incubated for 20 min. The catalase content was finally quantified by UV-vis.
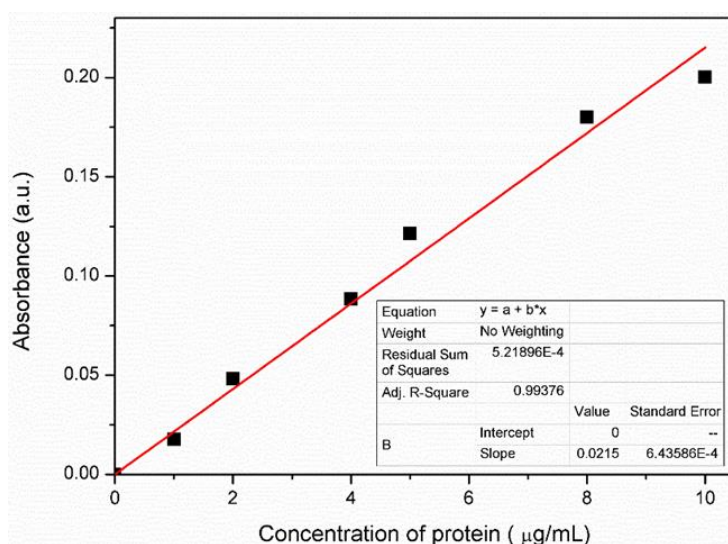

Figure 3.10 The standard calibration line of Bradford assay for determining the amount of catalase in ozonated Zr-**fcu**-azo/sti-30%.

3.4.4 Motion recording and analysis (in collaboration with Prof. Dr. Samuel Sánchez)

Glass slides used for the imaging of the MOftors were previously coated with APTES to avoid charge interactions and particles sticking to the glass surface. For this, glass slides were initially sonicated in acetone for 10 min. After, they were immersed in a solution of 3 ml APTES and 150 ml of acetone for 5 minutes to apply the coating. The glass slide was washed 3 times with ultrapure water and let it to dry. Then, 10 μL of micromotors solution were mixed with 10 μL of an aqueous solution on the APTES-coated glass slide to obtain a final concentration of 0.25% of Triton X-100 and different H_2O_2 concentrations (0.5, 1, 1.5 and 3% v/v). The MOFtors were recorded during, at least, 10 s at a rate of 25 frames per second (FPS), using an inverted optical microscope (Leica DMi8) equipped with a water immersion 63x objective and a Hamamatsu Digital Camera (C11440). For the motion lifetime at 1.5% H_2O_2, each individual video was taken every 30 seconds of motion until the MOFtors stop. The videos obtained were analyzed using an in-house designed Python-based code, which allowed to extract the trajectories along the X and Y axis, from which the speed was calculated as a function of the total distance/total time. After, based on the MOFtor size, the speed value was translated into bodylength per second.

3.4.5 Determination of the O₂ production

The O₂ generation from the different MOFtors was measured via the water displacement method.[57] Figure 3.11 shows the experimental setup. In this setup, 30 mg of MOFtors and 6 mL water were added into the conical flask. Next, 15 µL of trition X-100 was added into the suspension. After shaking the flask for few seconds, 300 µL of H_2O_2 (30 wt. %) was introduced into the system. Immediately, the generated O₂ gas occupied the space in the measuring cylinder, lowering the water level in it. The occupied level in the measuring cylinder was recorded based on time.
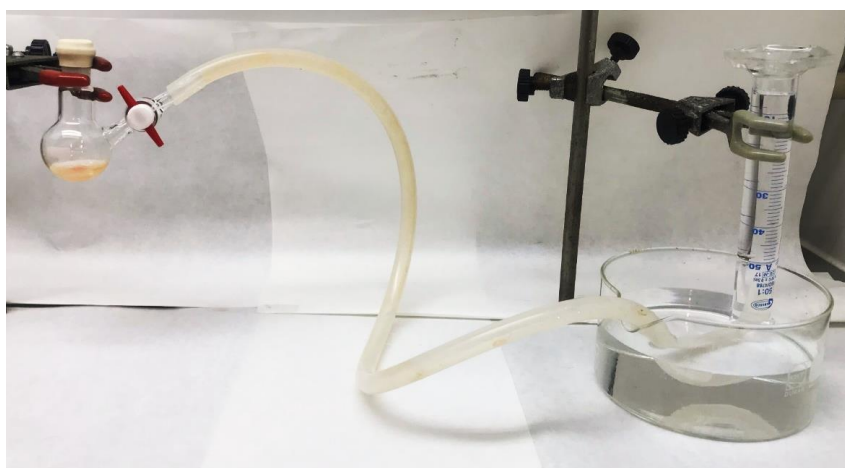
Figure 3.11 Photography of the experimental setup used for measuring the O₂ production via the water displacement method.

3.4.6 Adsorption of rhodamine B in MOFtors

MOFtors (5 mg) were incubated into an aqueous solution (1 mL) containing 0.5 mg of rhodamine B and 1.5% H_2O_2 and 0.25 % Triton X-100 for 5 min. The final product was collected by centrifugation and intensively washed with water until the separated solution is colorless. The discarded supernatants were used to measure the free rhodamine that was not encapsulated through spectrophotometry reading at 555 nm. The rhodamine B concentration is calculated using Beer-Lambert law Equation:

$$A = \varepsilon c l \qquad\qquad 1$$

where A is absorbance, ε is the molar extinction coefficient, c is the molar concentration and l is the path length. The molar extinction coefficient of rhodamine B is 106000 $M^{-1}cm^{-1}$ and the path length of the reading is 0.866 cm. The encapsulated rhodamine B is calculated by extracting the concentration in the supernatants to the initial 0.5 mg/ml of rhodamine B. For comparison, we also repeated this process without using H_2O_2/Triton X-100.

3.4.7 N$_2$ adsorption fitting
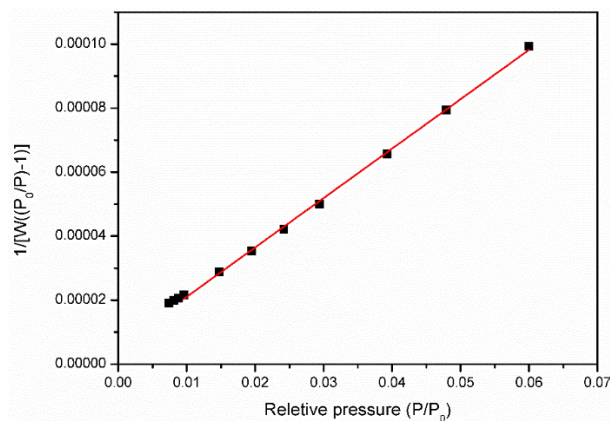
BET surface area: 2830 m^2/g

Slope: 1.54×10^{-3}

Intercept: 6×10^{-6}

Correlation coefficient, r = 0.9995

C constant: 276

Figure 3.12 BET linear fit of as-synthesized Zr-**fcu**-azo/sti-30%.

BET surface area: 2470 m^2/g

Slope: 1.78×10^{-3}

Intercept: 7×10^{-6}

Correlation coefficient, r = 0.9999

C constant: 274

Figure 3.13 BET linear fit of ozonated Zr-**fcu**-azo/sti-30%.

BET surface area: 1715 m^2/g
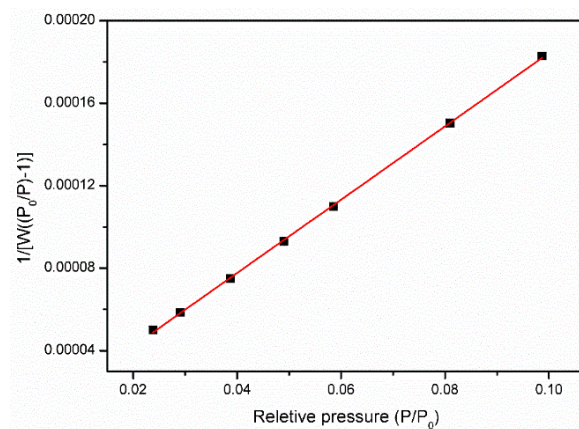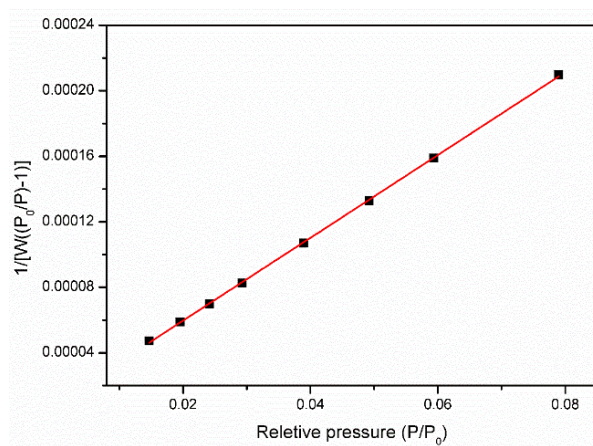
Slope: 2.52×10^{-3}

Intercept: 9×10^{-6}

Correlation coefficient, r = 0.9999

C constant: 278

Figure 3.14 BET linear fit of MOFtor.

3.5 References

(1) Sánchez, S.; Soler, L.; Katuri, J. *Angew. Chem. Int. Ed.* **2015**, *54* (5), 1414–1444.

(2) Ou, J.; Liu, K.; Jiang, J.; Wilson, D. A.; Liu, L.; Wang, F.; Wang, S.; Tu, Y.; Peng, F. *Small* **2020**, *1906184*, 1–16.

(3) Wang, S.; Liu, X.; Wang, Y.; Xu, D.; Liang, C.; Guo, J.; Ma, X. *Nanoscale* **2019**, *11* (30), 14099–14112.

(4) Li, J.; Esteban-Fernández de Ávila, B.; Gao, W.; Zhang, L.; Wang, J. *Sci. Robot.* **2017**, *2* (4), eaam6431.

(5) Joseph, A.; Contini, C.; Cecchin, D.; Nyberg, S.; Ruiz-Perez, L.; Gaitzsch, J.; Fullstone, G.; Tian, X.; Azizi, J.; Preston, J.; Volpe, G.; Battaglia, G. *Sci. Adv.* **2017**, *3* (8), e1700362.

(6) Wang, J.; Toebes, B. J.; Plachokova, A. S.; Liu, Q.; Deng, D.; Jansen, J. A.; Yang, F.; Wilson, D. A. *Adv. Healthc. Mater.* **2020**, *1901710*, 1–8.

(7) Wu, Y.; Lin, X.; Wu, Z.; Möhwald, H.; He, Q. *ACS Appl. Mater. Interfaces* **2014**, *6* (13), 10476–10481.

(8) Parmar, J.; Vilela, D.; Villa, K.; Wang, J.; Sánchez, S. *J. Am. Chem. Soc.* **2018**, *140* (30), 9317–9331.

(9) Guix, M.; Orozco, J.; Gracía, M.; Gao, W.; Sattayasamitsathit, S.; Merkoçi, A.; Escarpa, A.; Wang, J. *ACS Nano* **2012**, *6* (5), 4445–4451.

(10) Gao, W.; Wang, J. *ACS Nano* **2014**, *8* (4), 3170–3180.

(11) Orozco, J.; García-Gradilla, V.; D'Agostino, M.; Gao, W.; Cortés, A.; Wang, J. *ACS Nano* **2013**, *7* (1), 818–824.

(12) Medina-Sánchez, M.; Xu, H.; Schmidt, O. G. *Ther. Deliv.* **2018**, *9* (4), 303–316.

(13) Eskandarloo, H.; Kierulf, A.; Abbaspourrad, A. *Nanoscale* **2017**, *9* (37), 13850–13863.

(14) Llopis-Lorente, A.; Garciá-Fernández, A.; Murillo-Cremaes, N.; Hortelaõ, A. C.; Patiño, T.; Villalonga, R.; Sancenón, F.; Martínez-Máñez, R.; Sánchez, S. *ACS Nano* **2019**, *13* (10), 12171–12183.

(15) Hortelão, A. C.; Patiño, T.; Perez-Jiménez, A.; Blanco, À.; Sánchez, S. *Adv. Funct. Mater.* **2017**, *28* (25), 1–10.

(16) Wu, Y.; Lin, X.; Wu, Z.; Möhwald, H.; He, Q. *ACS Appl. Mater. Interfaces* **2014**, *6* (13), 10476–10481.

(17) Llopis-Lorente, A.; García-Fernández, A.; Lucena-Sánchez, E.; Díez, P.; Sancenón, F.; Villalonga, R.; Wilson, D. A.; Martínez-Máñez, R. *Chem. Commun.* **2019**, *55* (87), 13164–13167.

(18) Terzopoulou, A.; Nicholas, J. D.; Chen, X.-Z.; Nelson, B. J.; Pané, J.; Puigmartí-Luis, J. Metal-Organic Frameworks in Motion. *Chem. Rev.* **2020**, *120* (20), 11175–11193.

(19) Gao, S.; Hou, J.; Zeng, J.; Richardson, J. J.; Gu, Z.; Gao, X.; Li, D.; Gao, M.; Wang, D.-W.; Chen, P.; Chen, V.; Liang, K.; Zhao, D.-Y.; Kong, B. *Adv. Funct. Mater.* **2018**, *29*, 1808900.

(20) Themed Issue Metal-Organic Frameworks: *Chem. Soc. Rev.* Zhou, H. C., Kitagawa, S., Eds.; **2014**, *43* (5), 5415– 6172.

(21) Themed Issue Porous Framework Chemistry: *Chem. Rev.* Long, J.; Dinca, M., Eds; **2020**, *120* (16), 8037-9014.

(22) Khezri, B.; Pumera, M. *Adv. Mater.* **2019**, *31* (14), 1–11.

(23) Ikezoe, Y.; Fang, J.; Wasik, T. L.; Shi, M.; Uemura, T.; Kitagawa, S.; Matsui, H. *Nano Lett.* **2015**, *15* (6), 4019–4023.

(24) Ikezoe, Y.; Washino, G.; Uemura, T.; Kitagawa, S.; Matsui, H. *Nat. Mater.* **2012**, *11* (12), 1081–1085.

(25) Ikezoe, Y.; Fang, J.; Wasik, T. L.; Uemura, T.; Zheng, Y.; Kitagawa, S.; Matsui, H. *Adv. Mater.* **2015**, *27* (2), 288–291.

(26) Park, J. H.; Lach, S.; Polev, K.; Granick, S.; Grzybowski, B. A. *ACS Nano* **2017**, *11* (11), 10914–10923.

(27) Wang, X.; Chen, X. Z.; Alcântara, C. C. J.; Sevim, S.; Hoop, M.; Terzopoulou, A.; de Marco, C.; Hu, C.; de Mello, A. J.; Falcaro, P.; Furukawa, S.; Nelson, B. J.; Puigmartí-Luis, J.; Pané, S. *Adv. Mater.* **2019**, *31* (27), 2–8.

(28) Terzopoulou, A.; Wang, X.; Chen, X. Z.; Palacios-Corella, M.; Pujante, C.; Herrero-Martín, J.; Qin, X. H.; Sort, J.; J deMello, A.; Nelson, B. J.; Puigmartí-Luis, J.; Pané, S. *Adv. Healthc. Mater.* **2020**, 2001031.

(29) Wang, R.; Guo, W.; Li, X.; Liu, Z.; Liu, H.; Ding, S. *RSC Adv.* **2017**, *7* (67), 42462–42467.

(30) Ayala, A.; Carbonell, C.; Imaz, I.; Maspoch, D. *Chem. Commun.* **2016**, *52* (29), 5096–5099.

(31) Ying, Y.; Pourrahimi, A. M.; Sofer, Z.; Matějková, S.; Pumera, M. *ACS Nano* **2019**, *13* (10), 11477–11487.

(32) Wang, L.; Zhu, H.; Shi, Y.; Ge, Y.; Feng, X.; Liu, R.; Li, Y.; Ma, Y.; Wang, L. *Nanoscale* **2018**, *10* (24), 11384–11391.

(33) Tan, T. T. Y.; Cham, J. T. M.; Reithofer, M. R.; Andy Hor, T. S.; Min Chin, J. *Chem. Commun.* **2014**, *50* (96), 15175–15178.

(34) Li, J.; Yu, X.; Xu, M.; Liu, W.; Sandraz, E.; Lan, H.; Wang, J.; Cohen, S. M. *J. Am. Chem. Soc.* **2017**, *139* (2), 611–614.

(35) Liu, J.; Li, J.; Wang, G.; Yang, W.; Yang, J.; Liu, Y. *J. Colloid Interface Sci.* **2019**, *555*, 234–244.

(36) Liang, K.; Coghlan, C. J.; Bell, S. G.; Doonan, C.; Falcaro, P. *Chem. Commun.* **2016**, *52* (3), 473-476.

(37) Peng, L.; Moon, S-Y; Guelta, M. A.; Lin, L.; Gómez-Gualdrón, D. A., Snurr, R. Q., Harvey, S. P.; Hupp, J. T.; Farha, O. K. *ACS Nano* **2016**, *10*, 9174-9182.

(38) Lian, X.; Chen, Y.-P.; Liu, T.-F.; Zhou, H,-C. *Chem. Sci.* **2016**, *7*, 6969-6973

(39) Chen, Y.; Han, S.; Li, X.; Valencia, V.; Zhang, Z.; Ma, S. *Inorg. Chem.* **2014**, *53* (19), 10006-10008.

(40) Sánchez, S.; Solovev, A. A.; Mei, Y.; Schmidt, O. G. *Adv. Funct. Mater.* **2010**, *132* (38), 13144–13145.

(41) Sitt, A.; Soukupova, J.; Miller, D.; Verdi, D.; Zboril, R.; Hess, H.; Lahann, J. *Small* **2016**, *12* (11), 1432–1439.

(42) Singh, V. V.; Kaufmann, K.; Esteban-Fernández de Ávila, B.; Uygun, M.; Wang, J. *Chem. Commun.* **2016**, *52* (16), 3360–3363.

(43) Wu, Z.; Lin, X.; Zou, X.; Sun, J.; He, Q. *ACS Appl. Mater. Interfaces* **2015**, *7* (1), 250–255.

(44) Cavka, J. H.; Jakobsen, S.; Olsbye, U.; Guillou, N.; Lamberti, C.; Bordiga, S.; Lillerud, K. P. *J. Am. Chem. Soc.* **2008**, *130* (42), 13850–13851.

(45) Albalad, J.; Xu, H.; Gándara, F.; Haouas, M.; Martineau-Corcos, C.; Mas-BAllesté, R.; Barnett, S. A.; Juanhuix, J.; Imaz, I.; Maspoch, D. *J. Am. Chem. Soc.* **2018**, *140* (6), 2028–2031.

(46) Guillerm, V.; Xu, H.; Albalada, J.; Imaz, I.; Maspoch, D. *J. Am. Chem. Soc.* **2018**, *140* (44), 15022–15030.

(47) Dubinin, M. M.; Zaverina, E. D.; Radushkevich, L. V.; Sorbtsiya, I. *Zh. Fiz. Khim.* **1947**, *21* (11), 1351–1362.

(48) Simmchen, J.; Magdanz, V.; Sánchez, S.; Chokmaviroj, S.; Ruiz-Molina, D.; Baeza, A.; Schmidt, O. G. *RSC Adv.* **2014**, *4* (39), 20334–20340.

(49) Manesh, K. M.; Cardona, M.; Yuan, R.; Clark, M.; Kagan, D.; Balasubramanian, S.; Wang, J. *ACS Nano* **2010**, *4* (4), 1799–1804.

(50) Solovev, A. A.; Sánchez, S.; Pumera, M.; Mei, Y. F.; Schmidt, O. C. *Adv. Funct. Mater.* **2010**, *20* (15), 2430–2435.

(51) Solovev, A. A.; Sánchez, S.; Mei, Y.; Schmidt, O. G. *Phys. Chem. Chem. Phys.* **2011**, *13* (21), 10131–10135.

(52) Solovev, A. A.; Mei, Y.; Ureña, E. B.; Huang, G.; Schmidt, O. G. *Small* **2009**, *5* (14), 1688–1692.

(53) Chi, Q.; Wang, Z.; Tian, F.; You, J.; Xu, S. *Micromachines* **2018**, *9* (10), 537.

(54) Fomin, V. M.; Hippler, M.; Magdanz, V.; Soler, L.; Sánchez, S.; Schmidt, O. G. *IEEE Trans. Robot.* **2014**, *30* (1), 40–48.

(55) Ma, X.; Jang, S.; Popescu, M. N.; Uspal, W. E.; Miguel-López, A.; Hahn, K.; Kim, D. P.; Sánchez, S. *ACS Nano* **2016**, *10* (9), 8751–8759.

(56) Solovev, A. A.; Sánchez, S.; Mei, Y.; Schmidt, O. G. *Phys. Chem. Chem. Phys.* **2011**, *13* (21), 10131–10135.

(57) Phung, K. K.; Sethupathi, S.; Piao C. S. *IOP CONf. Series: Earth and Environmental Science* **2018**, *140*, 012020.

Chapter 4

Clip-off Chemistry: Synthesis by Programmed Disassembly of Metal–Organic Frameworks

4.1 Introduction

Throughout history, innovations in chemical synthesis have yielded previously inaccessible new molecules and materials that have enabled vast improvements in human life, ranging from fine chemicals to complex functional materials. Each new reaction and methodology not only help to expand accessible chemical space, but also inspire researchers to further innovate in the iterative design and preparation of new chemical targets of social, economic or industrial value. To date, most state-of-the-art synthetic approaches use bottom-up strategies that, at the latter stage, mainly entail controlling the formation of new bonds. A relatively recent example of this is reticular chemistry,[1-7] in which judiciously-designed, rigid molecular building blocks (MBBs) are linked by strong bonds to create crystalline open-framework materials[8] such as metal-organic frameworks (MOFs),[1-4] covalent-organic frameworks (COFs)[9] and metal-organic polyhedra (MOPs).[10-12] Reticular materials are a fascinating source of metal-organic and purely organic structures built up from an endless variety of fragments and MBBs[13] (e.g. metal clusters, cages, cycles, metal layers, metal chains, etc.) that often do not exist in their isolated form.

We envisaged that by selectively breaking certain bonds in reticular materials, we could transform them into new frameworks or break them into new molecular fragments or isolated MBBs, as a synthetic strategy towards new materials and molecules. We hypothesized that we could use a chemical reaction for programmed bond-breaking, such that the de-reticulation process would occur at the molecular level. We reasoned that this would require the presence of cleavable groups at specific positions within the structures of the corresponding reticular materials, and that reported reticular materials that contain linkers featuring alkene bonds would be ideal starting materials for this strategy. However, we thought that, in the likely event that the targeted structure-precursor did not contain any alkene groups, we could generalize this approach to numerous reticular materials by inserting such groups into the pre-selected linkers without modifying their size or geometry, via reticular chemistry. Indeed, reticular chemistry dictates that for a given framework, the constituents can be chemically functionalized pre- and/or post-synthetically,[14,15] without any loss to framework connectivity. Thus, we extended this concept to the ability to encode the organic linker of an existing MOF by inserting cleavable alkene groups into it, without modifying the linker size or topology, to ultimately enable assembly of the corresponding isoreticular MOF structures containing the desired cleavable group.[16]

Reticular chemistry dictated that, for a given framework, constituents could be chemically functionalized either before or after synthesis, without any compromise to framework connectivity. This concept was extended to enable the encoding of the organic linker of an existing MOF by inserting cleavable alkene groups into it. This was done without modifying the linker's size or topology, ultimately facilitating the assembly of the corresponding isoreticular MOF structures containing the desired cleavable group.

In this chapter, the aim is to develop a new synthetic approach, called Clip-off Chemistry, which is based on the programmed disassembly of reticular materials by controlled breaking of selected bonds. Clip-off Chemistry was verified by the synthesis of two topologically distinct, three-dimensional (3D) MOFs from two 3D MOFs in single-crystal-to-single-crystal transformations. Through these two examples, it was demonstrated that reticular materials (in this study, MOFs) could be modified via the cleavage, rather than formation, of bonds in their frameworks, enabling alterations to the connectivity of their constituent MBBs and therefore, to their topology. In all the examples presented here, ozonolysis was employed as the chemical reaction to cut off constituent organic MBBs or linkers via direct cleavage of their alkene bonds.

4.2 Results and discussion

4.2.1 Reaction design in Clip-off Chemistry: synthesis of a first 3D MOF

Clip-off Chemistry is based on using, as starting materials, structures that contain cleavable groups (in this study, alkenes) at specific positions, such that cleavage of said groups generates new molecules or materials. Following this principle, the first target was to achieve the clip-off synthesis of a new 3D MOF from a 3D MOF precursor. When selecting precursors in Clip-off Chemistry, reticular analysis of their underlying nets[17-19] is important, as bond-breaking in the structure relates to disassembly of certain circuits of connections.[20] In reticular materials this disassembly can be performed mainly by erasing some of the edges or nodes. Translating this analysis to the chemical field, the clip-off synthesis of a structure (here, a 3D MOF) from the disassembly of another structure (here, another 3D MOF) can be achieved by selecting either of two potential precursors: i) a structure built from one type of polytopic linker that contains different circuits of connections between the clusters, containing a cleavable bond in at least one of the circuits; or ii) a mixed-linker structure, in which linkers are located at different crystallographic positions, and one of them contains a cleavable bond (Figure 4.1).
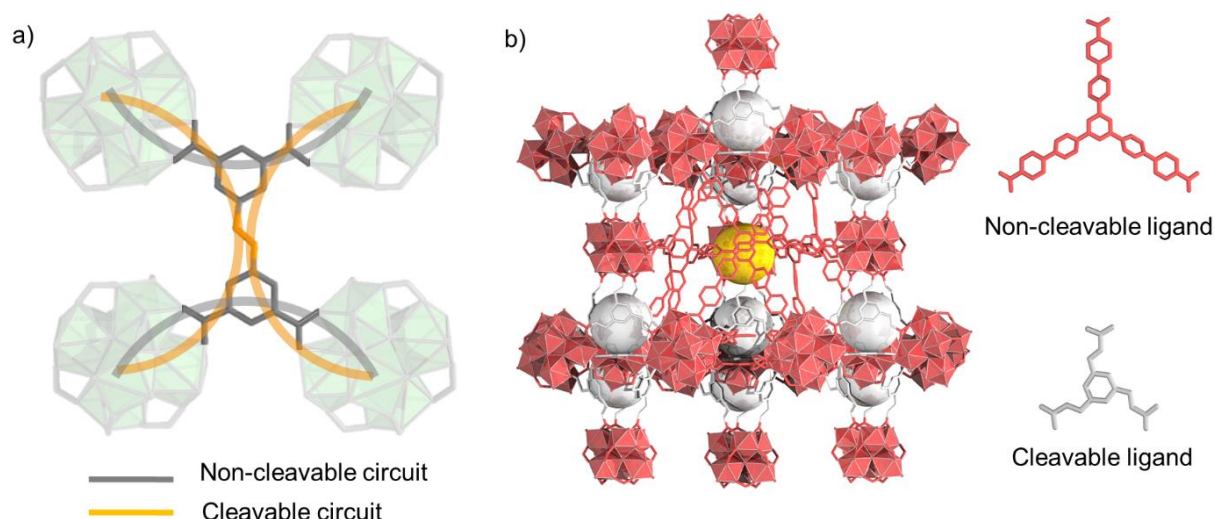
Figure 4.1 (a) A 3D MOF structure built from one type of polytopic linker displaying various circuits of connections. By removing cleavable circuits (orange), a new 3D MOF structure can be obtained based on those non-cleavable circuits (grey). (b) A mixed-linker 3D MOF structure containing both cleavable (light grey) and non-cleavable linkers (red). By removing cleavable linker, a new 3D MOF structure can be obtained based on those non-cleavable linkers.

In the case of the polytopic linker-based MOF, cleavage of the polytopic linker will provoke disassembly of the circuits of connections in which the cleavable bond is involved, thereby forming a structure built up exclusively from those circuits that do not contain the cleavable groups, with a distinct underlying topology. Similarly, in the mixed-linker structure, cleavage of the linker containing the cleavable bond will provoke disassembly of the circuits of connections in which it is involved, thereby forming a structure built up exclusively from those circuits that involve the metal clusters and the other linkers that do not contain the cleavable groups.
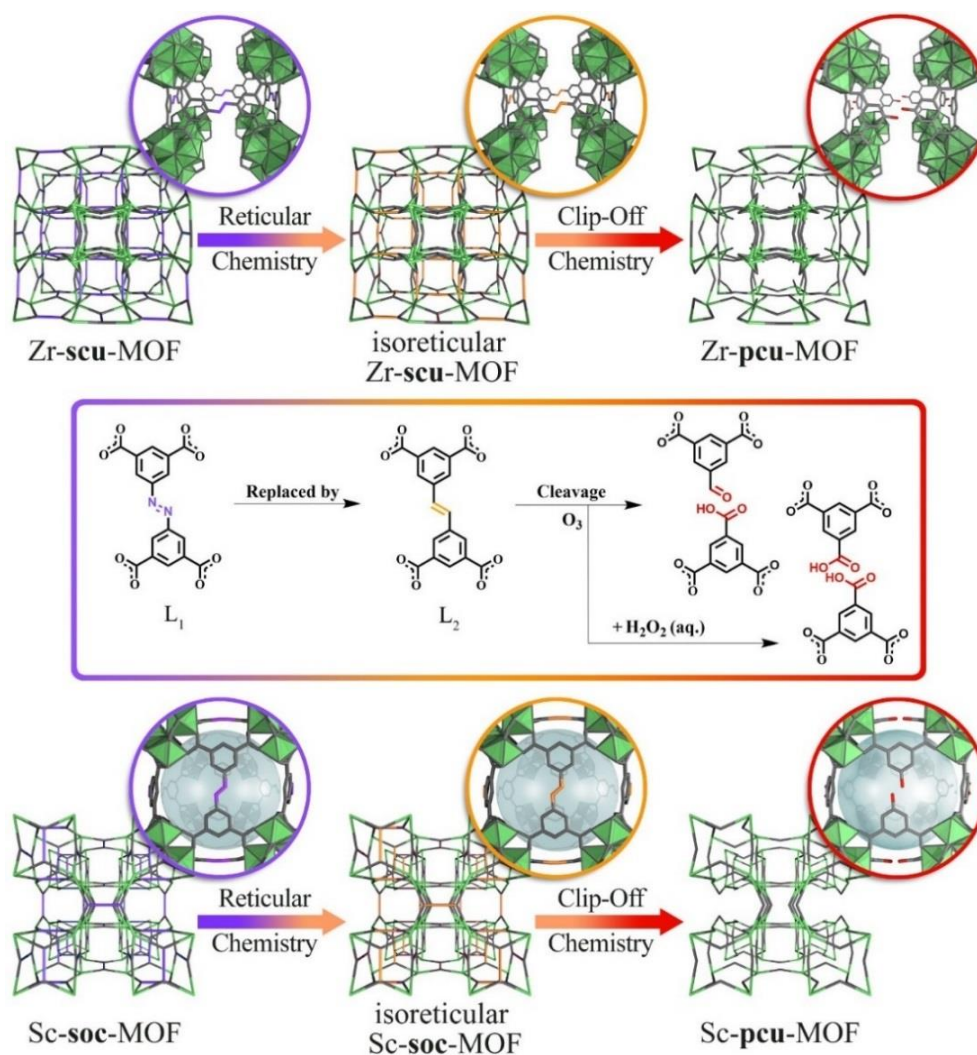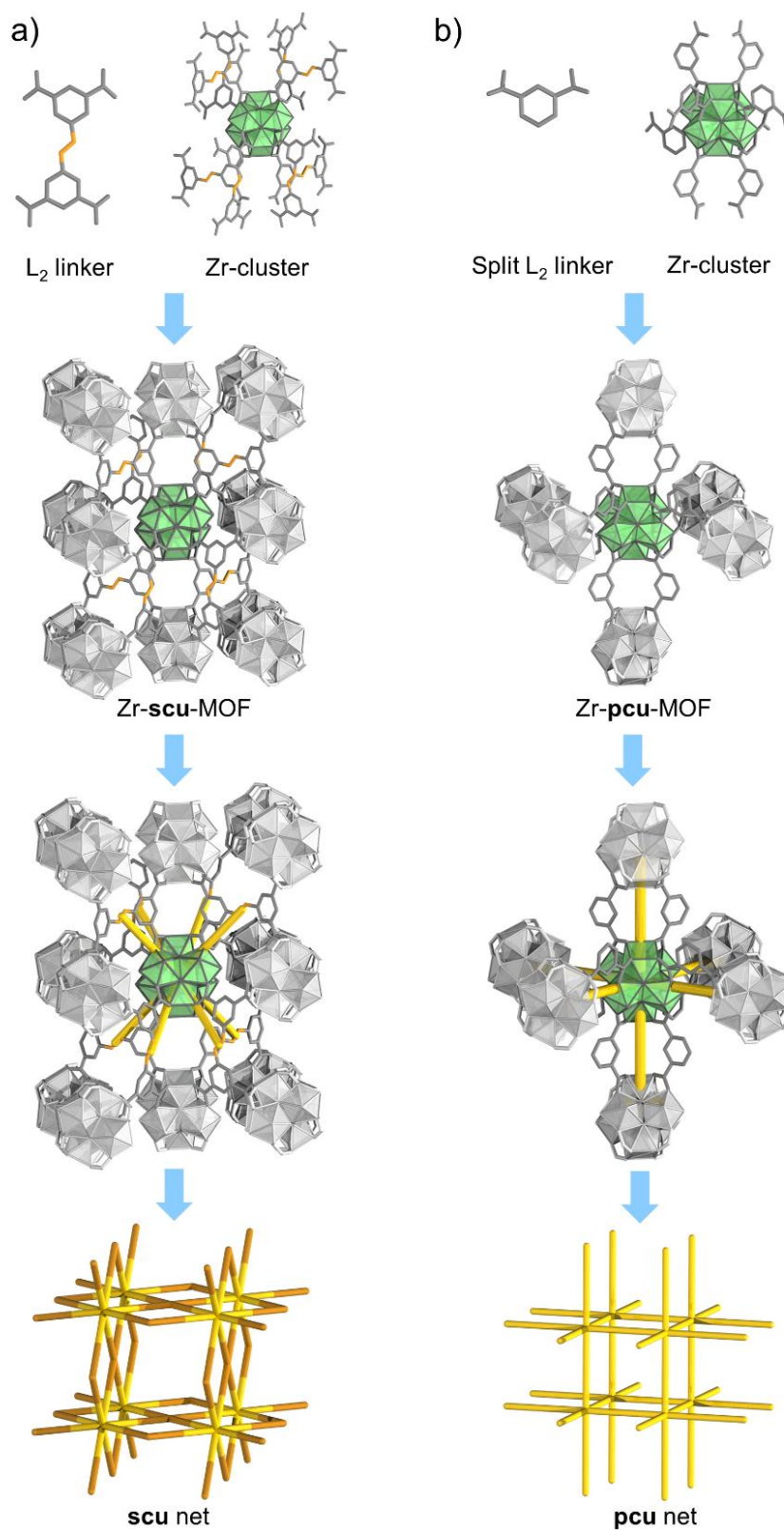
Figure 4.2 Representative examples of Clip-off Chemistry, starting with the isoreticular insertion of cleavable (here, alkene) groups into a MOF structure,[16] followed by the quantitative breaking of these cleavable groups by ozonolysis to afford a new structure. Top: clip-off synthesis of Zr-**pcu**-MOF from Zr-**scu**-MOF. Bottom: clip-off synthesis of Sc-**pcu**-MOF from Sc-**soc**-MOF. Middle: chemical reaction for both syntheses. The formation of aldehyde/carboxylic acid groups after ozonolysis is not shown in the lower magnification nets for better illustration of the breaking process. The formation of these groups is shown in the magnified structures, wherein the red groups represent aldehyde or carboxylic acid groups.

In our choice of precursor for the first 3D MOF synthesis, the polytopic linker approach described above was followed (Figure 4.2). Thus, the Zr-**scu**-MOF was selected,[21] in which the assembly of eight-connected (8-c), quadrangular prismatic $Zr_6O_4(OH)_4$ clusters to 4-c rectangular linkers 5-[(3,5-dicarboxyphenyl)diazenyl]benzene-1,3-dicarboxylate (L₁) forms a 3D framework with a 4,8-c **scu/3,3,8T132** underlying topology[22] and 1D channels (size: ≈7 Å) along one axis. However, as this reported structure does not contain any cleavable alkene groups, they had to be inserted chemically, using the well-known isoreticular principle.[16] This step of introducing cleavable groups into precursors

can be performed before the cleavage step as needed, by replacing at least one of the original linkers with one of similar size and geometry that contains the desired cleavable groups at strategic positions. Once inserted into the isoreticular structure, such linkers generate different circuits of connections, in which at least one circuit contains the cleavable bonds.

In our example, the linker L_1 was replaced with 5-[2-(3,5-dicarboxyphenyl)ethenyl]benzene-1,3-dicarboxylate (L_2), which contains olefinic bonds for cleavage. Thus, an isoreticular Zr-**scu**-MOF framework was synthesized and built up from different circuits of connections, wherein only some of them contain the cleavable olefinic bonds of L_2. It was anticipated that, upon treatment of this framework with ozone,[23-27] each 4-c L_2 linker would be split into two 2-c linkers (doubly deprotonated trimesic acid and/or 5-formylisophthalate). Consequently, only the circuits of connections between the $Zr_6O_4(OH)_4$ clusters and these 2-c linkers would remain, forming a Zr-**pcu**-MOF. In contrast to the isoreticular Zr-**scu**-MOF precursor, which is based on quadrangular prismatic 8-c Zr-clusters, each $Zr_6O_4(OH)_4$ cluster is still coordinated by 8 linkers in this new Zr-**pcu**-MOF, however its topological connectivity decreases from 8-c to a 6-c because two pairs of the eight 2-c linkers connect the same two clusters (Figure 4.3).[28]

It was expected that this first clip-off reaction would afford the first-ever example of a 3D MOF made of archetypical Zr-oxo-hydroxo-clusters linked by isophthalate-like linkers in a **pcu** underlying net. Interestingly, the closest literature example of such a structure is that of a 2D MOF made of Zr-oxo-hydroxo-clusters linked by isophthalate, albeit in an **hcb** topology.[29] Our target 3D Zr-**pcu**-MOF could also be seen as exemplifying a connection of Zr-oxo-hydroxo-clusters through trimesate linkers, which are coordinated only through two of their three carboxylate groups. Accordingly, it could also be considered as the first example of a Zr-structure with a free carboxylic acid using trimesate, as researchers have previously reported combination of Zr-oxo-hydroxo-clusters with this linker in a **spn** topology of 3,6-connectivity.[30]

**Figure 4.3** Comparison of the cluster environment in (a) Zr-**scu**-MOF and (b) Zr-**pcu**-MOF. In Zr-**scu**-MOF, each Zr-oxo-hydroxo-cluster is connected to 14 neighboring Zr-oxo-hydroxo-clusters by eight 4-c L_2 linkers. After clip-off treatment, each Zr-oxo-hydroxo-cluster in Zr-**pcu**-MOF is surrounded by 6 neighboring Zr-oxo-hydroxo-clusters, which are interconnected by eight 2-c linkers.

4.2.2 Clip-off synthesis: from Zr-scu-MOF to Zr-pcu-MOF

Colorless cubic crystals of isoreticular Zr-**scu**-MOF were synthesized by solvothermal reaction (120 °C) of a mixture of $ZrOCl_2 \cdot 8\,H_2O$ and L_2 in *N,N*-dimethylformamide (DMF) and formic acid for 5 days. The crystal structure revealed the expected isoreticular **scu** framework, in which L_1 had been replaced by L_2 (Figure 4.4a). Next, the phase purity of the bulk sample was confirmed by powder X-ray diffraction (PXRD) and field emission scanning electron microscopy (FESEM) (Figure 4.4 and Figure 4.5, more PXRD patterns see section 4.4.3).
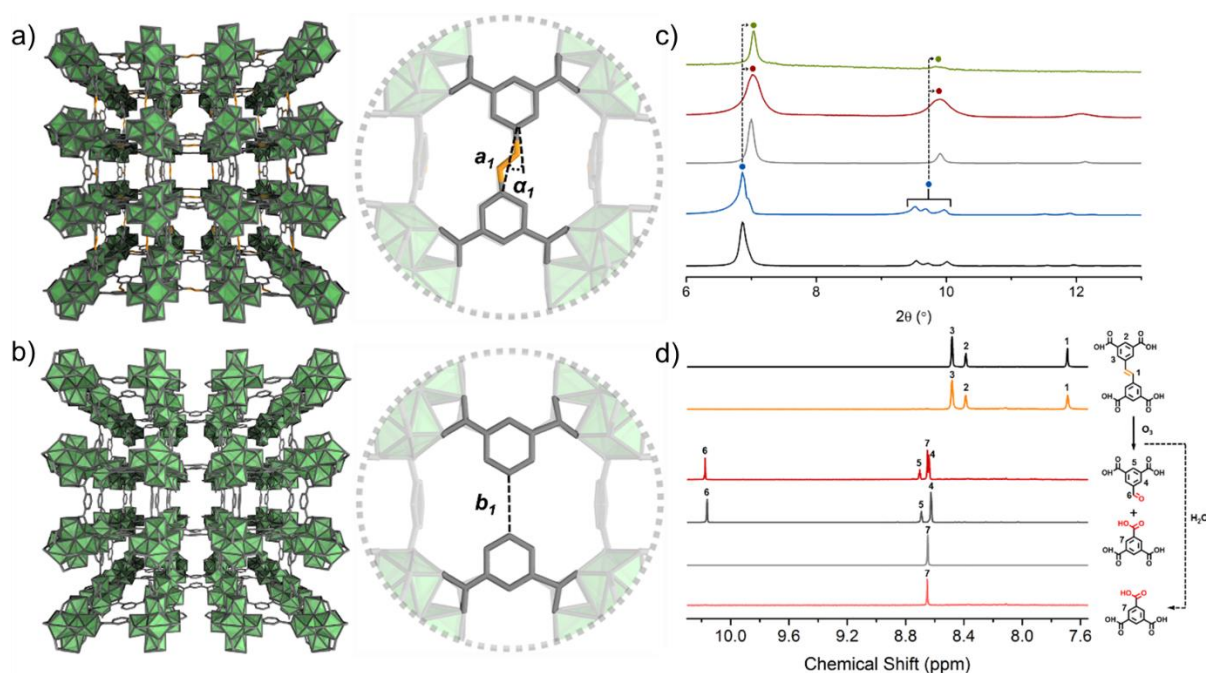
Figure 4.4 Structural and molecular characterization of Zr-**pcu**-MOF and Sc-**pcu**-MOF. (a,b) Crystal structures of isoreticular Zr-**scu**-MOF (a) and Zr-**pcu**-MOF (b). Magnified views highlight the changes observed in the distances and angles of opposite phenyl rings (from a_1 = 3.77-3.79 Å and α_1 = 14.95-19.71° to b_1 = 3.39-3.65 Å and β_1 = 0°). (c) Magnified view of PXRD spectra for calculated Zr-**scu**-MOF (black), synthesized Zr-**scu**-MOF (blue), calculated Zr-**pcu**-MOF (grey), synthesized Zr-**pcu**-MOF (red) and oxidized Zr-**pcu**-MOF (green). The main structural changes with signal shifts are highlighted. (d) ^{1}H NMR spectra (360 MHz, DMSO-d_6) of digested L_2 (black), Zr-**scu**-MOF (orange), Zr-**pcu**-MOF (red), 5-formylisophthalic acid (dark grey), trimesic acid (light grey) and oxidized Zr-**pcu**-MOF (light red).
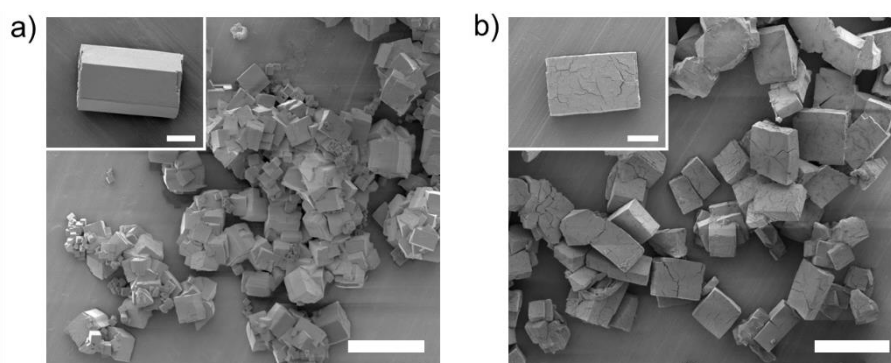
Figure 4.5 FESEM images of (a) Zr-**scu**-MOF and (b) Zr-**pcu**-MOF. Scale bars: 25 μm (a, b) and 5 μm (insets). In these images, it can be observed that the surface of Zr-**pcu**-MOF crystals shows some degree of cracking. Nevertheless, this cracking does not prevent keeping their single crystal nature.
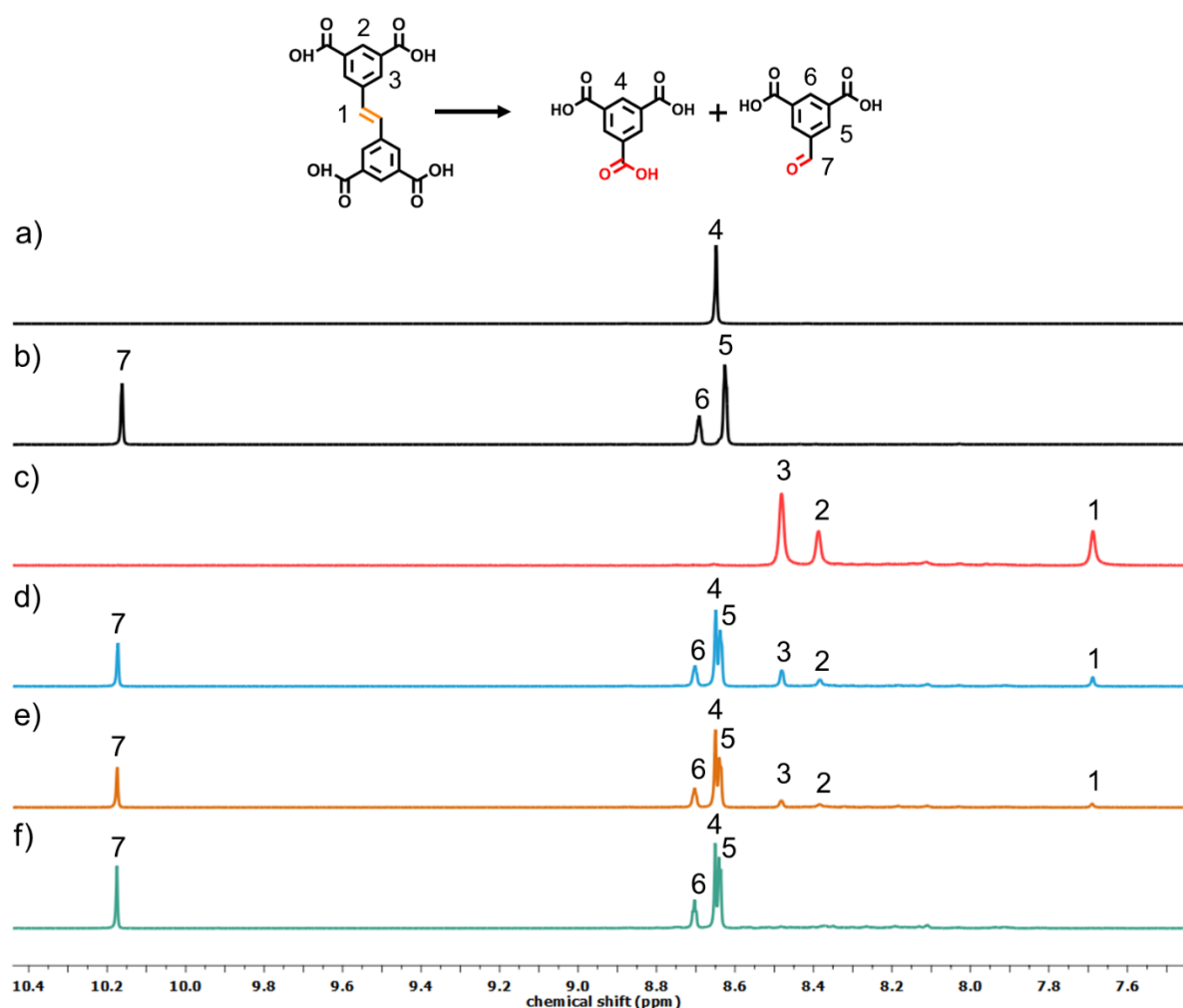
Figure 4.6 ^{1}H NMR spectra (360 MHz, DMSO-d_6) of digested (a) trimesic acid, (b) 5-formylisophthalic acid, (c) Zr-**scu**-MOF, (d-f) Zr-**scu**-MOF after (d) 3rd, (e) 6th and (f) 9th cycle of the ozonolysis solid-gas reaction. Note that the spectrum of the 9th cycle corresponds to that of the synthesized Zr-**pcu**-MOF.

To start the clip-off synthesis of Zr-**pcu**-MOF, 20 mg of synthesized Zr-**scu**-MOF crystals were packed into a plastic tube which was connected on one side to the ozonator (through a $CaCl_2$ humidity trap) and, on the other side, to a vacuum pump (through a KI trap), to ensure a continuous flow of ozone through the column.[23,24] The reaction was run at room temperature for 30 min. Afterwards, the sample was connected to vacuum for another 30 min. This ozonation/vacuum cycle was repeated nine times for the complete cleavage of all the alkene bonds in Zr-**scu**-MOF, as evidenced by the gradual disappearance of the characteristic olefinic peak at 7.69 ppm in the ^{1}H NMR spectra of the digested Zr-**scu**-MOF crystals (Figure 4.6, more ^{1}H NMR spectra see section 4.4.3). After nine cycles, the resulting solid was directly collected from the tube and stored in tetrahydrofuran.

Next, the ozonated Zr-**scu**-MOF crystals was characterized by single crystal X-ray diffraction (SCXRD), which confirmed that they had retained the single-crystal character (Figure 4.4b). For these crystals, synchrotron diffraction data were collected at a maximum resolution of 1.2 Å. Data analyses revealed a variation in the lattice parameters, as compared to the pristine structure. Both pre- and post-ozonolysis crystal structures were solved in the monoclinic $C2/m$ space group. However, the cell volume of the ozonated crystal was found to be $16\,076.00(10)$ Å^3, whereas that of the pristine Zr-**scu**-MOF was $16\,957.46(10)$ Å^3. Analysis of the diffraction data demonstrated the integrity of the inorganic Zr-oxo-hydroxo-clusters after post-synthetic reaction, with no changes in their coordination. Thus, the position of all the atoms in the inorganic secondary building units (SBUs, metal and carboxylate atoms) were assigned and anisotropically refined. As for the rest of the organic linker, carbon atoms belonging to the phenyl ring were located in the difference electron density maps. However, their high thermal parameter values indicated a possible positional disorder. Moreover, the olefinic carbon atoms could no longer be located, supporting the completeness of the ozonolysis reaction. This is in stark contrast to the pristine MOF, in which the positions of these atoms were clearly visible and refined. The position of the resulting aldehydes or carboxylic groups, newly inserted in the MOF upon cleavage of the carbon-carbon double bond, could not be determined from the analysis of the difference electron density maps. Instead, a large residual electron density was observed in the vicinity of the positions that were initially occupied by the olefinic group. When comparing the two structures, additional differences could be observed in the arrangement of other framework atoms. Most notably, the relative orientation of opposite phenyl rings in a same linker in Zr-**scu**-MOF was different after ozonolysis (Figures 4.4b and Figure 4.7), indicating that the olefinic bond was no longer present to fix the angle between these rings.
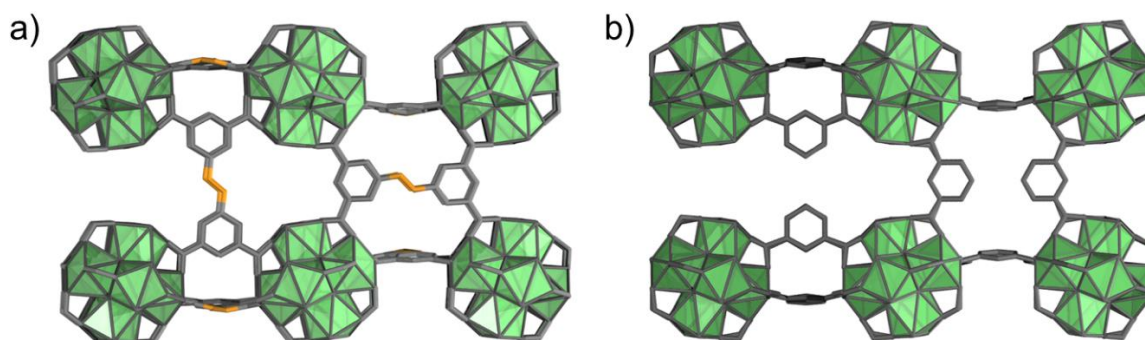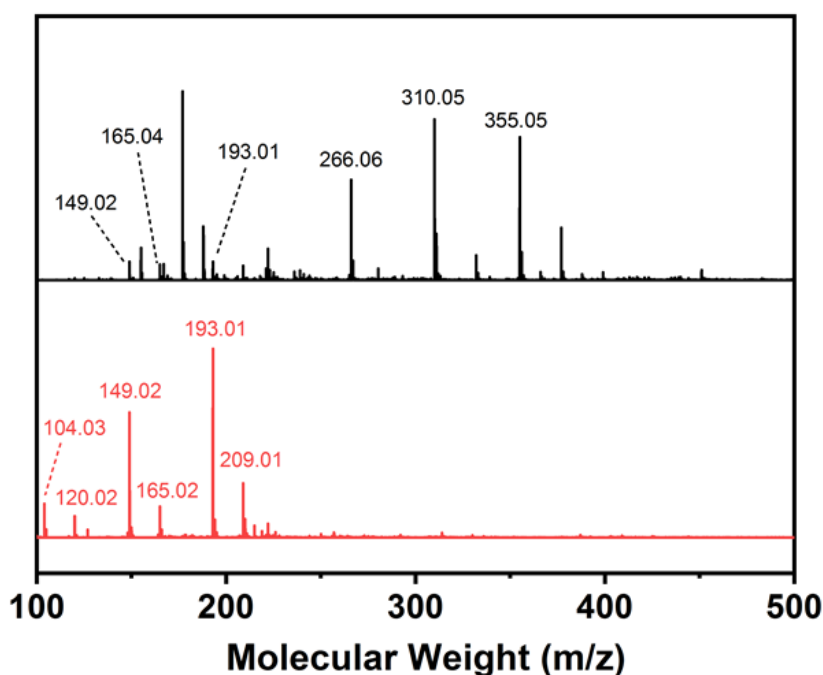
Figure 4.7 Representation of the single-crystal structures of (a) Zr-**scu**-MOF and (b) Zr-**pcu**-MOF, showing the differences in the orientation of the phenyl rings of the linkers before (a) and after (b) the cleavage of the olefinic bonds.

Since the crystal structure of pristine Zr-**scu**-MOF differed markedly to that of ozonated Zr-**scu**-MOF (or Zr-**pcu**-MOF), these ozonated MOFs were also studied by PXRD. Remarkably, the PXRD patterns for each sample perfectly matched those calculated from the corresponding structures determined by SCXRD and full-pattern profile refinements further demonstrated phase purity of the samples (Figure 4.4c and Figure 4.8). Altogether, these results corroborate two crucial phenomena for validation of Clip-off Chemistry: firstly, that it is indeed possible to cleave all the periodic olefinic bonds in a 3D structure without destroying it or its single-crystal character; and secondly, that said cleavage, and the resultant formation of a new structure (in this case, Zr-**pcu**-MOF),[19] are homogeneous throughout the bulk crystalline sample.
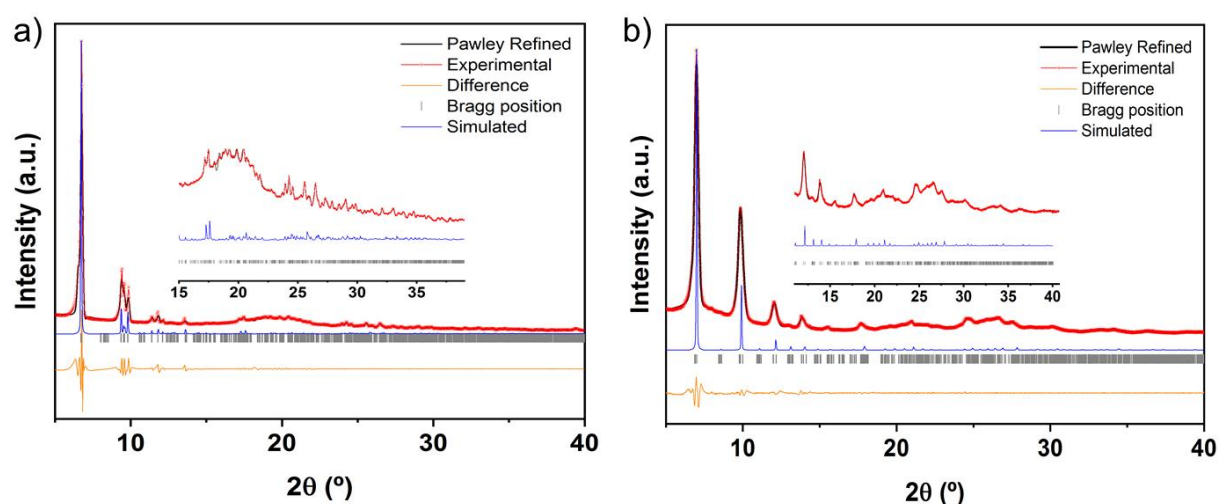

Figure 4.8 PXRD pattern and Pawley refinement of (a) Zr-**scu**-MOF and (b) Zr-**pcu**-MOF. The experimental pattern (red), the refined Pawley fitting (black), the difference plot (orange), simulated pattern (blue) and the Bragg positions (grey) are provided.

Next, further evidence of the formation of Zr-**pcu**-MOF was gained by recording the ^{1}H NMR spectra of the digested ozonated samples (5 % HF/DMSO-d_6) after each cycle, and then comparing each spectrum to that of the starting Zr-**scu**-MOF (Figure 4.4d and Figure 4.6, more ^{1}H NMR spectra see section 4.4.3). Under these digestion conditions, the MOF structures are destroyed and the linkers, released, thus enabling use of ^{1}H NMR to unveil the composition of the initial MOF structures. The spectrum of the digested Zr-**scu**-MOF showed the characteristic peak of equivalent olefinic protons of L$_2$ at δ=7.69 ppm. In contrast, the spectra of ozonated crystals after each cycle confirmed a gradual fading of this olefinic signal, which, by the ninth cycle, had fully disappeared. Indeed, ^{1}H NMR of digested ozonated Zr-**scu**-MOF after the ninth cycle confirmed the full conversion of L$_2$ into doubly deprotonated trimesic acid and 5-formylisophthalate. Beyond the disappearance of the olefinic protons at δ=7.69 ppm, there was also fading of the phenyl (δ=8.49 ppm and 8.39 ppm) and the carboxylic acid (δ=13.32 ppm) protons of L$_2$, whereas the characteristic signals for the trimesic acid (δ=13.57 ppm and 8.65 ppm) and 5-formylisophthalic acid (δ=10.18 ppm, 8.70 ppm and 8.64 ppm) were clearly identifiable.

Figure 4.9 ESI-MS spectrometry of digested Zr-**scu**-MOF (black) and Zr-**pcu**-MOF (red). The peak at m/z 355.05 is assigned to [L$_2$−H]$^-$ in Zr-**scu**-MOF, corresponding to the formula [C$_{18}$H$_{12}$O$_8$−H]$^-$: expected = 355.05, found = 355.05. The peak at m/z 193.01 in both samples is assigned to 5-formylisophthalic acid, corresponding to the formula [C$_6$H$_3$(COOH)$_2$(CHO)−H]$^-$: expected = 193.02, found = 193.01. The peak at m/z 209.01 in both samples is assigned to trimesic acid, corresponding to the formula [C$_6$H$_3$(COOH)$_3$−H]$^-$: expected = 209.02, found = 209.01.

Cleavage of the olefinic bonds was corroborated by negative-mode mass spectrometry and Fourier transform infrared (FTIR) spectroscopy of both pristine and ozonated Zr-MOFs (Figure 4.9 and Figure 4.10). In the mass spectrum, the molecular ions $[M-H]^-$ corresponding to trimesic acid ($m/z = 209.01$) and 5-formylisophthalic acid ($m/z = 193.01$) were found, in strong contrast to the absence of any molecular ion $[M-H]^-$ corresponding to L_2 ($m/z = 355.05$). Similarly, in comparison to the spectrum of pristine Zr-**scu**-MOF, the FTIR spectrum of ozonated Zr-**pcu**-MOF revealed the appearance of a typical carbonyl (C=O) stretching band at 1700 cm^{-1} and the complete disappearance of an alkene (C=C) stretching band at 1622 cm^{-1}.
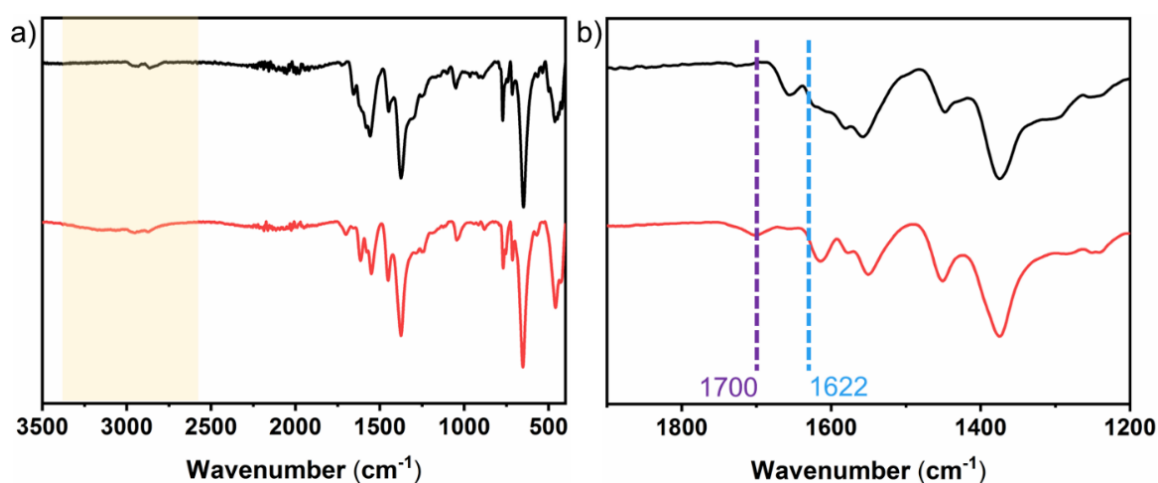
Figure 4.10 (a) Full FTIR spectra of Zr-**scu**-MOF (black), Zr-**pcu**-MOF (red) and (b) magnified area. In FTIR spectra, Zr-**pcu**-MOF displayed a broad band in the region of 3300-2500 cm^{-1}, which was not found in Zr-**scu**-MOF. This could be ascribed to the O-H stretching of the free carboxyl groups. The enhanced vibration signal of the stretching carbonyl (C=O) groups at 1700 cm^{-1} was seen in Zr-**pcu**-MOF. The olefinic bond, which has the characteristic absorbance at 1622 cm^{-1}, disappeared in Zr-**pcu**-MOF, demonstrating the total cleavage of linker L_2 from Zr-**scu**-MOF.

Having demonstrated the single-crystal-to-single-crystal synthesis of Zr-**pcu**-MOF by selectively cleaving the olefinic bonds in Zr-**scu**-MOF into a mixture of aldehyde and carboxylic acid groups, the next step was to perform analogous chemistry to synthesize Zr-**pcu**-MOF functionalized exclusively with carboxylic acids to show enhanced control over the final output of the Clip-off Chemistry. To this end, ozonated crystals were soaked in 1 mL of hydrogen peroxide (30 wt. % in H$_2$O) solution for 3 weeks. During this period, the sample was refreshed with fresh hydrogen peroxide every 24 h. Next, the sample was centrifuged, and then washed twice with water. The transformation to carboxylic acid groups was quantitative, as confirmed by ^{1}H NMR (Figure 4.4d, more ^{1}H NMR spectra see section

4.4.2). Moreover, the Zr-**pcu**-MOF framework had been preserved, as confirmed by PXRD (Figure 4.4c, more PXRD patterns see section 4.4.2).

4.2.3 Clip-off synthesis: from Sc-soc-MOF to Sc-pcu-MOF

To show that Clip-off Chemistry could be generalized to other 3D MOF structures, the subsequent trial aimed to synthesize a 3D Sc-**pcu**-MOF from an Sc-**soc**-MOF precursor (Figure 4.1),[31] a 3D structure built up from linking 6-c trigonal, prismatic Sc_3O clusters to 4-c L_1 linkers in a 4,6-c **soc**/**edq** topology.[32] This structure exhibits a mixture of cubic cavities (size: 11 Å) and 1D channels (size: 8 Å) along the three axes. As in the previous case, the precursor by replacing L_1 with L_2 was intentionally designed, thus resulting in the formation of an isoreticular Sc-**soc**-MOF that contains different circuits of connections, some of which contains the cleavable olefins. It is envisioned that, upon treatment with ozone, this circuit would be disrupted to form a 3D Sc-**pcu**-MOF whose Sc_3O clusters would be connected through trimesate/5-formylisophthalate linkers.

To start the clip-off synthesis of Sc-**pcu**-MOF via the aforementioned route, the isoreticular Sc-**soc**-MOF precursor was first prepared. Colorless cubic crystals of Sc-**soc**-MOF were synthesized by heating a solution of $Sc(NO_3)_3 \cdot x\, H_2O$ and L_2 in DMF, ethanol and formic acid at 120 °C for 48 h. However, all attempts at complete ozonolysis were unsuccessful, whether using the same synthetic protocol as for Zr-**scu**-MOF or trying slight modifications (*e.g.* extending the reaction time up to 8 h and/or the number of ozonolysis cycles up to twelve; Figure 4.11, more ^{1}H NMR spectra see section 4.3.2). Consequently, cleavage of the olefinic bonds was incomplete, reaching a maximum value of 60 % to 70 % under certain conditions (*e.g.* exposing the Sc-**soc**-MOF crystals to ozone gas for 2 h). A distinct ozonolysis protocol was employed: Sc-**soc**-MOF crystals were immersed in water, and then ozone was bubbled through the suspension under stirring at room temperature for 12 h. These conditions afforded greater cleavage of the olefinic bonds than in the previous strategy, leading to a mixture of trimesic acid, 5-formylisophthalic acid and the intermediate 1,2,4-trioxolane ring (Figure 4.12). Importantly, the presence of this intermediate indicated that the olefinic bonds had not all been completely cleaved to aldehyde/carboxylic acid groups. Moreover, increasing the reaction time under these solid/liquid conditions did not provide any major improvement in cleavage, although it did lead to a slight decrease in the crystallinity of the ozonated Sc-**pcu**-MOF.
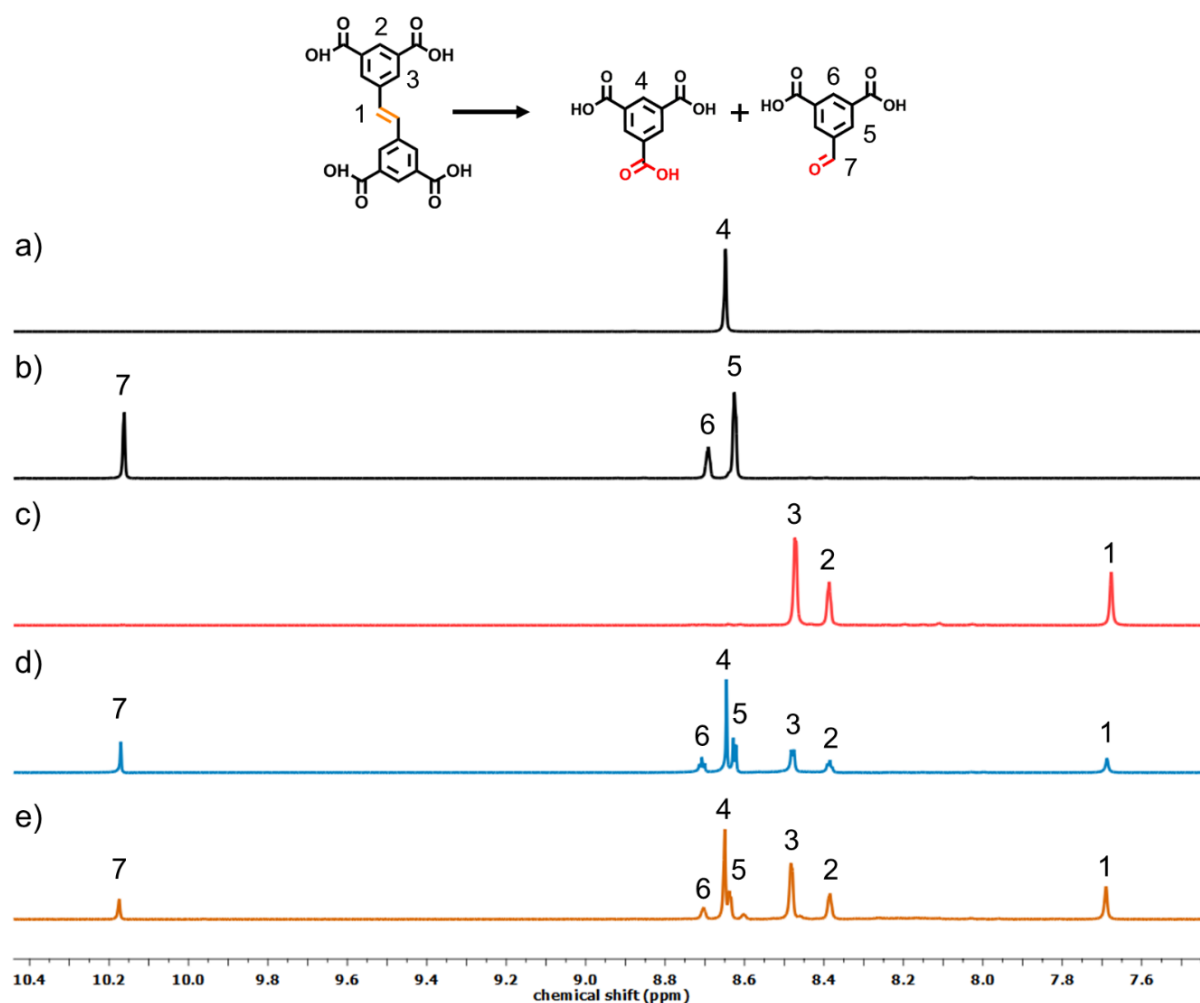
Figure 4.11 ^{1}H NMR spectra (360 MHz, DMSO-d_6) of digested (a) trimesic acid, (b) 5-formylisophthalic acid, (c) Sc-**soc**-MOF, (d) Sc-**soc**-MOF after solid-gas reaction for 8 h, and (e) Sc-**soc**-MOF after solid-gas reaction for 12 cycles. Note that the characteristic protons from the olefinic bond signal at 7.68 ppm of Sc-**soc**-MOF could still be observed after both solid-gas phase ozonolysis reactions, confirming that the cleavage of olefinic bonds under these synthetic conditions was not quantitative.
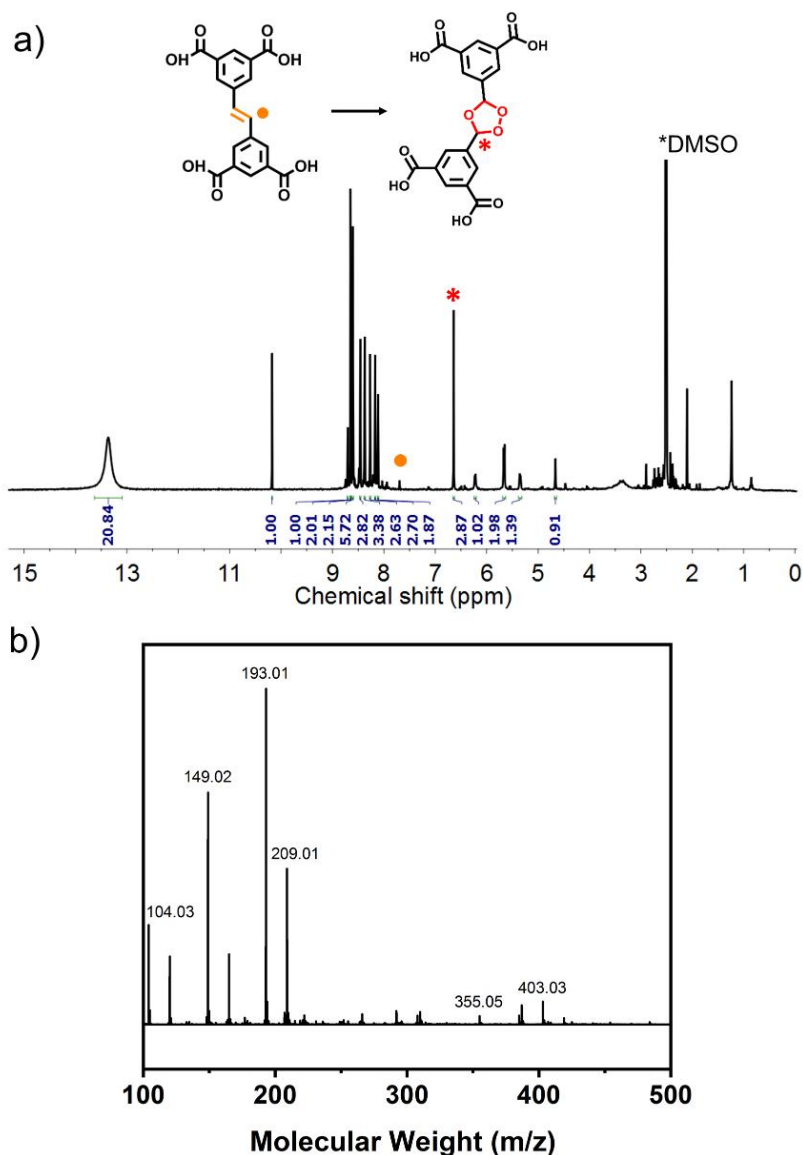
Figure 4.12 Characterization of Sc-**soc**-MOF after ozonolysis only in water suspension for 12 h. (a) ^{1}H NMR spectrum (360 MHz, DMSO-d_6) of digested Sc-**soc**-MOF after only in water suspension ozonolysis reaction for 12 h. Note that the peak intensity of protons from the olefinic bond at 7.70 ppm (orange dot) was very weak but it could still be observed, indicating a high degree of cleavage but not quantitative. Moreover, the signal of the proton at 6.64 ppm (red star) was identified as the intermediate trioxolane-metathesis product, which is in accordance with the previous paper published by our group.[6] (b) ESI-MS spectrometry of digested Sc-**soc**-MOF after in water suspension ozonolysis reaction for 12 h. The peak at m/z 355.05 is assigned to $[L_2−H]^−$ in Sc-**soc**-MOF, corresponding to the formula $[C_{18}H_{12}O_8−H]^−$: excepted = 355.05, found = 355.05. The peak at m/z 193.01 in both samples is assigned to 5-formylisophthalic acid, corresponding to the formula $[C_6H_3(COOH)_2(CHO)−H]^−$: expected = 193.02, found = 193.01. The peak at m/z 209.01 is assigned to H$_3$BTC, corresponding to the formula $[C_6H_3(COOH)_3−H]^−$: expected = 209.02, found= 209.01. The peak at m/z 403.03 is assigned to the trioxolane intermediate, $[C_{18}H_{12}O_{11}−H]^−$: expected = 403.04, found = 403.03. Altogether, these results confirm that, under these suspension-gas conditions, ozonolysis could not fully cleave the olefinic bonds. Moreover, the trioxolane intermediate was also detected.

To address the above drawbacks, the two ozonolysis strategies were combined by first running a solid–gas reaction for 2 h and then, cleaving the remaining alkene bonds via suspension/gas reaction for an additional 6 h. Under these conditions, olefinic bonds were able to be quantitatively cleaved, which has been proven by a series of characterizations including SCXRD, ^{1}H NMR and mass spectrometry.

SCXRD of the resulting crystals confirmed quantitative single-crystal-to-single-crystal cleavage of the olefinic bonds of Sc-**soc**-MOF to synthesize Sc-**pcu**-MOF (Figure 4.13b).[19] However, in this case, no changes were observed in the volume of the $R\bar{3}$ rhombohedral unit cell relative to that of the precursor, as also confirmed by PXRD (Figure 4.13c, more PXRD patterns see section 4.4.4). Nevertheless, SCXRD analysis showed a very similar case to that of ozonated Zr-**scu**-MOF. Thus, the connectivity of the atoms belonging to the inorganic trimeric ScO_3 clusters remained identical to that of the pristine Sc-**soc**-MOF (Figure 4.14).
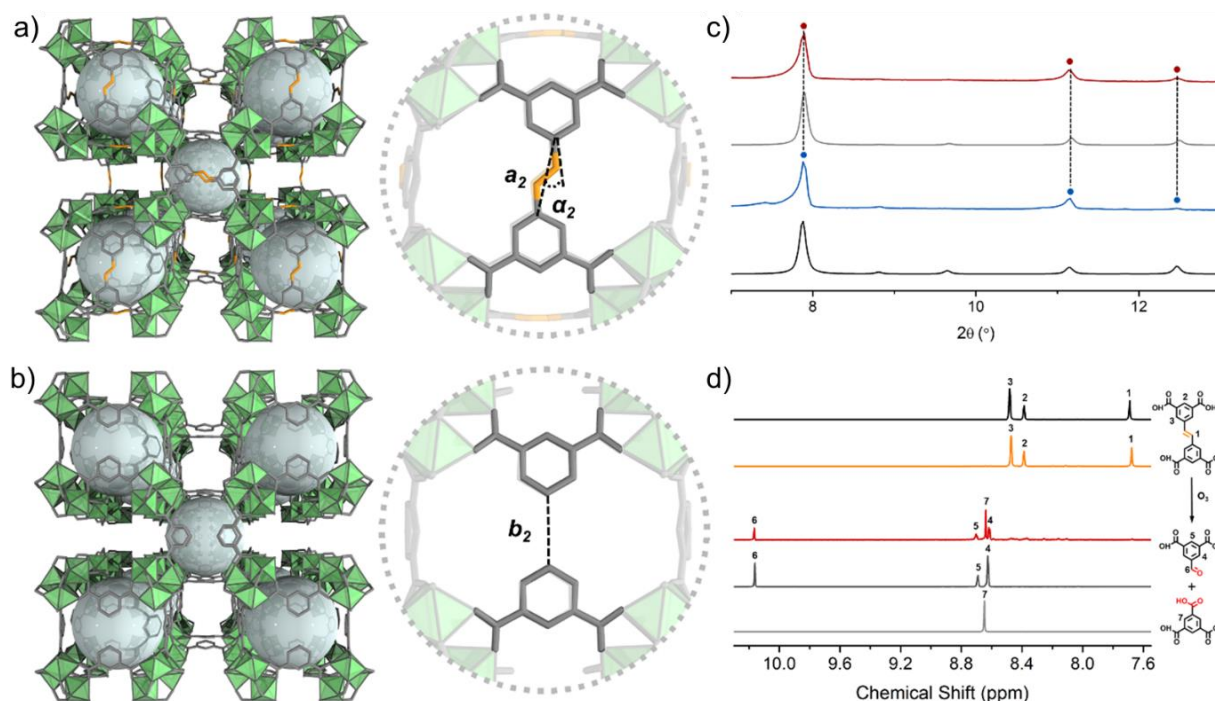
Figure 4.13 Structural and molecular characterization of Sc-**pcu**-MOF. (a,b) Crystal structures of isoreticular Sc-**soc**-MOF (a) and Sc-**pcu**-MOF (b). Magnified views highlight the changes observed in the distances and angles in both phenyl rings (from $a_2 = 3.82$-3.84 Å and $\alpha_2 = 15.63$-$17.34°$ to $b_2 = 3.62$-3.63 Å and $\beta_2 = 0°$) initially composing L_2. (c) Magnified view of the PXRD spectra for calculated Sc-**soc**-MOF (black), synthesized Sc-**soc**-MOF (blue), calculated Sc-**pcu**-MOF (grey) and synthesized Zr-**pcu**-MOF (red). (d) ^{1}H NMR spectra (360 MHz, DMSO-d_6) of digested L_2 (black), Sc-**soc**-MOF (orange), Sc-**pcu**-MOF (red), 5-formylisophthalic acid (dark grey) and trimesic acid (light grey).
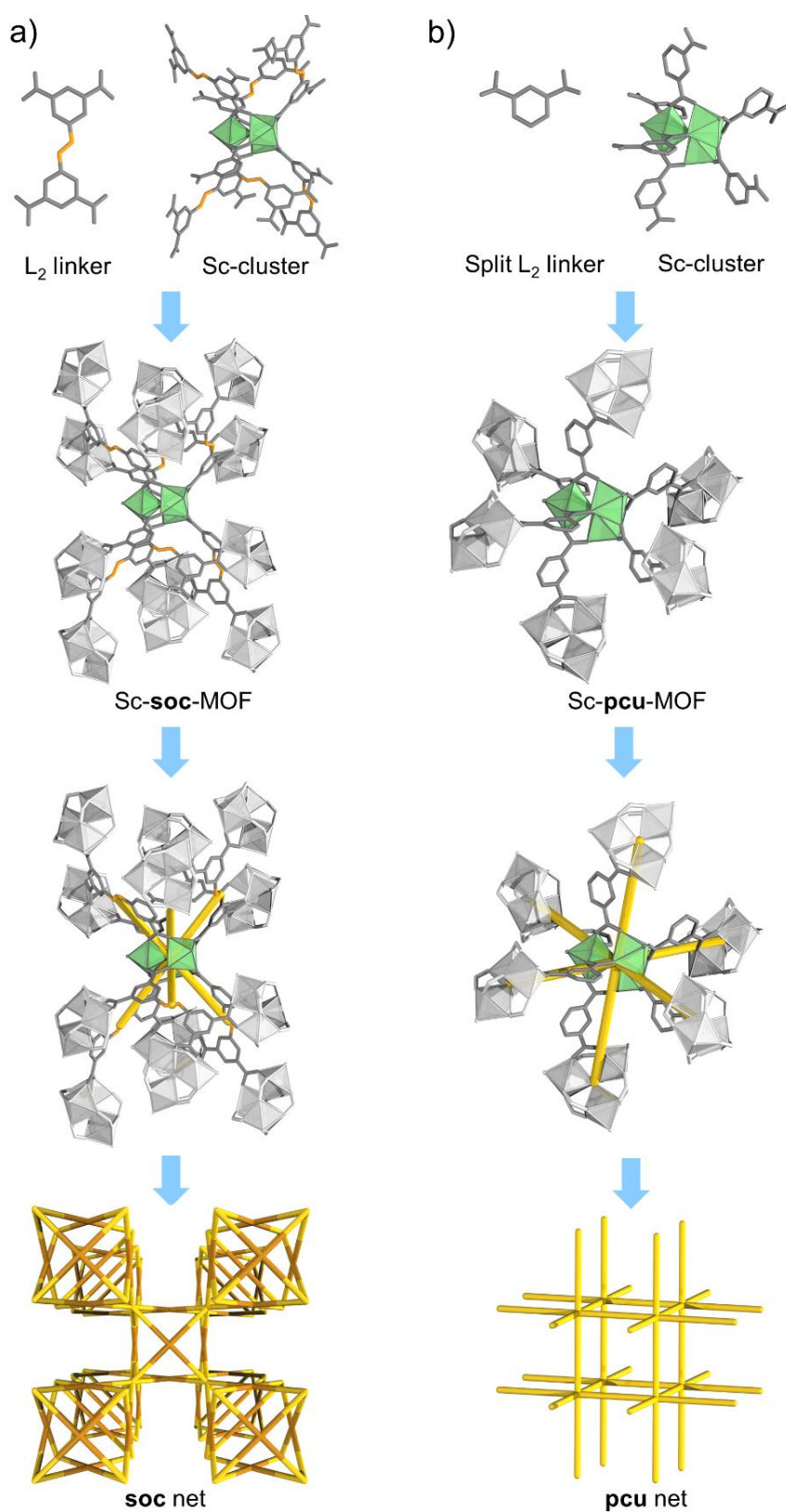
Figure 4.14 Comparison of the cluster environment in (a) Sc-**soc**-MOF and (b) Sc-**pcu**-MOF. In Sc-**soc**-MOF, each Sc_3O cluster is connected to 12 neighboring clusters by six 4-c linkers L_2. After clip-off treatment, each Sc_3O in Sc-**pcu**-MOF is surrounded by only 6 neighboring clusters, which are interconnected by six 2-c linkers.

Further refinement of the carbon atoms from the organic linkers evidenced a positional disorder for some of them, and, unlike Sc-**soc**-MOF, the Sc-**pcu**-MOF product did not contain any olefinic atoms. Instead, areas of electron density were observed only between the opposite phenyl rings, with a maximum value at the middle point between the two rings, but at a distance longer than that expected for a C=C bond. This area of higher electron-density points perpendicularly above and below the plane of the phenyl rings. Although the refinement indicates the presence of atoms in this area, these atoms could not be unambiguously assigned to aldehyde or carboxylate groups (Figure 4.15). These findings indicate that the functional groups are not arranged in an orderly fashion within the crystals after ozonolysis but are instead randomly oriented in the pores. This is not surprising, considering that the resulting aldehydes and/or carboxylic groups are randomly distributed and most likely dangle in different orientations into the pores, rather than having a periodically fixed position, such that they would not contribute to the periodic diffraction of the crystal.
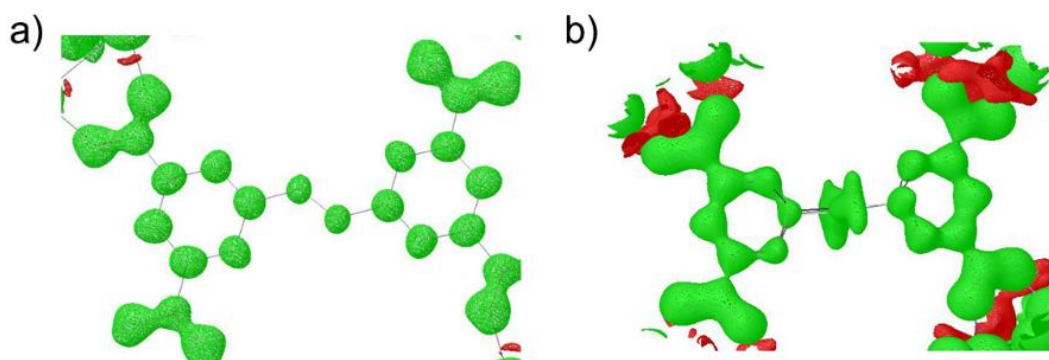
Figure 4.15 2Fo-Fc maps calculated for both (a) Sc-**soc**-MOF and (b) Sc-**pcu**-MOF, showing only presence of electron density above and below the plane of the phenyl rings, with no presence of the olefinic carbon atoms.

Consistent with these SCXRD data, cleavage of all olefinic bonds was confirmed by ^{1}H NMR (Figure 4.13d, more ^{1}H NMR spectra see section 4.4.4) and negative-mode mass spectrometry of the digested ozonated samples (5 % HF/DMSO-d_6) (Figure 4.16), and FTIR of ozonated Sc-**pcu**-MOF (Figure 4.17), from which the olefinic protons (δ=7.68 ppm), molecular ion [M−H]⁻ of L$_2$ and the typical alkene (C=C) stretching band, respectively, were not observed. On the contrary, the ^{1}H NMR signals, the molecular ions [M−H]⁻ and the carbonyl (C=O) stretching band corresponding to doubly deprotonated trimesic acid and 5-formylisophthalate were all clearly identifiable, thus further corroborating the clip-off synthesis of Sc-**pcu**-MOF.
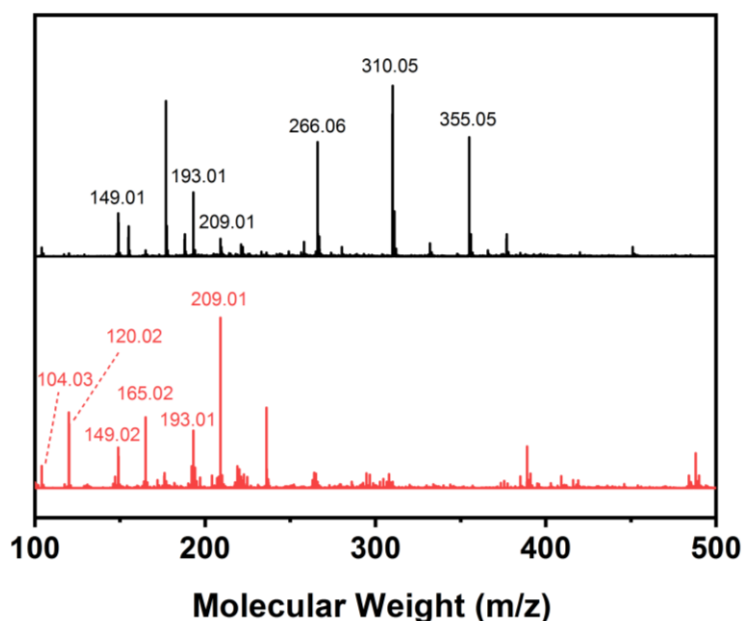
Figure 4.16 ESI-MS spectrometry of digested Sc-**soc**-MOF (black) and Sc-**pcu**-MOF (red). The peak at m/z 355.05 is assigned to [L$_2$−H]$^-$ in Sc-**soc**-MOF, corresponding to the formula [C$_{18}$H$_{12}$O$_8$−H]$^-$: expected = 355.05, found = 355.05. The peak at m/z 193.01 in both samples is assigned to 5-formylisophthalic acid, corresponding to the formula [C$_6$H$_3$(COOH)$_2$(CHO)−H]$^-$: expected = 193.02, found = 193.01. The peak at m/z 209.01 in both samples is assigned to trimesic acid, corresponding to the formula [C$_6$H$_3$(COOH)$_3$−H]$^-$: expected = 209.02, found = 209.01.
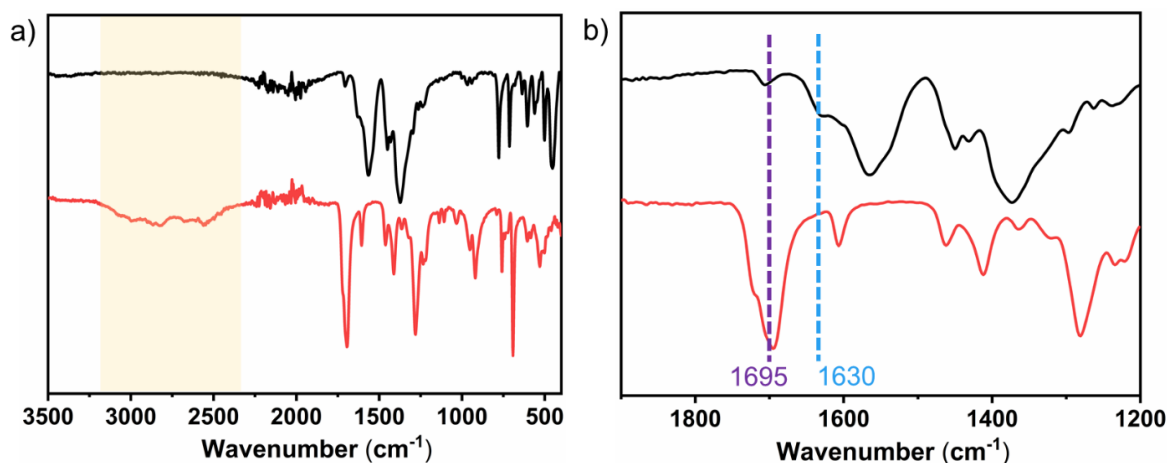
Figure 4.17 (a) Full FTIR spectra of Sc-**soc**-MOF (black), Sc-**pcu**-MOF (red) and (b) magnified area. In FTIR spectra, Sc-**pcu**-MOF displayed a broad band in the region of 3300-2500 cm^{-1}, which was not found in Sc-**soc**-MOF. This could be ascribed to the O-H stretching of the free carboxyl groups. The enhanced vibration signal of the stretching carbonyl (C=O) groups at 1695 cm^{-1} was seen in Sc-**pcu**-MOF. The olefinic bond, which has the characteristic absorbance at 1630 cm^{-1}, disappeared in Sc-**pcu**-MOF, demonstrating the total cleavage of linker L$_2$ from Sc-**soc**-MOF.

4.3 Conclusions

We have introduced Clip-off Chemistry, a new approach to synthesizing molecules and materials based on selective bond-breaking in reticular precursors materials via common organic transformations, via programmed de-reticulation and controlled etching at the molecular level. As proof-of-concept, we transformed two 3D MOFs (Zr-**scu**-MOF and Sc-**soc**-MOF) into two topologically distinct 3D MOFs (Zr-**pcu**-MOF and Sc-**pcu**-MOF, respectively). In the examples that we have reported here, we demonstrated that the cleavage was quantitative and selective; was effective both in solid-phase and solution-phase chemistry; and occurred in a single-crystal-to-single crystal fashion across the entire bulk precursor sample. Moreover, we demonstrated control over the cleavage of each olefinic bond into carboxylic acid groups using oxidative conditions.

Our preliminary results suggest that Clip-off Chemistry is ripe for further exploration. Since it is based on bond cleavage, the dimensionality of the parent reticular material dictates the synthetic feasibility of the target molecules and/or materials (Figure 4.18). Thus, it offers the possibility to modify structures of reticular materials without changing their dimensionality (*e.g.* 3D → 3D, or 2D → 2D). For example, one might employ Clip-off Chemistry for post-synthetic modification of the topology and/or the porosity of a given material. Moreover, it could be applied to 3D structures to augment the diversity of new 2D materials: for instance, by converting well-known 3D pillared reticular materials into isolated 2D layers, via selective clipping of the pillaring linkers. Similarly, it shows promise for using 3D or 2D structures to isolate 1D materials in the form of metallic chains, or to synthesize 0-D systems, including MOPs, macrocycles and clusters, from 3D/2D/1D structures and even from other 0-D systems (*e.g.* MOPs). Cleavage of bonds in reticular materials may also be expanded to purely organic structures. Indeed, COFs and organic cages are another endless source of precursors in Clip-off Chemistry for possible synthesis of organic polymers, cages, macrocycles or other organic compounds. Similarly, other reactions involving the cleavage of bonds (*e.g.* photolysis) are potential candidates to be applied in reticular materials for their programmable disassembly.[33-35] In summary, our results prove that the programmed disassembly of reticular materials is feasible, and that Clip-off Chemistry could provide researchers with access to myriad new molecular architectures.
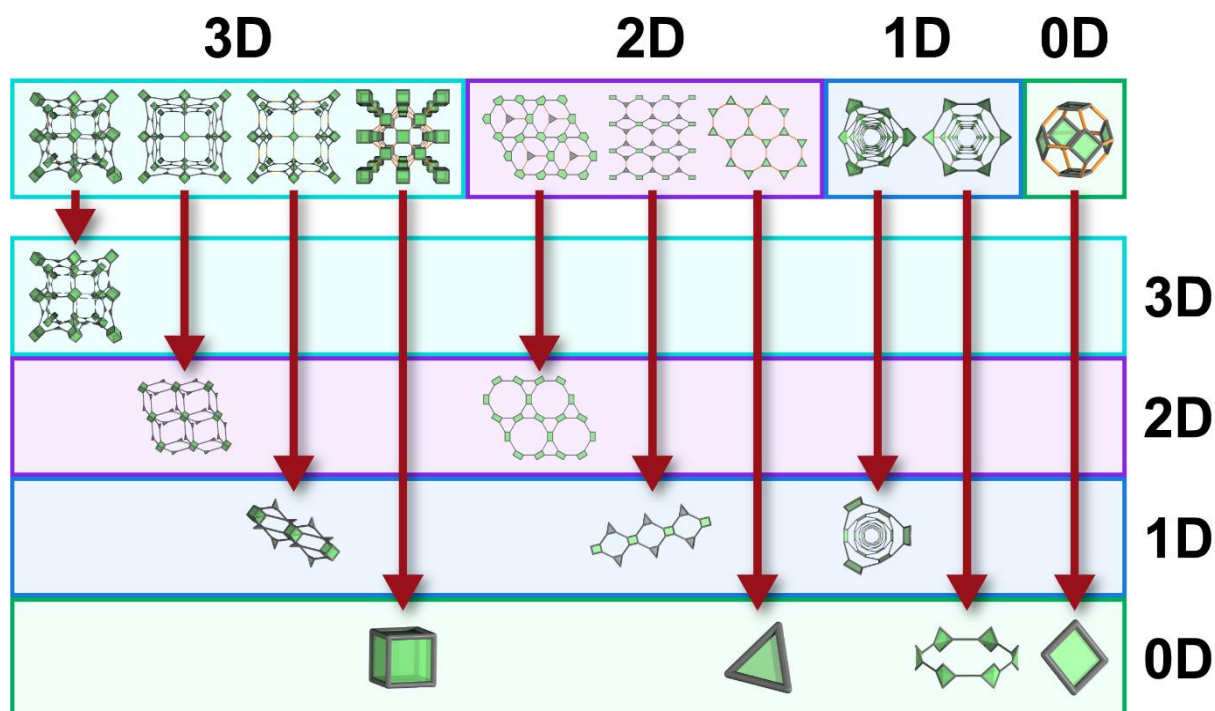
Figure 4.18 Clip-off Chemistry for the synthesis of molecular architectures of different dimensionality. Schematic illustrating the potential outcomes of Clip-off Chemistry, in which the dimensionality of the parent reticular material dictates the dimensionality of the target molecules and structures.

4.4 Experimental section

4.4.1 Chemicals and characterizations

Zirconium oxychloride octahydrate (ZrOCl$_2$·8H$_2$O), formic acid, potassium iodide (KI), scandium(III) nitrate hydrate, trimesic acid (H$_3$BTC), formic acid, anhydrous granular CaCl$_2$ (2-6 mm) and hydrogen peroxide 30 wt. % in H$_2$O were purchased from Sigma-Aldrich Co. *N,N*-dimethylformamide (DMF), absolute ethanol (EtOH) and tetrahydrofuran (THF), acetone were obtained from Fisher Chemical. 5-[(E)-2-(3,5-dicarboxyphenyl)ethenyl]benzene-1,3-dicarboxylic acid (linker L$_2$) was obtained from Chemextention Co. All the reagents and solvents were used without further purification unless otherwise specified. Deionized water was obtained with a Milli-Q® system (18.2 MΩ·cm). The ozone generator (model N1668A, 10.4 mmol/h O$_3$ at room temperature) was purchased from Ozonotec.

Powder X-Ray Diffraction (PXRD) data were collected on a Panalytical X'pert PRO MPD diffractometer with monochromatic Cu-Kα radiation (λ_{Cu} = 1.5406 Å). Proton Nuclear Magnetic Resonance (^{1}H NMR) spectra were acquired in Bruker Avance DPX of 250 MHz, 360 MHz NMR spectrometer at "Servei de Ressonància Magnètica Nuclear" from Autonomous University of Barcelona

(UAB). Field-emission Scanning Electron Microscopy (FESEM) images were performed in a SEM Quanta 650 scanning electron microscopy at an acceleration voltage of 2 KV, using aluminium as a support. Fourier Transform Infrared (FTIR) spectra were recorded on a Bruker Tensor 27FT-IR spectrometer equipped with a Golden Gate diamond attenuated total reflection (ATR) cell, in transmittance mode at room temperature. Electrospray Ionization Mass Spectrometry (ESI-MS) spectra were obtained in an Agilent 6210 G1969A LC/MSD TOF mass spectrometer. All the digested MOFs were measured in the negative-ionization mode. The samples for MS analysis were obtained from the ^{1}H NMR digestion samples.

Single-Crystal X-Ray Diffraction (SCXRD) data of Zr-**scu**-MOF, Zr-**pcu**-MOF, Sc-**soc**-MOF, Sc-**pcu**-MOF were collected at 100 K at BL13-XALOC beamline at the ALBA synchrotron ($\lambda = 0.82656$ Å).[36] Data for Rh-MOP was collected with a Bruker four-circle kappa diffractometer equipped with a Cu INCOATED microsource, operated at 50-W power (50 kV, 1.00 mA) to generate Cu Kα radiation ($\lambda = 1.54178$ Å), and a Bruker VANTEC-500 area detector (microgap technology). Data frames were indexed, integrated and scaled using the XDS program, and the APEX3 software.[37] The structures were solved by direct methods and subsequently refined by corrections of F^2 against all reflections, using SHELXST2013[38] and SHELXL2013[39] within the Olex2 package.[40] Non-hydrogen atoms were refined with anisotropic thermal parameters by full-matrix least-squares calculations on F^2 using the program SHELXL2013. Hydrogens atoms were inserted at calculated positions and constrained with isotropic thermal parameters.

4.4.2 Synthetic procedures

Synthesis of Zr-scu-MOF. A solution of ZrOCl$_2$·8H$_2$O (16 mg, 0.05 mmol) and L$_2$ (7 mg, 0.02 mmol) in DMF (8 mL) and formic acid (8 mL) was prepared in a 23 mL scintillation vial. Then, the sealed vial was placed into a preheated oven at 120 ºC for 5 days. After this period, colourless cubic crystals suitable for single-crystal X-ray diffraction (SCXRD) were collected by filtration and washed three times by incubating them with 20 mL of fresh DMF for 12 h. Afterwards, solvent exchange with THF was performed by incubating the crystals three times with 20 mL of THF for 12 h, and the resulting Zr-**scu**-MOF crystals were dried at room temperature (15 mg).

Clip-off synthesis of Zr-pcu-MOF *via* ozonolysis. The synthesis of Zr-**pcu**-MOF was achieved by a solid-gas ozonolysis reaction. This reaction started by packing 20 mg of Zr-**scu**-MOF crystals into a plastic tube, connected on one side to the ozonator (through a CaCl$_2$ humidity trap), and on the other side, to a vacuum pump (through a KI trap), to ensure a continuous flow of ozone through the column. The reaction was run at room temperature for 30 min. Afterwards, the sample was held in vacuum for another 30 min. This ozonation/vacuum cycle was repeated nine times. Finally, the resulting solid (20 mg) was directly collected from the plastic tube and stored in THF.

Oxidation of Zr-pcu-MOF to full –COOH pending groups. Dried ozonated crystals were soaked in 1 mL of aqueous H_2O_2 solution (30 wt. % in H_2O) for 3 weeks. During this period, the sample was exchanged with a fresh hydrogen peroxide solution every 24 h. After that, the sample was centrifuged and washed twice with water.

Synthesis of Sc-soc-MOF. A solution of $Sc(NO_3)_3 \cdot xH_2O$ (48 mg, 0.21 mmol) and L_2 (16 mg, 0.04 mmol) in DMF (8 mL), EtOH (3.2 mL) and formic acid (1.84 mL) was prepared in a 23 mL scintillation vial. Then, the sealed vial was placed into a preheated oven at 120 ºC for 48 h. Colourless cubic crystals suitable for SCXRD were collected by filtration and washed three times by incubating them with 20 mL of fresh DMF for 12 h. Afterwards, solvent exchange with acetone was performed by incubating the crystals three times with 20 mL of acetone for 12 h, and the resulting crystals were dried at room temperature (20 mg).

Clip-off synthesis of Sc-pcu-MOF *via* ozonolysis. The clip-off synthesis of Sc-**pcu**-MOF was done in two steps: a first step consisting of a solid-gas ozonolysis reaction; and a second step based on a suspension-gas ozonolysis reaction. In the first step, 20 mg of synthesized Sc-**soc**-MOF crystals were packed into the plastic tube, connected on one side to the ozonator (through a $CaCl_2$ humidity trap), and on the other side, to a vacuum pump (through a KI trap). The reaction was run at room temperature for 2 hours. Afterwards, the crystals were collected from the plastic tube and suspended in 4 ml of water. The ozone generator was directly connected to the vial through a syringe. Ozone was bubbled in the suspension for 6 h while magnetically stirring at 880 rpm. The resulting crystals (20 mg) were collected by centrifugation and stored in acetone.

4.4.3 Characterization: from Zr-scu-MOF to Zr-pcu-MOF

Single-crystal XRD analysis

Diffraction data for Zr-**scu**-MOF and Zr-**pcu**-MOF was collected at the BL13-XALOC beamline at the ALBA synchrotron with $\lambda = 0.82653$ Å. All tested specimens were found to be grown as twinned crystals, and they could not be separated as single components. Best results were obtained by indexing and reducing the data with the cell parameters corresponding to a single component, although with unavoidable presence of a number of overlying reflections, which eventually resulted in high refinement residual values, and negative anisotropic displacement parameters for some atoms. Nonetheless, the structure could be solved, and the location of the framework atoms unambiguously determined, confirming the formation of the isoreticular Zr-**scu**-MOF.

Table 4.1 Crystal data and structure refinement for Zr-**scu**-MOF.

Identification code	CCDC-2080949	
Formula	$C_{72}O_{64}Zr_{12}$	
Formula weight (g.mol^{-1})	2983.36	
Temperature (K)	100(2)	
Wavelength (Å)	0.82653	
Crystal system	Monoclinic	
Space group	*C2/m*	
Unit cell dimensions	$a = 25.637(5)$Å	$\alpha = 90°$
	$b = 36.223(7)$ Å	$\beta = 122.54(3)°$
	$c = 21.661(4)$ Å	$\gamma = 90°$
Volume (Å^3)	16958(8)	
Z	4	
Density calculated (g/cm^{-3})	1.169	
Absorption coefficient (mm^{-1})	1.157	
F(000)	5696.0	
Crystal size (mm)	$0.33 \times 0.30 \times 0.30$ mm	
2Theta range for data collection (°)	2.594 to 58.182	
Index ranges	$-30 \leq h \leq 25, 0 \leq k \leq 42, 0 \leq l \leq 25$	
Reflection collected	44506	
Independent reflections	14607 [Rint = 0.0968, Rsigma = 0.1369]	
Refinement method	Full-matrix least-squares on F^2	
Data / restraints / parameters	14607/114/556	
Goodness-of-fit on F^2	1.942	
Final R indices [I>2sigma(I)]	$R_1 = 0.1983$, $wR_2 = 0.4825$	
R indices (all data)	$R_1 = 0.2125$, $wR_2 = 0.5069$	
Largest diff. peak and hole	8.61, -6.78e.Å^{-3}	

Table 4.2 Crystal data and structure refinement for Zr-**pcu**-MOF.

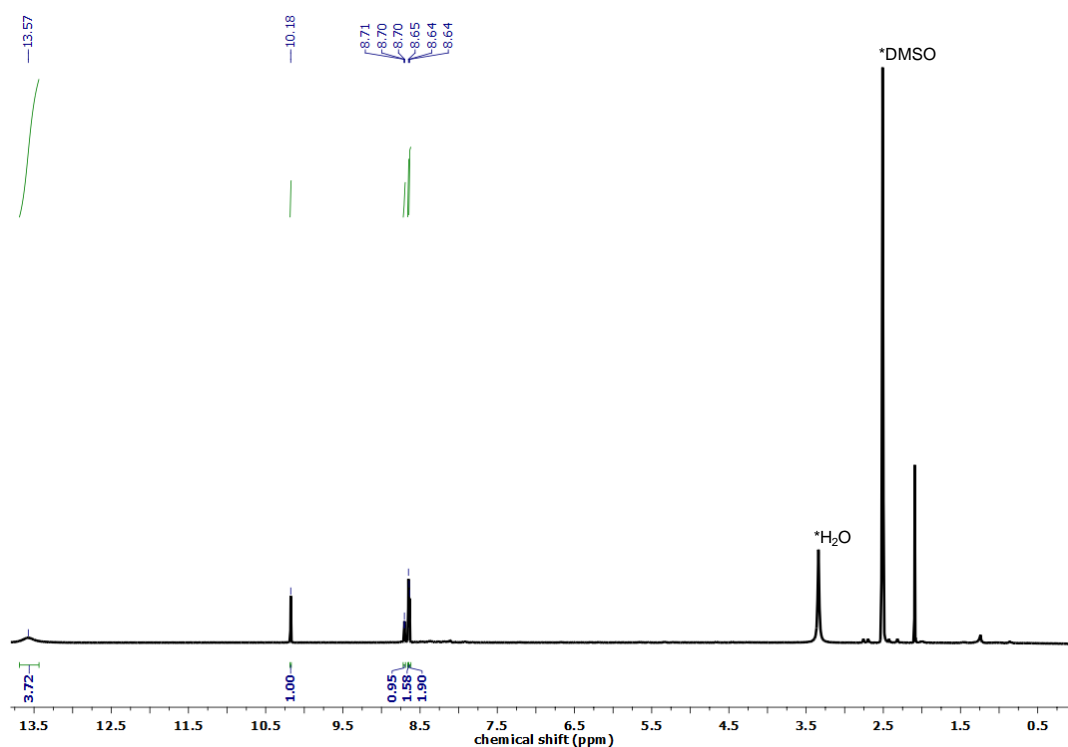|	
Identification code	CCDC-2080950
Formula	$C_{71.25}O_{67.5}Zr_{12}$
Formula weight (g.mol^{-1})	3030.35
Temperature (K)	100(2)
Wavelength (Å)	0.82653
Crystal system	Monoclinic
Space group	*C2/m*
Unit cell dimensions	$a = 35.703(7)$Å $\quad$ $\alpha = 90°$
	$b = 25.210(5)$ Å $\quad$ $\beta = 134.89(3)°$
	$c = 25.210(5)$ Å $\quad$ $\gamma = 90°$
Volume (Å^3)	16076(8)
Z	4
Density calculated (g/cm^{-3})	1.252
Absorption coefficient (mm^{-1})	0.812
F(000)	5790.0
Crystal size (mm)	$0.38 \times 0.32 \times 0.32$ mm
2Theta range for data collection (°)	2.28 to 34.45
Index ranges	$-29 \leq h \leq 29$, $-20 \leq k \leq 20$, $-20 \leq l \leq 20$
Reflection collected	28412
Independent reflections	4867 [Rint = 0.1337, Rsigma = 0.0877]
Refinement method	Full-matrix least-squares on F^2
Data / restraints / parameters	4867/0/513
Goodness-of-fit on F^2	1.336
Final R indices [I>2sigma(I)]	$R_1 = 0.1277$, $wR_2 = 0.3291$
R indices (all data)	$R_1 = 0.1736$, $wR_2 = 0.3849$
Largest diff. peak and hole	1.13, -0.76 e.Å^{-3}

PXRD
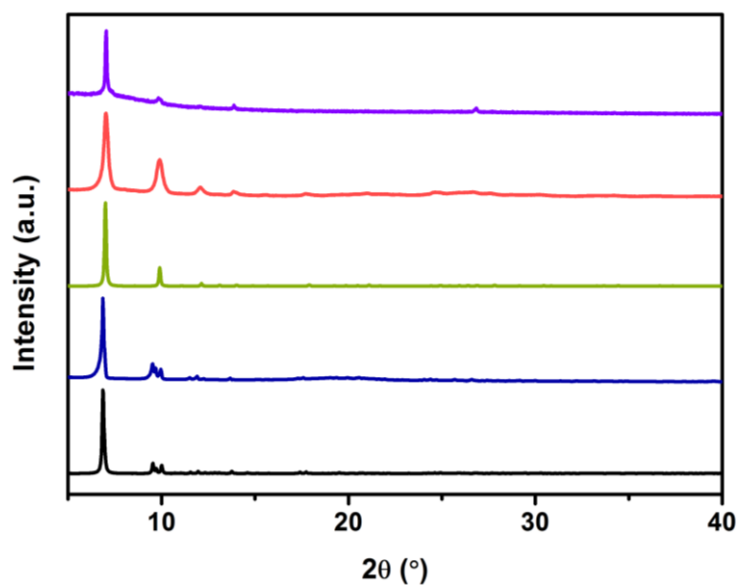
Figure 4.19 PXRD of calculated Zr-**scu**-MOF (black), pristine Zr-**scu**-MOF (blue), calculated Zr-**pcu**-MOF (green), synthesized Zr-**pcu**-MOF (red) and oxidized Zr-**pcu**-MOF (purple).

¹H NMR
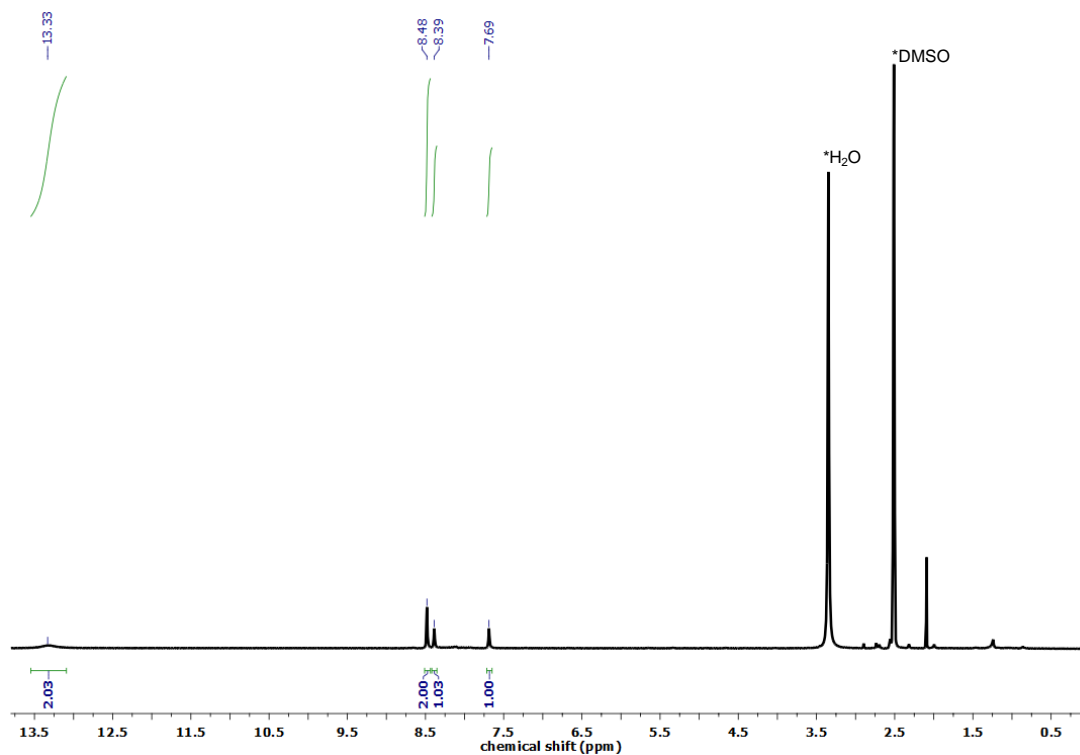
Figure 4.20 ¹H NMR spectrum (360 MHz, DMSO-d_6) of the digested Zr-**scu**-MOF. Zr-**scu**-MOF crystals were digested in 5% HF aqueous solutions at 120 ℃ overnight.

Figure 4.21 ^{1}H NMR spectrum (360 MHz, DMSO-d_6) of the digested Zr-**pcu**-MOF after ozonolysis solid reaction. Zr-**pcu**-MOF crystals were digested in 5% HF aqueous solutions at 120 ℃ overnight.

Figure 4.22 ^{1}H NMR spectrum (360 MHz, DMSO-d_6) of the digested oxidized Zr-**pcu**-MOF. Zr-**pcu**-MOF crystals were digested in 5% HF aqueous solutions at 120 ℃ overnight.

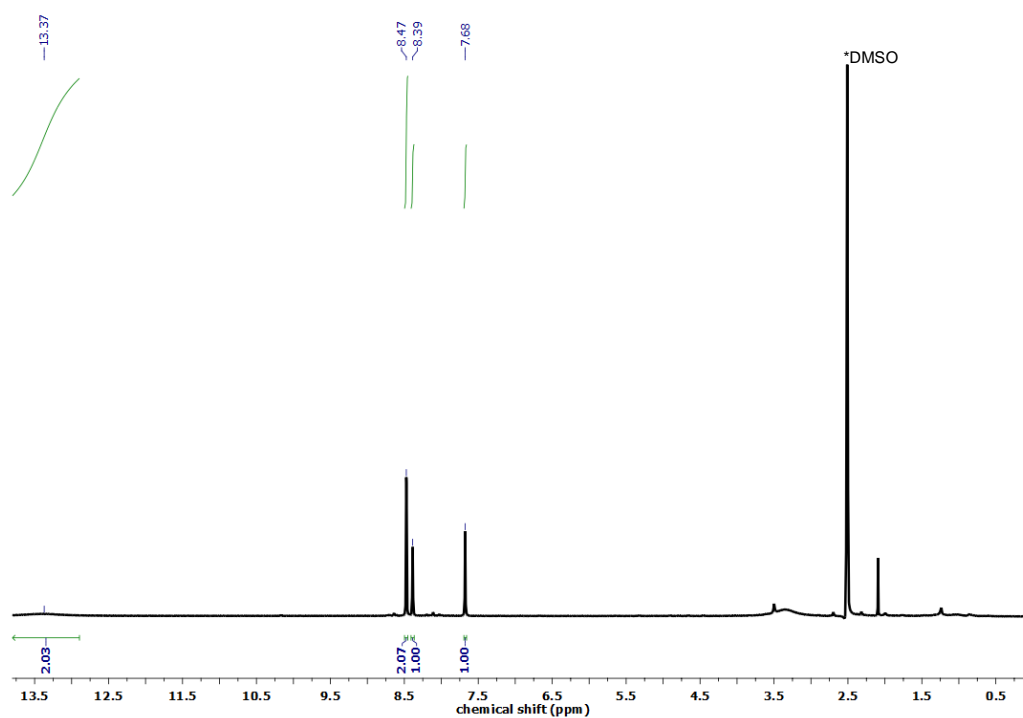**Figure 4.23** ^{1}H NMR spectrum (360 MHz, DMSO-d_6) of the digested Sc-**soc**-MOF. Sc-**soc**-MOF crystals were digested in 5% HF aqueous solutions at 120 ℃ overnight.

Figure 4.24 ^{1}H NMR spectrum (360 MHz, DMSO-d_6) of the digested Sc-**soc**-MOF after solid-gas ozonolysis reaction for 8 h. The resulting crystals were digested in 5% HF aqueous solutions at 120 ℃ overnight.

Figure 4.25 ^{1}H NMR spectrum (360 MHz, DMSO-d_6) of the digested Sc-**soc**-MOF after 12 cycles of solid-gas ozonolysis reaction. The resulting crystals were digested in 5% HF aqueous solutions at 120 °C overnight.

4.4.4 Characterization: from Sc-soc-MOF to Sc-pcu-MOF

Single-crystal XRD analysis

Table 4.3 Crystal data and structure refinement for Sc-**soc**-MOF.

Identification code	CCDC-2080951
Formula	$C_{108}O_{64}Sc_{12}$
Formula weight (g.mol^{-1})	2860.60
Temperature (K)	100
Wavelength (Å)	0.82653
Crystal system	Trigonal
Space group	*R -3*
Unit cell dimensions	$a = 31.750(5)$ Å $\quad$ α = 90º
	$b = 31.750(5)$ Å $\quad$ β = 90º
	$c = 38.800\ (5)$ Å $\quad$ γ = 120º
Volume (Å^3)	33872.7
Z	6
Density calculated (g/cm^{-3})	0.842
Absorption coefficient (mm^{-1})	0.594
F(000)	8480
Crystal size (mm)	$0.27 \times 0.23 \times 0.21$ mm
2Theta range for data collection (º)	2.584 to 24.409
Index ranges	-31<=h<=31, -31<=k<=31, -38<=l<=38
Reflection collected	78341
Independent reflections	7872 [Rint = 0.0448, Rsigma = 0.0741]
Refinement method	Full-matrix least-squares on F^2
Data / restraints / parameters	7872 / 0 / 548
Goodness-of-fit on F^2	1.161
Final R indices [I>2sigma(I)]	$R_1 = 0.0998$, $wR_2 = 0.2812$
R indices (all data)	$R_1 = 0.1047$, $wR_2 = 0.2870$
Largest diff. peak and hole	0.949, -1.316 e.Å^{-3}

Table 4.4 Crystal data and structure refinement for Sc-**pcu**-MOF.

Identification code	CCDC-2080952
Formula	$C_{31.75}O_{21.83}Sc_4$
Formula weight (g.mol^{-1})	910.49
Temperature (K)	293(2)
Wavelength (Å)	0.82653
Crystal system	Trigonal
Space group	*R -3*
Unit cell dimensions	a = 31.650(5) Å $\quad$ α = 90º
	b = 31.650(5) Å $\quad$ β = 90º
	c = 38.763(8) Å $\quad$ γ = 120º
Volume (Å^3)	33628 (12)
Z	18
Density calculated (g/cm^{-3})	0.809
Absorption coefficient (mm^{-1})	0.392
F(000)	8085
Crystal size (mm)	$0.21 \times 0.18 \times 0.17$ mm
2Theta range for data collection (º)	0.910 to 20.797
Index ranges	-31<=h<=31, -31<=k<=31, -38<=l<=38
Reflection collected	74052
Independent reflections	7822 [Rint=0.0494, Rsigma = 0.0241]
Refinement method	Full-matrix least-squares on F^2
Data / restraints / parameters	7822 / 0 / 539
Goodness-of-fit on F^2	2.036
Final R indices [I>2sigma(I)]	R_1 = 0.1497, wR_2 = 0.4331
R indices (all data)	R_1 = 0.1610, wR_2 = 0.4579
Largest diff. peak and hole	0.559, -0.530 e.Å^{-3}
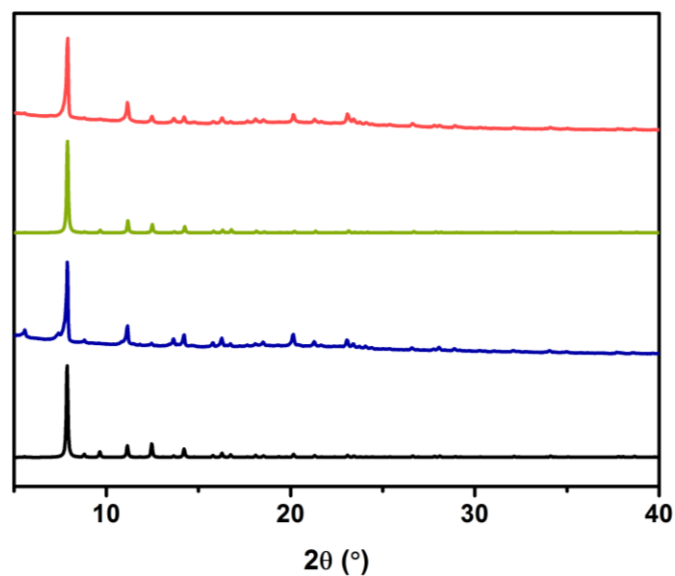
PXRD

Figure 4.26 PXRD of calculated Sc-**soc**-MOF (black), pristine Sc-**soc**-MOF (blue), calculated Sc-**pcu**-MOF (green) and synthesized Sc-**pcu**-MOF (red).

^{1}H NMR
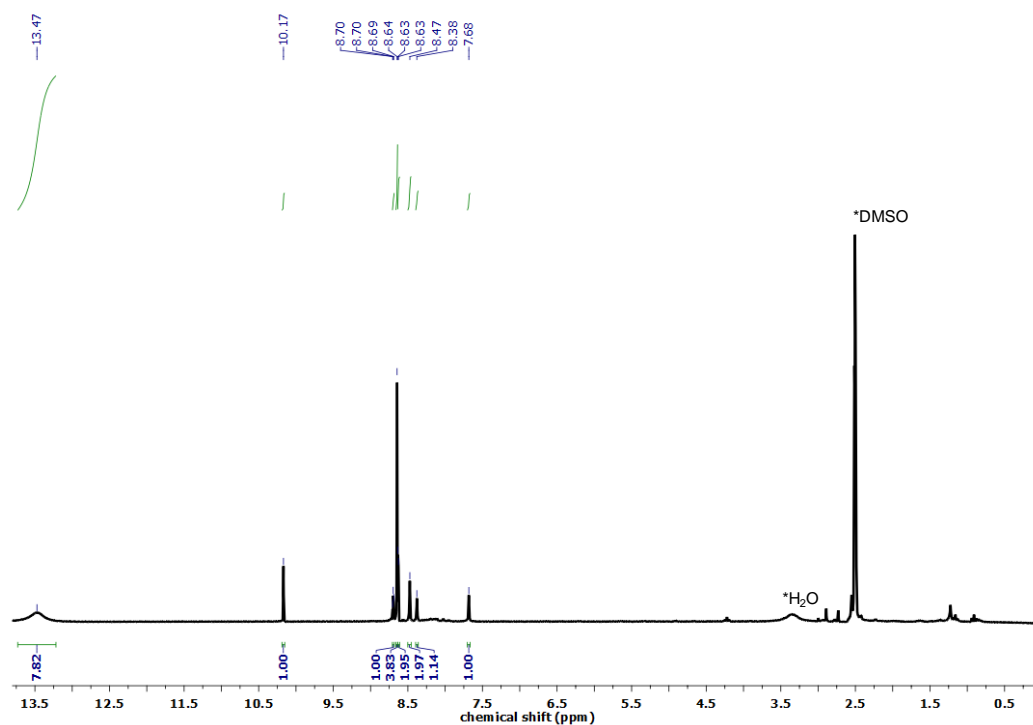
Figure 4.27 ^{1}H NMR spectrum (360 MHz, DMSO-d_6) of the digested Sc-**soc**-MOF after the solid-gas ozonolysis reaction for 2 h. Sc-**soc**-MOF crystals were digested in 5% HF aqueous solutions at 120 ℃ overnight.
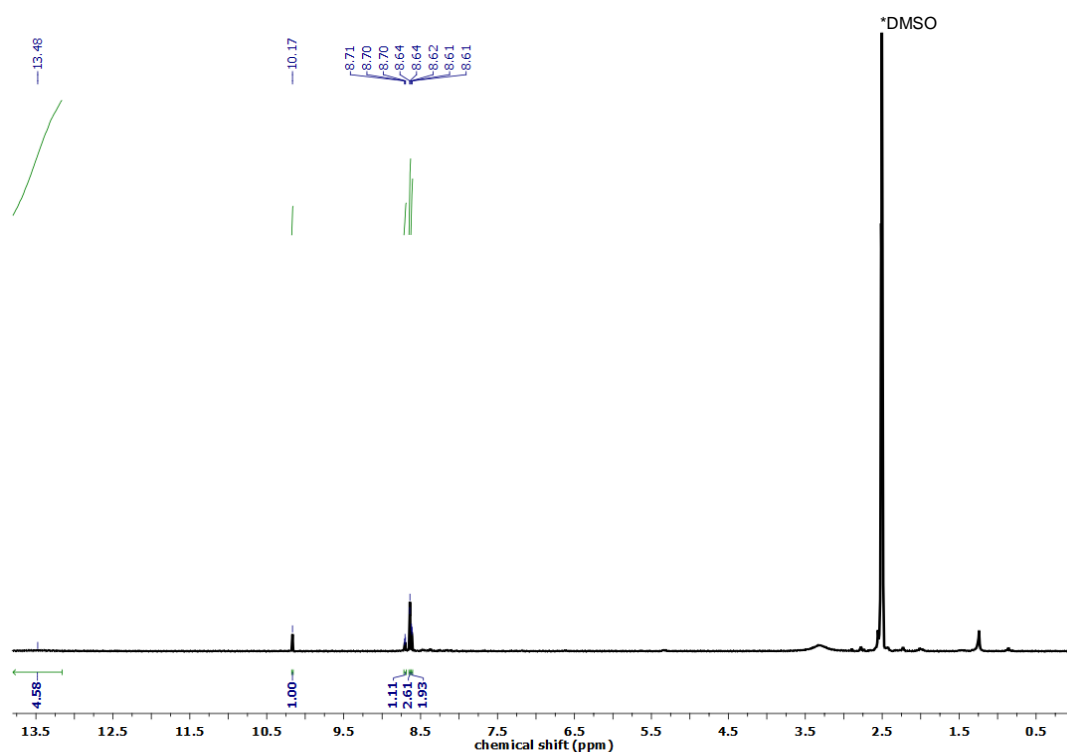
Figure 4.28 ^{1}H NMR spectrum (360 MHz, DMSO-d_6) of the digested Sc-**pcu**-MOF synthesized after the two-step ozonolysis reaction (solid-gas ozonolysis for 2 h and suspension-gas ozonolysis for 6 h). Sc-**pcu**-MOF crystals were digested in 5% HF aqueous solutions at 120 ℃ overnight.
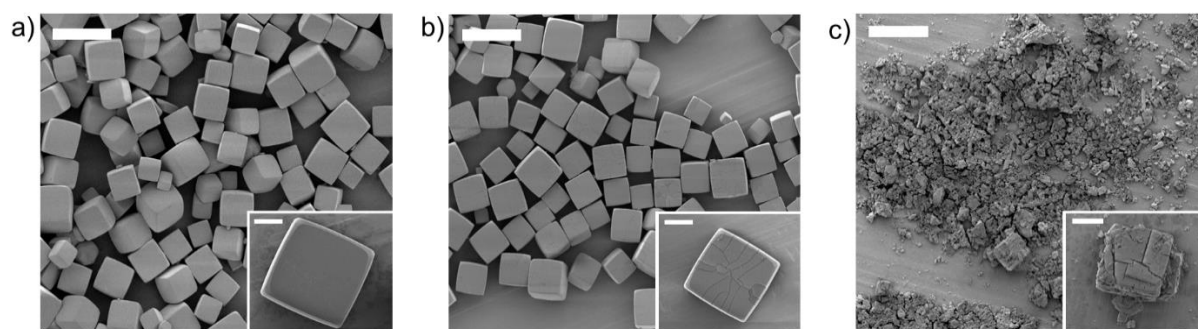
FESEM

Figure 4.29 FESEM images of (a) Sc-**soc**-MOF, (b) Sc-**soc**-MOF after the solid-gas ozonolysis for 2 h, and (c) Sc-**pcu**-MOF synthesized after solid-gas and suspension-gas ozonolysis. Scale bars: 50 μm (a-c) and 10 μm (insets). The FESEM images revealed that, after the solid-gas ozonolysis reaction for 2 h, the surface of Sc-**soc**-MOF crystals suffered some degree of cracking. Moreover, after the suspension-gas ozonolysis step, the crystals were broken into smaller crystals. These transformations did not change their single-crystals character, which enabled to collect SCXRD data for the fully ozonized sample.

4.5 References

(1) Li, H.; Eddaoudi, M.; Groy, T. L.; Yaghi, O. M. *J. Am. Chem. Soc.* **1998**, *120*, 8571−8572.

(2) Yaghi, O. M.; O'Keeffe, M.; Ockwig, N. W.; Chae, H. K.; Eddaoudi, M.; Kim, J. *Nature* **2003**, *423*, 705−714.

(3) Li, H.; Eddaoudi, M.; O'Keeffe, M; Yaghi, O. M. *Nature* **1999**, *402*, 276−279.

(4) Yaghi, O. M.; Li, G.; Li, H. *Nature* **1995**, *378*, 703−706.

(5) Kitagawa, S.; Kitaura, R.; Noro, S. *Angew. Chem. Int. Ed.* **2004**, *43*, 2334−2375.

(6) Abrahams, B. F.; Hoskins, B. F.; Michail, D. M.; Robson, R. *Nature* **1994**, *369*, 727−729.

(7) Hoskins, B. F; Robson, R. *J. Am. Chem. Soc.* **1989**, *111*, 5962−5964.

(8) Yaghi, O. M.; Kalmutzki, M. J.; Diercks, C. S. *Introduction to Reticular Chemistry: Metal-Organic Frameworks and Covalent Organic Frameworks*; Wiley, 2019.

(9) Feng, X.; Ding, X.; Jiang, D. *Chem. Soc. Rev.* **2012**, *41*, 6010−6022.

(10) Tranchemontagne, D. J.; Ni, Z.; O'Keeffe, M.; Yaghi, O. M. *Angew. Chem. Int. Ed.* **2008**, *47*, 5136−5147.

(11) Perry IV, J. J.; Perman, J. A.; Zaworotko, M. J. *Chem. Soc. Rev.* **2009**, *38*, 1400−1417.

(12) Lee, S.; Jeong H.; Nam, D.; Lah, M. S.; Choe, W. *Chem. Soc. Rev.* **2021**, *50*, 528−555.

(13) Eddaoudi, M.; Moler, D. B.; Li., H.; Chen, B.; Reineke, T. M.; O'Keeffe, M.; Yaghi, O. M. *Acc. Chem. Res.* **2001**, *34*, 319−330.

(14) Eddaoudi, M.; Kim, J.; Rosi, N.; Vodak, D.; Wachter, J.; O'Keeffe, M.; Yaghi, O. M. *Science* **2002**, *295*, 469−472.

(15) Cohen, S. M. *Chem. Rev. 2012*, *112*, 970−1000.

(16) Yaghi, O. M. *Mol. Front. J.* **2019**, *3*, 66−83.

(17) O'Keeffe, M.; Yaghi, O. M. *Chem. Rev.* **2012**, *112*, 675−702.

(18) O'Keeffe, M.; Peskov, M. A.; Ramsden, S. J.; Yaghi, O. M. *Acc. Chem. Res.* **2008**, *41*, 1782−1789.

(19) Blatov, V. A.; Shevchenko, A. P.; Proserpio, D. M. *Cryst. Growth Des.* **2014**, *14*, 3576−3586.

(20) Wells, A. F. *Three-Dimensional Nets and Polyhedral;* Wiley, 1977.

(21) Wang, H.; Dong, X.; Lin, J.; Teat, S. J.; Jensen, S.; Cure, J.; Alexandrov, E. V.; Xia, Q.; Tan, K.; Wang, Q.; Olson, D. H.; Proserpio, D. M.; Chabal, Y. J.; Thonhauser, T.; Sun, J.; Han, Y.; Li, J. *Nat. Commun.* **2018**, *9*, 1745.

(22) Li, M.; Li, D.; O'Keeffe, M.; Yaghi, O. M. *Chem. Rev.* **2014**, *114*, 1343−1370.

(23) Albalad, J.; Xu, H.; Gándara, F.; Haouas, M.; Martineau-Corcos, C.; Mas-Ballesté, R.; Barnett, S. A.; Juanhuix, J.; Imaz, I.; Maspoch, D. *J. Am. Chem. Soc.* **2018**, *140*, 2028−2031.

(24) Guillerm, V.; Xu, H.; Albalad, J.; Imaz, I.; Maspoch, D. *J. Am. Chem. Soc.* **2018**, *140,* 15022−15030.

(25) Criegee, R. *Angew. Chem. Int. Ed.* **1975**, *14*, 745−752.

(26) Schiaffo, C. E.; Dussault, P. H. *J. Org. Chem.* **2008**, *73*, 4688−4690.

(27) Harding, L. B.; Goddard, A. W. *J. Am. Chem. Soc.* **1978**, *100*, 7180−7188.

(28) Xie, L. H.; Liu, X. M.; He, T.; Li, J. R. *Chem* **2018**, *4*, 1911−1927.

(29) Wang, S.; Chen, L.; Wahiduzzaman, M.; Tissot, A.; Zhou, L.; Ibarra, I. A.; Gutiérrez-Alejandre, A.; Lee, J. S.; Chang, J. S.; Liu, Z.; Marrot, J.; Shepard, W.; Maurin, G.; Xu, Q.; Serre, C. *Matter* **2021**, *4*, 182−194.

(30) Furukawa, H.; Gándara, F.; Zhang, Y. B.; Jiang, J.; Queen, W. L.; Hudson, M. R.; Yaghi, O. M. *J. Am. Chem. Soc.* **2014**, *136*, 4369−4381.

(31) Zhang, J. W.; Qu, P.; Hu, M. C.; Li, S. N.; Jiang, Y. C.; Zhai, Q. G. *Inorg. Chem.* **2019**, *58*, 16792−16799.

(32) Liu, Y.; Eubank, J. F.; Cairns, A. J.; Eckert, J.; Kravtsov, V. C.; Luebke, R.; Eddaoudi, M. *Angew. Chem. Int. Ed.* **2007**, *46*, 3278−3283.

(33) Feng, L.; Wang, K. Y.; Day, G. S.; Ryder, M. R.; Zhou, H. C. *Chem. Rev.* **2020**, *120*, 13087−13133.

(34) Wang, K. W.; Feng, L.; Yan, T. H.; Wu, S.; Joseph, E. A.; Zhou, H. C. *Angew. Chem. Int. Ed.* **2020**, *59*, 11349−11354.

(35) Shieh, P.; Hill, M. R.; Zhang, W.; Kristufek, S. L.; Johnson, J. A. *Chem. Rev.* **2021**, 0c01282.

(36) Juanhuix J.; Gil-Ortiz F.; Cuní G.; Colldelram C.; Nicolás J.; Lidón J.; Boter E.; Ruget C.; Ferrer S.; Benach J. *J. Synchrotron Radiat.* **2014**, *21*, 679–689.

(37) Kabsch W. *Acta Cryst. D* **2010**, *66*, 125–132.

(38) Sheldrick G. M. IUCr, *Acta Cryst. A* **2015**, *71*, 3–8.

(39) Sheldrick G. M. IUCr, *Acta Cryst. C* **2015**, *71*, 3–8.

(40) Dolomanov O. V.; Bourhis L. J.; Gildea R. J.; Howard J. A. K.; Puschmann H. *J. Appl. Cryst.* **2009**, *42*, 339–341.

Chapter 5

Isoreticular Contraction of Metal–Organic Frameworks Induced by Cleavage of Covalent Bonds
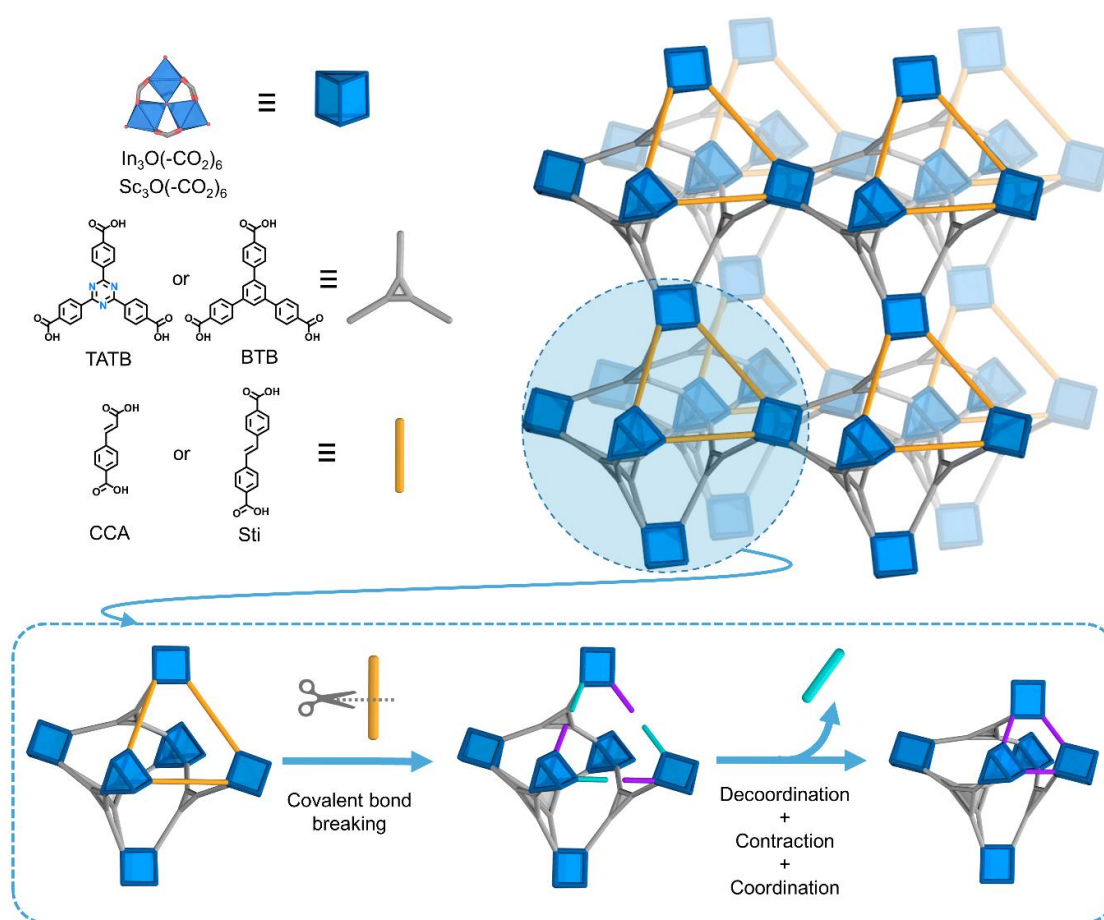
5.1 Introduction

MOFs are a class of crystalline materials assembled by combining inorganic metal-based nodes with organic linkers, which exhibit long-range ordered structures with permanent porosity.[1,2] Given the nearly infinite possible permutations of their building blocks, MOFs are highly versatile: they can be designed to have distinctive features such as an exceptionally large surface area and adjustable pore sizes.

The design and synthesis of MOFs have been expanded by reticular chemistry, which provides high levels of chemical control. This is achieved mainly by either of two strategies: (i) predesign of a novel target net through judicious design of the molecular building blocks or (ii) use of a known net as a blueprint for a novel material, designed by applying the isoreticular principle.[3-6] The primary aim of isoreticular chemistry is to tune or functionalize the organic or inorganic moieties without altering their underlying nets. Thus, it has proven invaluable for modulating the properties of MOFs and for optimizing their performance in myriad applications. Isoreticular MOFs can be synthesized by common direct synthesis[7-9] or by postsynthetic modification (PSM). PSM-based methodologies to synthesize isoreticular MOFs include linker functionalization, transmetalation, sequential linker installation, and solvent-assisted linker exchange (SALE).[10-12] Among these, SALE is based on substitution of a linker that bridges two metal ions/clusters, with an external linker, in the presence of a solvent. This enables generation of new isoreticular MOFs: for example, ones in which interpenetration can be controlled[13,14] or that can exhibit nondefault topologies.[15] In SALE, replacement is performed chiefly by using external linkers whose length is equal to or greater than that of the original linkers, thereby affording a lattice of the same or greater size.[16-18] Alternatively, a few studies have shown that the framework can also be contracted, by using shorter linkers, although this approach has not been widely explored.[14,19,20] The contraction of lattices can also confer the resultant MOFs[21] with unusual properties such as negative and stepwise gas-adsorption, modulation of the radical spin stated in solid state, or stimuli responsiveness and selectivity, which can be utile for applications such as gas storage and separation, catalysis, sensing, and controlled release.[22-28]

In this chapter, the aim is to report a new approach to isoreticular contraction of MOFs that is based on breaking of covalent bonds and does not require addition of any external linkers (Figure 5.1). Recently, Clip-off Chemistry, a new synthetic strategy to make new molecules and materials based on the selective, quantitative, and controlled cleavage of bonds in reticular materials, was well-established by our group.[29] Here, we show that this concept can be applied to control the stepwise synthesis of isoreticular MOFs exhibiting contracted structures relative to their parent MOFs. To this end, two new mixed-linker parent MOFs, which are isoreticular to the **nht**-(Fe)MIL-142 family:[30,31] (In)BCN-20B and (Sc)BCN-20C (BCN stands for Barcelona Material), have been delicately designed. This new isoreticular synthetic approach begins with the cleavage of an olefinic bond of one of the bridging

linkers, which splits the linker into two monocoordinated ligands. This periodic and quantitative fracture in the MOF is followed by the decoordination of one of the monocoordinated ligands, using solvents. This ligand removal instantaneously induces both contraction of the lattice and a self-healing phenomenon, which involves the migration and coordination of the monocoordinated ligand remaining in the structure to the accessible metal ions. Interestingly, this stepwise isoreticular contraction of MOFs, which involves breaking of a covalent bond, subsequent breaking of a coordination bond, and finally, formation of a new coordination bond supported by dynamic structural behavior, can be followed by single-crystal X-ray diffraction (SCXRD), as these events occur in a single-crystal to single-crystal manner.

Figure 5.1 Schematic of the isoreticular contraction of (In)BCN-20B and (Sc)BCN-20C induced by cleavage of covalent bonds.

5.2 Results and discussion

5.2.1 (In)BCN-20B system

In this section, the first system, (In)BCN-20B, will be mainly discussed by using our Clip-off Chemistry synthetic approach to produce an isoreticular contracted MOF.

5.2.1.1 Synthesis and characterization of (In)BCN-20B

The synthesis of (In)BCN-20B was achieved by the solvothermal reaction. First, a dispersion of $In(NO_3)_3 \cdot xH_2O$, 4,4′,4″-(1,3,5-triazine-2,4,6-triyl)tribenzoic acid (H_3TATB) and 4-carboxycinnamic acid (H_2CCA) in N,N-dimethylformamide (DMF) and HNO_3 (3.5 M in DMF) was heated at 120 °C for 30 h. Next, the resulting hexagonal prismatic crystals were analyzed by SCXRD, which confirmed formation of a 3D framework isoreticular to **nht**-(Fe)MIL-142B.
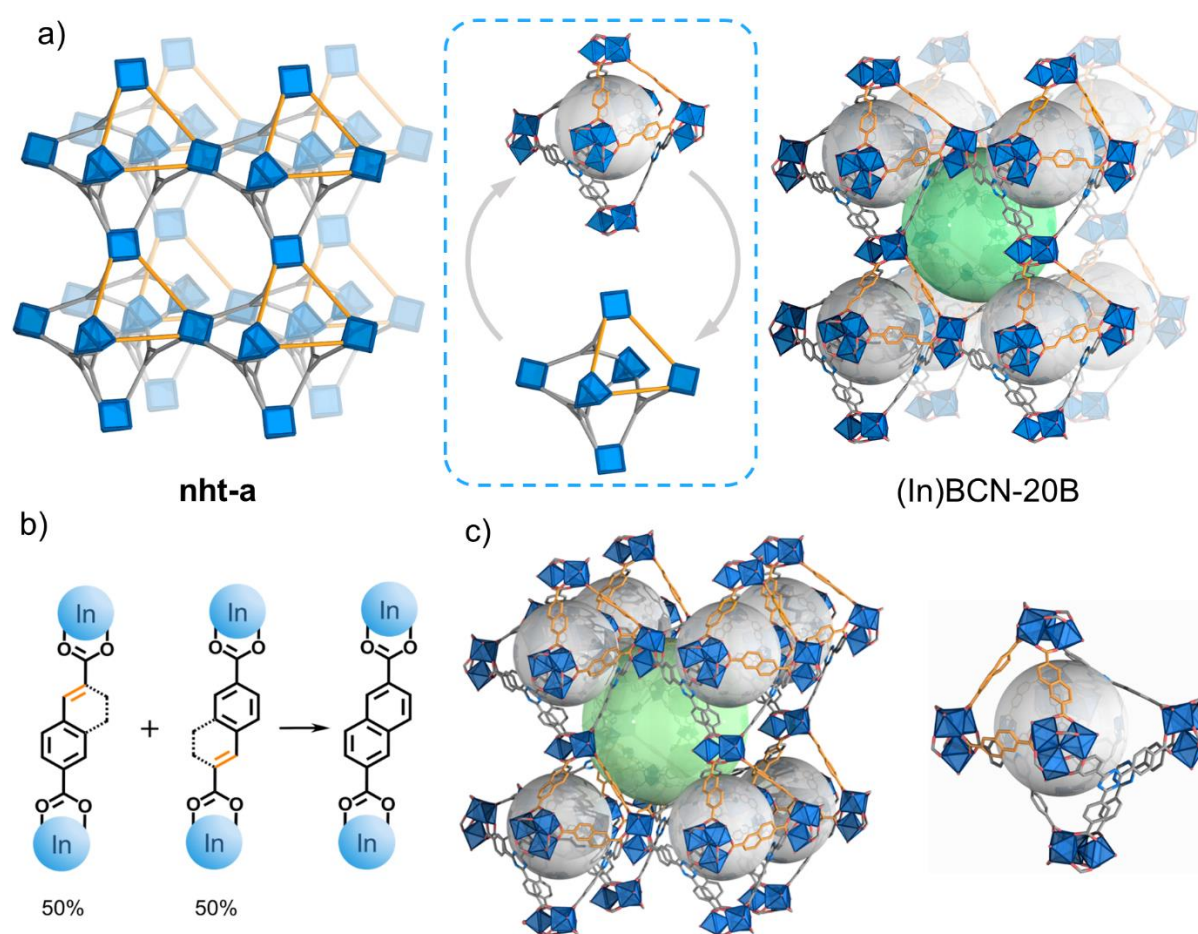
Figure 5.2 (a) Crystal structure of (In)BCN-20B, showing its **nht** net and octahedral cage. (b) Representation showing that the CCA linker is symmetrically disordered about an inversion center, which results in similarity of spatial occupation between the dislocated aromatic rings of CCA and naphthalene-2,6-dicarboxylate (NDC). (c) Crystal structure of (In)BCN-20B (left) and octahedral cage (right). Note that the disorder in the CCA linker resembles a naphthalene-2,6-dicarboxylate (NDC) linker.

(In)BCN-20B crystallizes in a trigonal lattice with an $R\bar{3}c$ (No. 167) space group, with unit cell parameters of $a = b = 30.820$ and $c = 95.540$ Å. The 3D structure of (In)BCN-20B is formed by vertex-sharing distorted octahedral cages, with an underlying **nht** topology (Figure 5.2a). Each cage is formed by six trigonal prismatic $In_3O(-CO_2)_6$ clusters located at vertices, which are connected by four tritopic TATB linkers and three ditopic CCA linkers. Note that these CCA linkers are symmetrically disordered about an inversion center, which results in similarity of spatial occupation between the dislocated aromatic rings of the CCA linker and those of a naphthalene molecule (Figure 5.2b,c). The location of the two types of linkers within the cage defines one triangular face, whose edges are occupied by three CCA linkers (Figure 5.3), and four triangular faces, each of which is occupied by one TATB linker. This means that each of the three remaining faces shares one of the edges occupied by a CCA linker with the first triangular face, whereas the other two edges are unoccupied.
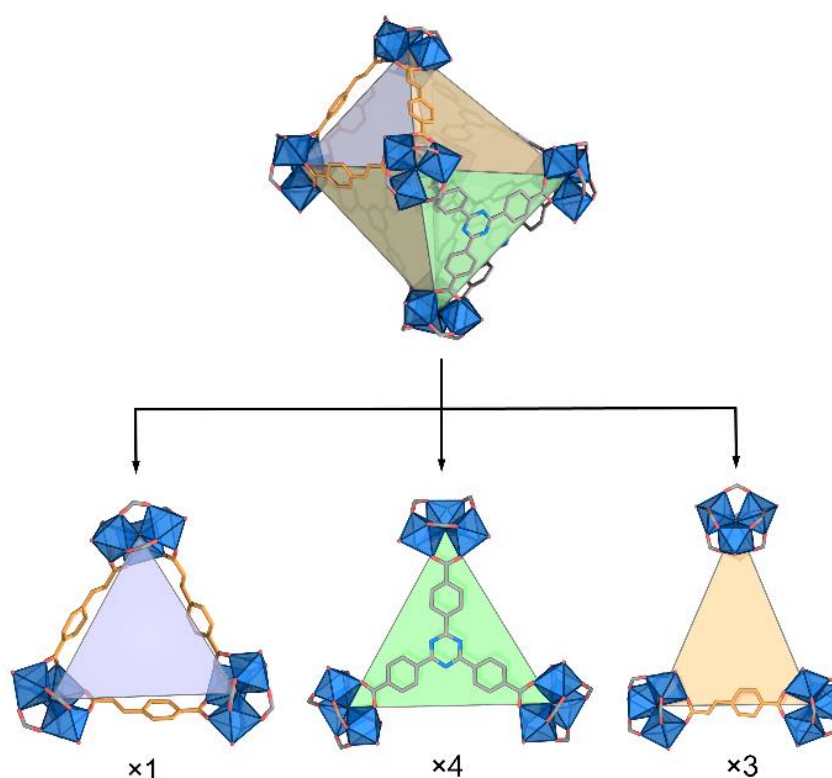
Figure 5.3 Representation of the three different types of triangular faces composing the octahedral cage in (In)BCN-20B.

The overall framework of (In)BCN-20B shows a 2-fold interpenetrated structure, in which two catenane-like octahedral cages from two different **nht** nets interlocked via one of their pure TATB triangular faces (Figure 5.4).
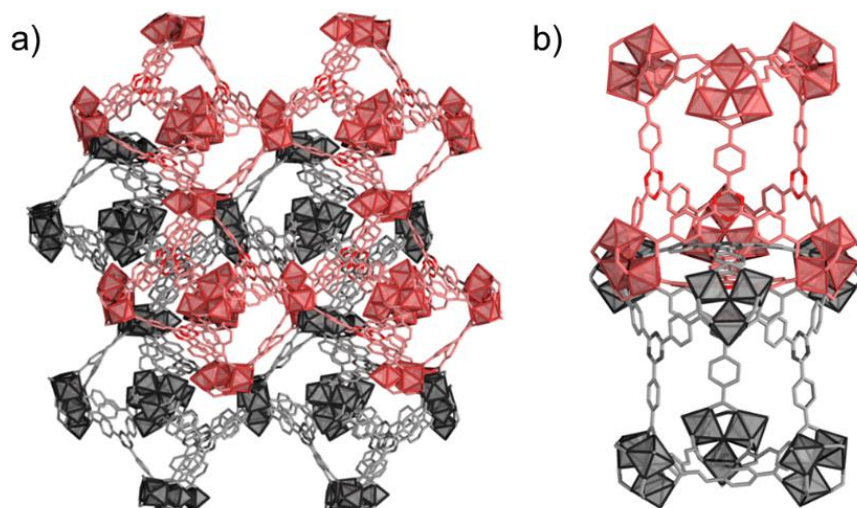
Figure 5.4 Crystal structure of (In)BCN-20B, showing (a) the 2-fold interpenetrated structure; and (b) two interlocked octahedral cages by interpenetration.

Further characterization of (In)BCN-20B confirmed its phase purity, as the experimental powder-XRD (PXRD) pattern matched the simulated one (Figure 5.5a). Furthermore, the ^{1}H NMR spectrum of the digested sample contained the expected TATB/CCA ratio of 4:3 (Figure 5.5b).
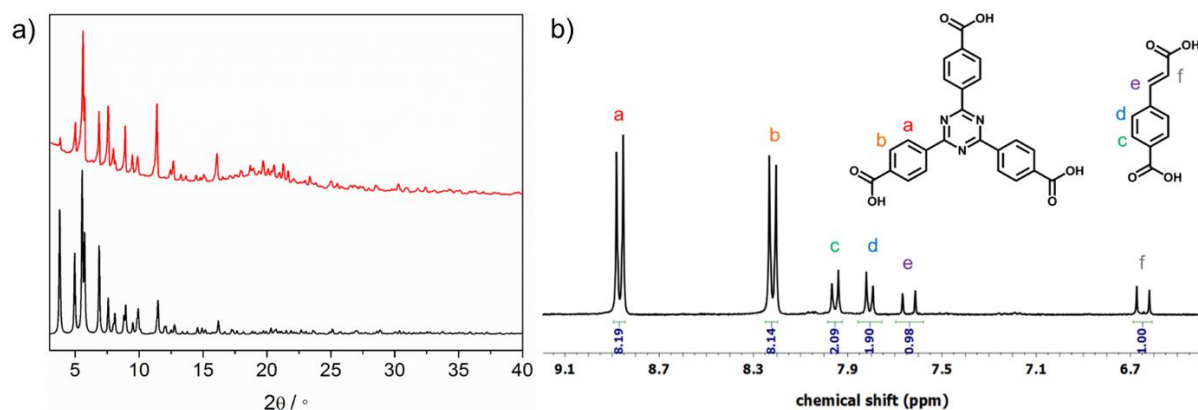
Figure 5.5 (a) PXRD patterns of simulated (In)BCN-20B (black) and as-made (In)BCN-20B (red). (b) ^{1}H NMR spectrum (400 MHz, DMSO-d_6) of digested (In)BCN-20B displaying the ratio between TATB and CCA. Note that the experimental ratio of TATB over CCA is 4/3, matching the expected one.

5.2.1.2 Synthesis and characterization of (In)BCN-20B′ by ozonolysis

Having synthesized (In)BCN-20B, attempted trials were made then to cleave all its alkene bonds and subsequently convert them into aldehyde/carboxylic acid groups via a solid–gas ozonolysis reaction.[29,32,33] First, 20 mg of single crystals of solvent-free (In)BCN-20B were packed into a plastic

tube. Next, dry ozone was flowed (~15 g/Nm^3) continuously through the sample for 35 min. Finally, the resultant crystals were analyzed by SCXRD, showing that ozonized (In)BCN-20B′ crystallized in a trigonal lattice with an $R\bar{3}m$ (No. 166) space group, having unit cell parameters of $a = b = 30.830$ and $c = 47.592$ Å. Overall, (In)BCN-20B′ exhibited a related 3D structure to that of (In)BCN-20B but with evident changes in its connectivity through the CCA linkers. Indeed, SCXRD data confirmed the integrity of the inorganic In-oxo clusters and of the TATB linkers. However, at the positions initially occupied by the CCA linkers, the similarity in spatial occupation between the dislocated aromatic rings of the CCA linker and the naphthalene molecule was lost (Figure 5.6). This observation clearly suggested that the CCA linkers no longer existed.
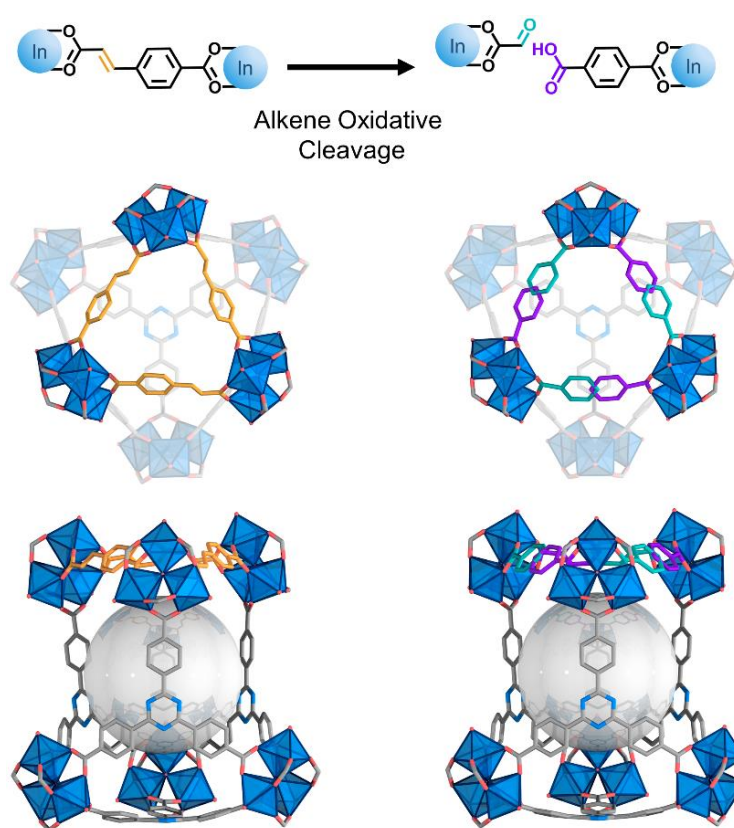
Figure 5.6 Schematic of the olefinic bonds breaking from (In)BCN-20B (left) to (In)BCN-20B′ (right) and corresponding SCXRD data, revealing the octahedral cages viewed along the crystallographic *c* and *b* axes, highlighting transformation of the CCA linker (orange) to the shorter BDC linker (violet) of the triangular face.

To confirm the oxidative cleavage of CCA linkers into the expected monocoordinated glyoxylate and single deprotonated terephthalic acid (BDC) ligands, a digested (In)BCN-20B′ sample was first analyzed by ^{1}H NMR and then compared the resulting spectrum to that of the starting (In)BCN-20B (Figure 5.7a,b). The spectrum of the digested (In)BCN-20B showed the characteristic peaks of the

olefinic protons of CCA at δ = 7.64 and δ = 6.65 ppm. In contrast, the spectrum of the digested (In)BCN-20B′ corroborated the disappearance of this olefinic signal. It also revealed the disappearance of the phenyl (δ = 7.94 and δ = 7.81 ppm) and the carboxylic acid (δ = 13.06 ppm) protons of the CCA but did show the characteristic signals for the terephthalic acid (BDC, δ = 8.04 ppm). The ratio of TATB over BDC is 4/3, matching well with the ratio expected from the cleavage of each CCA linker into a BDC linker (Figure 5.6).
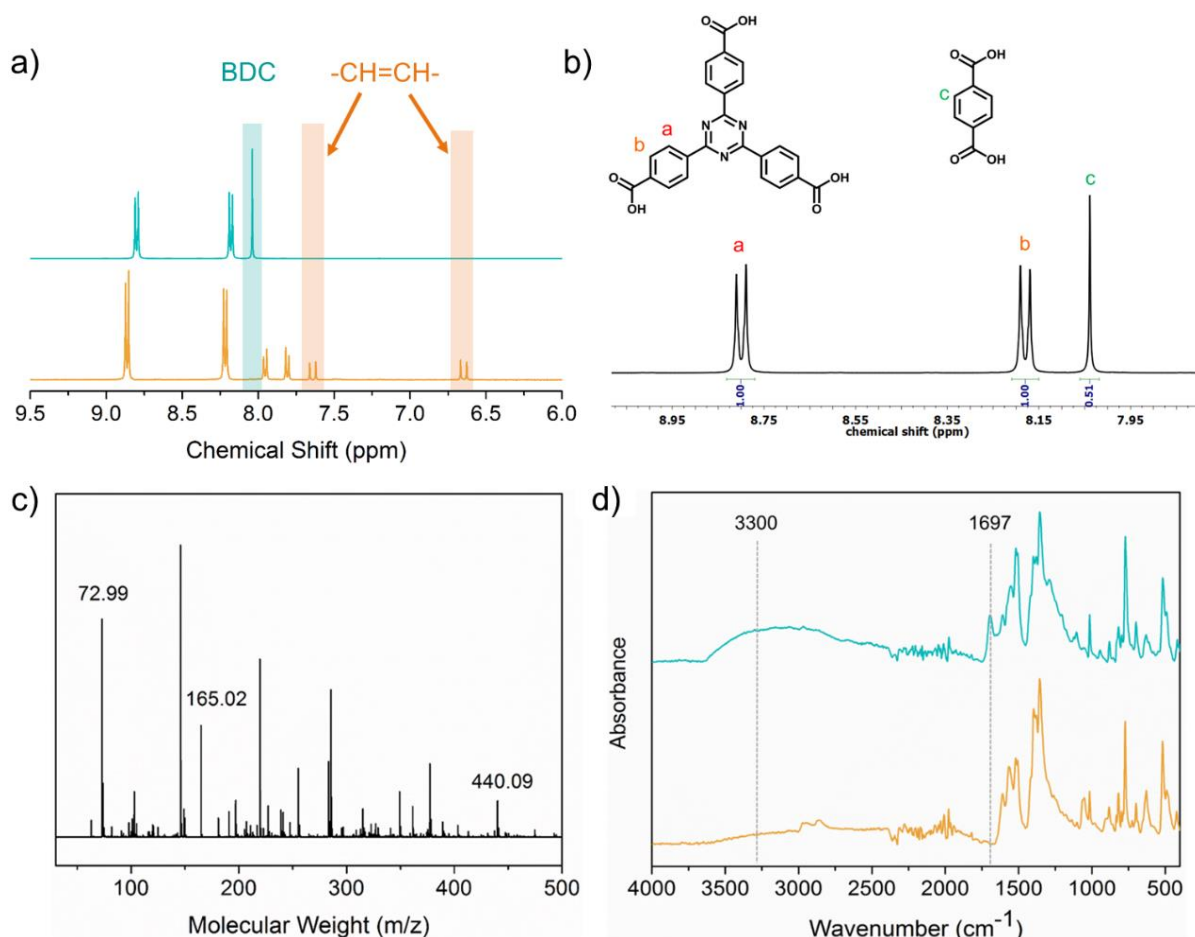
Figure 5.7 (a) ¹H NMR spectra (400 MHz, DMSO-*d₆*) of digested (In)BCN-20B (orange) and (In)BCN-20B′ (cyan), showing the formation of terephthalate (related protons were highlighted in cyan) and disappearance of olefinic bonds (related protons were highlighted in orange) after covalent bond breaking. (b) ¹H NMR spectrum of digested (In)BCN-20B′ displaying the ratio between TATB and BDC. (c) Negative mode ESI-MS spectrum of digested (In)BCN-20B′. (d) Full widths of FTIR spectra of (In)BCN-20B (orange) and (In)BCN-20B′ (cyan).

Unfortunately, from ¹H NMR spectrum, the aldehyde proton of the glyoxylic acid was not detected, presumably due to the fact that its boiling point (111 °C) is lower than the temperature (120 °C) at which the digestion took place overnight. However, the presence of glyoxylic acid was confirmed by

electrospray ionization mass spectrometry (ESI-MS) analysis in a negative ion mode using a (In)BCN-20B′ sample digested under milder conditions (HF in DMSO at room temperature). The ESI-MS spectrum (Figure 5.7c) showed a peak at $m/z = 72.99$, which matches the molecular mass of the deprotonated glyoxylate corresponding to the formula $[C_2H_2O_3-H]^-$ ($m/z = 73.03$). Meanwhile, other ligands existed in (In)BCN-20B′ were also detectable. The peak at $m/z = 165.02$ is assigned to BDC, corresponding to the formula $[C_8H_6O_4-H]^-$ ($m/z = 165.03$). The peak at $m/z = 440.09$ is assigned to H$_3$TATB, corresponding to the formula $[C_{24}H_{15}N_3O_6-H]^-$ ($m/z = 440.10$).

These results clearly indicated that the olefinic bond of the ditopic CCA linkers had been quantitatively cleaved by ozonolysis and subsequently converted into two monocoordinated ligands: a single deprotonated BDC and a glyoxylate.
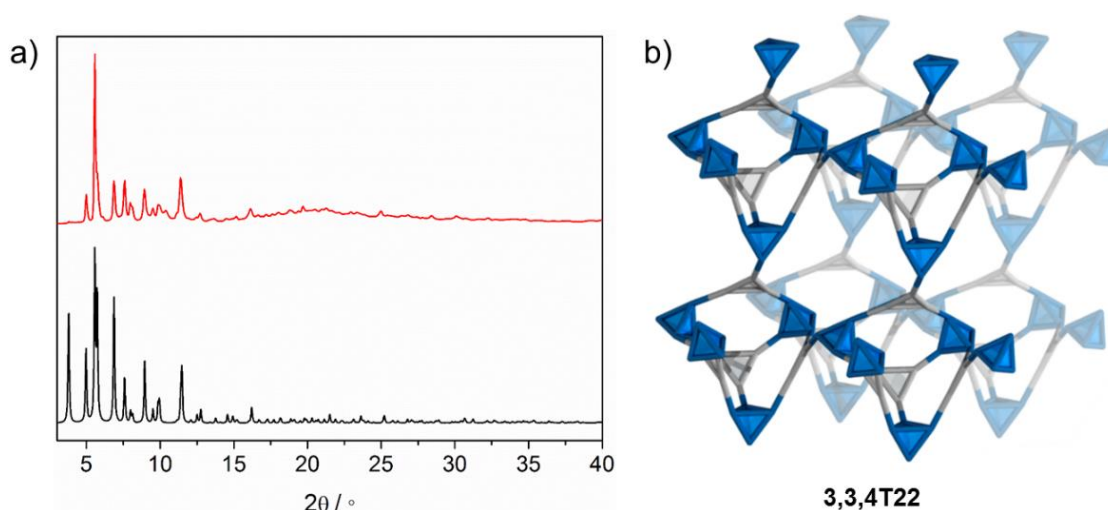
Figure 5.8 (a) PXRD patterns of simulated (In)BCN-20B′ (black) and as-made (In)BCN-20B′ (red). (b) Representation showing the augmented net of (In)BCN-20B′, containing two kinds of nodes: 4-c tetrahedral and 3-c triangular nodes.

Supporting this oxidative cleavage reaction, the FTIR spectrum of the ozonated (In)BCN-20B′ exhibited a more intense C=O stretch band at 1697 cm^{-1} relative to that in the spectrum of the non-ozonated (In)BCN-20B. Moreover, it showed enhanced, broad absorbance at around 3300 cm^{-1}, indicative of large perturbations caused by H-bonded hydroxyl groups of the free carboxylic acid groups (Figure 5.7d).[34,35] Next, PXRD on a bulk sample of ozonated (In)BCN-20B′ was performed to confirm its crystallinity and phase purity. The resulting PXRD pattern matched the one calculated from the crystal structure (Figure 5.8a), confirming that the cleavage of alkene bonds via ozonolysis did not compromise the crystallinity throughout the bulk sample. Together these results confirmed the quantitative cleavage of CCA linkers and the consequent formation of a new structure with less

connectivity among its trimeric In^{3+} clusters. Indeed, analysis of the topology of (In)BCN-20B′ using the TopatPro 5.3.3.5 software,[36] and considering TATB linkers as 3-connected points of extension (3-c), and In$_3$O($-$CO$_2$)$_6$ clusters as nodes that have four coordination points (4-c), revealed formation of a 2-fold interpenetrated MOF with two independent underlying trinodal (3,3,4)-c nets (topological code **3,3,4T22**, Figure 5.8b).

5.2.1.3 Solvent-assisted isoreticular contraction

After demonstrating that ditopic CCA linkers could be cleaved into two monocoordinated ligands, the possibility of substituting these monocoordinated ligands with solvent molecules was then explored. First, crystals of (In)BCN-20B′ were incubated in DMF for 1 week at room temperature. Next, the resultant crystals were analyzed by SCXRD, which revealed that a new 3D structure (In)BCN-20A had been formed (Figure 5.9a). This new MOF crystallizes in the trigonal lattice with the space group $R\overline{3}m$ (No. 166) and lattice parameters of $a = b = 28.783$ and $c = 47.708$ Å. (In)BCN-20A, which is isostructural to **nht**-(Fe)MIL-142A,[30] recovers the initial 3D **nht** framework formed by vertex-sharing distorted octahedral cages. However, its cages are instead formed by six In$_3$O($-$CO$_2$)$_6$ clusters connected by four tritopic TATB linkers and three ditopic BDC linkers, the latter occupying the analogous position of the CCA linkers in (In)BCN-20B (Figure 5.9b)
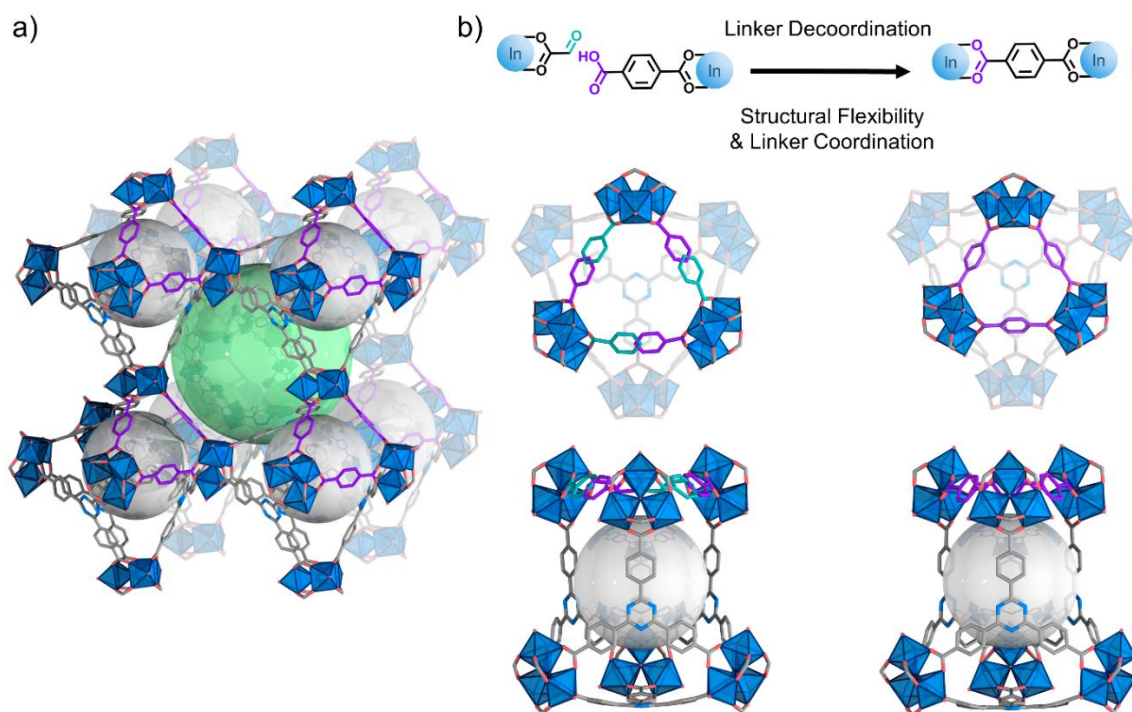
Figure 5.9 (a) Crystal structure of (In)BCN-20A. (b) Schematic of the isoreticular contraction from (In)BCN-20B′ (left) to (In)BCN-20A (right) and corresponding SCXRD data, revealing the octahedral cages viewed along the crystallographic c and b axes, highlighting transformation of the contraction of the triangular face.

The phase transition from (In)BCN-20B′ to (In)BCN-20A unambiguously unveiled a self-healing behavior, which was envisaged to occur in three steps within the pores. First, DMF molecules enter the pores and replace the glyoxylate linkers. Here, the release of glyoxylate from the MOF was experimentally confirmed by analyzing the DMF supernatant resulting from the incubation process by ESI-MS, from which the characteristic peak at $m/z = 72.99$ was detected (Figure 5.10). Second, the decoordination of glyoxylate causes the framework to act dynamically. In the third and final step, this behavior leads to coordination of the free carboxylic acid group of each BDC linker to the In^{3+} metal sites that were previously occupied by the glyoxylate. Accordingly, the BDC linker would have to migrate a distance of ~2.4 Å.
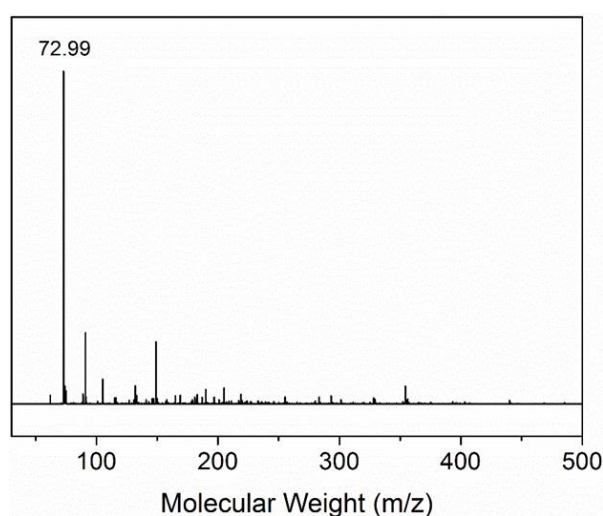
Figure 5.10 Negative mode ESI-MS spectrum of DMF supernatant after incubation of (In)BCN-20B′ in DMF for 1 week.

To further evaluate the degree of the aforementioned flexibility, a deliberate comparison of the unit cell volumes of the three MOFs was conducted: the initial (In)BCN-20B, the ozonated (In)BCN-20B′, and the self-healed (In)BCN-20A. Considering the fact that (In)BCN-20B crystallizes in the centrosymmetric trigonal space group $R\overline{3}c$ (No. 167) whereas both (In)BCN-20B′ and (In)BCN-20A crystallize in trigonal Bravais lattices with the space group $R\overline{3}m$ (No. 166), the structural relationship correlates to a group-subgroup relationship of the space groups. $R\overline{3}m$ has a maximal non-isomorphic subgroup $R\overline{3}c$ (a' = −a, b' = −b, c' = 2c) with *klassengleich* transition of index 2, indicating $R\overline{3}c$ possesses a two times larger unit cell. In order to reduce the symmetry of $R\overline{3}m$ for clear comparison, the c parameter in (In)BCN-20B′ and (In)BCN-20A is shown as $2c$ and the volume as $2V$. Based on this, the corresponding unit cell parameters of each MOF are summarized in Table 5.1.

From (In)BCN-20B to (In)BCN-20B′, the unit cell volume only shrunk by 0.3%. However, from (In)BCN-20B′ to (In)BCN-20A, the cell volume decreased by 12.6%, an obvious volumetric contraction.

Table 5.1 Comparison of the unit cell parameters of (In)BCN-20B, (In)BCN-20B′, and (In)BCN-20A.

MOFs	a (Å)	c (Å)	V (Å³)
(In)BCN-20B	30.820	95.540	78592.5
(In)BCN-20B′	30.830	95.184	78350.0
(In)BCN-20A	28.783	95.415	68457.8

It was reasoned that the movements involving this dynamic behavior could also be studied by comparing the structural changes in the octahedral cage units (Figure 5.11). In the octahedral cage of the initial (In)BCN-20B, the length (note: all lengths were calculated starting from the carbon atoms of the carboxylate groups of the linkers) of the edges of the face constructed with CCA linkers is 8.0 Å, and the average length of the remaining edges is 12.1 Å. As expected, the cleavage of the CCA linkers barely affected this octahedral cage unit: the length of the edges of the face occupied by the cleaved CCA linkers only increased to 8.2 Å. This slight increase was attributed to the steric hindrance effects of both the BDC and the glyoxylate linkers. In (In)BCN-20A, this length decreases significantly, down to 5.7 Å, because the BDC linker is much smaller than both the initial and the cleaved CCA linkers. Contrariwise, this contraction barely affects the other edges involving the TATB linker, exhibiting an average length of 12.0 Å.
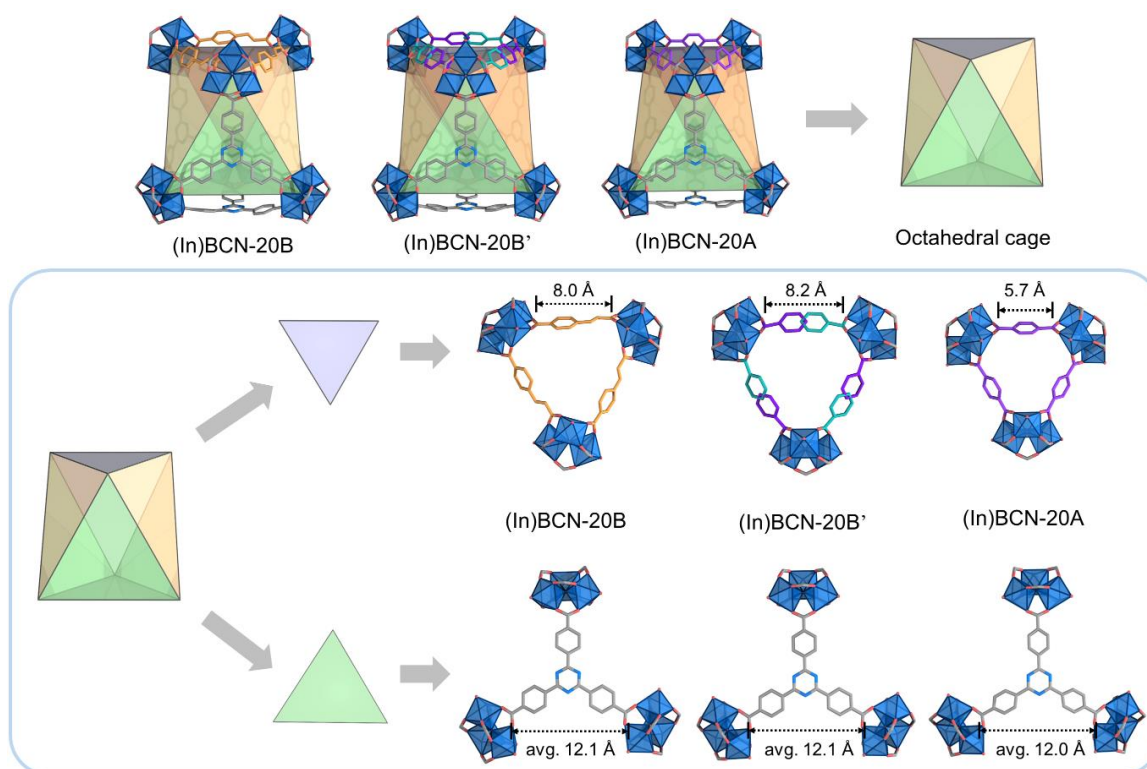
Figure 5.11 Schematic representation showing the single-crystal-to-single-crystal evolution from (In)BCN-20B to (In)BCN-20B′ to (In)BCN-20A, highlighting the changes in the octahedral cage.

Given that the structure of (In)BCN-20A differs markedly from that of (In)BCN-20B or (In)BCN-20B′, an investigation was conducted to determine whether this transformation would manifest throughout the bulk sample, using PXRD. Supporting a homogeneous transformation, the PXRD pattern of (In)BCN-20A matched the one calculated from the corresponding structure determined by SCXRD (Figure 5.12a, more PXRD patterns see 5.4.3). By comparing the PXRD patterns of (In)BCN-20A and (In)BCN-20B, it was observed that the diffraction peak of (In)BCN-20B at $2\theta = 3.8°$, corresponding to the $(10\overline{2})$ crystallographic plane, had shifted to a higher angle ($2\theta = 5.1°$) within the same plane of (In)BCN-20A. This observation confirmed the compression of the framework.
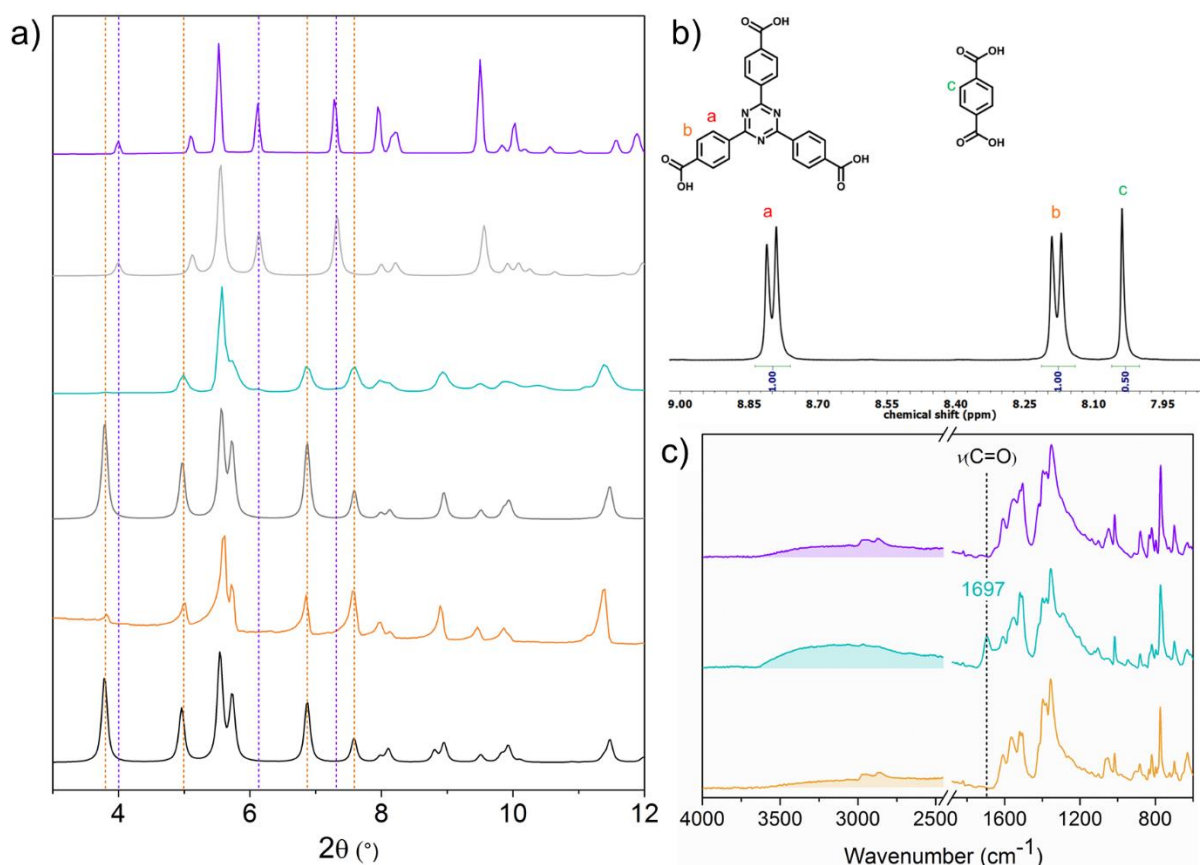
Figure 5.12 (a) PXRD patterns of simulated (black) and experimental (orange) (In)BCN-20B; simulated (gray) and experimental (cyan) (In)BCN-20B′; and simulated (light gray) and experimental (violet) (In)BCN-20A. (b) ^{1}H NMR spectrum (400 MHz, DMSO-d_6) of digested (In)BCN-20B′ displaying the ratio between TATB and BDC. (c) FTIR spectra of (In)BCN-20B (orange), (In)BCN-20B′ (cyan), and (In)BCN-20A (violet), showing the main changes at the wavenumber of 1697 cm^{-1}.

Phase homogeneity was also studied by FTIR and ^{1}H NMR. The FTIR spectrum revealed that the stretching band of characteristic carbonyl groups (1697 cm^{-1}) and the broad absorbance at around 3300 cm^{-1} had been dramatically attenuated, identically to that of the initial (In)BCN-20B (Figure 5.12c). The ^{1}H NMR spectrum confirmed the expected TATB/BDC ratio of 4:3 (Figure 5.12b).

It is worth noting that all our attempts to transform (In)BCN-20B into (In)BCN-20A by direct linker exchange of CCA by BDC were unsuccessful (see experimental section 5.4.2). This suggests that covalent bond cleavage of the CCA linker highly facilitates the internal restructuration of the framework, involving both flexible and self-healing behavior.

5.2.2 (Sc)BCN-20C system

5.2.2.1 Synthesis and characterization of (Sc)BCN-20C

In order to investigate whether such behavior could occur in an isoreticular framework with greater distances between metal clusters, the CCA linker was substituted with the 4,4′-stilbenedicarboxylic acid (H_2sti) linker, which is longer (Figure 5.13a). However, all our attempts at synthesizing the isostructural MOF using In^{3+} were unsuccessful. Fortunately, its Sc^{3+} analogue, using the (ditopic) sti linker and the (tritopic) 1,3,5-tris(4-carboxyphenyl)benzene (BTB) linker, were able to be synthesized (Figure 5.13b). (Sc)BCN-20C crystallizes in the monoclinic symmetry with a $C2/c$ space group (No. 15) and lattice parameters of a = 60.279, b = 34.723, and c = 37.136 Å. As its analogues, it contains a 2-fold interpenetrated structure with two underlying **nht** nets (Figure 5.14). Note that the two nets are interconnected by formate linkers that can be formed upon decomposition of DMF aided by HNO_3.[31,37] These nets are built up from vertex-sharing distorted octahedral cages, which are larger than those of (In)BCN-20B or (In)BCN-20A. Their main difference lies in the edges of the triangular face defined by three sti linkers, whose length is increased to 12.2 Å. The other edges of the octahedra are slightly longer (12.3 Å) than those of (In)BCN-20B (Figure 5.15).
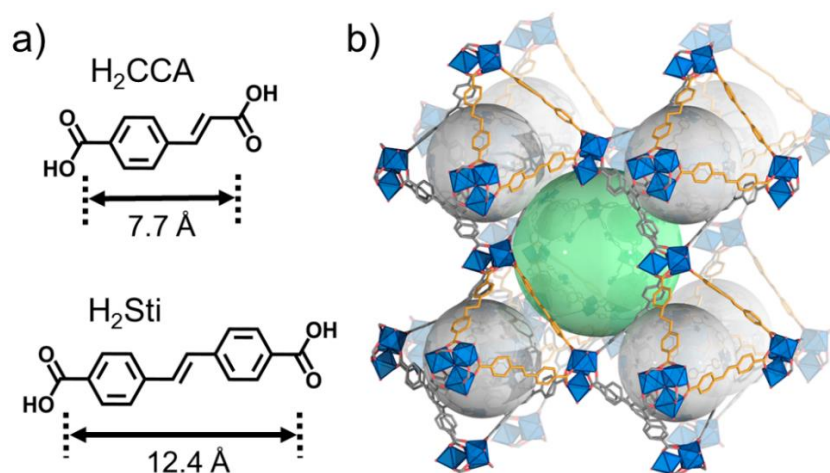
Figure 5.13 (a) Comparison of the linker length between H_2CCA and H_2sti. (b) Crystal structure of (Sc)BCN-20C.
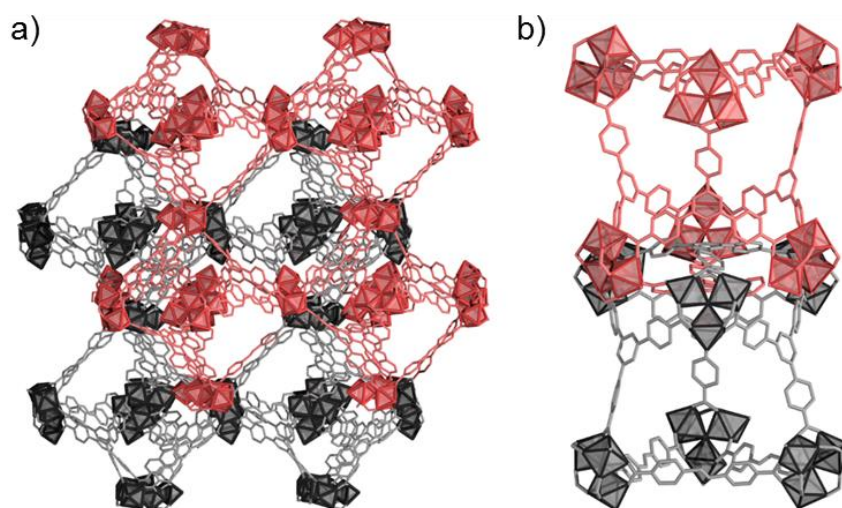
Figure 5.14 Crystal structure of (Sc)BCN-20C, showing (a) the 2-fold interpenetrated structure; and (b) two interlocked octahedral cages by interpenetration.
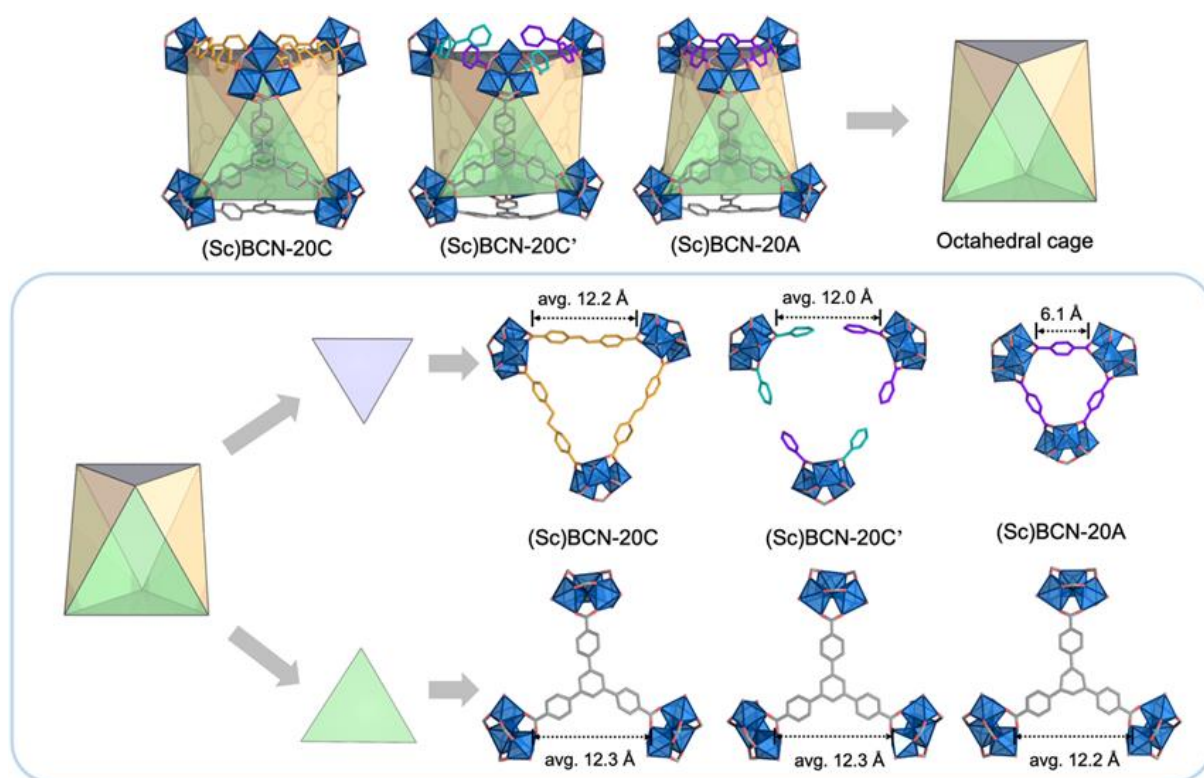
Figure 5.15 Schematic representation showing the single-crystal-to-single-crystal evolution from (Sc)BCN-20C to (Sc)BCN-20C′ to (Sc)BCN-20A, highlighting the changes in the octahedral cage.

The phase purity of (Sc)BCN-20C was confirmed by PXRD, whose pattern matched the one simulated from SCXRD data (Figure 5.15a), and by ^{1}H NMR, the spectrum of the digested sample confirmed the expected BTB/sti ratio of 4:3 (Figure 5.15b).

Figure 5.15 (a) PXRD of simulated (Sc)BCN-20C (black) and as-made (Sc)BCN-20C (red). (b) ^{1}H NMR spectrum (400 MHz, DMSO-d_6) of digested (Sc)BCN-20C displaying the ratio between BTB and sti.

5.2.2.2 Synthesis and characterization of (Sc)BCN-20C′ by ozonolysis
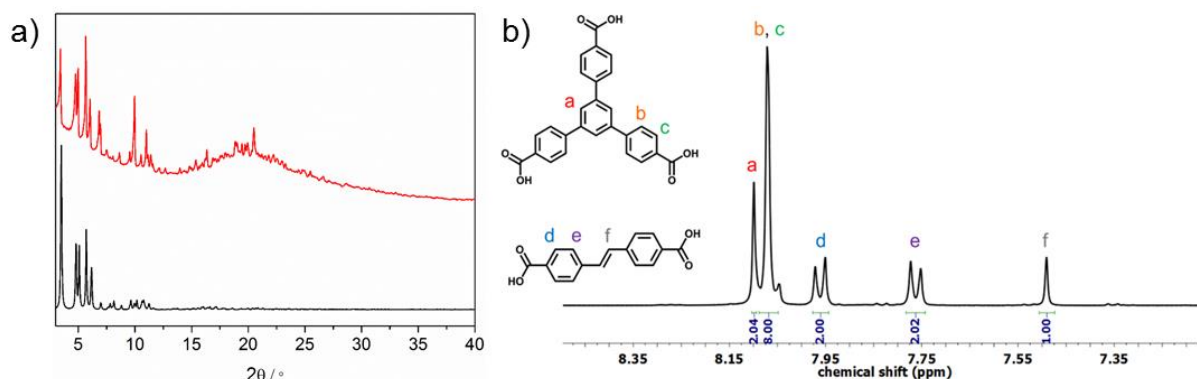
Next, a cleavage experiment on the sti linkers was performed, similar to the previous experiment on the CCA linkers. Thus, ozone was flowed (~15 g/Nm^3) continuously through a crystalline sample of solvent-free (Sc)BCN-20C for 5 min. The quantitative cleavage of sti linkers and conversion of the resultant fragments to the expected monocoordinated HBDC and 4-formylbenzoate (4-FBA) were corroborated by ^{1}H NMR, PXRD, and FTIR. ^{1}H NMR spectrum of the digested (Sc)BCN-20C′ (Figure 5.16a) showed that the characteristic peaks of the olefinic protons of sti at δ = 7.49 ppm completely disappeared. Instead, terephthalic acid (δ = 8.04 ppm) and formyl benzoic acid were able to be detected (δ = 8.14 ppm and 8.02 ppm). As expected, the ratio of BDC and 4-FBA, ozonated products from sti, was calculated to be 1:1 (Figure 5.16b). PXRD confirmed the phase purity and intrinsic crystallinity (Figure 5.16c). FTIR spectrum revealed that the ozonated (Sc)BCN-20C′ exhibits a more intense C=O stretch band at 1699 cm^{-1} relative to those of (Sc)BCN-20C. This is due to the cleavage of sti linkers into the BDC and 4-FBA ligands (Figure 5.16d).

In addition to that, SCXRD data revealed that the structure of (Sc)BCN-20C′ is very similar to that of the initial (Sc)BCN-20C, with the corresponding octahedral cage units having similar dimensions. However, one significant difference was observed: benzoate ligands─most likely, 4-FBA linkers with highly disordered aldehyde groups─bridging the two interpenetrated nets and partially substituting the formate ligands. This observation evidenced the mobility of these monocoordinated ligands inside the pores upon cleavage of the ditopic linkers.
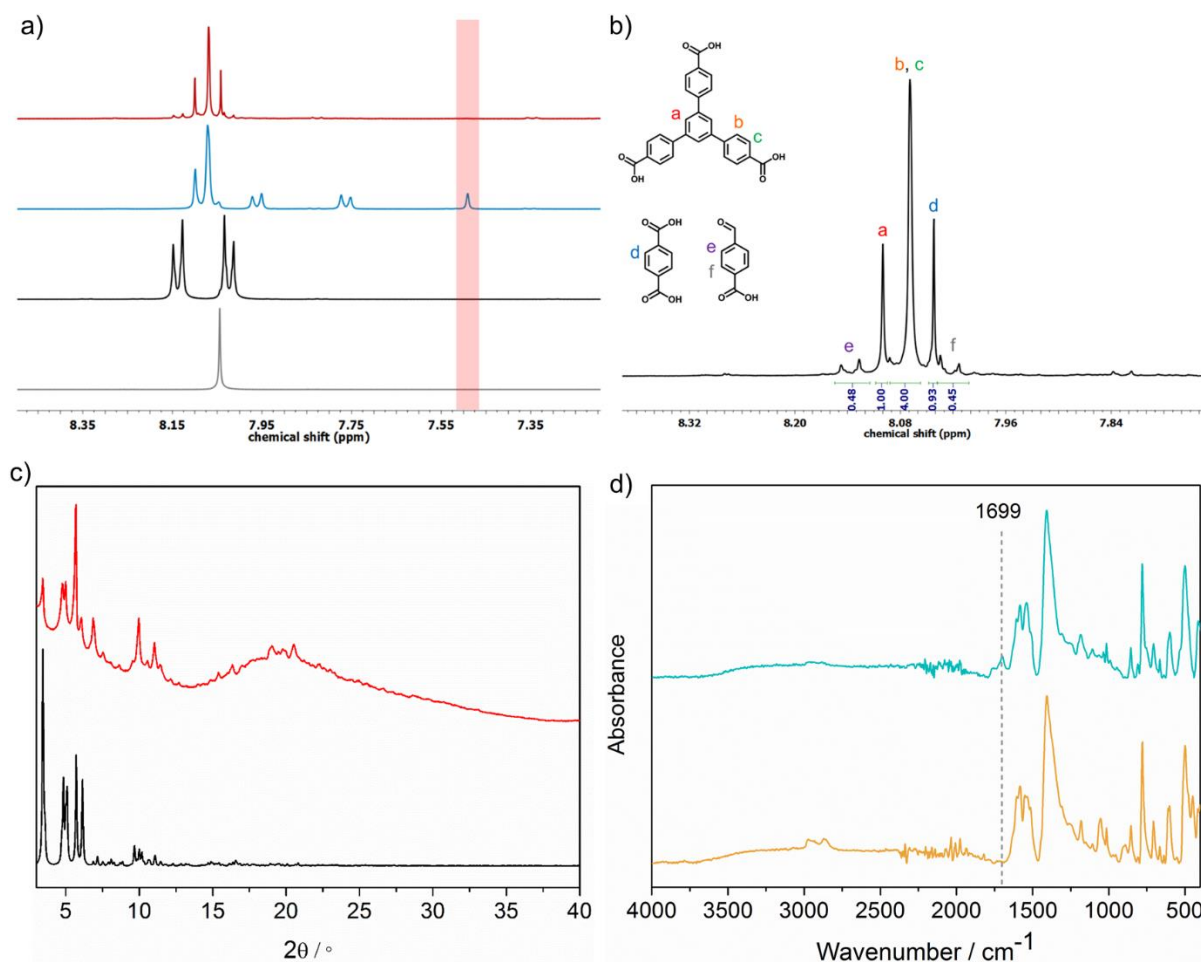
Figure 5.16 (a) ^{1}H NMR spectra (400 MHz, DMSO-d_6) of BDC (gray), 4-FBA (black), digested (Sc)BCN-20C (blue) and digested (Sc)BCN-20C′ (red). The proton signal of olefinic bonds (δ = 7.49 ppm) was highlighted in red. (b) Enlarged ^{1}H NMR spectrum of digested (Sc)BCN-20C′ displaying the ratio among BTB and ozonated products, BDC and 4-FBA (c) PXRD of simulated (Sc)BCN-20C′ (black) and as-made (Sc)BCN-20C′ (red). (d) FTIR spectra of (Sc)BCN-20C (orange), (Sc)BCN-20C′ (cyan).

5.2.2.3 Solvent-assisted isoreticular synthesis of (Sc)BCN-20A

Finally, in the pursuit of eliminating the 4-FBA ligands and inducing the dynamic and self-healing behavior for the formation of the isoreticular (Sc)-BCN-20A, (Sc)BCN-20C′ was immersed in DMF for a week. Interestingly, SCXRD of the resulting crystals confirmed the formation of this MOF, whose structure is isostructural to that of (In)BCN-20A (Figure 5.17a,c). (Sc)-BCN-20A crystallizes in a trigonal system with the space group $R\bar{3}c$ (No. 167) and lattice parameters of $a = b = 28.682$ and $c = 95.606$ Å. The bulk sample of (Sc)-BCN-20A were further corroborated by PXRD, FTIR and ^{1}H NMR.
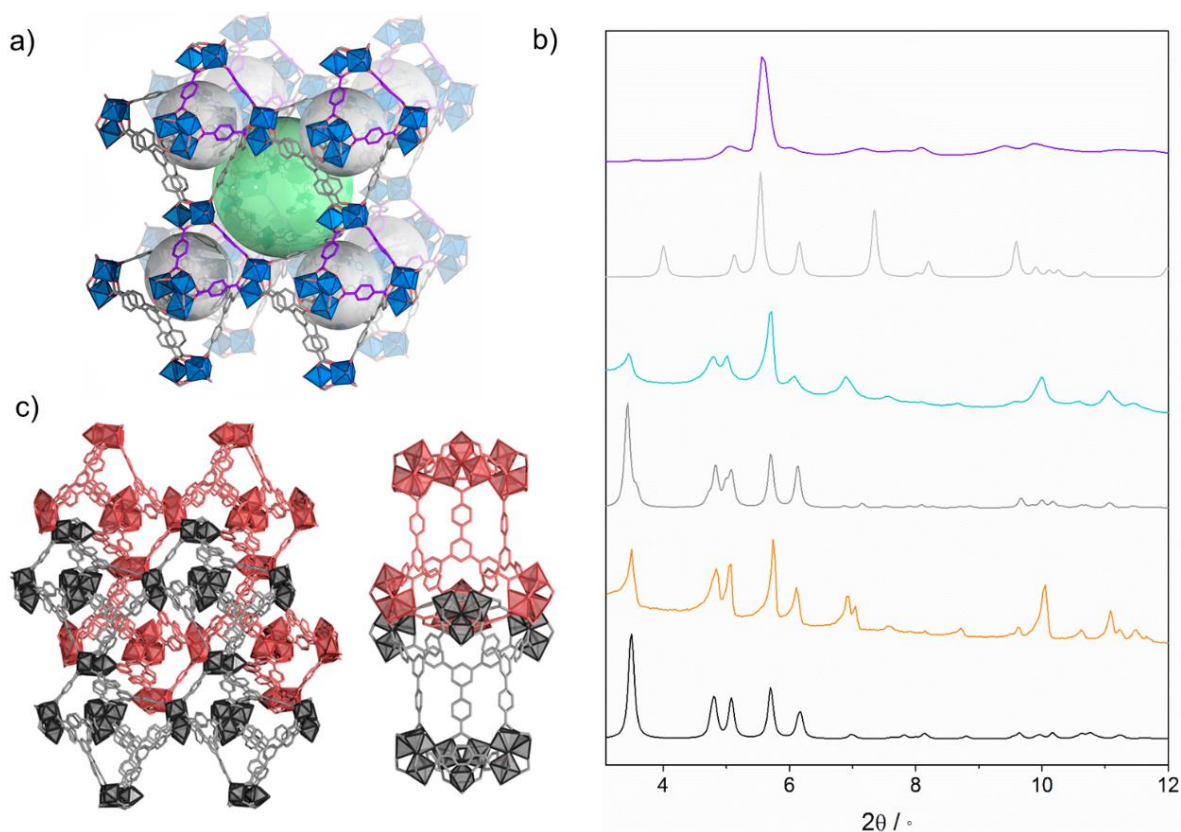
Figure 5.17 (a) Crystal structure of (Sc)BCN-20A. (b) PXRD spectra of simulated (black) and experimental (orange) (Sc)BCN-20C; simulated (grey) and experimental (cyan) (Sc)BCN-20C′; and simulated (light grey) and experimental (violet) (Sc)BCN-20A. (c) 2-fold interpenetrated structures (left) and interlocked octahedral cages by interpenetration (right).

PXRD of (Sc)BCN-20A confirmed the phase purity, which matched with the simulated data (Figure 5.17b). FTIR spectrum showed that the C=O stretch band at 1699 cm^{-1} from (Sc)BCN-20A had greatly attenuated, identically to that of the initial (Sc)BCN-20C (Figure 5.17b). The release of 4-FBA from the MOF was experimentally confirmed by analyzing the DMF supernatant resulting from the incubation process by ESI-MS, from which the characteristic peak at m/z = 149.03 was detected (Figure 5.18c). ^{1}H NMR of digested (Sc)BCN-20A exhibited the complete disappearance of 4-FBA as no aldehyde signal (δ = 10.11 ppm) could be found (Figure 5.18b). As expected, the ratio of BTB/BDC has determined to be ideal 4:3.

Accordingly, the unit cell volumes of the three MOFs were compared for assessing their flexibility during the phase transition. For comparison, the unit cells of (Sc)BCN-20C and (Sc)BCN-20A were intentionally indexed into the lower symmetry, triclinic crystal systems. As summarized in table 5.2, this dynamic, self-healing phenomenon uncovered that the cell volume had been dramatically compressed by 30.7%.
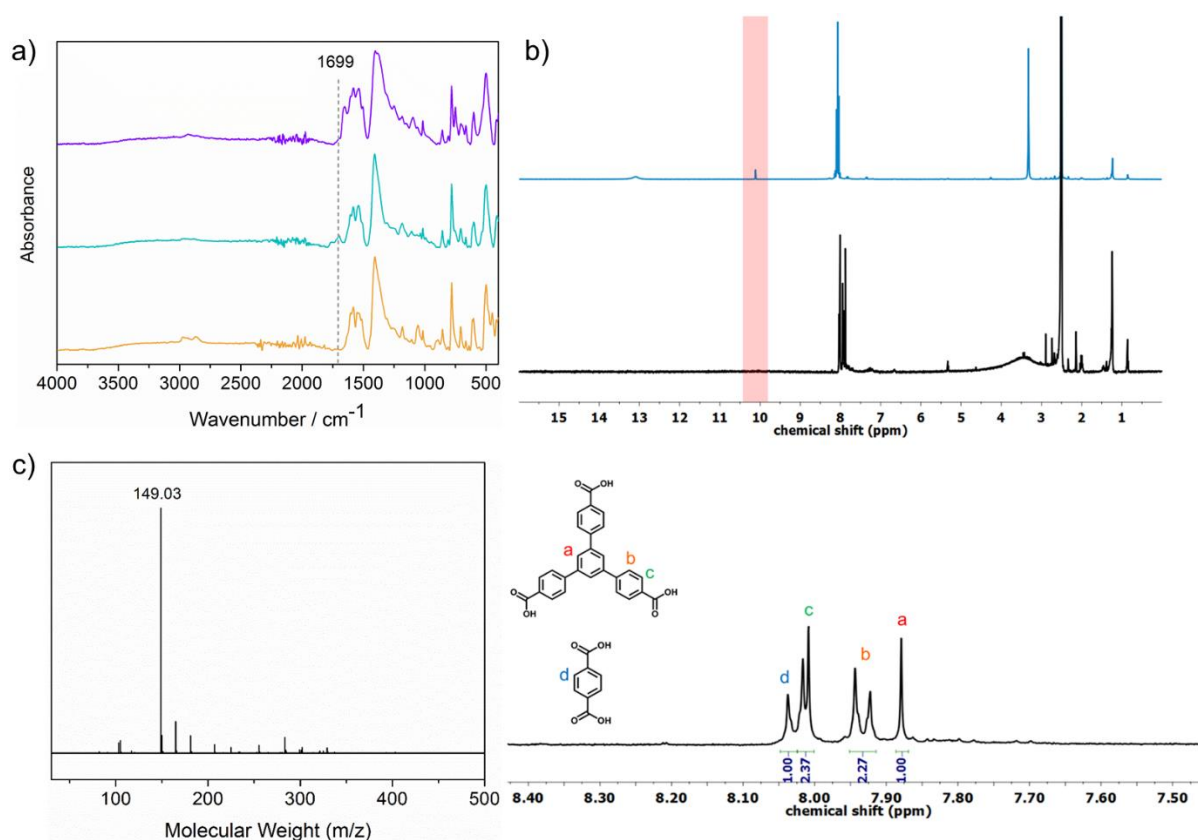
Figure 5.18 (a) FTIR spectra of (Sc)BCN-20C (orange), (Sc)BCN-20C′ (cyan) and (Sc)BCN-20A (violet), showing the main changes at the wavenumber of 1699 cm⁻¹. (b) ^{1}H NMR spectra (400 MHz, DMSO-d_6; top) of the digested (Sc)BCN-20A (black) and (Sc)BCN-20C′ (blue) and enlarged ^{1}H NMR spectrum (bottom) of the digested (Sc)BCN-20A displaying the ratio of BTB and BDC. The proton signal of aldehyde groups ($\delta = 10.11$ ppm) was highlighted in red. (c) Negative mode ESI-MS spectrum of DMF supernatant after incubation of (In)BCN-20C′ in DMF for 1 week.

Table 5.2 Comparison of the unit cell parameters of (Sc)BCN-20C, BCN-20C′ and (Sc)BCN-20A.

MOFs	*a* (Å)	*b* (Å)	*c* (Å)	*α* (°)	*β* (°)	*γ* (°)	*V* (Å³)
(Sc)BCN-20C	37.136	34.723	25.362	83.628	94.365	90	32406.1
(Sc)BCN-20C′	37.528	35.374	24.761	90	94.24	90	32780.7
(Sc)BCN-20A	35.914	28.682	22.987	91.344	106.436	90	22704.2

During this stepwise isoreticular contraction process, all BDC linkers traveled a distance of ~6.4 Å to coordinate to the Sc^{3+} metal sites, shrinking one of the triangular faces of the cages from 12.2 to 6.1 Å (Figure 5.15 and Figure 5.19).
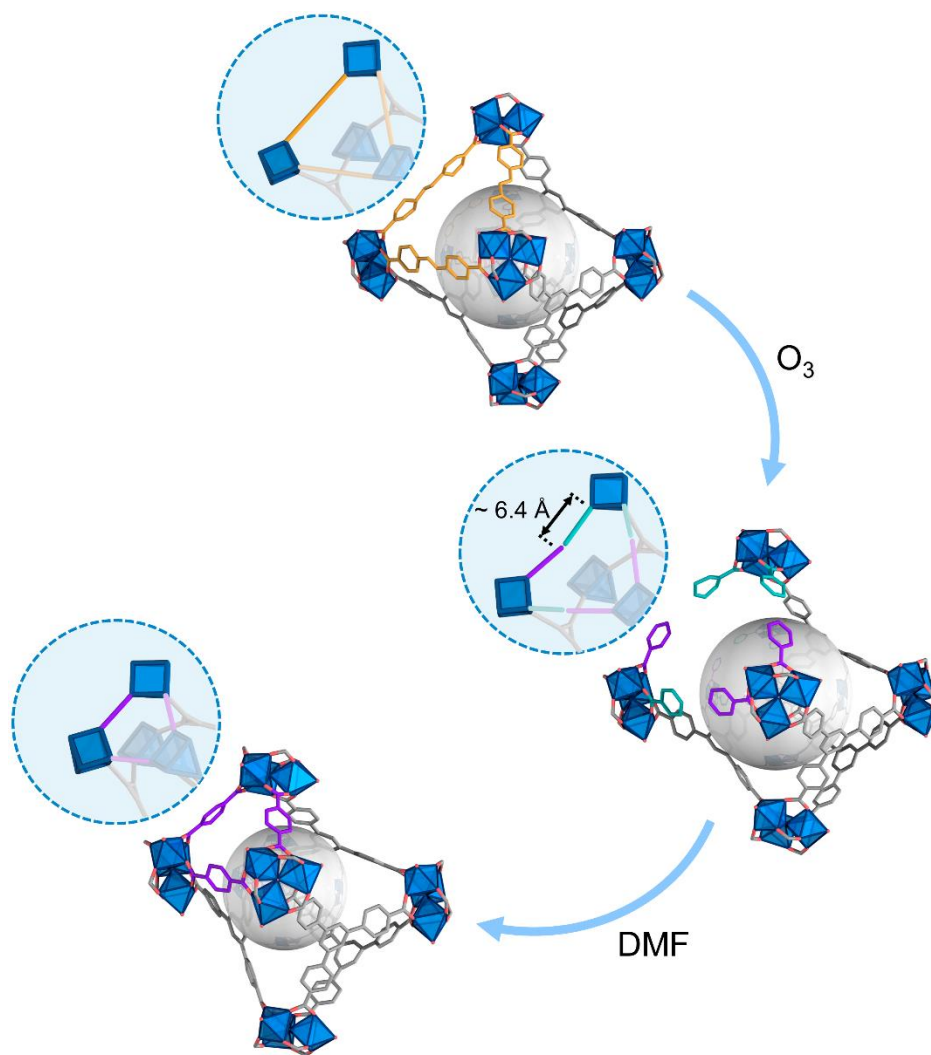
Figure 5.19 Schematic and corresponding SCXRD structures of the stepwise isoreticular contraction from (Sc)BCN-20C (top) to (Sc)BCN-20C′ (middle) to (Sc)BCN-20A (down).

5.3 Conclusions

In conclusion, we have shown that the cleavage of covalent bonds within bridging organic linkers in an MOF can trigger a series of chemical and structural dynamic processes that drive the formation of an isoreticular contracted MOF. Remarkably, as the single-crystal character of the parent MOF is retained throughout the entire isoreticular transformation, we were able to use SCXRD to obtain invaluable crystallographic snapshots of the stepwise processes. Initially, applying our concept of Clip-off Chemistry, we were able to cleave each bridging alkene-containing organic linker into two monocoordinated ligands via ozonolysis, thereby disconnecting two metal clusters. Among these monocoordinated ligands, one is terminated with a carboxylic acid group, whereas the other ends in an aldehyde group. As this latter ligand is weaker, we were able to decoordinate it from the metal center

by simply treating the MOF with DMF. This removal process conferred the structure with dynamic behavior that involved the migration and subsequent coordination of the other monocoordinated ligand with a free carboxylic acid group to the open metal site. In what we have called "self-healing behavior", the metal clusters that had been disconnected during cleavage of the linker bond reconnected to form a new MOF isoreticular to the initial one, with a contracted structure. Thus, the complete transformation involves breaking of covalent bonds, breaking and formation of coordination bonds, and contraction of the crystal structure, with reductions in the cell volume of up to 30.7%, all occurring in a single-crystal to single-crystal manner. Overall, these stepwise isoreticular transformations exemplify the rich chemistry that can be done inside MOF pores. They also underscore the potential of Clip-off Chemistry (*i.e.*, breaking of covalent bonds) to discover new phenomena in MOFs and to synthesize new MOFs or other materials.

5.4 Experimental section

5.4.1 Chemicals and methods

Scandium(III) nitrate hydrate and indium(III) nitrate hydrate were purchased from Alfa Aesar. 4-Carboxycinnamic acid (H_2CCA) was purchased from Biosynth. 1,3,5-Tris(4-carboxyphenyl)benzene (H_3BTB) was purchased from Chemextension. Concentrated nitric acid was purchased from Fischer Scientific. Toluene was purchased from Labkem. Acetic anhydride, chromium(VI) oxide, cyanuric chloride and NaOH were purchased from Sigma-Aldrich. Acetic acid, chloroform, *N,N*-dimethylformamide (DMF), methanol, tetrahydrofuran (THF) and 4,4'-stilbenedicarboxylic acid (H_2sti) were purchased from TCI Chemicals. All the reagents and solvents were used as received without further purification. The deionized water from all the aqueous solutions in the article was obtained from a Milli-Q® system (18.2 MΩ·cm).

Single-Crystal X-Ray Diffraction (SCXRD) data of (In)BCN-20B, (In)BCN-20B′, (In)BCN-20A, (Sc)BCN-20C, (Sc)BCN-20C′ and (Sc)BCN-20A were collected at 100 K at XALOC beamline at ALBA synchrotron (0.82653 Å).[38] Data were indexed, integrated and scaled using the XDS program.[39] Absorption correction was not applied. The structures were solved by direct methods and subsequently refined by correction of F2 against all reflections, using SHELXT2018 within Olex2 package and WinGX (version 2021.3).[40,41] All non-hydrogen atoms were refined with anisotropic thermal parameters by full-matrix least-squares calculations on F2 using the program SHELXL2018.[42] We treated the presence of disordered solvent molecules in the cavities of all structures running solvent mask using Olex2 solvent mask or after location of the cage atoms.[43,44] Hydrogens atoms were inserted at calculated positions and constrained with isotropic thermal parameters.

Powder X-ray Diffraction (PXRD) data were recorded on an X'Pert PRO MPD analytical diffractometer (Panalytical) at 45 KV, 40 mA using CuKα radiation ($\lambda = 1.5418$ Å). Synchrotron X-ray powder diffraction patterns were collected at the BL13-XALOC beamline at the ALBA synchrotron using a capillary of 1.0 mm inner diameter. Experiments were carried out using a monochromatic x-ray beam with a wavelength of $\lambda = 0.82653$ Å. Data were collected using a PILATUS 6M DECTRIS detector. The powder diffraction patterns were radially integrated using FIT2D program.[45]

Proton Nuclear Magnetic Resonance (^{1}H NMR) spectra were collected in a Bruker Avance NEO 400 MHz Spectrometer at "Servei de Ressonància Magnètica Nuclear" from Autonomous University of Barcelona (UAB). Fourier Transform Infrared (FTIR) spectra were acquired on a Bruker Tensor 27FT-IR spectrometer equipped with a Golden Gate diamond attenuated total reflection (ATR) cell. All spectra were collected neat in ambient atmosphere. Optical Microscopy images were obtained with a digital camera connected to a Nikon Eclipse LV100 light microscope and the software NIS-Elements F 3.0. Electrospray Ionization Mass Spectrometry (ESI-MS) spectra were obtained in an Agilent 6210 G1969A LC/MSD TOF mass spectrometer. All the samples were measured in the negative-ionization mode. Ozonolysis was carried out using an ozone generator GHBZO3-E Commercial Ozone Generator from ZonoSistem equipped with ozone analyzer UVOZ-1200.

5.4.2 Synthetic procedures

Synthesis of 4,4′,4″-s-triazine-2,4,6-triyl-tribenzoic acid (H₃TATB). H₃TATB ligand was synthesized as reported elsewhere.[46,47] ^{1}H NMR (400 MHz, DMSO-d_6): δ 8.22 (d, 6H), 8.87 (d, 6 H), 8.64 (d, 6 H), 13.36 (s, 3H) ppm.

Synthesis of (In)BCN-20B. A mixture of In(NO₃)₃·xH₂O (30 mg, 0.10 mmol), H₃TATB (16 mg, 0.04 mmol) and H₂CCA (9 mg, 0.05 mmol) was dispersed in 3 mL of DMF in a 23 mL scintillation vial. The procedure was followed by addition of 0.6 mL of 3.5 M HNO₃ in DMF solution. The vial was sealed and heated in an isothermal oven at 120 °C for 30 h. After cooling down to room temperature, colorless hexagon-shaped crystals suitable for SCXRD were collected by filtration and then washed with DMF (3 × 20 mL) for 3 days. Afterwards, the sample was exchanged by THF (3 × 20 mL) for another 3 days and the resulting (In)BCN-20B crystals were dried at room temperature (25 mg).

Synthesis of (In)BCN-20B′. (In)BCN-20B′ was obtained through a solid-gas ozonolysis reaction using a similar procedure previously reported by our group.[29,32,33] Briefly, ~25 mg of (In)BCN-20B was filtered and air-dried for 15 min and then packed into the plastic tube and subsequently subject to the ozonator setup. The concentration of ozone was set at 15 g/Nm³. The ozonolysis reaction was held for 35 min. Afterwards, the sample was directly collected from the plastic tube.

Synthesis of (In)BCN-20A. (In)BCN-20A was obtained by immersion of ~20 mg of (In)BCN-20B′ into 2 mL of DMF for 1 week. The sample was then exchanged with THF for three times and dried (~20 mg).

Solvent-Assisted Linker Exchange (SALE) Experiments in (In)BCN-20B system. Note that these reactions were done to evaluate the possibility to replace directly the CCA linkers in (In)BCN-20B by BDC linkers, to form (In)BCN-20A. These reactions were done by incubating (In)BCN-20B with a DMF solution of terephthalic acid (H_2BDC), systematically changing the concentration of H_2BDC and the temperature. Briefly, 10 mg of (In)BCN-20B crystals were soaked into the DMF solution containing H_2BDC at different concentrations (1, 2, 4, 10, 20, 40 and 60 mM) under different temperatures (25 °C 65 °C and 85 °C) for 3 days. The supernatant was decanted and refreshed with the DMF solution of H_2BDC every 12 hours. In all cases, we did not observe the transformation from (In)BCN-20B to (In)BCN-20A.

Synthesis of (Sc)BCN-20C. A mixture of $Sc(NO_3)_3 \cdot xH_2O$ (21 mg, 0.08 mmol), H_3BTB (20 mg, 0.05 mmol) and H_2sti (13.6 mg, 0.05 mmol) was dispersed in 3.5 mL of DMF in a 23 mL scintillation vial. The procedure was followed by addition of 0.3 mL of 3.5 M HNO_3 aqueous solution. The vial was sealed and heated in an isothermal oven at 120 °C for 30 h. After cooling down to room temperature, colorless hexagon-shaped crystals suitable for SCXRD were collected by filtration and then washed with DMF (3 × 20 mL) for 3 days. After that, the sample was exchanged by THF (3 × 20 mL) for another 3 days, and the resulting (Sc)BCN-20C crystals were dried at room temperature (26 mg).

Synthesis of (Sc)BCN-20C′. (Sc)BCN-20C′ was obtained through a solid-gas ozonolysis reaction using a similar procedure previously reported by our group.[29,32,33] Briefly, ~25 mg of (Sc)BCN-20C was filtered and air-dried for 15 min and then packed into the plastic tube and subsequently subject to the ozonator setup. The concentration of ozone was set at 15 g/Nm³. The ozonolysis reaction was held for 5 mins. Afterwards, the sample was directly collected from the plastic tube.

Synthesis of (Sc)BCN-20A. (Sc)BCN-20A was obtained by immersion of ~20 mg of (Sc)BCN-20C′ into 2 mL of DMF for 1 week. The sample was then exchanged with THF for three times and dried (~20 mg).

Solvent-Assisted Linker Exchange (SALE) Experiments in (Sc)BCN-20C system. Note that these reactions were done to evaluate the possibility to replace directly the CCA linkers in (Sc)BCN-20C by BDC linkers, to form (Sc)BCN-20A. These reactions were done by incubating (Sc)BCN-20C with a DMF solution of terephthalic acid (H_2BDC), systematically changing the concentration of H_2BDC and the temperature. Briefly, 10 mg of (Sc)BCN-20C crystals were soaked into the DMF solution containing H_2BDC at different concentrations (1, 2, 4, 10, 20, 40 and 60 mM) under different temperatures (25 °C 65 °C and 85 °C) for 3 days. The supernatant was decanted and refreshed with the

DMF solution of H₂BDC every 12 hours. In all cases, we did not observe the transformation from (Sc)BCN-20C to (Sc)BCN-20A.

5.4.3 Characterization: (In)BCN-20B system

Table 5.3 Crystal data and structure refinement for (In)BCN-20B.

Identification code	(In)BCN-20B
CCDC Number	2264126
Empirical formula	$C_{135}H_{90}In_9N_{15}O_{51}$
Formula weight	3771.59
Temperature/K	100.15
Crystal system	trigonal
Space group	$R\bar{3}c$
a/Å	30.820(1)
b/Å	30.820(1)
c/Å	95.540(1)
α/°	90
β/°	90
γ/°	120
Volume/Å³	78592.5(1)
Z	12
$\rho_{calc}g/cm^3$	0.956
μ/mm⁻¹	1.243
F(000)	22248.0
Crystal size/mm³	0.1 × 0.08 × 0.08
Radiation	Synchrotron ($\lambda = 0.82653$ Å)
2Θ range for data collection/°	2.032 to 68.158
Index ranges	$-41 \leq h \leq 41, -37 \leq k \leq 37, -128 \leq l \leq 128$
Reflections collected	332592
Independent reflections	20442 [$R_{int} = 0.0565$, $R_{sigma} = 0.0212$]
Data/restraints/parameters	20442/0/652
Goodness-of-fit on F²	1.092
Final R indexes [I>=2σ (I)]	$R_1 = 0.0622$, $wR_2 = 0.2025$
Final R indexes [all data]	$R_1 = 0.0700$, $wR_2 = 0.2089$
Largest diff. peak/hole / e Å⁻³	1.44/-1.61

Table 5.4 Crystal data and structure refinement for (In)BCN-20B′.

Identification code	(In)BCN-20B′
CCDC Number	2264123
Empirical formula	$C_{129}H_{48}In_9N_{13.5}O_{49.5}$
Formula weight	3612.19
Temperature/K	100.15
Crystal system	trigonal
Space group	$R\overline{3}m$
a/Å	30.8299(10)
b/Å	30.8299(10)
c/Å	47.5919(20)
α/°	90
β/°	90
γ/°	120
Volume/Å^3	39175.0(22)
Z	6
ρ_{calc}g/cm^3	0.919
μ/mm^{-1}	1.243
F(000)	10521.0
Crystal size/mm^3	$0.1 \times 0.07 \times 0.07$
Radiation	Synchrotron ($\lambda = 0.82653$ Å)
2Θ range for data collection/°	3.072 to 53.382
Index ranges	$0 \leq h \leq 28, 0 \leq k \leq 16, -51 \leq l \leq 51$
Reflections collected	108168
Independent reflections	6247 [$R_{int} = 0.1242$, $R_{sigma} = 0.0535$]
Data/restraints/parameters	6247/12/295
Goodness-of-fit on F^2	1.206
Final R indexes [I>=2σ (I)]	$R_1 = 0.1061$, $wR_2 = 0.2997$
Final R indexes [all data]	$R_1 = 0.1279$, $wR_2 = 0.3275$
Largest diff. peak/hole / e Å^{-3}	2.32/-0.95

Table 5.5 Crystal data and structure refinement for (In)BCN-20A.

Identification code	(In)BCN-20A
CCDC Number	2264121
Empirical formula	$C_{120}H_{60}In_9N_{12}O_{48}$
Formula weight	3471.18
Temperature/K	100
Crystal system	trigonal
Space group	$R\overline{3}m$
a/Å	28.7831(5)
b/Å	28.7831(5)
c/Å	47.7075(15)
α/°	90
β/°	90
γ/°	120
Volume/Å^3	34228.9(11)
Z	6
$\rho_{calc}g/cm^3$	1.010
μ/mm^{-1}	1.419
F(000)	10134.0
Crystal size/mm^3	0.11 × 0.09 × 0.09
Radiation	Synchrotron (λ = 0.82653 Å)
2Θ range for data collection/°	2.748 to 54.628
Index ranges	$0 \le h \le 27, 0 \le k \le 15, -52 \le l \le 52$
Reflections collected	99893
Independent reflections	5836 [R_{int} = 0.1013, R_{sigma} = 0.0450]
Data/restraints/parameters	5836/0/304
Goodness-of-fit on F^2	1.161
Final R indexes [I>=2σ (I)]	R_1 = 0.1052, wR_2 = 0.2921
Final R indexes [all data]	R_1 = 0.1232, wR_2 = 0.3116
Largest diff. peak/hole / e Å^{-3}	1.99/-0.62

PXRD
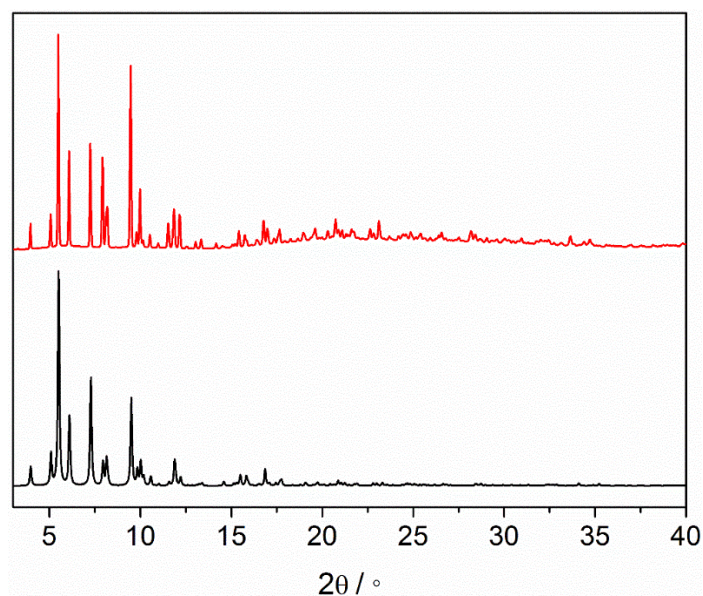
Figure 5.20 PXRD patterns of simulated (In)BCN-20A (black) and as-made (In)BCN-20A (red).

Optical microscope
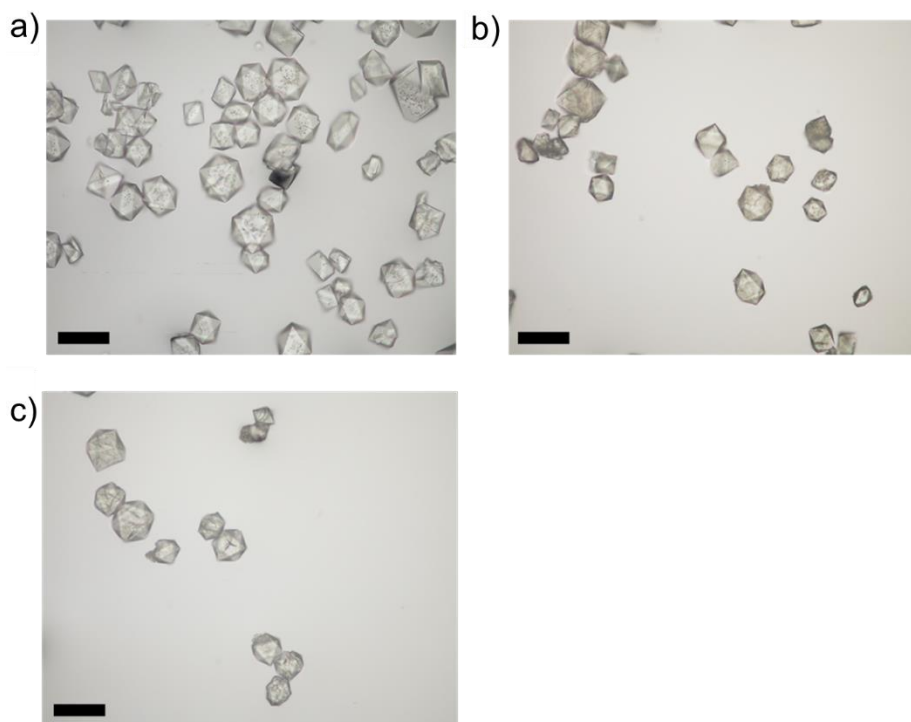
Figure 5.21 Comparison between the optical microscopy images of (a) (In)BCN-20B, (b) (In)BCN-20B′, (c) (In)BCN-20A. Scale bars: 10 μm. Note that no apparent damage of the crystals is observed during the transformation from (In)BCN-20B to (In)BCN-20A.

5.4.4 Characterization: (Sc)BCN-20C system

Table 5.6 Crystal data and structure refinement for (Sc)BCN-20C.

Identification code	(Sc)BCN-20C
CCDC Number	2264124
Empirical formula	$C_{325}H_{178}N_3O_{99}Sc_{18}$
Formula weight	6517.97
Temperature/K	100.00
Crystal system	monoclinic
Space group	C2/c
a/Å	60.2793(3)
b/Å	34.7226(2)
c/Å	37.1357(1)
α/°	90
β/°	123.5062(3)
γ/°	90
Volume/Å^3	64811.2
Z	4
ρ_{calc}g/cm^3	0.668
μ/mm^{-1}	0.329
F(000)	13276.0
Crystal size/mm^3	0.07 × 0.06 × 0.06
Radiation	Synchrotron (λ = 0.82653 Å)
2Θ range for data collection/°	1.658 to 67.832
Index ranges	-74 ≤ h ≤ 62, 0 ≤ k ≤ 39, 0 ≤ l ≤ 45
Reflections collected	399678
Independent reflections	69415 [R_{int} = 0.0717, R_{sigma} = 0.0580]
Data/restraints/parameters	69415/0/1996
Goodness-of-fit on F^2	1.072
Final R indexes [I>=2σ (I)]	R_1 = 0.0726, wR_2 = 0.2328
Final R indexes [all data]	R_1 = 0.0850, wR_2 = 0.2419
Largest diff. peak/hole / e Å^{-3}	1.72/-0.92

Table 5.7 Crystal data and structure refinement for (Sc)BCN-20C′.

Identification code	(Sc)BCN-20C′
CCDC Number	2264122
Empirical formula	$C_{164}H_{92}O_{48}Sc_9$
Formula weight	3235.01
Temperature/K	100.00
Crystal system	monoclinic
Space group	C2/m
a/Å	37.5283(2)
b/Å	35.3742(3)
c/Å	24.7609(2)
α/°	90
β/°	94.2397(5)
γ/°	90
Volume/Å^3	32780.9(3)
Z	4
ρ_{calc}g/cm^3	0.655
μ/mm^{-1}	0.324
F(000)	6596.0
Crystal size/mm^3	0.08 × 0.07 × 0.06
Radiation	Synchrotron (λ = 0.82653 Å)
2Θ range for data collection/°	1.918 to 62.21
Index ranges	$-46 \leq h \leq 46, 0 \leq k \leq 43, 0 \leq l \leq 30$
Reflections collected	189834
Independent reflections	33389 [R_{int} = 0.0602, R_{sigma} = 0.0453]
Data/restraints/parameters	33389/0/914
Goodness-of-fit on F^2	1.100
Final R indexes [I>=2σ (I)]	R_1 = 0.0924, wR_2 = 0.2906
Final R indexes [all data]	R_1 = 0.1169, wR_2 = 0.3167
Largest diff. peak/hole / e Å^{-3}	1.26/-0.61

Table 5.8 Crystal data and structure refinement for (Sc)BCN-20A.

Identification code	(Sc)BCN-20A
CCDC Number	2264125
Empirical formula	$C_{135}O_{48}Sc_9$
Formula weight	2793.99
Temperature/K	100.00
Crystal system	trigonal
Space group	$R\bar{3}c$
a/Å	28.6819(8)
b/Å	28.6819(8)
c/Å	95.6062(43)
α/°	90
β/°	90
γ/°	120
Volume/Å^3	68113.4(33)
Z	12
ρ_{calc}g/cm^3	0.817
μ/mm^{-1}	0.459
F(000)	16596.0
Crystal size/mm^3	0.06 × 0.06 × 0.06
Radiation	Synchrotron (λ = 0.82635 Å)
2Θ range for data collection/°	2.75 to 32.202
Index ranges	$0 \leq h \leq 16, 0 \leq k \leq 9, -63 \leq l \leq 64$
Reflections collected	45160
Independent reflections	2406 [R_{int} = 0.1354, R_{sigma} = 0.1093]
Data/restraints/parameters	2406/73/331
Goodness-of-fit on F^2	1.437
Final R indexes [I>=2σ (I)]	R_1 = 0.1343, wR_2 = 0.3641
Final R indexes [all data]	R_1 = 0.1654, wR_2 = 0.3940
Largest diff. peak/hole / e Å^{-3}	0.42/-0.31

PXRD
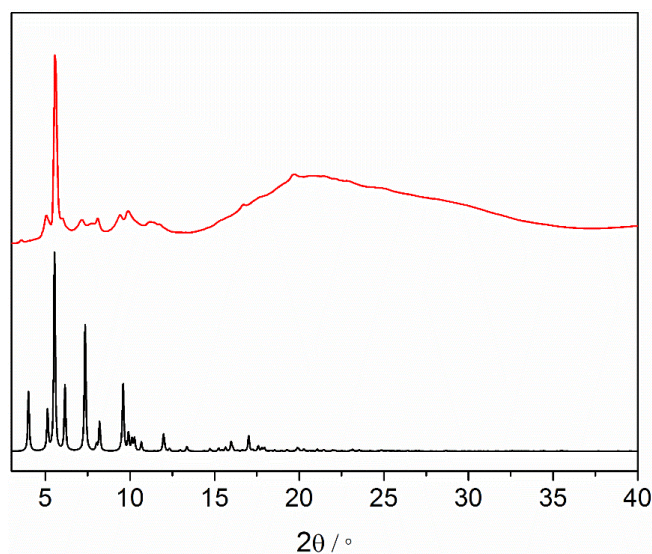
Figure 5.22 PXRD of simulated (Sc)BCN-20A (black) and as-made (Sc)BCN-20A (red).

Optical Microscope
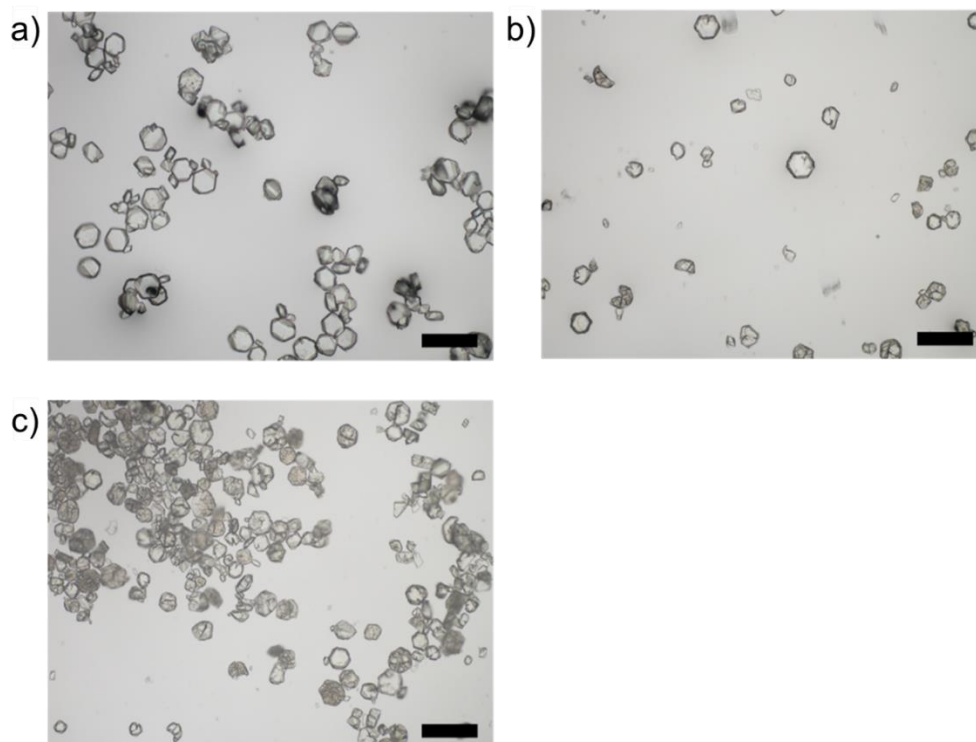
Figure 5.23 Comparison between the optical microscopy images of (a) (Sc)BCN-20C, (b) (Sc)BCN-20C′, (c) (Sc)BCN-20A. Scale bars: 10 μm. Note that no apparent damage of the crystals is observed during the transformation from (Sc)BCN-20C to (Sc)BCN-20A.

5.5 References

(1) Zhou, H.-C.; Long, J. R.; Yaghi, O. M. *Chem. Rev.* **2012**, *112*, 673-674.

(2) Howarth, A. J.; Liu, Y.; Li, P.; Li, Z.; Wang, T. C.; Hupp, J. T.; Farha, O. K. *Nat. Rev. Mater.* **2016**, *1*, 15018.

(3) Yaghi, O. M.; O'Keeffe, M.; Ockwig, N. W.; Chae, H. K.; Eddaoudi, M.; Kim, J. *Nature* **2003**, *423*, 705-714.

(4) Chen, Z.; Hanna, S. L.; Redfern, L. R.; Alezi, D.; Islamoglu, T.; Farha, O. K. *Coord. Chem. Rev.* **2019**, *386*, 32-49.

(5) Jiang, H.; Alezi, D.; Eddaoudi, M. *Nat. Rev. Mater.* **2021**, *6*, 466-487.

(6) Yaghi, O. M. *Molecular Frontiers Journal* **2019**, *03*, 66-83.

(7) Eddaoudi, M.; Kim, J.; Rosi, N.; Vodak, D.; Wachter, J.; O'Keeffe, M.; Yaghi, O. M. *Science* **2002**, *295*, 469-472.

(8) Deng, H.; Grunder, S.; Cordova, K. E.; Valente, C.; Furukawa, H.; Hmadeh, M.; Gándara, F.; Whalley, A. C.; Liu, Z.; Asahina, S.; Kazumori, H.; O'Keeffe, M.; Terasaki, O.; Stoddart, J. F.; Yaghi, O. M. *Science* **2012**, *336*, 1018-1023.

(9) Li, P.; Chen, Q.; Wang, T. C.; Vermeulen, N. A.; Mehdi, B. L.; Dohnalkova, A.; Browning, N. D.; Shen, D.; Anderson, R.; Gómez-Gualdrón, D. A.; Cetin, F. M.; Jagiello, J.; Asiri, A. M.; Stoddart, J. F.; Farha, O. K. *Chem* **2018**, *4*, 1022-1034.

(10) Wang, Z.; Cohen, S. M. *Chem. Soc. Rev.* **2009**, *38*, 1315-1329.

(11) Deria, P.; Mondloch, J. E.; Karagiaridi, O.; Bury, W.; Hupp, J. T.; Farha, O. K. *Chem. Soc. Rev.* **2014**, *43*, 5896-5912.

(12) Kirchon, A.; Feng, L.; Drake, H. F.; Joseph, E. A.; Zhou, H.-C. *Chem. Soc. Rev.* **2018**, *47*, 8611-8638.

(13) Bury, W.; Fairen-Jimenez, D.; Lalonde, M. B.; Snurr, R. Q.; Farha, O. K.; Hupp, J. T. *Chem. Mater.* **2013**, *25*, 739-744.

(14) Feng, L.; Yuan, S.; Qin, J.-S.; Wang, Y.; Kirchon, A.; Qiu, D.; Cheng, L.; Madrahimov, S. T.; Zhou, H.-C. *Matter* **2019**, *1*, 156-167.

(15) Li, Y.; Su, J.; Zhao, Y.; Feng, L.; Gao, L.; Xu, X.; Yin, Y.; Liu, Y.; Xiao, P.; Yuan, L.; Qin, J.-S.; Wang, Y.; Yuan, S.; Zheng, H.; Zuo, J.-L. *J. Am. Chem. Soc.* **2023**, *145*, 10227–10235.

(16) Li, T.; Kozlowski, M. T.; Doud, E. A.; Blakely, M. N.; Rosi, N. L. *J. Am. Chem. Soc.* **2013**, *135*, 11688-11691.

(17) Yuan, S.; Zhang, P.; Zhang, L.; Garcia-Esparza, A. T.; Sokaras, D.; Qin, J.-S.; Feng, L.; Day, G. S.; Chen, W.; Drake, H. F.; Elumalai, P.; Madrahimov, S. T.; Sun, D.; Zhou, H.-C. *J. Am. Chem. Soc.* **2018**, *140*, 10814-10819.

(18) Yuan, S.; Qin, J.-S.; Su, J.; Li, B.; Li, J.; Chen, W.; Drake, H. F.; Zhang, P.; Yuan, D.; Zuo, J.; Zhou, H.-C. *Angew. Chem. Int. Ed.* **2018**, *57*, 12578-12583.

(19) Burnett, B. J.; Barron, P. M.; Hu, C.; Choe, W. *J. Am. Chem. Soc.* **2011**, *133*, 9984-9987.

(20) Cao, L.-H.; Liu, X.; Tang, X.-H.; Liu, J.; Xu, X.-Q.; Zang, S.-Q.; Ma, Y.-M. *Chem. Commun.* **2019**, *55*, 12671-12674.

(21) Xiao, Y.; Chen, Y.; Wang, W.; Yang, H.; Hong, A. N.; Bu, X.; Feng, P. *J. Am. Chem. Soc.* **2023**, *145*, 10980-10986.

(22) Krause, S.; Bon, V.; Senkovska, I.; Stoeck, U.; Wallacher, D.; Többens, D. M.; Zander, S.; Pillai, R. S.; Maurin, G.; Coudert, F.-X.; Kaskel, S. *Nature* **2016**, *532*, 348-352.

(23) Schneemann, A.; Bon, V.; Schwedler, I.; Senkovska, I.; Kaskel, S.; Fischer, R. A. *Chem. Soc. Rev.* **2014**, *43*, 6062-6096.

(24) Douvali, A.; Tsipis, A. C.; Eliseeva, S. V.; Petoud, S.; Papaefstathiou, G. S.; Malliakas, C. D.; Papadas, I.; Armatas, G. S.; Margiolaki, I.; Kanatzidis, M. G. *Angew. Chem. Int. Ed.* **2015**, *127*, 1671-1676.

(25) Chang, Z.; Yang, D.-H.; Xu, J.; Hu, T.-L.; Bu, X.-H. *Adv. Mater.* **2015**, *27*, 5432-5441.

(26) Zhang, Y.; Zhang, X.; Lyu, J.; Otake, K.-i.; Wang, X.; Redfern, L. R.; Malliakas, C. D.; Li, Z.; Islamoglu, T.; Wang, B.; Farha, O. K. *J. Am. Chem. Soc.* **2018**, *140*, 11179-11183.

(27) Chen, X.; Xie, H.; Lorenzo, E. R.; Zeman, C. J. I. V.; Qi, Y.; Syed, Z. H.; Stone, A. E. B. S.; Wang, Y.; Goswami, S.; Li, P.; Islamoglu, T.; Weiss, E. A.; Hupp, J. T.; Schatz, G. C.; Wasielewski, M. R.; Farha, O. K. *J. Am. Chem. Soc.* **2022**, *144*, 2685-2693.

(28) Yang, H.; Chen, Y.; Dang, C.; Hong, A. N.; Feng, P.; Bu, X. *J. Am. Chem. Soc.* **2022**, *144*, 20221-20226.

(29) Yang, Y.; Broto-Ribas, A.; Ortín-Rubio, B.; Imaz, I.; Gándara, F.; Carné-Sánchez, A.; Guillerm, V.; Jurado, S.; Busqué, F.; Juanhuix, J.; Maspoch, D. *Angew. Chem. Int. Ed.* **2022**, *61*, e202111228.

(30) Chevreau, H.; Devic, T.; Salles, F.; Maurin, G.; Stock, N.; Serre, C. *Angew. Chem. Int. Ed.* **2013**, *52*, 5056-5060.

(31) Prasad, R. R. R.; Pleass, C.; Rigg, A. L.; Cordes, D. B.; Lozinska, M. M.; Georgieva, V. M.; Hoffmann, F.; Slawin, A. M. Z.; Wright, P. A. *CrystEngComm* **2021**, *23*, 804-812.

(32) Albalad, J.; Xu, H.; Gándara, F.; Haouas, M.; Martineau-Corcos, C.; Mas-Ballesté, R.; Barnett, S. A.; Juanhuix, J.; Imaz, I.; Maspoch, D. *J. Am. Chem. Soc.* **2018**, *140*, 2028-2031.

(33) Guillerm, V.; Xu, H.; Albalad, J.; Imaz, I.; Maspoch, D. *J. Am. Chem. Soc.* **2018**, *140*, 15022-15030.

(34) Ragon, F.; Campo, B.; Yang, Q.; Martineau, C.; Wiersum, A. D.; Lago, A.; Guillerm, V.; Hemsley, C.; Eubank, J. F.; Vishnuvarthan, M.; Taulelle, F.; Horcajada, P.; Vimont, A.; Llewellyn, P. L.; Daturi, M.; Devautour-Vinot, S.; Maurin, G.; Serre, C.; Devic, T.; Clet, G. *J. Mater. Chem. A* **2015**, *3*, 3294-3309.

(35) Hadjiivanov, K. I.; Panayotov, D. A.; Mihaylov, M. Y.; Ivanova, E. Z.; Chakarova, K. K.; Andonova, S. M.; Drenchev, N. L. *Chem. Rev.* **2021**, *121*, 1286-1424.

(36) Blatov, V. A.; Shevchenko, A. P.; Proserpio, D. M. *Crystal Growth & Design* **2014**, *14*, 3576-3586.

(37) Reinares-Fisac, D.; Aguirre-Díaz, L. M.; Iglesias, M.; Snejko, N.; Gutiérrez-Puebla, E.; Monge, M. Á.; Gándara, F. *J. Am. Chem. Soc.* **2016**, *138*, 9089-9092.

(38) Juanhuix, J.; Gil-Ortiz, F.; Cuní, G.; Colldelram, C.; Nicolás, J.; Lidón, J.; Boter, E.; Ruget, C.; Ferrer, S.; Benach, J. *J. Synchrotron Radiat.* **2014**, *21*, 679-689.

(39) Kabsch, W. *Acta Cryst. D* **2010**, *66*, 125-132.

(40) Sheldrick, G. M. *Acta Cryst. A* **2015**, *71*, 3-8.

(41) Farrugia, L. J. *J. Appl. Cryst.* **2012**, *45*, 849-854.

(42) Sheldrick, G. M. *J. Acta Cryst. C* **2015**, *71*, 3-8.

(43) Dolomanov, O. V.; Bourhis, L. J.; Gildea, R. J.; Howard, J. A. K.; Puschmann, H. J. *Appl. Cryst.* **2009**, *42*, 339-341.

(44) Spek, A. L. *J. Appl. Crystallogr.* **2003**, *36*, 7-13.

(45) A P Hammersley, *ESRF Internal Report*, **ESRF97HA02T**, ``FIT2D: An Introduction and Overview'', (1997).

(46) Park, J.; Feng, D.; Zhou, H.-C. *J. Am. Chem. Soc.* **2015**, *137*, 11801-11809.

(47) Zou, L.; Feng, D.; Liu, T.-F.; Chen, Y.-P.; Yuan, S.; Wang, K.; Wang, X.; Fordham, S.; Zhou, H.-C. *Chem. Sci.* **2016**, *7*, 1063-1069.

Chapter 6

Conclusions

General conclusions

This dissertation has focused on the cleavage of organic linkers containing covalent olefinic bonds in 3-D MOFs. If these cleavable bonds are disordered inside the structure, the hierarchically porous MOFs containing mesopores are able to be synthesized. If these cleavable bonds are located in an ordered fashion, new structures and phenomena in MOFs can be uncovered. In the latter case, we have dedicated to establish the basis for using Clip-off Chemistry as a new alternative synthetic strategy to generate new molecules and materials.

In the first step, we have prepared a hierarchically porous UiO-type Zr-**fcu**-MOF and used it to prepare a porous motor. In particular, by mixing 4,4′-azobenzenedicarboxylic acid (H$_2$azo; ozone-inert linker) with olefin-containing 4,4′-stilbenedicarboxylic acid (H$_2$sti; ozone-active linker) at a molar ratio of 7:3, we successfully synthesized a microporous Zr-**fcu**-MOF referred to as Zr-**fcu**-azo/sti-30%. Subsequent ozonolysis treatment and acid washing of this MOF showed the complete cleavage and removal of all sti linkers, resulting in the fusion of micropores into mesopores within the framework. Thus, a hierarchically porous Zr-**fcu**-MOF containing 24% of mesopores has been made. Inspired by these created mesoporosity, our focus then shifted toward encapsulating a sizable molecule, the enzyme catalase (size: 6-10 nm), inside this ozonated Zr-**fcu**-MOF. Excitingly, the encapsulation experiments confirmed the presence of catalase inside the MOF, quantified by Bradford protein assay. The enzyme was found to be hosted in the mesopores and compartmentalized at the subsurface of the MOF crystals. In the presence of H$_2$O$_2$ as a fuel, the MOF crystals (MOFtors) exhibited a jet-like propulsion through enzymatic generation of O$_2$ bubbles. Remarkably, the speed of MOFtors was able to be controlled by varying enzyme incubation times and H$_2$O$_2$ concentrations. Moreover, the remaining free space, encompassing both micro- and mesopores, proved useful for adsorbing additional targeted species. This capability was verified by testing MOFtors for the capture of rhodamine B, a common water pollutant, during its self-propulsion in water.
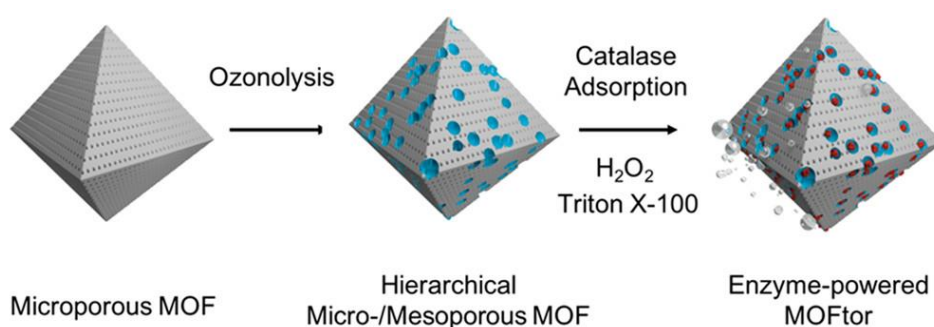
Next, we switch to a more controllable system, aiming to localize the olefin-containing linkers at precise crystallographic positions within the framework, as opposed to their random distribution. To this end, we extend the concept of bond breaking to reticular materials by introducing a new synthetic approach called Clip-off Chemistry. This strategy allows us to predict precisely the outcomes whether they be clusters, molecules, or new framework structures. Based on this concept, we started the first clip-off synthesis of a new 3-D MOF from a 3-D MOF precursor. Our focus was on a structure built from one type of polytopic linker that contains both cleavable and non-cleavable circuits. By selectively removing the cleavable circuits that involve cleavable bonds, we expected to obtain a new structure only built from the non-cleaved circuits. This would likely result in a potentially different topology for this new structure. As proof-of-concept, we chose two different 3-D MOF precursors for this study, Zr-**scu**-MOF and Sc-**pcu**-MOF. These two 3-D MOF were constructed from the same tetratopic linker, 5-[2-(3,5-dicarboxyphenyl)ethenyl]benzene-1,3-dicarboxylate (L_2), where the olefinic groups were located at specific positions. Subsequent ozonolysis treatment of these MOFs triggered the disassembly of certain circuits of connection in their underlying nets, resulting in the corresponding topology transformations from (4,8)-c **scu** to 6-c **pcu** and from (4,6)-c **soc** to 6-c **pcu**. Remarkably, we demonstrated that bond breaking in these structures could be precisely controlled at the molecular level. The process was periodic, quantitative, and selective. It effectively occured in either solid or liquid phases and took place in a single-crystal-to-single-crystal fashion.

(4,8)-c **scu**   6-c **pcu**   (4,6)-c **soc**   6-c **pcu**
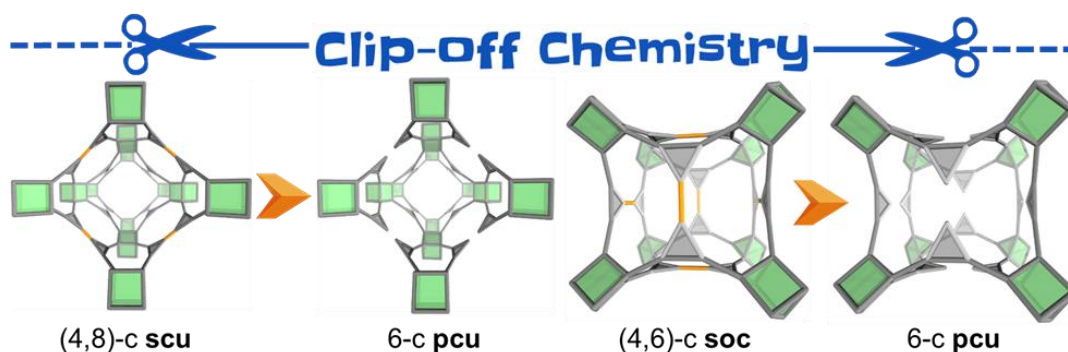
Finally, we aim to extend the potential of clip-off synthesis from 3-D to 3-D MOFs by increasing the complexity of the precursor materials. In this case, our focus was on multicomponent MOFs, where mixed linkers are situated at distinct crystallographic positions, with the presence of (at least) one of these linkers containing olefinic bonds. With this in mind, we selected MIL-142 family as the ideal candidates which allowed us to utilize two geometrically distinct linkers, a cleavable ditopic linker and a non-cleavable tritopic linker, for the MOF construction based on the well-known isoreticular principle. Thus, we successfully synthesized two new MOFs, namely (In)BCN-20B and (Sc)BCN-20C,

isoreticular to MIL-142 family. By selective and quantitative cleavage of their ditopic linkers via ozonolysis, we were able to obtain their ozonated products, a pair of monocoordinated linkers, of which one was terminated with a carboxylic acid group whereas the other ended with an aldehyde group. Through subsequent incubation of these crystals in DMF, the latter ligand could spontaneously decoordinate from the metal center. This ligand removal process conferred the structure with dynamic behavior involving the migration and subsequent coordination of another monocoordinated ligand with a free carboxylic acid group to this open metal site. In what we called "self-healing behavior", the metal clusters that had been disconnected during the linker cleavage, reconnected to form a new MOF that was isoreticular to the initial one but with a contracted structure. This stepwise isoreticular contraction involved a series of bond forming and breaking processes, starting with the breaking of a covalent bond, followed by the breaking of a coordination bond, and ultimately the formation of a new coordination bond. Remarkably, the overall lattice contraction in the cell volume could reach up to 30.7%. Moreover, considering that the single crystal character of the parent MOF was retained throughout the entire transformation, we were able to obtain invaluable crystallographic snapshots of the stepwise processes by using SCXRD.
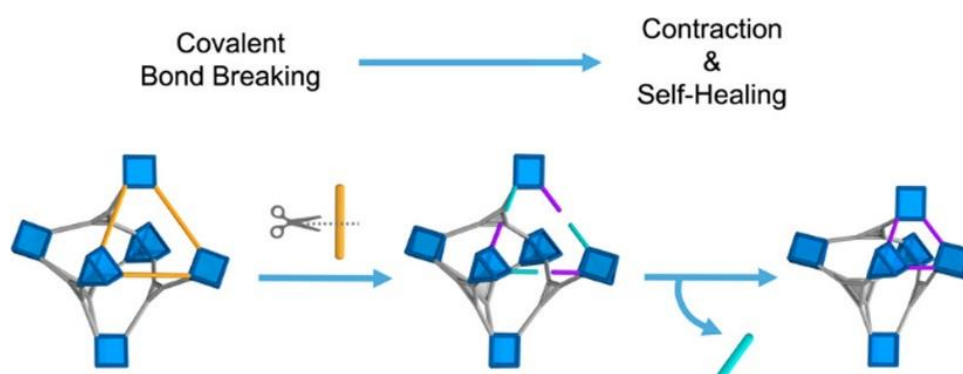
These findings presented in this dissertation demonstrate the ability of covalent bond breaking inside MOFs to not only offer specific "defects" for accessing new porosity profiles within the framework but also serve as a new strategy (Clip-off Chemistry) for synthesizing unprecedented structures or molecules that are hard to be achieved through conventional bottom-up methodology. It also opens new avenues for discovering new phenomena in MOFs. Moreover, the scope of Clip-off Chemistry extends beyond MOFs and can be applied to other porous materials including MOPs and COFs. This expansion opens up exciting avenues for designing and synthesizing limitless molecules and materials with a broad range of compositions, ranging from purely organic to metal-organic, and dimensionalities (*e.g.* 3-D to 0-D). As a result, this approach paves the way for a vast array of possibilities in the field of reticular chemistry and materials science, offering new opportunities for the innovation and discovery.

Glossary

General Acronyms

MOF	Metal–organic framework
COF	Covalent–organic framework
MOP	Metal–organic polyhedra
IRMOF	Isoreticular MOF
RCSR	Reticular Chemistry Structure Resource
3-D MOFs	Three-dimensional MOFs
SBU	Secondary building unit
MBB	Molecular building block
PSM	Post–synthetic modification
SALE	Solvent–assisted linker exchange
MTV MOFs	Multivariate MOFs
4-c	4-connected
CLSM	Confocal laser scanning microscopy
NMR	Nuclear magnetic resonance
FESEM	Field-emission scanning electron microscopy
BET (S_{BET})	Brunauer–Emmett–Teller surface area
FTIR	Fourier transform infrared spectroscopy
ESI-MS	Electrospray ionization mass spectrometry
PXRD	Powder X-ray diffraction
SCXRD	Single-crystal X-ray diffraction
UV-vis	Ultraviolet-visible
DMF	*N,N*-dimethylformamide
DMSO	Dimethyl sulfoxide
DEF	*N,N*-diethylformamide
THF	Tetrahydrofuran
FTIC	Fluorescein isothiocyanate

Materials Acronyms

UiO	Universitetet i Oslo
HKUST	Hong Kong University of Science and Technology
MIL	Material Institute Lavoisier
PCN	Porous Coordination Network
NU	Northwestern University
BCN	Barcelona Material

Ligands Acronyms

BDC	Terephthalate/1,4-benzenedicarboxylate
BTC	1,3,5-Benzenetricarboxylate
olz	(E)-5,5′-(diazene-1,2-diyl)bis(2-oxidobenzoate)
dcpby	2,2'-bipyridine-dicarboxylate
bpdc	Biphenyldicarboxylate
TzDB	4,4'-(1,2,4,5-tetrazine-3,6-diyl)dibenzoate
TCPP	Tetrakis(4-carboxyphenyl)porphyrin
DPDS	4,4'-dipyridyl disulfide
CBAB	4-carboxybenzylidene-4-aminobenzate
TPDC	Terphenyl-4,4''-dicarboxylate
BDC-NH$_2$	2-amino-1,4-benzenedicarboxylate
EBDC	2-ethenylbenzene-1,4-dicarboxylate
pdac	1,4-phenylenediacrylate
bpdc	4,4'-biphenyldicarboxylate
4-FBA	4-formylbenzoate
BDC	Terephthalate/1,4-benzenedicarboxylate
sti	4,4'-stilbenedicarboxylate
azo	4,4'-azobenzene-dicarboxylate
CCA	4-carboxycinnamate
NDC	Naphthalene-2,6-dicarboxylate
BTB	4,4′,4″-benzene-1,3,5-triyl-trisbenzoate
TATB	4,4',4''-s-triazine-2,4,6-triyl-tribenzoate
Linker L$_1$	5-[(3,5-dicarboxyphenyl)diazenyl]benzene-1,3-dicarboxylate
Linker L$_2$	5-[2-(3,5-dicarboxyphenyl)ethenyl]benzene-1,3-dicarboxylate

Topology Acronyms

rht	rhombicuboctahedron, triangle
fcu	face-centered cubic
reo	ReO$_3$
spn	spinel
hcb	honeycomb
pcu	primitive cubic

scu	square, cube
soc	square, octahedron
nht	Nguyen Ha, Nguyen Trang
ftw	four, twelve
gea	Guillerm, Eddaoudi, net A
tbo	twisted boracite
sql	square lattice
kgm	Kagomé lattice
ths	$ThSi_2$

Annex

List of publications

The scientific publications of the author during the PhD thesis are listed below:

1. **Yang, Y.**;† Arque, X.;† Patino, T.; Guillerm, V.; Blersch, P. R.; Perez-Carvajal, J.; Imaz, I.; Maspoch, D.; Sanchez, S. Enzyme-powered porous micromotors built from a hierarchical micro- and mesoporous UiO-type metal-organic framework. *J. Am. Chem. Soc.* **2020**, *142*, 20962-20967. († co-first author)

2. **Yang, Y.**;† Broto-Ribas, A.;† Ortín-Rubio, B.;† Imaz, I.; Gándara, F.; Carné-Sánchez, A.; Guillerm, V.; Jurado, S.; Busqué, F.; Juanhuix, J.; Maspoch, D. Clip-off Chemistry: Synthesis by Programmed Disassembly of Reticular Materials. *Angew. Chem. Int. Ed.* **2022**, *61*, e202111228. († co-first author)

3. **Yang, Y.**; Fernández-Seriñán, P.; Imaz, I.; Gándara, F.; Handke, M.; Ortín-Rubio, B.; Juanhuix, J.; Maspoch, D. Isoreticular Contraction of Metal–Organic Frameworks Induced by Cleavage of Covalent Bonds. *J. Am. Chem. Soc.*, **2023**, 145, 17398-17405.

4. Zhang, T.; Liu, H.; Han, X.; Biset-Peiró, M.; **Yang, Y.**; Imaz, I.; Maspoch, D.; Yang, B.; Morante, J. R.; Arbiol, J. Improvement of carbon dioxide electroreduction by crystal surface modification of ZIF-8. *Dalton Trans.*, **2023**, 52, 5234-5242.

5. Broto-Ribas, A.; Ruiz-Relaño, S.; Albalad, J.; **Yang, Y.**; Gándara, F.; Juanhuix, J.; Imaz, I.; Maspoch, D. Retrosynthetic analysis applied to Clip-off Chemistry: synthesis of four Rh(II)-based complexes as proof-of-concept. *Angew. Chem. Int. Ed.* **2023**, e202310354.

J|A|C|S

JOURNAL OF THE AMERICAN CHEMICAL SOCIETY

Communication

Enzyme-Powered Porous Micromotors Built from a Hierarchical Micro- and Mesoporous UiO-Type Metal−Organic Framework

Yunhui Yang,[#] Xavier Arqué,[#] Tania Patiño,* Vincent Guillerm, Pascal-Raphael Blersch, Javier Pérez-Carvajal, Inhar Imaz,* Daniel Maspoch,* and Samuel Sánchez*

Read Online

ACCESS | Metrics & More | Article Recommendations | Supporting Information

ABSTRACT: Here, we report the design, synthesis, and functional testing of enzyme-powered porous micromotors built from a metal−organic framework (MOF). We began by subjecting a presynthesized microporous UiO-type MOF to ozonolysis, to confer it with mesopores sufficiently large to adsorb and host the enzyme catalase (size: 6−10 nm). We then encapsulated catalase inside the mesopores, observing that they are hosted in those mesopores located at the subsurface of the MOF crystals. In the presence of H_2O_2 fuel, MOF motors (or MOFtors) exhibit jet-like propulsion enabled by enzymatic generation of oxygen bubbles. Moreover, thanks to their hierarchical pore system, the MOFtors retain sufficient free space for adsorption of additional targeted species, which we validated by testing a MOFtor for removal of rhodamine B during self-propulsion.

The field of bioinspired micro- and nanomotors has evolved extensively so many synthetic structures have been reported over the past decade.[1] From the various ways these tiny motors can be powered, self-propulsion *via* chemical reactions is one of the most widely used being natural catalysts, such as enzymes, a promising alternative to achieve efficient and biocompatible systems. Several milestones toward real-world applications of such motors have been achieved, primarily in the fields of biomedicine[2−7] and environmental applications.[8−11] In those applications, porosity of the motor chassis is crucial, as it enables adsorption, transport, and/or release of cargo (e.g., drugs or pollutants),[8,12,13] its performance being dictated mainly by its sorption capacity and its cargo transport versatility.[14−17]

Among the alternatives available for developing enzyme-powered porous motors, metal−organic frameworks (MOFs) are an attractive choice.[18,19] MOFs exhibit very high surface areas, tunable pore sizes and shapes, and adjustable pore-surface functionality, suggesting their potential for myriad applications, including gas storage, separation, catalysis, contaminant removal, and drug delivery.[20,21] In fact, researchers have used MOFs to build a stable and adaptable chassis for micro- and nanomotors,[18,22] in which motion is based on Marangoni effects,[23−26] magnetically driven cork-screw locomotion,[27,28] or bubble propulsion.[29−35] In parallel, researchers have demonstrated that biomolecules, particularly enzymes, can be encapsulated within MOFs for protection and to confer the MOFs with new functionalities, mainly in catalysis. For instance, Falcaro, Doonan, and co-workers explored biomimetic mineralization and controlled co-precipitation to encapsulate several enzymes in ZIF-8.[36] Another challenging approach has required custom-made linkers to assemble MOFs with pores large enough (mesopores) to adsorb and host enzymes. For instance, the groups of Farha,[37] Zhou,[38] and Ma[39] exploited MOF mesopores to encapsulate various enzymes. Importantly, for a MOF to be used as the

chassis of an enzyme-powered porous motor, it must combine mesopores sufficiently large to host the enzyme used for propulsion, with micropores of an appropriate size to adsorb and release additional guest species.

Herein we report the design of an enzyme-powered, porous, MOF-based micromotor via compartmentalized encapsulation of the enzyme catalase within a hierarchical micro- and mesoporous MOF (Figure 1a). We chose catalase as a model enzyme, as it has been extensively used to induce ballistic propulsion through bubble propulsion via decomposition of H_2O_2.[40−43] Moreover, we selected a UiO-type Zr-MOF as the chassis because of its well-known water stability,[44] a condition that should fulfill any MOF intended to be used for the fabrication of motors powered by enzymatic reactions. In this design, another essential condition was the use of a UiO-type MOF with mesopores sufficiently large to host catalase (size: 6−10 nm) and micropores that preserve the ability to adsorb and/or release additional guest species. In order to rationally design this MOF, we decided to use an approach that we had developed earlier, whereby we subject presynthesized micro-porous MOFs functionalized with a mixture of linkers that do or do not contain olefins to ozonolysis, which selectively oxidizes the olefins to generate new mesopores.[45,46] To do so, we subjected a presynthesized UiO-type MOF to this ozonolysis process and then exploited the newly formed mesopores to host the catalase molecules.

We began with the synthesis of a UiO-type Zr-**fcu**-MOF (hereafter called *Zr*-**fcu**-*azo/sti-30%*), formed by mixing 4,4′-

20962
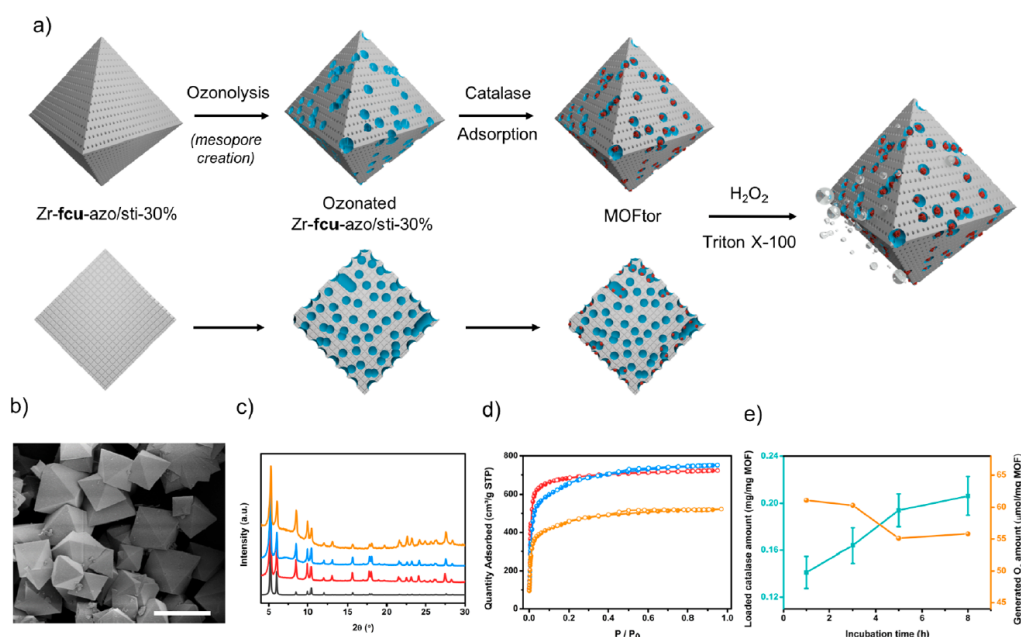
Figure 1. (a) Schematic representation of the multistep process used to synthesize the MOFtors. Cross sections of the crystals at bottom. (b) FESEM image of ozonated Zr-**fcu**-azo/sti-30%. Scale bar: 10 μm. (c, d) PXRD and N_2 isotherms of Zr-**fcu**-azo/sti-30% before (red) and after (blue) ozonolysis and after catalase encapsulation (orange). In (c), simulated pattern for Zr-**fcu**-azo (black). (e) Encapsulation efficiency (blue) and oxygen generated (orange) vs time.

azobenzenedicarboxylic acid (H$_2$azo) with olefin-containing 4,4′-stilbenedicarboxylic acid (H$_2$sti) linkers at a molar ratio of 7:3, respectively. Field-emission scanning electron microscopy (FESEM) revealed the formation of octahedral microcrystals (size: 2−15 μm) characteristic of Zr-**fcu**-MOFs (Figure S3), and powder X-ray diffraction (PXRD; Figure 1c) confirmed the phase purity. ^{1}H NMR of digested crystals confirmed the formation of Zr-**fcu**-azo/sti-30% in an azo/sti molar ratio of 7:3 (Figure S4). Moreover, N_2 sorption analysis (77 K) confirmed the microporosity of Zr-**fcu**-azo/sti-30%, with a Brunauer−Emmett−Teller surface area (S_{BET}) of 2830 m^2/g (Figures 1d and S5).

Next, we selectively removed the sti linkers and residual Zr(IV) fragments in Zr-**fcu**-azo/sti-30% by our ozonolysis protocol[45,46] and washing the ozonated solid with 0.5 M solution of acetic acid in DMF. The ozonated Zr-**fcu**-azo/sti-30% particles did not exhibit any marked difference in their octahedral shape and crystallinity compared to the initial nonozonated samples (Figure 1b,c). The ozonated Zr-**fcu**-azo/sti-30% was analyzed by ^{1}H NMR, which revealed that these linkers had been completely removed from the crystals (Figure S4). The creation of mesopores was confirmed by N_2 sorption tests at 77 K (Figures 1d, S6 and S7). The isotherm did not show the type-I shape of the isotherm of the starting MOF: instead, it exhibited a small hysteresis between the adsorption and desorption branch, characteristic of mesoporosity. As expected, ozonolysis reduced the apparent S_{BET} down to 2470 m^2/g. However, this decrease was offset by the creation of mesopores, at a proportion of 24%.[47]

Once we had confirmed the formation of Zr-**fcu**-MOF containing hierarchical porosity, we proceeded to study the adsorption of catalase into the latter. For this, 5 mg of ozonated Zr-**fcu**-azo/sti-30% was incubated in 1 mL of an

aqueous solution of catalase (3 mg/mL) for different periods of time. After each period, the amount of encapsulated catalase was quantified by the standard Bradford protein assay. The amount of catalase confined in the ozonated Zr-**fcu**-azo/sti-30% was gradually increased from 1 h (0.14 ± 0.01 mg catalase/mg MOF) to 8 h (0.21 ± 0.01 mg catalase/mg MOF) (Figure 1e). To further demonstrate the encapsulation of catalase into the mesopores, we used confocal laser scanning microscopy (CLSM) to study the spatial distribution of catalase within the Zr-**fcu**-azo/sti-30% crystals. For this, we repeated the encapsulation process over 8 h, using a catalase tagged with the green dye fluorescein isothiocyanate (FITC). For comparison, we also repeated this encapsulation process using a nonozonated Zr-**fcu**-azo/sti-30%, which does not contain mesopores. Micrographs of the ozonated and the nonozonated Zr-**fcu**-azo/sti-30% demonstrated that catalase is encapsulated only within the crystals of the former, where it is predominantly compartmentalized at the subsurface (Figure 2a,b). We attributed the preferential localization of catalase at the subsurface of each MOF crystal to the initial random distribution of azo- and sti- linkers that, following removal of the latter via ozonolysis, produce crystals in which the meso- and micropores are randomly localized. This makes the external mesoscale cavities more accessible for catalase than the internal ones, as the diffusion of catalase into the internal large cavities is highly restricted by the probability of encountering pores smaller than the size of catalase.

We next studied the self-propulsion of Zr-**fcu**-azo/sti-30% crystals into which we had incorporated catalase (hereafter called MOFtors) for 1, 3, 5, or 8 h. For these experiments, we considered that bubble propulsion is improved by the addition of surfactants to the media;[48−52] thus, we recorded the MOFtor crystals in an aqueous solution containing 0.5% H_2O_2
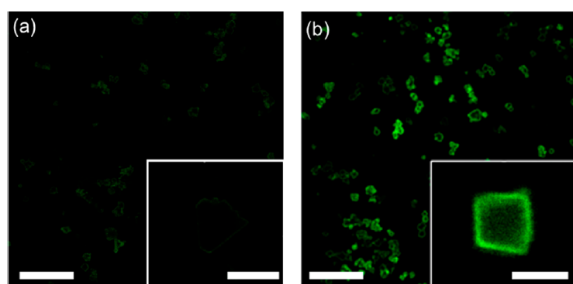
Figure 2. CLSM micrographs of (a) as-synthesized and (b) ozonated Zr-**fcu**-azo/sti-30% crystals after incubation with FITC-tagged catalase (green) for 8 h. Scale bars: 50 μm (a, b); 5 μm (inset, a); and 3 μm (inset, b).

and Triton X-100 at a 0.25% (v/v) concentration. Remarkably, all four samples showed bubble generation and motion capability (Figure 3a), propelling themselves by a thrust of
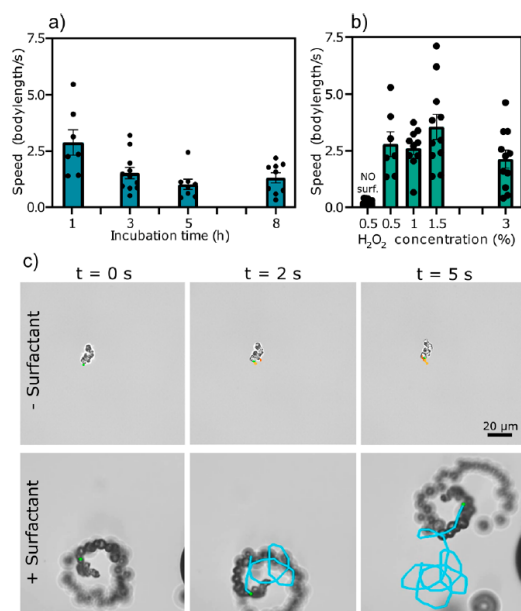
Figure 3. (a) Speed of MOFtors obtained at different incubation times. (b) Speed of the MOFtors at different H_2O_2 concentrations. (c) Snapshots of the trajectories of MOFtors at different times in the presence (bottom) or absence (top) of 0.25% Triton X-100.

oxygen bubbles released asymmetrically from a point of nucleation (Video S1). In this regard, researchers have reported that any cavity in a micromotor structure, in this case in the MOF crystal, due to porosity, surface defects, or crystal aggregation, can enable accumulation of oxygen bubbles for jet-like propulsion.[53,54]

Among the MOFtors generated at different incubation times, the one corresponding to 1 h incubation reached the highest maximum speed (2.79 ± 0.55 body-lengths/s). Interestingly, incubation time was indirectly proportional to speed (Figure 3a). To explore this trend, we quantified the enzymatic activity (O_2 production) of the catalase confined inside the MOFtors, using the displacement method. For all samples, the amount of generated O_2 increased during the first

2 min and then gradually plateaued at a saturation value (Figure S11). The MOFtor from 1 h of incubation generated the greatest amount of O_2 (61.1 μmol/mg$_{MOFtor}$) and highest speed of O_2 generation ([49 μmol O_2/min]/mg$_{MOFtor}$) (Figure 1e). These results are consistent with those of the aforementioned motion experiments. We have tentatively attributed this slight decrease in activity and motion to either a certain degree of inactivation of catalase inside the MOF crystals or to the fact that the catalase molecules diffuse into the interior of MOF crystals more at longer incubation times, thereby complicating both arrival of the H_2O_2 molecules to the enzymes and release of the O_2 bubbles produced by the enzymatic reaction.

Once we had confirmed the optimum incubation time of 1 h, we further investigated the motion capabilities of the corresponding MOFtor. Initially, we studied the influence of the surfactant, by reproducing the recording of MOFtors in an aqueous solution containing 0.5% H_2O_2 in the presence and absence of Triton X-100 (Figure 3b,c). Figure 3c shows different snapshots from the video recordings with their corresponding trajectories where MOFtors in a Triton X-100 dilution displayed high bubble production, leading to propulsion (Video S2). However, in the absence of surfactant (Figure 3c), we did not observe any bubbles or self-propulsion. We reasoned that the surfactant in the medium reduced the surface tension of the liquid, which in turn promoted formation of and stabilized the bubbles.[40,55] We also assessed the self-propulsion of the MOFtor as a function of H_2O_2 concentration (Figure 3b). We observed self-propulsion at low surfactant and fuel concentrations[56] compared to those in other studies, in which 3% to 5% H_2O_2 was utilized.[53] Given its toxicity, minimizing the concentration of the H_2O_2 is important for biological and environmental applications. When we increased the H_2O_2 concentration to 1.5%, the self-propulsion increased, reaching a maximum speed of 3.56 ± 0.56 body-lengths/s and propelling for 7.0 ± 0.4 min (Video S3). Yet, motion can be resumed after addition of fresh fuel.

Given that our MOFtor combines both meso- and micropores and that the catalase enzymes are encapsulated mainly in the mesopores located at the crystal subsurface, we envisioned using the remaining empty pores to adsorb other guest molecules. To this end, N_2-sorption measurements confirmed that MOFtors has accessible porosity, with an S_{BET} of 1715 m^2/g, and that their mesopore proportion is 20%. We also studied the capacity of MOFtors to capture rhodamine B, a common water pollutant from the textile, plastic, and dye industries, during self-propulsion in water. To this end, catalase-powered MOFtors (5 mg) were dispersed in an aqueous solution (1 mL) of 0.5 mg/mL rhodamine B and 1.5% H_2O_2/0.25% Triton X-100 at room temperature. After 5 min of incubation, the rhodamine B content adsorbed by the MOFtors was determined by UV−vis spectrometry. We observed that they had captured 51.0 ± 2.7 % of rhodamine B from the solution. For comparison, without using H_2O_2/ Triton X-100, nonpowered MOFtors adsorbed only 14.6 ± 6.4% of rhodamine B, thus confirming the positive effect of self-propulsion in the performance of MOFtors. Adsorption of rhodamine B in the catalase-powered MOFtors was also confirmed by CLSM. Indeed, Figure 4 shows that, while catalase remains localized at the subsurface of the crystals, rhodamine B molecules are adsorbed throughout the entire crystal.
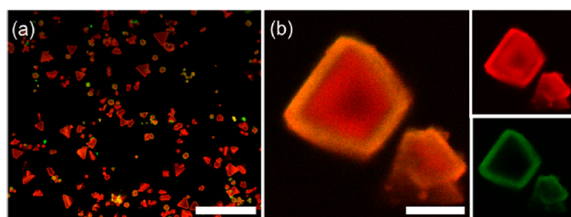
Figure 4. CLSM micrographs of MOFtors after adsorption of rhodamine B (red). In (b), the left image is the superposition of both right images showing adsorbed rhodamine B (red, top) and compartmentalized FITC-tagged catalase (green, bottom). Scale bars: 50 μm (a) and 5 μm (b).

In conclusion, we have reported the multistep synthesis of enzyme-powered MOF-based porous motors, which involves generating new mesopores in a microporous UiO-66-type MOF, via ozonolysis. We exploited the newly generated mesopores to adsorb and host the enzyme catalase, which were compartmentalized at the subsurface of each MOF crystal. This encapsulation enabled jet-like bubble propulsion of the MOF crystals using H_2O_2 as fuel, even at very low concentrations. Moreover, the remaining unoccupied micro- and mesopores in these MOFtors can be used for adsorbing additional species, as we demonstrated with capture of rhodamine B in water. Our work demonstrates the versatility of MOFs as the structural basis of enzyme-powered porous motors for delivery, sorption, and catalytic applications.

■ ASSOCIATED CONTENT

Ⓢ Supporting Information

The Supporting Information is available free of charge at https://pubs.acs.org/doi/10.1021/jacs.0c11061.

> Video S1: Representative MOFtor bubble self-propulsion for different catalase incubation times (AVI)
> Video S2: Representative MOFtor bubble self-propulsion with and without surfactant (AVI)
> Video S3: Representative MOFtor bubble self-propulsion for different H_2O_2 concentrations (AVI)
> Chemicals, instrumentation, synthetic procedures, FESEM, PXRD, and porosity data (PDF)

■ AUTHOR INFORMATION

Corresponding Authors

Tania Patiño − *Institute for Bioengineering of Catalonia (IBEC), The Barcelona Institute of Science and Technology (BIST), 08028 Barcelona, Spain; Chemistry Department, University of Rome, 00133 Rome, Italy;* Email: tpatino@ibecbarcelona.eu, tania.patino@uniroma2.eu

Inhar Imaz − *Catalan Institute of Nanoscience and Nanotechnology (ICN2), CSIC and Barcelona Institute of Science and Technology, Bellaterra 08193, Barcelona, Spain;* ⓞ orcid.org/0000-0002-0278-1141; Email: inhar.imaz@icn2.cat

Daniel Maspoch − *Catalan Institute of Nanoscience and Nanotechnology (ICN2), CSIC and Barcelona Institute of Science and Technology, Bellaterra 08193, Barcelona, Spain; Catalan Institute for Research and Advanced Studies (ICREA), 08010 Barcelona, Spain;* ⓞ orcid.org/0000-0003-1325-9161; Email: daniel.maspoch@icn2.cat

Samuel Sánchez − *Institute for Bioengineering of Catalonia (IBEC), The Barcelona Institute of Science and Technology (BIST), 08028 Barcelona, Spain; Catalan Institute for Research and Advanced Studies (ICREA), 08010 Barcelona, Spain;* ⓞ orcid.org/0000-0002-5845-8941; Email: ssanchez@ibecbarcelona.eu

Authors

Yunhui Yang − *Catalan Institute of Nanoscience and Nanotechnology (ICN2), CSIC and Barcelona Institute of Science and Technology, Bellaterra 08193, Barcelona, Spain*

Xavier Arqué − *Institute for Bioengineering of Catalonia (IBEC), The Barcelona Institute of Science and Technology (BIST), 08028 Barcelona, Spain*

Vincent Guillerm − *Catalan Institute of Nanoscience and Nanotechnology (ICN2), CSIC and Barcelona Institute of Science and Technology, Bellaterra 08193, Barcelona, Spain;* ⓞ orcid.org/0000-0003-3460-223X

Pascal-Raphaël Blersch − *Institute for Bioengineering of Catalonia (IBEC), The Barcelona Institute of Science and Technology (BIST), 08028 Barcelona, Spain*

Javier Pérez-Carvajal − *Catalan Institute of Nanoscience and Nanotechnology (ICN2), CSIC and Barcelona Institute of Science and Technology, Bellaterra 08193, Barcelona, Spain*

Complete contact information is available at:
https://pubs.acs.org/10.1021/jacs.0c11061

Author Contributions

#Y.Y. and X.A. contributed equally to this work.

Notes

The authors declare no competing financial interest.

■ ACKNOWLEDGMENTS

■ REFERENCES

(1) Sánchez, S.; Soler, L.; Katuri, J. Chemically Powered Micro- and Nanomotors. *Angew. Chem., Int. Ed.* **2015**, *54* (5), 1414−1444.

(2) Ou, J.; Liu, K.; Jiang, J.; Wilson, D. A.; Liu, L.; Wang, F.; Wang, S.; Tu, Y.; Peng, F. Micro-/Nanomotors toward Biomedical Applications: The Recent Progress in Biocompatibility. *Small* **2020**, *16*, 1906184.

(3) Wang, S.; Liu, X.; Wang, Y.; Xu, D.; Liang, C.; Guo, J.; Ma, X. Biocompatibility of Artificial Micro/Nanomotors for Use in Biomedicine. *Nanoscale* **2019**, *11* (30), 14099−14112.

(4) Li, J.; Esteban-Fernández de Ávila, B.; Gao, W.; Zhang, L.; Wang, J. Micro/Nanorobots for Biomedicine: Delivery, Surgery, Sensing, and Detoxification. *Sci. Robot.* **2017**, *2* (4), eaam6431.

(5) Joseph, A.; Contini, C.; Cecchin, D.; Nyberg, S.; Ruiz-Perez, L.; Gaitzsch, J.; Fullstone, G.; Tian, X.; Azizi, J.; Preston, J.; Volpe, G.;

Battaglia, G. Chemotactic Synthetic Vesicles: Design and Applications in Blood-Brain Barrier Crossing. *Sci. Adv.* **2017**, *3* (8), No. e1700362.

(6) Wang, J.; Toebes, B. J.; Plachokova, A. S.; Liu, Q.; Deng, D.; Jansen, J. A.; Yang, F.; Wilson, D. A. Self-Propelled PLGA Micromotor with Chemotactic Response to Inflammation. *Adv. Healthcare Mater.* **2020**, *9*, 1901710.

(7) Wu, Y.; Lin, X.; Wu, Z.; Möhwald, H.; He, Q. Self-Propelled Polymer Multilayer Janus Capsules for Effective Drug Delivery and Light-Triggered Release. *ACS Appl. Mater. Interfaces* **2014**, *6* (13), 10476−10481.

(8) Parmar, J.; Vilela, D.; Villa, K.; Wang, J.; Sánchez, S. Micro- and Nanomotors as Active Environmental Microcleaners and Sensors. *J. Am. Chem. Soc.* **2018**, *140* (30), 9317−9331.

(9) Soler, L.; Sánchez, S. Catalytic Nanomotors for Environmental Monitoring and Water Remediation. *Nanoscale* **2014**, *6* (13), 7175−7182.

(10) Gao, W.; Wang, J. The Environmental Impact of Micro/Nanomachines: A Review. *ACS Nano* **2014**, *8* (4), 3170−3180.

(11) Orozco, J.; García-Gradilla, V.; D'Agostino, M.; Gao, W.; Cortés, A.; Wang, J. Artificial Enzyme-Powered Microfish for Water-Quality Testing. *ACS Nano* **2013**, *7* (1), 818−824.

(12) Medina-Sánchez, M.; Xu, H.; Schmidt, O. G. Micro- and Nano-Motors: The New Generation of Drug Carriers. *Ther. Delivery* **2018**, *9* (4), 303−316.

(13) Eskandarloo, H.; Kierulf, A.; Abbaspourrad, A. Nano- and Micromotors for Cleaning Polluted Waters: Focused Review on Pollutant Removal Mechanisms. *Nanoscale* **2017**, *9* (37), 13850−13863.

(14) Llopis-Lorente, A.; Garciá-Fernández, A.; Murillo-Cremaes, N.; Hortelaõ, A. C.; Patiñõ, T.; Villalonga, R.; Sancenón, F.; Martínez-Máñez, R.; Sánchez, S. Enzyme-Powered Gated Mesoporous Silica Nanomotors for on-Command Intracellular Payload Delivery. *ACS Nano* **2019**, *13* (10), 12171−12183.

(15) Hortelaõ, A. C.; Patiño, T.; Perez-Jiménez, A.; Blanco, À.; Sánchez, S. Enzyme-Powered Nanobots Enhance Anticancer Drug Delivery. *Adv. Funct. Mater.* **2018**, *28* (25), 1705086.

(16) Wu, Y.; Lin, X.; Wu, Z.; Möhwald, H.; He, Q. Self-Propelled Polymer Multilayer Janus Capsules for Effective Drug Delivery and Light-Triggered Release. *ACS Appl. Mater. Interfaces* **2014**, *6* (13), 10476−10481.

(17) Llopis-Lorente, A.; García-Fernández, A.; Lucena-Sánchez, E.; Díez, P.; Sancenón, F.; Villalonga, R.; Wilson, D. A.; Martínez-Máñez, R. Stimulus-Responsive Nanomotors Based on Gated Enzyme-Powered Janus Au-Mesoporous Silica Nanoparticles for Enhanced Cargo Delivery. *Chem. Commun.* **2019**, *55* (87), 13164−13167.

(18) Terzopoulou, A.; Nicholas, J. D.; Chen, X.-Z.; Nelson, B. J.; Pané, J.; Puigmartí-Luis, J. Metal-Organic Frameworks in Motion. *Chem. Rev.* **2020**, *120* (20), 11175−11193.

(19) Gao, S.; Hou, J.; Zeng, J.; Richardson, J. J.; Gu, Z.; Gao, X.; Li, D.; Gao, M.; Wang, D.-W.; Chen, P.; Chen, V.; Liang, K.; Zhao, D.-Y.; Kong, B. Superassembled Biocatalytic Porous Framework Micromotors with Reversible and Sensitive pH-Speed Regulation at Ultralow Physiological H_2O_2 Concentration. *Adv. Funct. Mater.* **2019**, *29*, 1808900.

(20) Themed Issue Metal-Organic Frameworks: *Chem. Soc. Rev.* Zhou, H. C., Kitagawa, S., Eds.; **2014**, *43* (5), 5415− 6172.

(21) Themed Issue Porous Framework Chemistry: *Chem. Rev.* Long, J.; Dinca, M., Eds; **2020**, *120* (16), 8037−9014.

(22) Khezri, B.; Pumera, M. Metal−Organic Frameworks Based Nano/Micro/Millimeter-Sized Self-Propelled Autonomous Machines. *Adv. Mater.* **2019**, *31* (14), 1806530.

(23) Ikezoe, Y.; Fang, J.; Wasik, T. L.; Shi, M.; Uemura, T.; Kitagawa, S.; Matsui, H. Peptide-Metal Organic Framework Swimmers That Direct the Motion toward Chemical Targets. *Nano Lett.* **2015**, *15* (6), 4019−4023.

(24) Ikezoe, Y.; Washino, G.; Uemura, T.; Kitagawa, S.; Matsui, H. Autonomous Motors of a Metal-Organic Framework Powered by Reorganization of Self-Assembled Peptides at Interfaces. *Nat. Mater.* **2012**, *11* (12), 1081−1085.

(25) Ikezoe, Y.; Fang, J.; Wasik, T. L.; Uemura, T.; Zheng, Y.; Kitagawa, S.; Matsui, H. Peptide Assembly-Driven Metal-Organic Framework (MOF) Motors for Micro Electric Generators. *Adv. Mater.* **2015**, *27* (2), 288−291.

(26) Park, J. H.; Lach, S.; Polev, K.; Granick, S.; Grzybowski, B. A. Metal-Organic Framework "Swimmers" with Energy-Efficient Autonomous Motility. *ACS Nano* **2017**, *11* (11), 10914−10923.

(27) Wang, X.; Chen, X. Z.; Alcântara, C. C. J.; Sevim, S.; Hoop, M.; Terzopoulou, A.; de Marco, C.; Hu, C.; de Mello, A. J.; Falcaro, P.; Furukawa, S.; Nelson, B. J.; Puigmartí-Luis, J.; Pané, S. MOFBOTS: Metal−Organic-Framework-Based Biomedical Microrobots. *Adv. Mater.* **2019**, *31* (27), 1970192.

(28) Terzopoulou, A.; Wang, X.; Chen, X.-Z.; Palacios-Corella, M.; Pujante, C.; Herrero-Martin, J.; Qin, X.-H.; Sort, J.; deMello, A. J.; Nelson, B. J.; Puigmarti-Luis, J.; Pane, S. Biodegradable Metal−Organic Framework-Based Microrobots (MOFBOTs). *Adv. Healthcare Mater.* **2020**, *9* (20), 2001031.

(29) Wang, R.; Guo, W.; Li, X.; Liu, Z.; Liu, H.; Ding, S. Highly Efficient MOF-Based Self-Propelled Micromotors for Water Purification. *RSC Adv.* **2017**, *7* (67), 42462−42467.

(30) Ayala, A.; Carbonell, C.; Imaz, I.; Maspoch, D. Introducing Asymmetric Functionality into MOFs: Via the Generation of Metallic Janus MOF Particles. *Chem. Commun.* **2016**, *52* (29), 5096−5099.

(31) Ying, Y.; Pourrahimi, A. M.; Sofer, Z.; Matějková, S.; Pumera, M. Radioactive Uranium Preconcentration via Self-Propelled Autonomous Microrobots Based on Metal-Organic Frameworks. *ACS Nano* **2019**, *13* (10), 11477−11487.

(32) Wang, L.; Zhu, H.; Shi, Y.; Ge, Y.; Feng, X.; Liu, R.; Li, Y.; Ma, Y.; Wang, L. Novel Catalytic Micromotor of Porous Zeolitic Imidazolate Framework-67 for Precise Drug Delivery. *Nanoscale* **2018**, *10* (24), 11384−11391.

(33) Tan, T. T. Y.; Cham, J. T. M.; Reithofer, M. R.; Andy Hor, T. S.; Chin, J. M. Motorized Janus Metal Organic Framework Crystals. *Chem. Commun.* **2014**, *50* (96), 15175−15178.

(34) Li, J.; Yu, X.; Xu, M.; Liu, W.; Sandraz, E.; Lan, H.; Wang, J.; Cohen, S. M. Metal-Organic Frameworks as Micromotors with Tunable Engines and Brakes. *J. Am. Chem. Soc.* **2017**, *139* (2), 611−614.

(35) Liu, J.; Li, J.; Wang, G.; Yang, W.; Yang, J.; Liu, Y. Bioinspired Zeolitic Imidazolate Framework (ZIF-8) Magnetic Micromotors for Highly Efficient Removal of Organic Pollutants from Water. *J. Colloid Interface Sci.* **2019**, *555*, 234−244.

(36) Liang, K.; Coghlan, C. J.; Bell, S. G.; Doonan, C.; Falcaro, P. Enzyme encapsulation in zeolitic imidazolate frameworks: a comparison between controlled co-precipitation and biomimetic mineralisation. *Chem. Commun.* **2016**, *52* (3), 473−476.

(37) Li, P.; Moon, S.-Y.; Guelta, M. A.; Lin, L.; Gomez-Gualdron, D. A.; Snurr, R. Q.; Harvey, S. P.; Hupp, J. T.; Farha, O. K. Nanosizing a Metal−Organic Framework Enzyme Carrier for Accelerating Nerve Agent Hydrolysis. *ACS Nano* **2016**, *10*, 9174−9182.

(38) Lian, X.; Chen, Y.-P.; Liu, T.-F.; Zhou, H.-C. Coupling two enzymes into a tandem nanoreactor utilizing a hierarchically structured MOF. *Chem. Sci.* **2016**, *7*, 6969−6973.

(39) Chen, Y.; Han, S.; Li, X.; Zhang, Z.; Ma, S. Why Does Enzyme Not Leach from Metal−Organic Frameworks (MOFs)? Unveiling the Interactions between an Enzyme Molecule and a MOF. *Inorg. Chem.* **2014**, *53* (19), 10006−10008.

(40) Sánchez, S.; Solovev, A. A.; Mei, Y.; Schmidt, O. G. Dynamics of Biocatalytic Microengines Mediated by Variable Friction Control. *J. Am. Chem. Soc.* **2010**, *132* (38), 13144−13145.

(41) Sitt, A.; Soukupova, J.; Miller, D.; Verdi, D.; Zboril, R.; Hess, H.; Lahann, J. Microscale Rockets and Picoliter Containers Engineered from Electrospun Polymeric Microtubes. *Small* **2016**, *12* (11), 1432−1439.

(42) Singh, V. V.; Kaufmann, K.; Esteban-Fernández de Ávila, B.; Uygun, M.; Wang, J. Nanomotors Responsive to Nerve-Agent Vapor Plumes. *Chem. Commun.* **2016**, *52* (16), 3360−3363.

(43) Wu, Z.; Lin, X.; Zou, X.; Sun, J.; He, Q. Biodegradable Protein-Based Rockets for Drug Transportation and Light-Triggered Release. *ACS Appl. Mater. Interfaces* **2015**, *7* (1), 250−255.

(44) Cavka, J. H.; Jakobsen, S.; Olsbye, U.; Guillou, N.; Lamberti, C.; Bordiga, S.; Lillerud, K. P. A New Zirconium Inorganic Building Brick Forming Metal Organic Frameworks with Exceptional Stability. *J. Am. Chem. Soc.* **2008**, *130* (42), 13850−13851.

(45) Albalad, J.; Xu, H.; Gándara, F.; Haouas, M.; Martineau-Corcos, C.; Mas-Ballesté, R.; Barnett, S. A.; Juanhuix, J.; Imaz, I.; Maspoch, D. Single-Crystal-to-Single-Crystal Postsynthetic Modification of a Metal−Organic Framework via Ozonolysis. *J. Am. Chem. Soc.* **2018**, *140* (6), 2028−2031.

(46) Guillerm, V.; Xu, H.; Albalad, J.; Imaz, I.; Maspoch, D. Postsynthetic Selective Ligand Cleavage by Solid−Gas Phase Ozonolysis Fuses Micropores into Mesopores in Metal−Organic Frameworks. *J. Am. Chem. Soc.* **2018**, *140* (44), 15022−15030.

(47) Dubinin, M. M.; Zaverina, E. D.; Radushkevich, L. V.; Sorbtsiya, I. Struktura Aktivnykh Uglei 0.1. Issledovanie Adsorbtsii Organicheskikh Parov. *Zh. Fiz. Khim.* **1947**, *21* (11), 1351−1362.

(48) Simmchen, J.; Magdanz, V.; Sánchez, S.; Chokmaviroj, S.; Ruiz-Molina, D.; Baeza, A.; Schmidt, O. G. Effect of Surfactants on the Performance of Tubular and Spherical Micromotors - a Comparative Study. *RSC Adv.* **2014**, *4* (39), 20334−20340.

(49) Manesh, K. M.; Cardona, M.; Yuan, R.; Clark, M.; Kagan, D.; Balasubramanian, S.; Wang, J. Template-Assisted Fabrication of Salt-Independent Catalytic Tubular Microengines. *ACS Nano* **2010**, *4* (4), 1799−1804.

(50) Solovev, A. A.; Sánchez, S.; Pumera, M.; Mei, Y. F.; Schmidt, O. C. Magnetic Control of Tubular Catalytic Microbots for the Transport, Assembly, and Delivery of Micro-Objects. *Adv. Funct. Mater.* **2010**, *20* (15), 2430−2435.

(51) Solovev, A. A.; Sánchez, S.; Mei, Y.; Schmidt, O. G. Tunable Catalytic Tubular Micro-Pumps Operating at Low Concentrations of Hydrogen Peroxide. *Phys. Chem. Chem. Phys.* **2011**, *13* (21), 10131−10135.

(52) Solovev, A. A.; Mei, Y.; Ureña, E. B.; Huang, G.; Schmidt, O. G. Catalytic Microtubular Jet Engines Self-Propelled by Accumulated Gas Bubbles. *Small* **2009**, *5* (14), 1688−1692.

(53) Chi, Q.; Wang, Z.; Tian, F.; You, J.; Xu, S. A Review of Fast Bubble-Driven Micromotors Powered by Biocompatible Fuel: Low-Concentration Fuel, Bioactive Fluid and Enzyme. *Micromachines* **2018**, *9* (10), 537.

(54) Fomin, V. M.; Hippler, M.; Magdanz, V.; Soler, L.; Sánchez, S.; Schmidt, O. G. Propulsion Mechanism of Catalytic Microjet Engines. *IEEE Trans. Robot.* **2014**, *30* (1), 40−48.

(55) Ma, X.; Jang, S.; Popescu, M. N.; Uspal, W. E.; Miguel-López, A.; Hahn, K.; Kim, D. P.; Sánchez, S. Reversed Janus Micro/Nanomotors with Internal Chemical Engine. *ACS Nano* **2016**, *10* (9), 8751−8759.

(56) Solovev, A. A.; Sánchez, S.; Mei, Y.; Schmidt, O. G. Tunable Catalytic Tubular Micro-Pumps Operating at Low Concentrations of Hydrogen Peroxide. *Phys. Chem. Chem. Phys.* **2011**, *13* (21), 10131−10135.

VIP **Metal-Organic Frameworks** Very Important Paper

Clip-off Chemistry: Synthesis by Programmed Disassembly of Reticular Materials**

Yunhui Yang[+], Anna Broto-Ribas[+], Borja Ortín-Rubio[+], Inhar Imaz, Felipe Gándara, Arnau Carné-Sánchez, Vincent Guillerm, Sergio Jurado, Félix Busqué, Judith Juanhuix, and Daniel Maspoch*

Abstract: Bond breaking is an essential process in chemical transformations and the ability of researchers to strategically dictate which bonds in a given system will be broken translates to greater synthetic control. Here, we report extending the concept of selective bond breaking to reticular materials in a new synthetic approach that we call Clip-off Chemistry. We show that bond-breaking in these structures can be controlled at the molecular level; is periodic, quantitative, and selective; is effective in reactions performed in either solid or liquid phases; and can occur in a single-crystal-to-single-crystal fashion involving the entire bulk precursor sample. We validate Clip-off Chemistry by synthesizing two topologically distinct 3D metal-organic frameworks (MOFs) from two reported 3D MOFs, and a metal-organic macrocycle from metal-organic polyhedra (MOP). Clip-off Chemistry opens the door to the programmed disassembly of reticular materials and thus to the design and synthesis of new molecules and materials.

Introduction

Throughout history, innovations in chemical synthesis have yielded previously inaccessible new molecules and materials that have enabled vast improvements in human life, ranging from fine chemicals to complex functional materials. Each new reaction and methodology not only help to expand accessible chemical space, but also inspire researchers to further innovate in the iterative design and preparation of new chemical targets of social, economic or industrial value. To date, most state-of-the-art synthetic approaches use bottom-up strategies that, at the latter stage, mainly entail controlling the formation of new bonds. A relatively recent example of this is reticular chemistry,[1–7] in which judiciously-designed, rigid molecular building blocks (MBBs) are linked by strong bonds to create crystalline open-framework materials[8] such as metal-organic frameworks (MOFs),[1–4] covalent-organic frameworks (COFs)[9] and metal-organic polyhedra (MOPs).[10–12] Reticular materials are a fascinating source of metal-organic and purely organic structures built up from an endless variety of fragments and MBBs[13] (e.g. metal clusters, cages, cycles, metal layers, metal chains, etc.) that often do not exist in their isolated form.

We envisaged that by selectively breaking certain bonds in reticular materials, we could transform them into new frameworks or break them into new molecular fragments or isolated MBBs, as a synthetic strategy towards new materials and molecules. We hypothesized that we could use a chemical reaction for programmed bond-breaking, such that the de-reticulation process would occur at the molecular level. We reasoned that this would require the presence of cleavable groups at specific positions within the structures of the corresponding reticular materials, and that reported reticular materials that contain linkers featuring alkene bonds would be ideal starting materials for this strategy. However, we thought that, in the likely event that the targeted structure-precursor did not contain any alkene groups, we could generalize this approach to numerous reticular materials by inserting such groups into the pre-selected linkers without modifying their size or geometry, via reticular chemistry.

[*] Y. Yang,[+] A. Broto-Ribas,[+] B. Ortín-Rubio,[+] Dr. I. Imaz,
Dr. A. Carné-Sánchez, Dr. V. Guillerm, Prof. Dr. D. Maspoch
Catalan Institute of Nanoscience and Nanotechnology (ICN2), CSIC
and The Barcelona Institute of Science and Technology
Campus UAB, Bellaterra, 08193 Barcelona (Spain)
E-mail: inhar.imaz@icn2.cat
    daniel.maspoch@icn2.cat

Dr. F. Gándara
Department of New Architectures in Materials Chemistry, Materials
Science Institute of Madrid—CSIC
Sor Juana Inés de la Cruz 3, 28049 Madrid (Spain)

Dr. S. Jurado, Prof. Dr. F. Busqué
Departament de Química, Universitat Autònoma de Barcelona
(UAB)
Cerdanyola del Vallès, 08193 Barcelona (Spain)

Dr. J. Juanhuix
Alba Synchrotron Light Facility
Cerdanyola del Vallès, 08290 Barcelona (Spain)

Prof. Dr. D. Maspoch
ICREA
Pg. Lluís Companys 23, 08010 Barcelona (Spain)

[+] These authors contributed equally to this work.

[**] A previous version of this manuscript has been deposited on
a preprint server (10.26434/chemrxiv.14518632.v1).

Supporting information and the ORCID identification number(s) for
the author(s) of this article can be found under:
https://doi.org/10.1002/anie.202111228

Indeed, reticular chemistry dictates that for a given framework, the constituents can be chemically functionalized pre- and/or post-synthetically,[14, 15] without any loss to framework connectivity. Thus, we extended this concept to the ability to encode the organic linker of an existing MOF by inserting cleavable alkene groups into it, without modifying the linker size or topology, to ultimately enable assembly of the corresponding isoreticular MOF structures containing the desired cleavable group.[16]

Herein we report a new synthetic approach, called Clip-off Chemistry, which is based on the programmed disassembly of reticular materials by controlled breaking of selected bonds. We validated Clip-off Chemistry by synthesizing two topologically distinct, three-dimensional (3D) MOFs from two reported 3D MOFs in single-crystal-to-single-crystal transformations. Through these examples, we demonstrated that reticular materials could be modified via cleavage, rather than formation, of bonds in their frameworks, enabling alterations to the connectivity of their constituent MBBs and therefore, to their topology. Next, we anticipated that Clip-off Chemistry could be generalized by applying it to 0-D molecular systems. To this end, we synthesized a novel metal-organic macrocycle from a MOP precursor. In all the examples we report here, we used ozonolysis as the chemical reaction to cut off constituent organic MBBs or linkers via direct cleavage of their alkene bonds.

Results and Discussion

Clip-off Chemistry is based on using, as starting materials, structures that contain cleavable groups (in this study, alkenes) at specific positions, such that cleavage of said groups generates new molecules or materials. Following this principle, we first targeted the clip-off synthesis of a new 3D MOF from a 3D MOF precursor. When selecting precursors in Clip-off Chemistry, reticular analysis of their underlying nets[17–19] is important, as bond-breaking in the structure relates to disassembly of certain circuits of connections.[20] In reticular materials this disassembly can be performed mainly by erasing some of the edges or nodes. Translating this analysis to the chemical field, the clip-off synthesis of a structure (here, a 3D MOF) from the disassembly of another structure (here, another 3D MOF) can be achieved by selecting either of two potential precursors: i) a structure built from one type of polytopic linker that contains different circuits of connections between the clusters, containing a cleavable bond in at least one of the circuits; or ii) a mixed-linker structure, in which linkers are located at different crystallographic positions, and one of them contains a cleavable bond. Cleavage of the polytopic linker will provoke disassembly of the circuits of connections in which the cleavable bond is involved, thereby forming a structure built up exclusively from those circuits that do not contain the cleavable groups, with a distinct underlying topology. Similarly, in the mixed-linker structure, cleavage of the linker containing the cleavable bond will provoke disassembly of the circuits of connections in which it is involved, thereby forming a structure built up exclusively from those circuits that involve

the metal clusters and the other linkers that do not contain the cleavable groups.

In our choice of precursor for the first 3D MOF synthesis, we followed the polytopic linker approach described above (Figure 1). Thus, we selected the Zr-**scu**-MOF,[21] in which the assembly of eight-connected (8-c), quadrangular prismatic $Zr_6O_4(OH)_4$ clusters to 4-c rectangular linkers 5-[(3,5-dicarboxyphenyl)diazenyl]benzene-1,3-dicarboxylate (L_1) forms a 3D framework with a 4,8-c **scu/3,3,8T132** underlying topology[22] and 1D channels (size: ≈ 7 Å) along one axis. However, as this reported structure does not contain any cleavable alkene groups, we had to insert them chemically, using the well-known isoreticular principle.[16] This step of introducing cleavable groups into precursors can be performed before the cleavage step as needed, by replacing at least one of the original linkers with one of similar size and geometry that contains the desired cleavable groups at strategic positions. Once inserted into the isoreticular structure, such linkers generate different circuits of connections, in which at least one circuit contains the cleavable bonds. In our example, we replaced the linker L_1 with 5-[2-(3,5-dicarboxyphenyl)ethenyl]benzene-1,3-dicarboxylate (L_2), which contains olefinic bonds for cleavage. We thus synthesized an isoreticular Zr-**scu**-MOF framework built up from different circuits of connections, wherein only some of them contain the cleavable olefinic bonds of L_2. We anticipated that, upon treatment of this framework with ozone,[23–27] each 4-c L_2 linker would be split into two 2-c linkers (doubly deprotonated trimesic acid and/or 5-formylisophthalate). Consequently, only the circuits of connections between the $Zr_6O_4(OH)_4$ clusters and these 2-c linkers would remain, forming a Zr-**pcu**-MOF. In contrast to the isoreticular Zr-**scu**-MOF precursor, which is based on quadrangular prismatic 8-c Zr-clusters, each $Zr_6O_4(OH)_4$ cluster is still coordinated by 8 linkers in this new Zr-**pcu**-MOF, however its topological connectivity decreases from 8-c to a 6-c because two pairs of the eight 2-c linkers connect the same two clusters (Figure S2).[28]

We expected that this first clip-off reaction would afford the first-ever example of a 3D MOF made of archetypical Zr-oxo-hydroxo-clusters linked by isophthalate-like linkers in a **pcu** underlying net. Interestingly, the closest literature example of such a structure is that of a 2D MOF made of Zr-oxo-hydroxo-clusters linked by isophthalate, albeit in an **hcb** topology.[29] Our target 3D Zr-**pcu** MOF could also be seen as exemplifying a connection of Zr-oxo-hydroxo-clusters through trimesate linkers, which are coordinated only through two of their three carboxylate groups. Accordingly, it could also be considered as the first example of a Zr-structure with a free carboxylic acid using trimesate, as researchers have previously reported combination of Zr-oxo-hydroxo-clusters with this linker in a **spn** topology of 3,6-connectivity.[30]

We synthesized colorless cubic crystals of isoreticular Zr-**scu**-MOF by solvothermal reaction (120 °C) of a mixture of $ZrOCl_2 \cdot 8H_2O$ and L_2 in N,N-dimethylformamide (DMF) and formic acid for 5 days. The crystal structure revealed the expected isoreticular **scu** framework, in which L_1 had been replaced by L_2 (Figure 2a; see Supporting Information (SI), section S2). Next, we confirmed the phase purity of the bulk
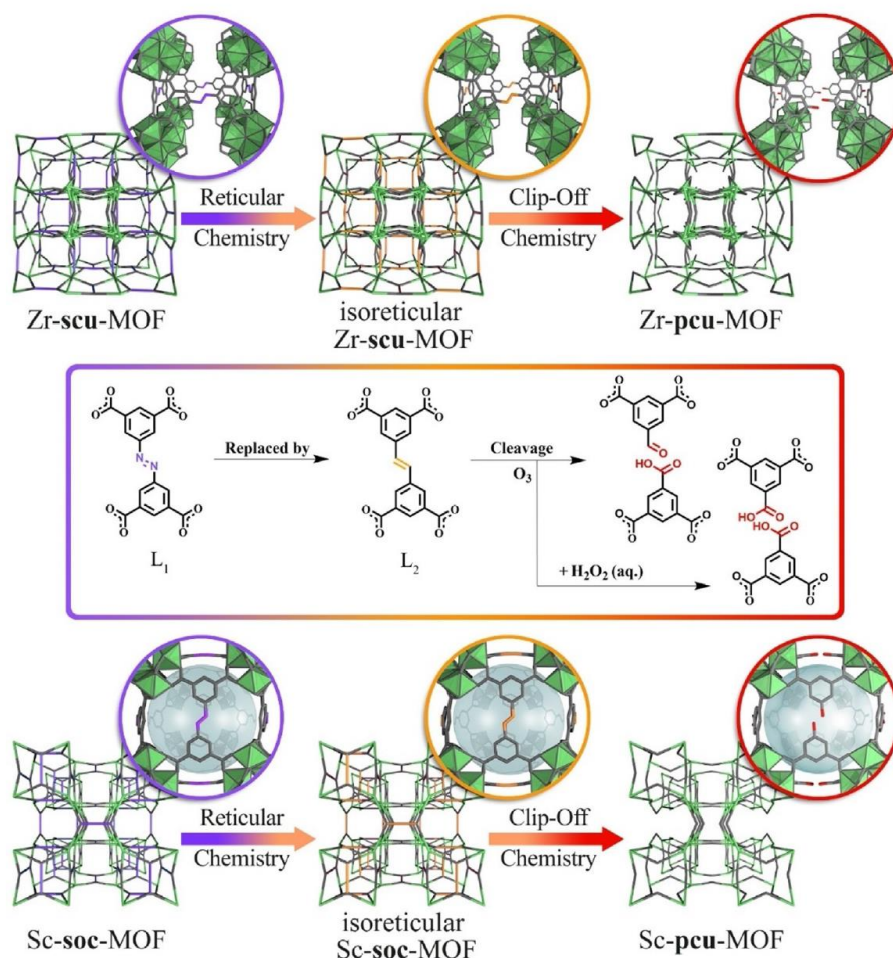
Figure 1. Clip-off Chemistry. Representative examples of Clip-off Chemistry, starting with the isoreticular insertion of cleavable (here, alkene) groups into a MOF structure,[16] followed by the quantitative breaking of these cleavable groups by ozonolysis to afford a new structure. Top: clip-off synthesis of Zr-**pcu**-MOF from Zr-**scu**-MOF. Bottom: clip-off synthesis of Sc-**pcu**-MOF from Sc-**soc**-MOF. Middle: chemical reaction for both syntheses. The formation of aldehyde/carboxylic acid groups after ozonolysis is not shown in the lower magnification nets for better illustration of the breaking process. The formation of these groups is shown in the magnified structures, wherein the red groups represent aldehyde or carboxylic acid groups.
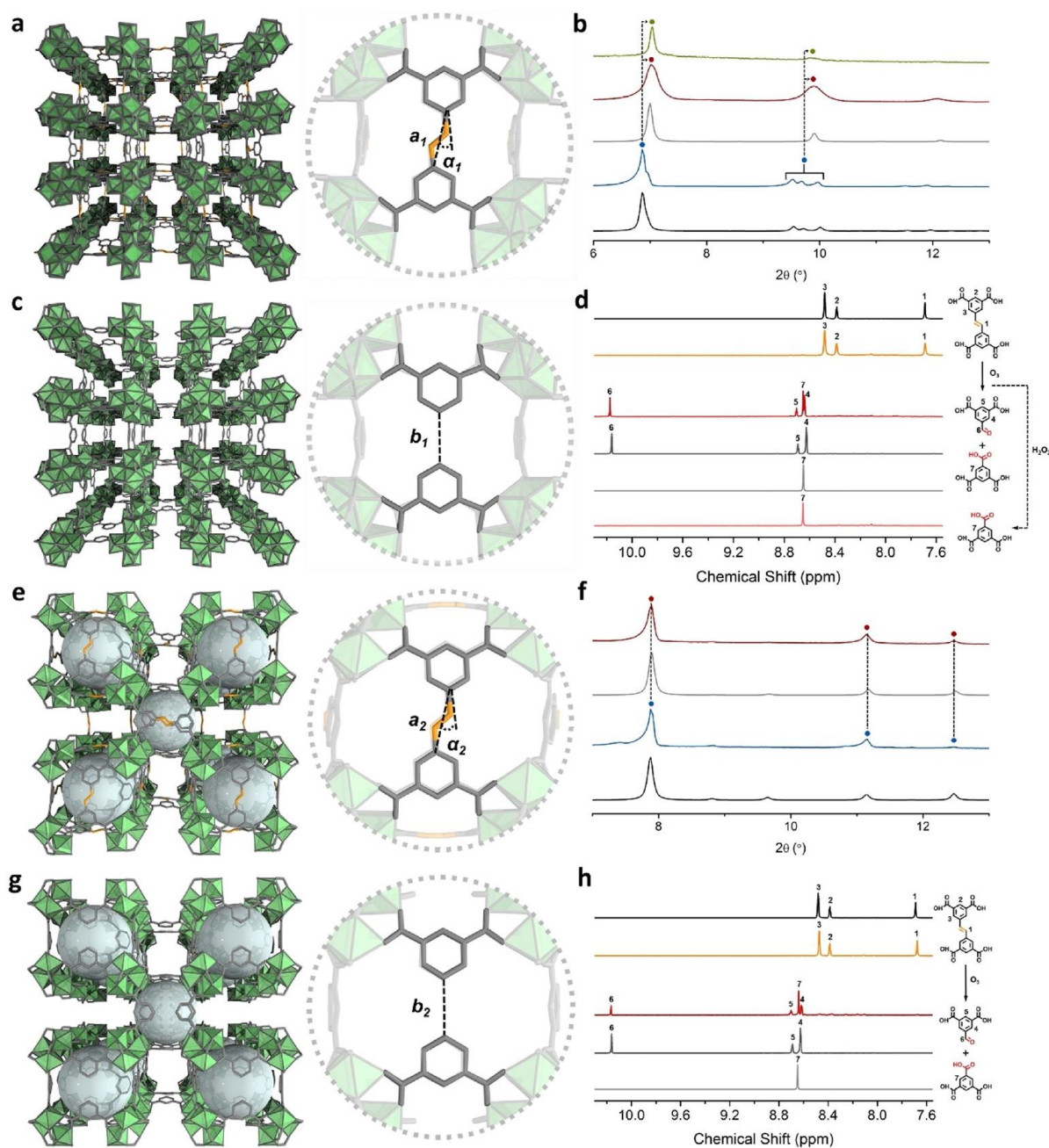
was directly collected from the tube and stored in tetrahydrofuran.

Next, we characterized the ozonated Zr-**scu**-MOF crystals by single crystal X-ray diffraction (SCXRD), which confirmed that they had retained the single-crystal character (Figures 2c, S1, S2). For these crystals, synchrotron diffraction data were collected at a maximum resolution of 1.2 Å. Data analyses revealed a variation in the lattice parameters, as compared to the pristine structure. Both pre- and post-ozonolysis crystal structures were solved in the monoclinic $C2/m$ space group. However, the cell volume of the ozonated crystal was found to be 16 076.00(10) Å³, whereas that of the pristine Zr-**scu**-MOF was 16 957.46(10) Å³. Analysis of the diffraction data demonstrated the integrity of the inorganic Zr-oxo-hydroxo-clusters after post-synthetic reaction, with no changes in their coordination. Thus, the position of all the atoms in the inorganic secondary building units (SBUs, metal and carboxylate atoms) were assigned and anisotropically refined. As for the rest of the organic linker, carbon atoms belonging to the phenyl ring were located in the difference electron density maps. However, their high thermal parameter values indicated a possible positional disorder. Moreover, the olefinic carbon atoms could no longer be located, supporting the completeness of the ozonolysis reaction. This is in stark contrast to the pristine MOF, in which the positions of these atoms were clearly visible and refined. The position of the resulting aldehydes or carboxylic groups, newly inserted in the MOF upon cleavage of the carbon-carbon double bond, could not be determined from the analysis of the difference electron density maps. Instead, a large residual electron density was observed in the vicinity of the positions that were initially occupied by the olefinic group. When comparing the two structures, additional differences could be observed in the arrangement of other framework atoms. Most notably, the relative orientation of opposite phenyl rings in a same linker

sample by X-ray powder diffraction (XRPD) and scanning electron microscopy (SEM) (Figures 2b, S3, S12).

We began the clip-off synthesis of Zr-**pcu**-MOF by packing 20 mg of synthesized Zr-**scu**-MOF crystals into a plastic tube, connected on one side to the ozonator (through a CaCl₂ humidity trap) and, on the other side, to a vacuum pump (through a KI trap), to ensure a continuous flow of ozone through the column.[23,24] The reaction was run at room temperature for 30 min. Afterwards, the sample was connected to vacuum for another 30 min. This ozonation/vacuum cycle was repeated nine times for the complete cleavage of all the alkene bonds in Zr-**scu**-MOF, as evidenced by the gradual disappearance of the characteristic olefinic peak at 7.69 ppm in the ¹H NMR spectra of the digested Zr-**scu**-MOF crystals (vide infra; Figure S8). After nine cycles, the resulting solid

Research Articles

Figure 2. Structural and molecular characterization of Zr-**pcu**-MOF and Sc-**pcu**-MOF. a,c) Crystal structures of isoreticular Zr-**scu**-MOF (a) and Zr-**pcu**-MOF (c). Magnified views highlight the changes observed in the distances and angles of both phenyl rings (from $a_1 = 3.77$–3.79 Å and $\alpha_1 = 14.95$–$19.71°$ to $b_1 = 3.39$–3.65 Å and $\beta_1 = 0°$) initially composing L_2.[41] b) Magnified view of XRPD spectra for calculated Zr-**scu**-MOF (black), synthesized Zr-**scu**-MOF (blue), calculated Zr-**pcu**-MOF (grey), synthesized Zr-**pcu**-MOF (red) and oxidized Zr-**pcu**-MOF (green). The main structural changes with signal shifts are highlighted. d) ^{1}H NMR spectra (360 MHz, [D$_6$]DMSO) of digested L_2 (black), Zr-**scu**-MOF (orange), Zr-**pcu**-MOF (red), 5-formylisophthalic acid (dark grey), trimesic acid (light grey) and oxidized Zr-**pcu**-MOF (light red). Assigned proton signals: $\delta_1 = 7.69$ ppm (s, 2H), $\delta_2 = 8.39$ ppm (s, 2H), $\delta_3 = 8.49$ ppm (s, 4H), $\delta_4 = 8.64$ ppm (m, 2H), $\delta_5 = 8.70$ ppm (m, 1H), $\delta_6 = 10.18$ ppm (s, 1H) and $\delta_7 = 8.65$ ppm (s, 3H). e,g) Crystal structures of isoreticular Sc-**soc**-MOF (e) and Sc-**pcu**-MOF (g). Magnified views highlight the changes observed in the distances and angles in both phenyl rings (from $a_2 = 3.82$–3.84 Å and $\alpha_2 = 15.63$–$17.34°$ to $b_2 = 3.62$–3.63 Å and $\beta_2 = 0°$) initially composing L_2.[41] (f) Magnified view of the XRPD spectra for calculated Sc-**soc**-MOF (black), synthesized Sc-**soc**-MOF (blue), calculated Sc-**pcu**-MOF (grey) and synthesized Sc-**pcu**-MOF (red). h) ^{1}H NMR spectra (360 MHz, [D$_6$]DMSO) of digested L_2 (black), Sc-**soc**-MOF (orange), Sc-**pcu**-MOF (red), 5-formylisophthalic acid (dark grey) and trimesic acid (light grey). Assigned proton signals: $\delta_1 = 7.68$ ppm (s, 2H), $\delta_2 = 8.38$ ppm (s, 2H), $\delta_3 = 8.47$ ppm (s, 4H), $\delta_4 = 8.64$ ppm (m, 2H), $\delta_5 = 8.71$ ppm (m, 1H), $\delta_6 = 10.17$ ppm (s, 1H) and $\delta_7 = 8.65$ ppm (s, 3H).

in Zr-**scu**-MOF was different after ozonolysis (Figures 2 a,c), indicating that the olefin bond was no longer present to fix the angle between these rings.

Since the crystal structure of pristine Zr-**scu**-MOF differed markedly to that of ozonated Zr-**scu**-MOF (or Zr-**pcu**-MOF), we also studied these MOFs by XRPD. Remarkably, the XRPD patterns for each sample perfectly matched those calculated from the corresponding structures determined by SCXRD and full-pattern profile refinements further demonstrated phase purity of the samples (Figures 2 b, S3–S5). Altogether, these results corroborate two crucial phenomena for validation of Clip-off Chemistry: firstly, that it is indeed possible to cleave all the periodic olefinic bonds in a 3D structure without destroying it or its single-crystal character; and secondly, that said cleavage, and the resultant formation of a new structure (in this case, Zr-**pcu**-MOF),[19] are homogeneous throughout the bulk crystalline sample.

Next, we gained further evidence of the formation of Zr-**pcu**-MOF by recording the ^{1}H NMR spectra of the digested ozonized samples (5% HF/[D$_6$]DMSO) after each cycle, and then comparing each spectrum to that of the starting Zr-**scu**-MOF (Figures 2 d, S6–S8). Under these digestion conditions, the MOF structures are destroyed and the linkers, released, thus enabling use of ^{1}H NMR to unveil the composition of the initial MOF structures. The spectrum of the digested Zr-**scu**-MOF showed the characteristic peak of equivalent olefinic protons of L$_2$ at $\delta = 7.69$ ppm. In contrast, the spectra of ozonated crystals after each cycle confirmed a gradual fading of this olefinic signal, which, by the ninth cycle, had fully disappeared. Indeed, ^{1}H NMR of digested ozonated Zr-**scu**-MOF after the ninth cycle confirmed the full conversion of L$_2$ into doubly deprotonated trimesic acid and 5-formylisophthalate. Beyond the disappearance of the olefinic protons at $\delta = 7.69$ ppm, there was also fading of the phenyl ($\delta = 8.49$ ppm and 8.39 ppm) and the carboxylic acid ($\delta = 13.32$ ppm) protons of L$_2$, whereas the characteristic signals for the trimesic acid ($\delta = 13.57$ ppm and 8.65 ppm) and 5-formylisophthalic acid ($\delta = 10.18$ ppm, 8.70 ppm and 8.64 ppm) were clearly identifiable. Cleavage of the olefinic bonds was corroborated by negative-mode mass spectrometry and Fourier transform infrared (FT-IR) spectroscopy of both pristine and ozonated Zr-MOFs (Table S3, Figures S10, S11). In the mass spectrum, the molecular ions $[M-H]^-$ corresponding to trimesic acid ($m/z = 209.01$) and 5-formylisophthalic acid ($m/z = 193.01$) were found, in strong contrast to the absence of any molecular ion $[M-H]^-$ corresponding to L$_2$ ($m/z = 355.05$). Similarly, in comparison to the spectrum of pristine Zr-**scu**-MOF, the FT-IR spectrum of ozonated Zr-**pcu**-MOF revealed the appearance of a typical carbonyl (C= O) stretching band at 1700 cm^{-1} and the complete disappearance of an alkene (C=C) stretching band at 1622 cm^{-1}.

Having demonstrated the single-crystal-to-single-crystal synthesis of Zr-**pcu**-MOF by selectively cleaving the olefinic bonds in Zr-**scu**-MOF into a mixture of aldehyde and carboxylic acid groups, we next sought to perform analogous chemistry to synthesize Zr-**pcu**-MOF functionalized exclusively with carboxylic acids to show enhanced control over the final output of the Clip-off Chemistry. To this end, ozonated crystals were soaked in 1 mL of hydrogen peroxide (30 wt.%

in H$_2$O) solution for 3 weeks. During this period, the sample was refreshed with fresh hydrogen peroxide every 24 h. Next, the sample was centrifuged, and then washed twice with water. The transformation to carboxylic acid groups was quantitative, as confirmed by ^{1}H NMR (Figures 2 d, S9). Moreover, the Zr-**pcu**-MOF framework had been preserved, as confirmed by XRPD (Figures 2 b, S3).

To show that we could generalize Clip-off Chemistry to other 3D MOF structures, we next attempted to synthesize a 3D Sc-**pcu**-MOF from an Sc-**soc**-MOF precursor (Figure 1; see SI, section 3),[31] a 3D structure built up from linking 6-c trigonal, prismatic Sc$_3$O clusters to 4-c L$_1$ linkers in a 4,6-c **soc**/**edq** topology.[32] This structure exhibits a mixture of cubic cavities (size: 11 Å) and 1D channels (size: 8 Å) along the three axes. As in the previous case, we designed the precursor by replacing L$_1$ with L$_2$, thus forming an isoreticular Sc-**soc**-MOF that contains different circuits of connections, some of which contains the cleavable olefins. We envisioned that, upon treatment with ozone, this circuit would be disrupted to form a 3D Sc-**pcu**-MOF whose Sc$_3$O clusters would be connected through trimesate/5-formylisophthalate linkers.

We began the clip-off synthesis of Sc-**pcu**-MOF via the aforementioned route by first preparing the isoreticular Sc-**soc**-MOF precursor. Colorless cubic crystals of Sc-**soc**-MOF were prepared by heating a solution of Sc(NO$_3$)$_3$·xH$_2$O and L$_2$ in DMF, ethanol and formic acid at 120°C for 48 h (Figure 2 e). However, all attempts at complete ozonolysis were unsuccessful, whether using the same synthetic protocol as for Zr-**scu**-MOF or trying slight modifications (e.g. extending the reaction time up to 8 h and/or the number of ozonolysis cycles up to twelve; Figures S13–S16). Consequently, cleavage of the olefinic bonds was incomplete, reaching a maximum value of 60% to 70% under certain conditions (e.g. exposing the Sc-**soc**-MOF crystals to ozone gas for 2 h). Consequently, a distinct ozonolysis protocol was employed: Sc-**soc**-MOF crystals were immersed in water, and then ozone was bubbled through the suspension under stirring at room temperature for 12 h. These conditions afforded greater cleavage of the olefinic bonds than in the previous strategy, leading to a mixture of trimesic acid, 5-formylisophthalic acid and the intermediate 1,2,4-trioxolane ring (Figure S17). Importantly, the presence of this intermediate indicated that the olefinic bonds had not all been completely cleaved to aldehyde/carboxylic acid groups. Moreover, increasing the reaction time under these solid/liquid conditions did not provide any major improvement in cleavage, although it did lead to a slight decrease in the crystallinity of the ozonated Sc-**pcu**-MOF.

To address the above drawbacks, we decided to combine the two ozonolysis strategies by first running a solid–gas reaction for 2 h and then, cleaving the remaining alkene bonds via suspension/gas reaction for an additional 6 h. Under these conditions, SCXRD of the resulting crystals confirmed quantitative single-crystal-to-single-crystal cleavage of the olefinic bonds of Sc-**soc**-MOF to synthesize Sc-**pcu**-MOF (Figure 2 g, S19, S26).[19] However, in this case, no changes were observed in the volume of the *R-3* rhombohedral unit cell relative to that of the precursor, as also confirmed by XRPD (Figures 2 f, S20). Nevertheless, SCXRD analysis

showed a very similar case to that of ozonated Zr-**scu**-MOF. Thus, the connectivity of the atoms belonging to the inorganic trimeric ScO₃ clusters remained identical to that of the pristine Sc-**soc**-MOF. Refinement of the carbon atoms from the organic linkers evidenced a positional disorder for some of them, and, unlike Sc-**soc**-MOF, the Sc-**pcu**-MOF product did not contain any olefinic atoms. Instead, areas of electron density were observed only between the opposite phenyl rings, with a maximum value at the middle point between the two rings, but at a distance longer than that expected for a C= C bond. This area of higher electron-density points perpendicularly above and below the plane of the phenyl rings. Although the refinement indicates the presence of atoms in this area, these atoms could not be unambiguously assigned to aldehyde or carboxylate groups (Figure S18). These findings indicate that the functional groups are not arranged in an orderly fashion within the crystals after ozonolysis but are instead randomly oriented in the pores. This is not surprising, considering that the resulting aldehydes and/or carboxylic groups are randomly distributed and most likely dangle in different orientations into the pores, rather than having a periodically fixed position, such that they would not contribute to the periodic diffraction of the crystal. Consistent with these SCXRD data, cleavage of all olefinic bonds was confirmed by ¹H NMR (Figures 2h, S21–S23) and negative-mode mass spectrometry of the digested ozonated samples (5% HF/[D₆]DMSO) (Figure S24, Table S6), and FT-IR of ozonated Sc-**pcu**-MOF (Figure S25), from which the olefinic protons ($\delta = 7.68$ ppm), molecular ion $[M-H]^-$ of L₂ and the typical alkene (C=C) stretching band, respectively, were not observed. On the contrary, the ¹H NMR signals, the molecular ions $[M-H]^-$ and the carbonyl (C=O) stretching band corresponding to doubly deprotonated trimesic acid and 5-
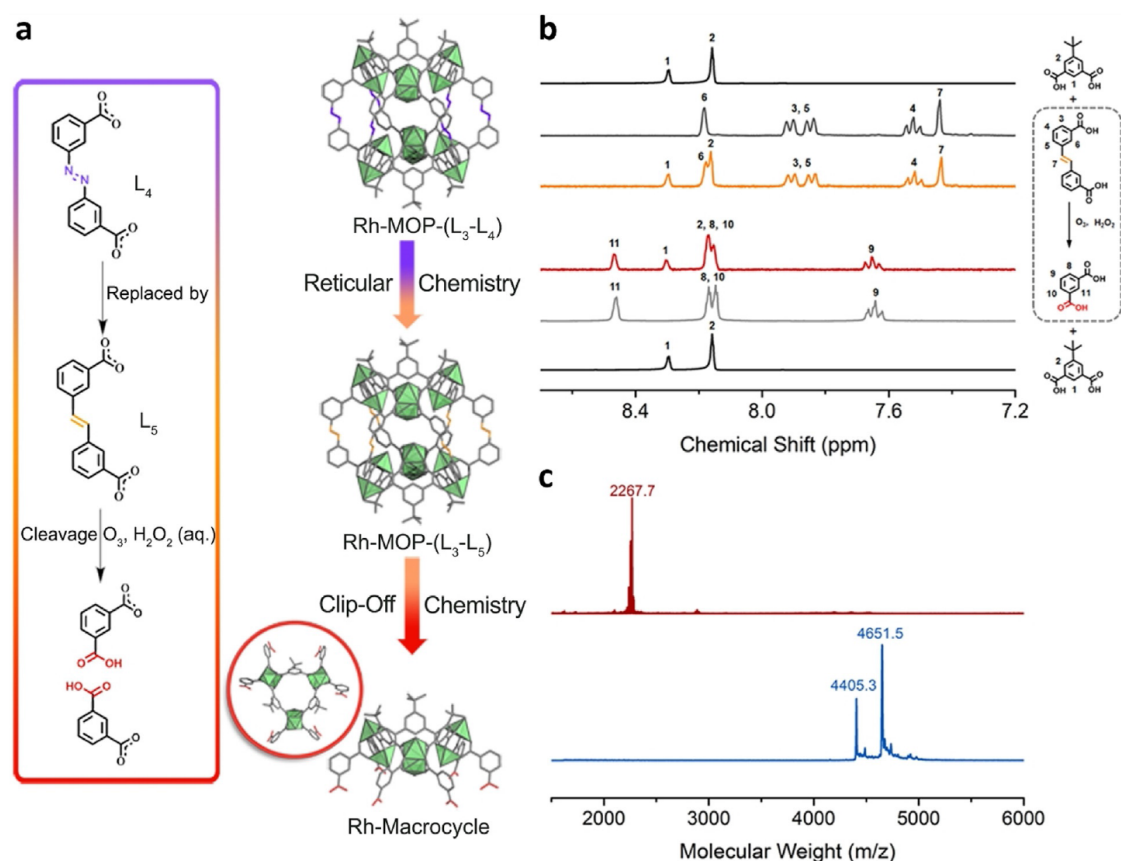
Figure 3. Clip-off synthesis of a triangular Rh-macrocycle. a) Schematic representation of the synthesis of a Rh-macrocycle from a discrete mixed-linker Rh-MOP, in which a linker containing an olefinic bond had been incorporated by reticular chemistry previous to ozonolysis.[41] b) ¹H NMR spectra (360 MHz, [D₆]DMSO) of digested L₃ (black), L₅ (dark grey), Rh-MOP (orange), Rh-macrocycle (red), and isophthalic acid (light grey). Assigned proton signals for digested Rh-MOP (orange): $\delta_1 = 8.30$ ppm (s, 1H), $\delta_2 = 8.16$ ppm (s, 2H), $\delta_{3,5} = 7.92$ ppm (d, $J = 7.7$ Hz, 2H), $\delta_{3,5} = 7.85$ ppm (d, $J = 7.7$ Hz, 2H), $\delta_4 = 7.51$ ppm (t, $J = 7.7$ Hz, 2H), $\delta_6 = 8.18$ ppm (s, 2H), and $\delta_7 = 7.43$ ppm (s, 2H). Assigned proton signals for digested Rh-macrocycle (red): $\delta_1 = 8.30$ ppm (s, 1H), $\delta_{2,8,10} = 8.17–8.15$ ppm (m, 6H), $\delta_9 = 7.65$ ppm (t, $J = 7.8$ Hz, 2H), and $\delta_{11} = 8.47$ ppm (s, 2H). c) MALDI-TOF spectra of Rh-MOP (blue) and of Rh-macrocycle fully functionalized with -COOH (red). The mass corresponding to the formula $[Rh_{12}(L_3)_6(L_5)_6(DMA) (H_2O)_2(MeOH)_4+H]^+$ (expected = 4403.8; found = 4405.3) and $[Rh_{12}(L_3)_6(L_5)_6(H_2O)_2(DMA)_2(CH_3CN)_7+H]^+$ (expected = 4650.0; found = 4651.5) have been highlighted for the Rh-MOP sample. In the case of the Rh-macrocycle, the mass corresponding to the formula $[Rh_6(L_3)_3(C_8H_5O_4)_6+H]^+$ has been highlighted (expected = 2268.8; found = 2267.7).

formylisophthalate were all clearly identifiable, thus further corroborating the clip-off synthesis of Sc-**pcu**-MOF.

Finally, we endeavoured to use Clip-off Chemistry to synthesize a metal-organic macrocycle[33–36] from a 0-D MOP system. To this end, we followed the second approach mentioned above, by designing a mixed-linker Rh-MOP that we could transform into a triangular metal-organic macrocycle (Figure 3a, S27–S34). We selected a Rh-MOP[37] built from six 4-c Rh paddle-wheel clusters linked by six 5-*tert*-butylbenzene-1,3-dicarboxylate (L_3) linkers and by six 3-[(3-carboxyphenyl)diazenyl]benzoate (L_4) linkers that together form a cage (diameter: 12 Å). In this cage, three paddle-wheel clusters are linked by three L_3 linkers to form a triangular macrocycle, and two of these units are linked by six L_4 linkers. Following a similar strategy as those explained in the previous examples, we functionalized this MOP with alkene groups by replacing L_4 with 3-[2-(3-carboxyphenyl)ethenyl]benzoate (L_5). We reasoned that the isoreticular Rh-MOP would contain a non-cleavable L_3 linker and a cleavable L_5 linker, which, upon cleavage via ozonolysis, would split the Rh-MOP into two equal fragments. We hypothesized that this splitting would release the metal-organic macrocycle built up from the three 4-c Rh^{II} paddle-wheel units linked to each other by the three L_3 linkers and with six pendant partly deprotonated isophthalic linkers.

We synthesized isoreticular Rh-MOP by heating a suspension of L_3, L_5, Na_2CO_3 and $Rh_2(OAc)_4$ in *N,N*-dimethylacetamide (DMA) at 100°C. After 4 days, the reaction yielded a dark precipitate that was centrifuged to separate out the Na_2CO_3. The resultant solution was precipitated in MeOH to yield a green powder, which was washed several times with MeOH. Finally, diffusion of diethyl ether into a solution of this green powder in DMF afforded green parallelogram-shaped crystals of Rh-MOP. SCXRD confirmed the formation of the expected isoreticular MOP, built up from six L_3 linkers and six cleavable L_5 linkers (Figure 3a). Next, the six linkers were cleaved to synthesize the metal-organic macrocycle by bubbling ozone through a suspension of Rh-MOP in DMA and hydrogen peroxide (50% wt. in H_2O) at room temperature for 30 min. Note that oxidative conditions were used in this clip-off reaction to obtain a pure Rh-macrocycle functionalized with six carboxylic acid groups. Afterwards, the resulting green suspension was centrifuged, and an aqueous HCl solution was added to the supernatant to precipitate out the Rh-macrocycle as a green solid. This solid was finally separated by centrifugation, washed with water three times, and dried at 85°C under vacuum.

We confirmed formation of the expected metal-organic Rh-macrocycle by ^{1}H NMR of the digested ozonated Rh-MOP (5% HF/[D_6]DMSO; Figure 3b), MALDI-TOF mass (Figure 3c) spectrometry and UV/Vis spectroscopy (Figure S33). The ^{1}H NMR spectrum lacked all the characteristic peaks of L_5 (olefinic protons at $\delta = 7.43$ ppm; and phenyl protons at $\delta = 8.18$ ppm, 7.92 ppm, 7.85 ppm and 7.51 ppm), yet it did reveal the characteristic signals of L_3 (phenyl protons at $\delta = 8.30$ ppm and 8.16 ppm; and *tert*-butyl protons at $\delta = 1.33$ ppm) and those of isophthalic acid (phenyl protons at $\delta = 8.47$ ppm, 8.17 ppm and 7.65 ppm; Figure 3b). This integrated spectrum indicated an L_3/isophthalic acid proton
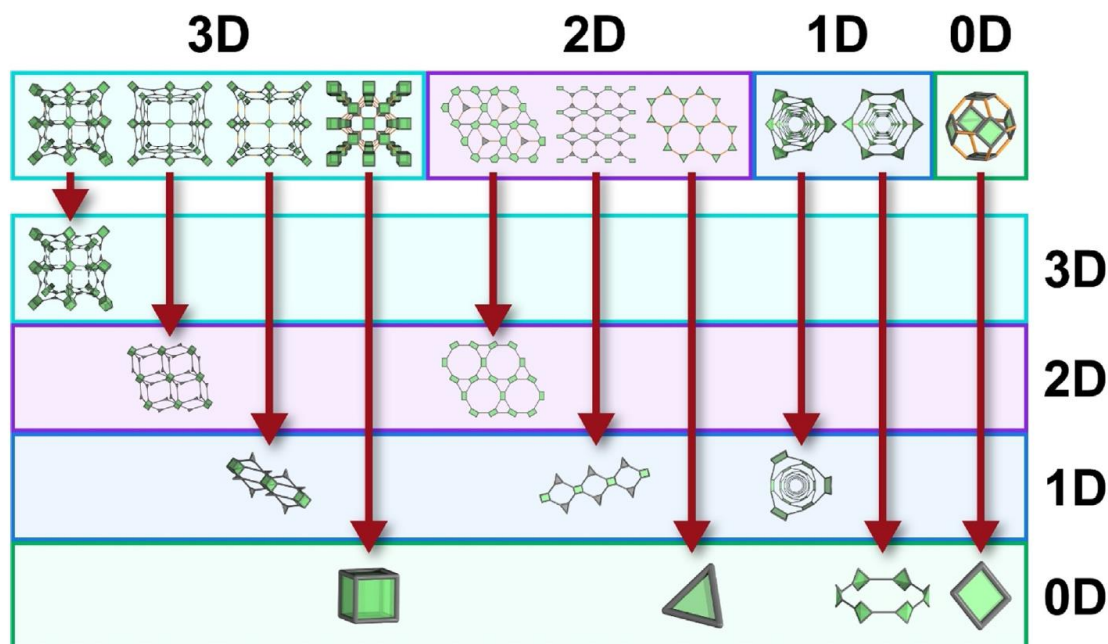
ratio of 1:2, consistent with the formula expected for the Rh-macrocycle (Figures S31, S32). Moreover, the absence of any proton signal corresponding to 3-formylbenzoic acid corroborated full cleavage of all the olefinic bonds in the Rh-MOP and their subsequent transformation to carboxylic acid groups.

Finally, we unambiguously confirmed the structure of the targeted macrocycle by positive-mode MALDI-TOF on pristine and ozonated samples of the Rh-MOP. The MALDI-TOF spectrum of the Rh-MOP showed its molecular ion $[M+H]^+$ ($m/z = 4651.5$), whereas that of the ozonated Rh-MOP did not, but did contain a new peak, for the molecular ion $[M+H]^+$ ($m/z = 2267.7$) corresponding to the Rh-macrocycle (Figure 3c). Moreover, UV/Vis analysis of both pristine and ozonated Rh-MOP samples did not reveal any shift in the low-energy absorption band I (λ_{max}) at 592 nm, indicating that the coordination of Rh^{II} ions in the ozonated solid had not changed, thus further corroborating formation of the desired Rh-macrocycle (Figure S33).

Conclusion

We have introduced Clip-off Chemistry, a new approach to synthesizing molecules and materials based on selective bond-breaking in reticular precursors materials via common organic transformations, via programmed de-reticulation and controlled etching at the molecular level. As proof-of-concept, we transformed two 3D MOFs (Zr-**scu**-MOF and Sc-**soc**-MOF) into two topologically distinct 3D MOFs (Zr-**pcu**-MOF and Sc-**pcu**-MOF, respectively). Moreover, we extended Clip-off Chemistry to a 0-D system, by transforming a MOP into a metal-organic macrocycle. In the examples that we have reported here, we demonstrated that the cleavage was quantitative and selective; was effective both in solid-phase and solution-phase chemistry; and occurred in a single-crystal-to-single crystal fashion across the entire bulk precursor sample. Moreover, we demonstrated control over the cleavage of each olefinic bond into carboxylic acid groups using oxidative conditions.

Our preliminary results suggest that Clip-off Chemistry is ripe for further exploration. Since it is based on bond cleavage, the dimensionality of the parent reticular material dictates the synthetic feasibility of the target molecules and/or materials (Figure 4). Thus, it offers the possibility to modify structures of reticular materials without changing their dimensionality (e.g. 3D → 3D, or 2D → 2D). For example, one might employ Clip-off Chemistry for post-synthetic modification of the topology and/or the porosity of a given material. Moreover, it could be applied to 3D structures to augment the diversity of new 2D materials: for instance, by converting well-known 3D pillared reticular materials into isolated 2D layers, via selective clipping of the pillaring linkers. Similarly, it shows promise for using 3D or 2D structures to isolate 1D materials in the form of metallic chains, or to synthesize 0-D systems, including MOPs, macrocycles and clusters, from 3D/2D/1D structures and even from other 0-D systems (e.g. MOPs). Cleavage of bonds in reticular materials may also be expanded to purely organic structures.

Research Articles

Angewandte *International Edition* *Chemie*

Figure 4. Clip-off Chemistry for the synthesis of molecular architectures of different dimensionality. Schematic illustrating the potential outcomes of Clip-off Chemistry, in which the dimensionality of the parent reticular materials dictates the dimensionality of the target molecules and structures.

Indeed, COFs and organic cages are another endless source of precursors in Clip-off Chemistry for possible synthesis of organic polymers, cages, macrocycles or other organic compounds. Similarly, other reactions involving the cleavage of bonds (e.g. photolysis) are potential candidates to be applied in reticular materials for their programmable disassembly.[38–40] In summary, our results prove that the programmed disassembly of reticular materials is feasible, and that Clip-off Chemistry could provide researchers with access to myriad new molecular architectures.

Acknowledgements

Conflict of Interest

The authors declare no conflict of interest.

[1] H. Li, M. Eddaoudi, T. L. Groy, O. M. Yaghi, *J. Am. Chem. Soc.* **1998**, *120*, 8571–8572.

[2] O. M. Yaghi, M. O'Keeffe, N. W. Ockwig, H. K. Chae, M. Eddaoudi, J. Kim, *Nature* **2003**, *423*, 705–714.

[3] H. Li, M. Eddaoudi, M. O'Keeffe, O. M. Yaghi, *Nature* **1999**, *402*, 276–279.

[4] O. M. Yaghi, G. Li, H. Li, *Nature* **1995**, *378*, 703–706.

[5] S. Kitagawa, R. Kitaura, S. I. Noro, *Angew. Chem. Int. Ed.* **2004**, *43*, 2334–2375; *Angew. Chem.* **2004**, *116*, 2388–2430.

[6] B. F. Abrahams, B. F. Hoskins, D. M. Michail, R. Robson, *Nature* **1994**, *369*, 727–729.

[7] B. F. Hoskins, R. Robson, *J. Am. Chem. Soc.* **1989**, *111*, 5962–5964.

[8] O. M. Yaghi, M. J. Kalmutzki, C. S. Diercks, *Introduction to Reticular Chemistry: Metal-Organic Frameworks and Covalent Organic Frameworks*, Wiley-VCH, Weinheim, **2019**.

[9] X. Feng, X. Ding, D. Jiang, *Chem. Soc. Rev.* **2012**, *41*, 6010–6022.

[10] D. J. Tranchemontagne, Z. Ni, M. O'Keeffe, O. M. Yaghi, *Angew. Chem. Int. Ed.* **2008**, *47*, 5136–5147; *Angew. Chem.* **2008**, *120*, 5214–5225.

[11] J. J. Perry IV, J. A. Perman, M. J. Zaworotko, *Chem. Soc. Rev.* **2009**, *38*, 1400–1417.

[12] S. Lee, H. Jeong, D. Nam, M. S. Lah, W. Choe, *Chem. Soc. Rev.* **2021**, *50*, 528–555.

GDCh

Research Articles

Angewandte International Edition *Chemie*

[13] M. Eddaoudi, D. B. Moler, H. Li, B. Chen, T. M. Reineke, M. O'Keeffe, O. M. Yaghi, *Acc. Chem. Res.* **2001**, *34*, 319–330.

[14] M. Eddaoudi, J. Kim, N. Rosi, D. Vodak, J. Wachter, M. O'Keeffe, O. M. Yaghi, *Science* **2002**, *295*, 469–472.

[15] S. M. Cohen, *Chem. Rev.* **2012**, *112*, 970–1000.

[16] O. M. Yaghi, *Mol. Front. J.* **2019**, *3*, 66–83.

[17] M. O'Keeffe, O. M. Yaghi, *Chem. Rev.* **2012**, *112*, 675–702.

[18] M. O'Keeffe, M. A. Peskov, S. J. Ramsden, O. M. Yaghi, *Acc. Chem. Res.* **2008**, *41*, 1782–1789.

[19] V. A. Blatov, A. P. Shevchenko, D. M. Proserpio, *Cryst. Growth Des.* **2014**, *14*, 3576–3586.

[20] A. F. Wells, *Three-Dimensional Nets and Polyhedral*, Wiley, Hoboke, **1977**.

[21] H. Wang, X. Dong, J. Lin, S. J. Teat, S. Jensen, J. Cure, E. V. Alexandrov, Q. Xia, K. Tan, Q. Wang, D. H. Olson, D. M. Proserpio, Y. J. Chabal, T. Thonhauser, J. Sun, Y. Han, J. Li, *Nat. Commun.* **2018**, *9*, 1745.

[22] M. Li, D. Li, M. O'Keeffe, O. M. Yaghi, *Chem. Rev.* **2014**, *114*, 1343–1370.

[23] J. Albalad, H. Xu, F. Gándara, M. Haouas, C. Martineau-Corcos, R. Mas-Ballesté, S. A. Barnett, J. Juanhuix, I. Imaz, D. Maspoch, *J. Am. Chem. Soc.* **2018**, *140*, 2028–2031.

[24] V. Guillerm, H. Xu, J. Albalad, I. Imaz, D. Maspoch, *J. Am. Chem. Soc.* **2018**, *140*, 15022–15030.

[25] R. Criegee, *Angew. Chem. Int. Ed. Engl.* **1975**, *14*, 745–752; *Angew. Chem.* **1975**, *87*, 765–771.

[26] C. E. Schiaffo, P. H. Dussault, *J. Org. Chem.* **2008**, *73*, 4688–4690.

[27] L. B. Harding, W. A. Goddard III, *J. Am. Chem. Soc.* **1978**, *100*, 7180–7188.

[28] L. H. Xie, X. M. Liu, T. He, J. R. Li, *Chem* **2018**, *4*, 1911–1927.

[29] S. Wang, L. Chen, M. Wahiduzzaman, A. Tissot, L. Zhou, I. A. Ibarra, A. Gutiérrez-Alejandre, J. S. Lee, J. S. Chang, Z. Liu, J. Marrot, W. Shepard, G. Maurin, Q. Xu, C. Serre, *Matter* **2021**, *4*, 182–194.

[30] H. Furukawa, F. Gándara, Y. B. Zhang, J. Jiang, W. L. Queen, M. R. Hudson, O. M. Yaghi, *J. Am. Chem. Soc.* **2014**, *136*, 4369–4381.

[31] J. W. Zhang, P. Qu, M. C. Hu, S. N. Li, Y. C. Jiang, Q. G. Zhai, *Inorg. Chem.* **2019**, *58*, 16792–16799.

[32] Y. Liu, J. F. Eubank, A. J. Cairns, J. Eckert, V. C. Kravtsov, R. Luebke, M. Eddaoudi, *Angew. Chem. Int. Ed.* **2007**, *46*, 3278–3283; *Angew. Chem.* **2007**, *119*, 3342–3347.

[33] P. J. Stang, B. Olenyuk, *Acc. Chem. Res.* **1997**, *30*, 502–518.

[34] B. Olenyuk, A. Fechtenkötter, P. J. Stang, *J. Chem. Soc. Dalton Trans.* **1998**, 1707–1728.

[35] M. Fujita, O. Sasaki, T. Mitsuhashi, T. Fujita, J. Yazaki, K. Yamaguchi, K. Ogura, *Chem. Commun.* **1996**, 1535–1536.

[36] F. A. Cotton, L. M. Daniels, C. Lin, C. A. Murillo, *J. Am. Chem. Soc.* **1999**, *121*, 4538–4539.

[37] J. R. Li, H. C. Zhou, *Nat. Chem.* **2010**, *2*, 893–898.

[38] L. Feng, K. Y. Wang, G. S. Day, M. R. Ryder, H. C. Zhou, *Chem. Rev.* **2020**, *120*, 13087–13133.

[39] K. Y. Wang, L. Feng, T. H. Yan, S. Wu, E. A. Joseph, H. C. Zhou, *Angew. Chem. Int. Ed.* **2020**, *59*, 11349–11354; *Angew. Chem.* **2020**, *132*, 11445–11450.

[40] P. Shieh, M. R. Hill, W. Zhang, S. L. Kristufek, J. A. Johnson, *Chem. Rev.* **2021**, *121*, 7059–7121.

[41] Deposition Numbers 2080949 (for Zr-**scu**-MOF), 2080950 (for Zr-**pcu**-MOF), 2080951 (for Sc-**soc**-MOF), 2080952 (for Sc-**pcu**-MOF) and 2080953 (for Rh-MOP) contain the supplementary crystallographic data for this paper. These data are provided free of charge by the joint Cambridge Crystallographic Data Centre and Fachinformationszentrum Karlsruhe Access Structures service www.ccdc.cam.ac.uk/structures.

JACS
JOURNAL OF THE AMERICAN CHEMICAL SOCIETY

Article

Isoreticular Contraction of Metal−Organic Frameworks Induced by Cleavage of Covalent Bonds

Yunhui Yang, Pilar Fernández-Seriñán, Inhar Imaz,* Felipe Gándara, Marcel Handke, Borja Ortín-Rubio, Judith Juanhuix, and Daniel Maspoch*

Read Online

ACCESS | 📊 Metrics & More | 📰 Article Recommendations | 🆂🅸 Supporting Information

ABSTRACT: Isoreticular chemistry, in which the organic or inorganic moieties of reticular materials can be replaced without destroying their underlying nets, is a key concept for synthesizing new porous molecular materials and for tuning or functionalization of their pores. Here, we report that the rational cleavage of covalent bonds in a metal−organic framework (MOF) can trigger their isoreticular contraction, without the need for any additional organic linkers. We began by synthesizing two novel MOFs based on the MIL-142 family, (In)BCN-20B and (Sc)BCN-20C, which include cleavable as well as noncleavable organic linkers. Next, we

selectively and quantitatively broke their cleavable linkers, demonstrating that various dynamic chemical and structural processes occur within these structures to drive the formation of isoreticular contracted MOFs. Thus, the contraction involves breaking of a covalent bond, subsequent breaking of a coordination bond, and finally, formation of a new coordination bond supported by structural behavior. Remarkably, given that the single-crystal character of the parent MOF is retained throughout the entire transformation, we were able to monitor the contraction by single-crystal X-ray diffraction.
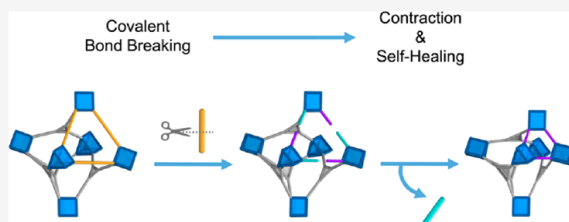
■ INTRODUCTION

Metal−organic frameworks (MOFs), a class of crystalline materials assembled by combining inorganic metal-based nodes with organic linkers, exhibit long-range ordered structures with permanent porosity.[1,2] Given the nearly infinite possible permutations of their building blocks, MOFs are highly versatile: they can be designed to have distinctive features such as an exceptionally large surface area and adjustable pore sizes.

The design and synthesis of MOFs have been expanded by reticular chemistry, which provides high levels of chemical control. This is achieved mainly by either of two strategies: (i) predesign of a novel target net through judicious design of the molecular building blocks or (ii) use of a known net as a blueprint for a novel material, designed by applying the isoreticular principle.[3−6] The primary aim of isoreticular chemistry is to tune or functionalize the organic or inorganic moieties without altering their underlying nets. Thus, it has proven invaluable for modulating the properties of MOFs and for optimizing their performance in myriad applications. Isoreticular MOFs can be synthesized by common direct synthesis[7−9] or by postsynthetic modification (PSM). PSM-based methodologies to synthesize isoreticular MOFs include linker functionalization, transmetalation, sequential linker installation, and solvent-assisted linker exchange (SALE).[10−12] Among these, SALE is based on substitution of a linker that bridges two metal ions/clusters, with an external

linker, in the presence of a solvent. This enables generation of new isoreticular MOFs: for example, ones in which interpenetration can be controlled[13,14] or that can exhibit nondefault topologies.[15] In SALE, replacement is performed chiefly by using external linkers whose length is equal to or greater than that of the original linkers, thereby affording a lattice of the same or greater size.[16−18] Alternatively, a few studies have shown that the framework can also be contracted, by using shorter linkers, although this approach has not been widely explored.[14,19,20] The contraction of lattices can also confer the resultant MOFs[21] with unusual properties such as negative and stepwise gas-adsorption, modulation of the radical spin stated in solid state, or stimuli responsiveness and selectivity, which can be utile for applications such as gas storage and separation, catalysis, sensing, and controlled release.[22−28]

Herein, we report a new approach to isoreticular contraction of MOFs that is based on breaking of covalent bonds and does not require addition of any external linkers (Figure 1). Recently, we described clip-off chemistry, a new synthetic
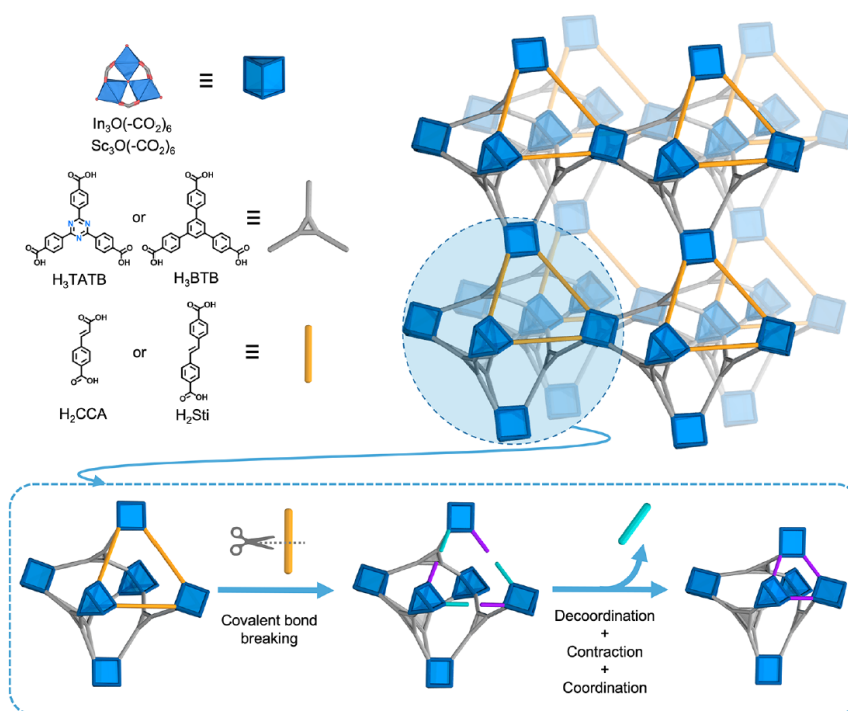
17398
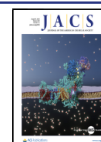
Figure 1. Schematic of the isoreticular contraction of (In)BCN-20B and (Sc)BCN-20C induced by cleavage of covalent bonds.
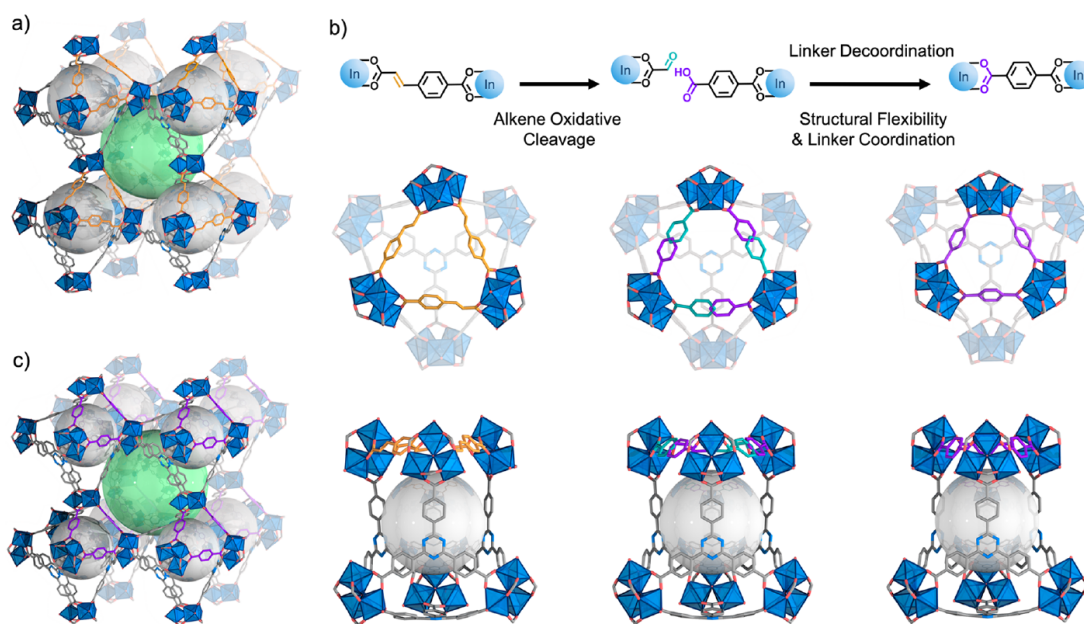

Figure 2. (a) Crystal structure of (In)BCN-20B. (b) Schematic of the stepwise isoreticular contraction from (In)BCN-20B (left) to (In)BCN-20B′ (middle) to (In)BCN-20A (right). Corresponding SCXRD data, revealing the octahedral cages viewed along the crystallographic *c* and *b* axes, highlighting transformation of the CCA linker (orange) to the shorter BDC linker (violet), and contraction of the triangular face. (c) Crystal structure of (In)BCN-20A.

strategy to make new molecules and materials based on the selective, quantitative, and controlled cleavage of bonds in reticular materials.[29] Here, we show that this concept can be applied to control the stepwise synthesis of isoreticular MOFs exhibiting contracted structures relative to their parent MOFs. To this end, we have designed two new mixed-linker parent MOFs that are isoreticular to the **nht**-(Fe)MIL-142 family:[30,31] (In)BCN-20B and (Sc)BCN-20C (BCN stands for Barcelona

Material). This new isoreticular synthetic approach begins with the cleavage of an olefinic bond of one of the bridging linkers, which splits the linker into two monocoordinated ligands. This periodic and quantitative fracture in the MOF is followed by the decoordination of one of the monocoordinated ligands, using solvents. This ligand removal instantaneously induces both contraction of the lattice and a self-healing phenomenon, which involves the migration and coordination of the monocoordinated ligand remaining in the structure to the accessible metal ions. Interestingly, this stepwise isoreticular contraction of MOFs, which involves breaking of a covalent bond, subsequent breaking of a coordination bond, and finally, formation of a new coordination bond supported by dynamic structural behavior, can be followed by single-crystal X-ray diffraction (SCXRD), as these events occur in a single-crystal to single-crystal manner.

■ RESULTS AND DISCUSSION

We began by synthesizing (In)BCN-20B. First, a dispersion of $In(NO_3)_3 \cdot xH_2O$, 4,4′,4″-(1,3,5-triazine-2,4,6-triyl)tribenzoic acid (H_3TATB) and 4-carboxycinnamic acid (H_2CCA) in N,N-dimethylformamide (DMF) and HNO_3 (3.5 M in DMF) was heated at 120 °C for 30 h. Next, the resulting hexagonal prismatic crystals were analyzed by SCXRD, which confirmed formation of a 3D framework isoreticular to **nht**-(Fe)MIL-142B. (In)BCN-20B crystallizes in a trigonal lattice with an $R\bar{3}c$ (No. 167) space group, with unit cell parameters of $a = b =$ 30.820 and $c = 95.540$ Å (Table S1). The 3D structure of (In)BCN-20B is formed by vertex-sharing distorted octahedral cages, with an underlying **nht** topology (Figure 2a). Each cage is formed by six trigonal prismatic $In_3O(-CO_2)_6$ clusters located at vertices, which are connected by four tritopic TATB linkers and three ditopic CCA linkers. Note that these CCA linkers are symmetrically disordered about an inversion center, which results in similarity of spatial occupation between the dislocated aromatic rings of the CCA linker and those of a naphthalene molecule (Figures S1 and S2). The location of the two types of linkers within the cage defines one triangular face, whose edges are occupied by three CCA linkers (Figure 2b, left and Figure S3), and four triangular faces, each of which is occupied by one TATB linker. This means that each of the three remaining faces shares one of the edges occupied by a CCA linker with the first triangular face, whereas the other two edges are unoccupied. The overall framework of (In)BCN-20B shows a 2-fold interpenetrated structure, in which two catenane-like octahedral cages from two different **nht** nets interlocked via one of their pure TATB triangular faces (Figure S4). Further characterization of (In)BCN-20B confirmed its phase purity, as the experimental powder-XRD (PXRD) pattern matched the simulated one (Figure 3a). Furthermore, the ^{1}H-NMR spectrum of the digested sample contained the expected TATB/CCA ratio of 4:3 (Figure S6).

Having synthesized (In)BCN-20B, we then cleaved all its alkene bonds and subsequently converted them into aldehyde/carboxylic acid groups via a solid−gas ozonolysis reaction.[29,32,33] First, 20 mg of single crystals of solvent-free (In)BCN-20B were packed into a plastic tube. Next, dry ozone was flowed (~15 g/Nm^3) continuously through the sample for 35 min. Finally, the resultant crystals were analyzed by SCXRD, showing that ozonized (In)BCN-20B′ crystallized in a trigonal lattice with an $R\bar{3}m$ (No. 166) space group, having unit cell parameters of $a = b = 30.830$ and $c = 47.592$ Å (Table S2). Overall, (In)BCN-20B′ exhibited a related 3D structure to
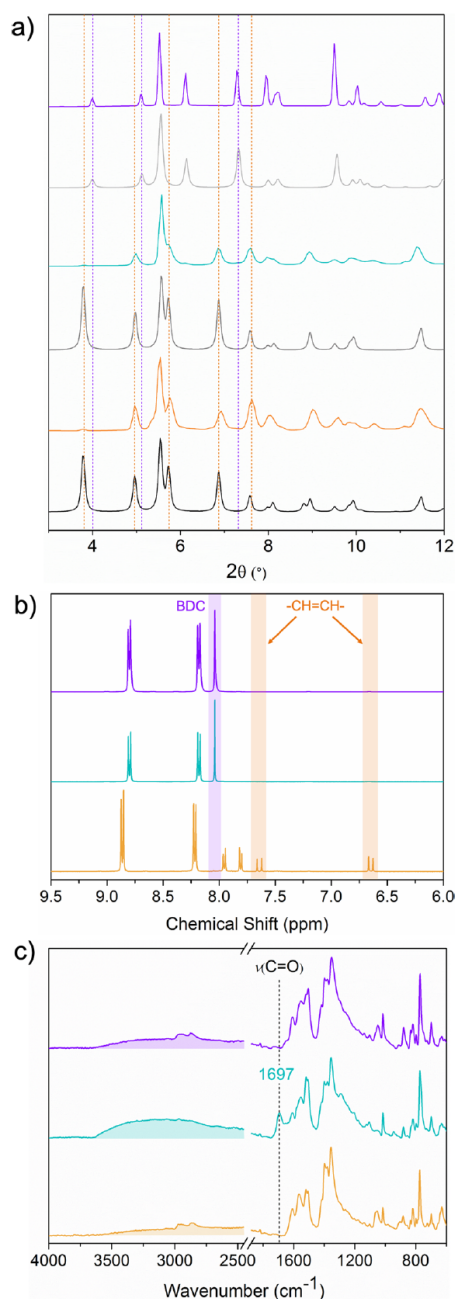
Figure 3. (a) PXRD patterns of simulated (black) and experimental (orange) (In)BCN-20B; simulated (gray) and experimental (cyan) (In)BCN-20B′; and simulated (light gray) and experimental (violet) (In)BCN-20A. (b) ^{1}H-NMR spectra of (In)BCN-20B (orange), (In)BCN-20B′ (cyan), and (In)BCN-20A (violet). The protons from olefinic bonds and terephthalate have been highlighted in orange and violet, respectively. (c) Infrared spectra of (In)BCN-20B (orange), (In)BCN-20B′ (cyan), and (In)BCN-20A (violet).

that of (In)BCN-20B but with evident changes in its connectivity through the CCA linkers. Indeed, SCXRD data confirmed the integrity of the inorganic In-oxo clusters and of the TATB linkers. However, at the positions initially occupied

Article

by the CCA linkers, the similarity in spatial occupation between the dislocated aromatic rings of the CCA linker and the naphthalene molecule was lost (Figure 2b, middle). This observation clearly suggested that the CCA linkers no longer existed.

To confirm the oxidative cleavage of CCA linkers into the expected monocoordinated glyoxylate and single deprotonated terephthalic acid (BDC) ligands (Figure 2b), we analyzed a digested (In)BCN-20B′ sample by ^{1}H NMR and then compared the resulting spectrum to that of the starting (In)BCN-20B (Figures 3b and S6, S8). The spectrum of the digested (In)BCN-20B showed the characteristic peaks of the olefinic protons of CCA at δ = 7.64 and δ = 6.65 ppm. In contrast, the spectrum of the digested (In)BCN-20B′ corroborated the disappearance of this olefinic signal. It also revealed the disappearance of the phenyl (δ = 7.94 and δ = 7.81 ppm) and the carboxylic acid (δ = 13.06 ppm) protons of the CCA but did show the characteristic signals for the terephthalic acid (BDC, δ = 8.04 ppm). Unfortunately, the aldehyde proton of the glyoxylic acid was not detected, presumably due to the fact that its boiling point (111 °C) is lower than the temperature (120 °C) at which the digestion took place overnight. However, the presence of glyoxylic acid was confirmed by electrospray ionization mass spectrometry (ESI-MS) analysis in a negative ion mode using a (In)BCN-20B′ sample digested under milder conditions (HF in DMSO at room temperature). The ESI-MS spectrum showed a peak at m/z = 72.99, which matches the molecular mass of the deprotonated glyoxylate $[C_2HO_3]^-$ (m/z = 73.03; Figure S9). These results clearly indicated that the olefinic bond of the ditopic CCA linkers had been quantitatively cleaved by ozonolysis and subsequently converted into two monocoordinated ligands: a single deprotonated BDC and a glyoxylate. Supporting this oxidative cleavage reaction, the FTIR spectrum of the ozonated (In)BCN-20B′ exhibited a more intense C=O stretch band at 1697 cm^{-1} relative to that in the spectrum of the non-ozonated (In)BCN-20B. Moreover, it showed enhanced, broad absorbance at around 3300 cm^{-1}, indicative of large perturbations caused by H-bonded hydroxyl groups of the free carboxylic acid groups (Figures 3c and S10).[34,35] Next, we performed PXRD on a bulk sample of ozonated (In)BCN-20B′ to confirm its crystallinity and phase purity. The resulting PXRD pattern matched the one calculated from the crystal structure (Figures 3a and S11), confirming that the cleavage of alkene bonds via ozonolysis did not compromise the crystallinity throughout the bulk sample. Together these results confirmed the quantitative cleavage of CCA linkers and the consequent formation of a new structure with less connectivity among its trimeric In^{3+} clusters. Indeed, analysis of the topology of (In)BCN-20B′ using the ToposPro 5.3.3.5 software,[36] and considering TATB linkers as 3-connected points of extension (3-c), and In$_3$O(−CO$_2$)$_6$ clusters as nodes that have four coordination points (4-c), revealed formation of a 2-fold interpenetrated MOF with two independent underlying trinodal (3,3,4)-c nets (topological code **3,3,4T22**, Figure S12).

Having demonstrated that ditopic CCA linkers could be cleaved into two monocoordinated ligands, we then explored the possibility of substituting these monocoordinated ligands with solvent molecules. First, crystals of (In)BCN-20B′ were incubated in DMF for 1 week at room temperature. Next, the resultant crystals were analyzed by SCXRD, which revealed that a new 3D structure (In)BCN-20A had been formed

(Figure 2c). This new MOF crystallizes in the trigonal lattice with the space group $R\bar{3}m$ (No. 166) and lattice parameters of $a = b$ = 28.783 and c = 47.708 Å (Table S3). (In)BCN-20A, which is isostructural to **nht**-(Fe)MIL-142A,[30] recovers the initial 3D **nht** framework formed by vertex-sharing distorted octahedral cages. However, its cages are instead formed by six In$_3$O(−CO$_2$)$_6$ clusters connected by four tritopic TATB linkers and three ditopic BDC linkers, the latter occupying the analogous position of the CCA linkers in (In)BCN-20B (Figure 2b, right).

The phase transition from (In)BCN-20B′ to (In)BCN-20A unambiguously unveiled a self-healing behavior, which we envisaged occurs in three steps within the pores. First, DMF molecules enter the pores and replace the glyoxylate linkers. Here, the release of glyoxylate from the MOF was experimentally confirmed by analyzing the DMF supernatant resulting from the incubation process by ESI-MS, from which the characteristic peak at m/z = 72.99 was detected (Figure S13). Second, the decoordination of glyoxylate causes the framework to act dynamically. In the third and final step, this behavior leads to coordination of the free carboxylic acid group of each BDC linker to the In^{3+} metal sites that were previously occupied by the glyoxylate. Accordingly, the BDC linker would have to migrate a distance of ∼2.4 Å.

To further evaluate the degree of the aforementioned flexibility, we compared the unit cell volumes of the three MOFs: the initial (In)BCN-20B, the ozonated (In)BCN-20B′, and the self-healed (In)BCN-20A (Table S4). From (In)BCN-20B to (In)BCN-20B′, the unit cell volume only shrunk by 0.3%. However, from (In)BCN-20B′ to (In)BCN-20A, the cell volume decreased by 12.6%, an obvious volumetric contraction. We reasoned that the movements involving this dynamic behavior could also be studied by comparing the structural changes in the octahedral cage units (Figures 2b and S14). In the octahedral cage of the initial (In)BCN-20B, the length (note: all lengths were calculated starting from the carbon atoms of the carboxylate groups of the linkers) of the edges of the face constructed with CCA linkers is 8.0 Å, and the average length of the remaining edges is 12.1 Å. As we had expected, cleavage of the CCA linkers barely affected this octahedral cage unit: the length of the edges of the face occupied by the cleaved CCA linkers only increased to 8.2 Å. We attributed this slight increase to the steric hindrance effects of both the BDC and the glyoxylate linkers. In (In)BCN-20A, this length decreases significantly, down to 5.7 Å, because the BDC linker is much smaller than both the initial and the cleaved CCA linkers. Contrariwise, this contraction barely affects the other edges involving the TATB linker, exhibiting an average length of 12.0 Å.

Given that the structure of (In)BCN-20A differs markedly from that of (In)BCN-20B or (In)BCN-20B′, we studied whether this transformation would occur throughout the bulk sample, using PXRD. Supporting a homogeneous transformation, the PXRD pattern of (In)BCN-20A matched the one calculated from the corresponding structure determined by SCXRD (Figures 3a and S15). Comparing the PXRD patterns of (In)BCN-20A and (In)BCN-20B, we found that the diffraction peak of (In)BCN-20B at 2θ = 3.8° which corresponds to the (10$\bar{2}$) crystallographic plane being shifted to a higher angle (2θ = 5.1°) in the same plane of (In)BCN-20A, thus confirming the compression of the framework. Phase homogeneity was also studied by FTIR and ^{1}H NMR (Figures S16 and S17). The FTIR spectrum revealed that the stretching
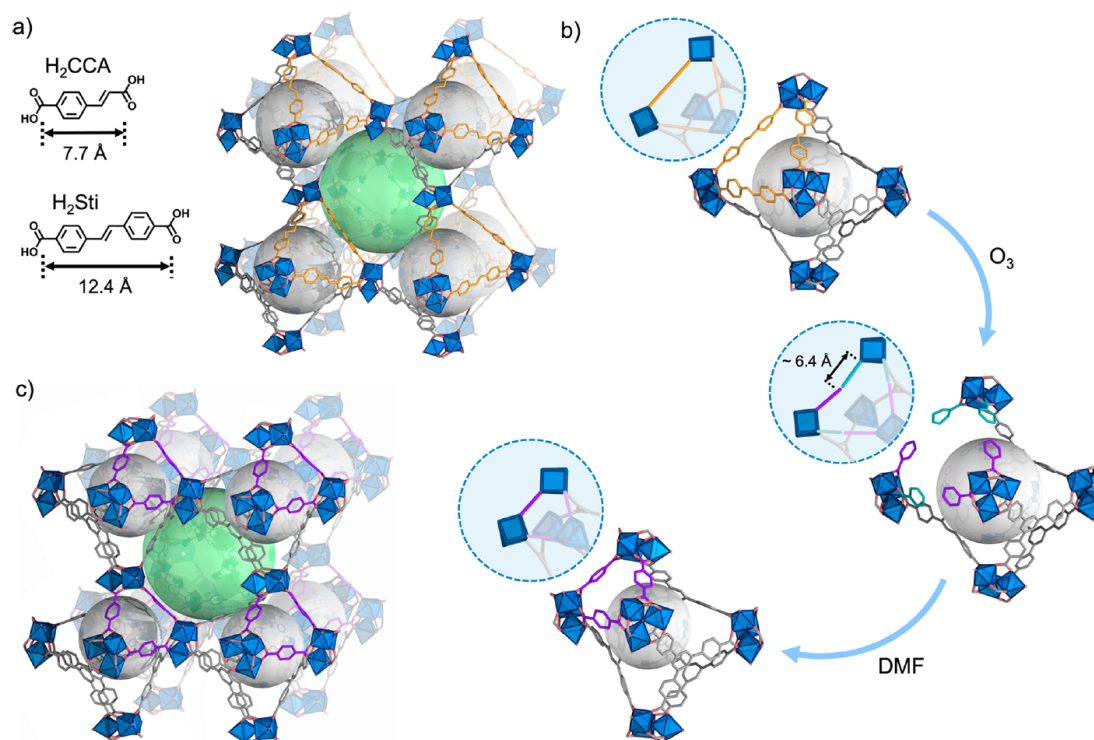
Figure 4. (a) Crystal structure of (Sc)BCN-20C. (b) Schematic and corresponding SCXRD structures of the stepwise isoreticular contraction from (Sc)BCN-20C (top) to (Sc)BCN-20C′ (middle) to (Sc)BCN-20A (down). (c) Crystal structure of (Sc)BCN-20A.

band of characteristic carbonyl groups (1697 cm^{-1}) and the broad absorbance at around 3300 cm^{-1} had been dramatically attenuated, identically to that of the initial (In)BCN-20B (Figure 3c). The ^{1}H NMR spectrum confirmed the expected TATB/BDC ratio of 4:3.

We would like to highlight that all our attempts to transform (In)BCN-20B into (In)BCN-20A by direct linker exchange of CCA by BDC were unsuccessful (see Section 2 of the Supporting Information). This suggests that covalent bond cleavage of the CCA linker highly facilitates the internal restructuring of the framework, involving both flexible and self-healing behavior.

Seeking to investigate whether such behavior could occur in an isoreticular framework with greater distances between metal clusters, we substituted the CCA linker with the 4,4′-stilbenedicarboxylic acid (H$_2$Sti) linker, which is longer (Figure 4a). However, all our attempts at synthesizing the isostructural MOF using In^{3+} were unsuccessful. Fortunately, we were able to synthesize its Sc^{3+} analogue using the (ditopic) Sti linker and the (tritopic) 1,3,5-tris(4-carboxyphenyl)-benzene (BTB) linker (Figure 4a). (Sc)BCN-20C crystallizes in the monoclinic symmetry with a $C2/c$ space group (No. 15) and lattice parameters of $a = 60.279$, $b = 34.723$, and $c = 37.136$ Å (Table S5). As its analogues, it contains a 2-fold interpenetrated structure with two underlying **nht** nets (Figure S18). Note that the two nets are interconnected by formate linkers that can be formed upon decomposition of DMF aided by HNO$_3$.[31,37] These nets are built up from vertex-sharing distorted octahedral cages, which are larger than those of (In)BCN-20B or (In)BCN-20A. Their main difference lies in the edges of the triangular face defined by three Sti linkers,

whose length is increased to 12.2 Å. The other edges of the octahedra are slightly longer (12.3 Å) than those of (In)BCN-20B. The phase purity of (Sc)BCN-20C was confirmed by PXRD, whose pattern matched the one simulated from SCXRD data (Figures S19 and S20), and by ^{1}H NMR, the spectrum confirmed the expected BTB/Sti ratio of 4:3 (Figure S23).

Next, we performed a cleavage experiment on the Sti linkers similar to the previous experiment on the CCA linkers (Figure 4b). Thus, ozone was flowed (~15 g/Nm^3) continuously through a crystalline sample of solvent-free (Sc)BCN-20C for 5 min. The quantitative cleavage of Sti linkers and conversion of the resultant fragments to the expected monocoordinated HBDC and 4-formylbenzoate (4-FBA) were corroborated by ^{1}H NMR, SCXRD, PXRD, and FTIR (Table S6, Figures S21, S24, S25, and S29). Additionally, SCXRD data revealed that the structure of (Sc)BCN-20C′ is very similar to that of the initial (Sc)BCN-20C, with the corresponding octahedral cage units having similar dimensions. However, we observed one significant difference: benzoate ligands—most likely, 4-FBA linkers with highly disordered aldehyde groups—bridging the two interpenetrated nets and partially substituting the formate ligands. This observation evidenced the mobility of these monocoordinated ligands inside the pores upon cleavage of the ditopic linkers.

Finally, endeavoring to remove the 4-FBA ligands and induce the dynamic and self-healing behavior for the formation of the isoreticular (Sc)-BCN-20A, we immersed (Sc)BCN-20C′ in DMF for a week. Interestingly, SCXRD of the resulting crystals confirmed the formation of this MOF (Table S7, Figures S18, S19, S22, and S26–S29), whose structure is

isostructural to that of (In)BCN-20A (Figure 4b,c). (Sc)-BCN-20A crystallizes in a trigonal system with the space group $R\bar{3}c$ (No. 167) and lattice parameters of $a = b = 28.682$ and $c = 95.606$ Å. Accordingly, through this dynamic, self-healing phenomenon, the cell volume had been dramatically compressed by 30.7% (Table S8 and Figure S31). In this process, all BDC linkers traveled a distance of ~6.4 Å to coordinate to the Sc^{3+} metal sites, shrinking one of the triangular faces of the cages from 12.2 to 6.1 Å.

CONCLUSIONS

In conclusion, we have shown that the cleavage of covalent bonds within bridging organic linkers in an MOF can trigger a series of chemical and structural dynamic processes that drive the formation of an isoreticular contracted MOF. Remarkably, as the single-crystal character of the parent MOF is retained throughout the entire isoreticular transformation, we were able to use SCXRD to obtain invaluable crystallographic snapshots of the stepwise processes. Initially, applying our concept of clip-off chemistry, we were able to cleave each bridging alkene-containing organic linker into two monocoordinated ligands via ozonolysis, thereby disconnecting two metal clusters. Among these monocoordinated ligands, one is terminated with a carboxylic acid group, whereas the other ends in an aldehyde group. As this latter ligand is weaker, we were able to decoordinate it from the metal center by simply treating the MOF with DMF. This removal process conferred the structure with dynamic behavior that involved the migration and subsequent coordination of the other monocoordinated ligand with a free carboxylic acid group to the open metal site. In what we have called "self-healing behavior", the metal clusters that had been disconnected during cleavage of the linker bond reconnected to form a new MOF isoreticular to the initial one, with a contracted structure. Thus, the complete transformation involves breaking of covalent bonds, breaking and formation of coordination bonds, and contraction of the crystal structure, with reductions in the cell volume of up to 30.7%, all occurring in a single-crystal to single-crystal manner. Overall, these stepwise isoreticular transformations exemplify the rich chemistry that can be done inside MOF pores. They also underscore the potential of clip-off chemistry (i.e., breaking of covalent bonds) to discover new phenomena in MOFs and to synthesize new MOFs or other materials.

ASSOCIATED CONTENT

Supporting Information

The Supporting Information is available free of charge at https://pubs.acs.org/doi/10.1021/jacs.3c05469.

Detailed syntheses, optical microscopy images, PXRD diffractogram, FT-IR, ESI-MS, NMR, and crystallographic details (PDF)

Accession Codes

CCDC 2264121−2264126 contain the supplementary crystallographic data for this paper. These data can be obtained free of charge via www.ccdc.cam.ac.uk/data_request/cif, or by emailing data_request@ccdc.cam.ac.uk, or by contacting The Cambridge Crystallographic Data Centre, 12 Union Road, Cambridge CB2 1EZ, UK; fax: +44 1223 336033.

AUTHOR INFORMATION

Corresponding Authors

Inhar Imaz − CSIC, and Barcelona Institute of Science and Technology, Catalan Institute of Nanoscience and Nanotechnology (ICN2), Bellaterra, Barcelona 08193, Spain; Departament de Química, Facultat de Ciències, Universitat Autònoma de Barcelona, Bellaterra 08193, Spain; orcid.org/0000-0002-0278-1141; Email: inhar.imaz@icn2.cat

Daniel Maspoch − CSIC, and Barcelona Institute of Science and Technology, Catalan Institute of Nanoscience and Nanotechnology (ICN2), Bellaterra, Barcelona 08193, Spain; Departament de Química, Facultat de Ciències, Universitat Autònoma de Barcelona, Bellaterra 08193, Spain; ICREA, Barcelona 08010, Spain; orcid.org/0000-0003-1325-9161; Email: daniel.maspoch@icn2.cat

Authors

Yunhui Yang − CSIC, and Barcelona Institute of Science and Technology, Catalan Institute of Nanoscience and Nanotechnology (ICN2), Bellaterra, Barcelona 08193, Spain; Departament de Química, Facultat de Ciències, Universitat Autònoma de Barcelona, Bellaterra 08193, Spain

Pilar Fernández-Seriñán − CSIC, and Barcelona Institute of Science and Technology, Catalan Institute of Nanoscience and Nanotechnology (ICN2), Bellaterra, Barcelona 08193, Spain; Departament de Química, Facultat de Ciències, Universitat Autònoma de Barcelona, Bellaterra 08193, Spain; orcid.org/0000-0002-6456-7386

Felipe Gándara − Consejo Superior de Investigaciones Científicas (CSIC), Materials Science Institute of Madrid (ICMM), Madrid 28049, Spain; orcid.org/0000-0002-1671-6260

Marcel Handke − CSIC, and Barcelona Institute of Science and Technology, Catalan Institute of Nanoscience and Nanotechnology (ICN2), Bellaterra, Barcelona 08193, Spain; Departament de Química, Facultat de Ciències, Universitat Autònoma de Barcelona, Bellaterra 08193, Spain

Borja Ortín-Rubio − CSIC, and Barcelona Institute of Science and Technology, Catalan Institute of Nanoscience and Nanotechnology (ICN2), Bellaterra, Barcelona 08193, Spain; Departament de Química, Facultat de Ciències, Universitat Autònoma de Barcelona, Bellaterra 08193, Spain; orcid.org/0000-0002-0533-3635

Judith Juanhuix − ALBA Synchrotron, Cerdanyola del Vallès, Barcelona 08290, Spain; orcid.org/0000-0003-3728-8215

Complete contact information is available at:
https://pubs.acs.org/10.1021/jacs.3c05469

Notes

The authors declare no competing financial interest.

■ REFERENCES

(1) Zhou, H.-C.; Long, J. R.; Yaghi, O. M. Introduction to Metal–Organic Frameworks. *Chem. Rev.* **2012**, *112*, 673–674.

(2) Howarth, A. J.; Liu, Y.; Li, P.; Li, Z.; Wang, T. C.; Hupp, J. T.; Farha, O. K. Chemical, thermal and mechanical stabilities of metal–organic frameworks. *Nat. Rev. Mater.* **2016**, *1*, 15018.

(3) Yaghi, O. M.; O'Keeffe, M.; Ockwig, N. W.; Chae, H. K.; Eddaoudi, M.; Kim, J. Reticular synthesis and the design of new materials. *Nature* **2003**, *423*, 705–714.

(4) Chen, Z.; Hanna, S. L.; Redfern, L. R.; Alezi, D.; Islamoglu, T.; Farha, O. K. Reticular chemistry in the rational synthesis of functional zirconium cluster-based MOFs. *Coord. Chem. Rev.* **2019**, *386*, 32–49.

(5) Jiang, H.; Alezi, D.; Eddaoudi, M. A reticular chemistry guide for the design of periodic solids. *Nat. Rev. Mater.* **2021**, *6*, 466–487.

(6) Yaghi, O. M. Reticular Chemistry: Molecular Precision in Infinite 2D and 3D. *Mol. Front. J.* **2019**, *03*, 66–83.

(7) Eddaoudi, M.; Kim, J.; Rosi, N.; Vodak, D.; Wachter, J.; O'Keeffe, M.; Yaghi, O. M. Systematic Design of Pore Size and Functionality in Isoreticular MOFs and Their Application in Methane Storage. *Science* **2002**, *295*, 469–472.

(8) Deng, H.; Grunder, S.; Cordova, K. E.; Valente, C.; Furukawa, H.; Hmadeh, M.; Gándara, F.; Whalley, A. C.; Liu, Z.; Asahina, S.; Kazumori, H.; O'Keeffe, M.; Terasaki, O.; Stoddart, J. F.; Yaghi, O. M. Large-Pore Apertures in a Series of Metal-Organic Frameworks. *Science* **2012**, *336*, 1018–1023.

(9) Li, P.; Chen, Q.; Wang, T. C.; Vermeulen, N. A.; Mehdi, B. L.; Dohnalkova, A.; Browning, N. D.; Shen, D.; Anderson, R.; Gómez-Gualdrón, D. A.; Cetin, F. M.; Jagiello, J.; Asiri, A. M.; Stoddart, J. F.; Farha, O. K. Hierarchically Engineered Mesoporous Metal-Organic Frameworks toward Cell-free Immobilized Enzyme Systems. *Chem* **2018**, *4*, 1022–1034.

(10) Wang, Z.; Cohen, S. M. Postsynthetic modification of metal–organic frameworks. *Chem. Soc. Rev.* **2009**, *38*, 1315–1329.

(11) Deria, P.; Mondloch, J. E.; Karagiaridi, O.; Bury, W.; Hupp, J. T.; Farha, O. K. Beyond post-synthesis modification: evolution of metal–organic frameworks via building block replacement. *Chem. Soc. Rev.* **2014**, *43*, 5896–5912.

(12) Kirchon, A.; Feng, L.; Drake, H. F.; Joseph, E. A.; Zhou, H.-C. From fundamentals to applications: a toolbox for robust and multifunctional MOF materials. *Chem. Soc. Rev.* **2018**, *47*, 8611–8638.

(13) Bury, W.; Fairen-Jimenez, D.; Lalonde, M. B.; Snurr, R. Q.; Farha, O. K.; Hupp, J. T. Control over Catenation in Pillared Paddlewheel Metal–Organic Framework Materials via Solvent-Assisted Linker Exchange. *Chem. Mater.* **2013**, *25*, 739–744.

(14) Feng, L.; Yuan, S.; Qin, J.-S.; Wang, Y.; Kirchon, A.; Qiu, D.; Cheng, L.; Madrahimov, S. T.; Zhou, H.-C. Lattice Expansion and Contraction in Metal-Organic Frameworks by Sequential Linker Reinstallation. *Matter* **2019**, *1*, 156–167.

(15) Li, Y.; Su, J.; Zhao, Y.; Feng, L.; Gao, L.; Xu, X.; Yin, Y.; Liu, Y.; Xiao, P.; Yuan, L.; Qin, J.-S.; Wang, Y.; Yuan, S.; Zheng, H.; Zuo, J.-L. Dynamic Bond-Directed Synthesis of Stable Mesoporous Metal–Organic Frameworks under Room Temperature. *J. Am. Chem. Soc.* **2023**, *145*, 10227–10235.

(16) Li, T.; Kozlowski, M. T.; Doud, E. A.; Blakely, M. N.; Rosi, N. L. Stepwise Ligand Exchange for the Preparation of a Family of Mesoporous MOFs. *J. Am. Chem. Soc.* **2013**, *135*, 11688–11691.

(17) Yuan, S.; Zhang, P.; Zhang, L.; Garcia-Esparza, A. T.; Sokaras, D.; Qin, J.-S.; Feng, L.; Day, G. S.; Chen, W.; Drake, H. F.; Elumalai, P.; Madrahimov, S. T.; Sun, D.; Zhou, H.-C. Exposed Equatorial

(18) Yuan, S.; Qin, J.-S.; Su, J.; Li, B.; Li, J.; Chen, W.; Drake, H. F.; Zhang, P.; Yuan, D.; Zuo, J.; Zhou, H.-C. Sequential Transformation of Zirconium(IV)-MOFs into Heterobimetallic MOFs Bearing Magnetic Anisotropic Cobalt(II) Centers. *Angew. Chem., Int. Ed.* **2018**, *57*, 12578–12583.

(19) Burnett, B. J.; Barron, P. M.; Hu, C.; Choe, W. Stepwise Synthesis of Metal–Organic Frameworks: Replacement of Structural Organic Linkers. *J. Am. Chem. Soc.* **2011**, *133*, 9984–9987.

(20) Cao, L.-H.; Liu, X.; Tang, X.-H.; Liu, J.; Xu, X.-Q.; Zang, S.-Q.; Ma, Y.-M. A fivefold linker length reduction in an interpenetrated metal–organic framework via sequential solvent-assisted linker exchange. *Chem. Commun.* **2019**, *55*, 12671–12674.

(21) Xiao, Y.; Chen, Y.; Wang, W.; Yang, H.; Hong, A. N.; Bu, X.; Feng, P. Simultaneous Control of Flexibility and Rigidity in Pore-Space-Partitioned Metal–Organic Frameworks. *J. Am. Chem. Soc.* **2023**, *145*, 10980–10986.

(22) Krause, S.; Bon, V.; Senkovska, I.; Stoeck, U.; Wallacher, D.; Többens, D. M.; Zander, S.; Pillai, R. S.; Maurin, G.; Coudert, F.-X.; Kaskel, S. A pressure-amplifying framework material with negative gas adsorption transitions. *Nature* **2016**, *532*, 348–352.

(23) Schneemann, A.; Bon, V.; Schwedler, I.; Senkovska, I.; Kaskel, S.; Fischer, R. A. Flexible metal–organic frameworks. *Chem. Soc. Rev.* **2014**, *43*, 6062–6096.

(24) Douvali, A.; Tsipis, A. C.; Eliseeva, S. V.; Petoud, S.; Papaefstathiou, G. S.; Malliakas, C. D.; Papadas, I.; Armatas, G. S.; Margiolaki, I.; Kanatzidis, M. G.; Lazarides, T.; Manos, M. J. Turn-on luminescence sensing and real-time detection of traces of water in organic solvents by a flexible metal–organic framework. *Angew. Chem., Int. Ed.* **2015**, *54*, 1651–1656.

(25) Chang, Z.; Yang, D.-H.; Xu, J.; Hu, T.-L.; Bu, X.-H. Flexible Metal–Organic Frameworks: Recent Advances and Potential Applications. *Adv. Mater.* **2015**, *27*, 5432–5441.

(26) Zhang, Y.; Zhang, X.; Lyu, J.; Otake, K.-I.; Wang, X.; Redfern, L. R.; Malliakas, C. D.; Li, Z.; Islamoglu, T.; Wang, B.; Farha, O. K. A Flexible Metal–Organic Framework with 4-Connected Zr6 Nodes. *J. Am. Chem. Soc.* **2018**, *140*, 11179–11183.

(27) Chen, X.; Xie, H.; Lorenzo, E. R.; Zeman, C. J. I. V.; Qi, Y.; Syed, Z. H.; Stone, A. E. B. S.; Wang, Y.; Goswami, S.; Li, P.; Islamoglu, T.; Weiss, E. A.; Hupp, J. T.; Schatz, G. C.; Wasielewski, M. R.; Farha, O. K. Direct Observation of Modulated Radical Spin States in Metal–Organic Frameworks by Controlled Flexibility. *J. Am. Chem. Soc.* **2022**, *144*, 2685–2693.

(28) Yang, H.; Chen, Y.; Dang, C.; Hong, A. N.; Feng, P.; Bu, X. Optimization of Pore-Space-Partitioned Metal–Organic Frameworks Using the Bioisosteric Concept. *J. Am. Chem. Soc.* **2022**, *144*, 20221–20226.

(29) Yang, Y.; Broto-Ribas, A.; Ortín-Rubio, B.; Imaz, I.; Gándara, F.; Carné-Sánchez, A.; Guillerm, V.; Jurado, S.; Busqué, F.; Juanhuix, J.; Maspoch, D. Clip-off Chemistry: Synthesis by Programmed Disassembly of Reticular Materials. *Angew. Chem., Int. Ed.* **2022**, *61*, No. e202111228.

(30) Chevreau, H.; Devic, T.; Salles, F.; Maurin, G.; Stock, N.; Serre, C. Mixed-Linker Hybrid Superpolyhedra for the Production of a Series of Large-Pore Iron(III) Carboxylate Metal–Organic Frameworks. *Angew. Chem., Int. Ed.* **2013**, *52*, 5056–5060.

(31) Prasad, R. R. R.; Pleass, C.; Rigg, A. L.; Cordes, D. B.; Lozinska, M. M.; Georgieva, V. M.; Hoffmann, F.; Slawin, A. M. Z.; Wright, P. A. Isoreticular chemistry of scandium analogues of the multicomponent metal–organic framework MIL-142. *CrystEngComm* **2021**, *23*, 804–812.

(32) Albalad, J.; Xu, H.; Gándara, F.; Haouas, M.; Martineau-Corcos, C.; Mas-Ballesté, R.; Barnett, S. A.; Juanhuix, J.; Imaz, I.; Maspoch, D. Single-Crystal-to-Single-Crystal Postsynthetic Modification of a Metal–Organic Framework via Ozonolysis. *J. Am. Chem. Soc.* **2018**, *140*, 2028–2031.

(33) Guillerm, V.; Xu, H.; Albalad, J.; Imaz, I.; Maspoch, D. Postsynthetic Selective Ligand Cleavage by Solid–Gas Phase

Ozonolysis Fuses Micropores into Mesopores in Metal–Organic Frameworks. *J. Am. Chem. Soc.* **2018**, *140*, 15022–15030.

(34) Ragon, F.; Campo, B.; Yang, Q.; Martineau, C.; Wiersum, A. D.; Lago, A.; Guillerm, V.; Hemsley, C.; Eubank, J. F.; Vishnuvarthan, M.; Taulelle, F.; Horcajada, P.; Vimont, A.; Llewellyn, P. L.; Daturi, M.; Devautour-Vinot, S.; Maurin, G.; Serre, C.; Devic, T.; Clet, G. Acid-functionalized UiO-66(Zr) MOFs and their evolution after intra-framework cross-linking: structural features and sorption properties. *J. Mater. Chem. A* **2015**, *3*, 3294–3309.

(35) Hadjiivanov, K. I.; Panayotov, D. A.; Mihaylov, M. Y.; Ivanova, E. Z.; Chakarova, K. K.; Andonova, S. M.; Drenchev, N. L. Power of Infrared and Raman Spectroscopies to Characterize Metal-Organic Frameworks and Investigate Their Interaction with Guest Molecules. *Chem. Rev.* **2021**, *121*, 1286–1424.

(36) Blatov, V. A.; Shevchenko, A. P.; Proserpio, D. M. Applied Topological Analysis of Crystal Structures with the Program Package ToposPro. *Cryst. Growth Des.* **2014**, *14*, 3576–3586.

(37) Reinares-Fisac, D.; Aguirre-Díaz, L. M.; Iglesias, M.; Snejko, N.; Gutiérrez-Puebla, E.; Monge, M. Á.; Gándara, F. A Mesoporous Indium Metal–Organic Framework: Remarkable Advances in Catalytic Activity for Strecker Reaction of Ketones. *J. Am. Chem. Soc.* **2016**, *138*, 9089–9092.

Dalton Transactions

PAPER

Check for updates

Improvement of carbon dioxide electroreduction by crystal surface modification of ZIF-8†

Ting Zhang,‡[a,b] Hong Liu, ‡[c,f] Xu Han,[a] Martí Biset-Peiró, [b] Yunhui Yang,[a] Inhar Imaz,[a] Daniel Maspoch, [a,d] Bo Yang, *[c] Joan Ramon Morante [b,e] and Jordi Arbiol *[a,d]

Metal–organic frameworks (MOFs) possess high CO_2 adsorption properties and are considered to be a promising candidate for the electrochemical carbon dioxide reduction reaction (eCO_2RR). However, their insufficient selectivity and current density constrain their further exploration in the eCO_2RR. In this work, by introducing a very small proportion of 2,5-dihydroxyterephthalic acid (DOBDC) into ZIF-8, a surface modified ZIF-8-5% catalyst was synthesized by a post-modification method, exhibiting enhanced selectivity (from 56% to 79%) and current density (from −4 mA cm^{-2} to −10 mA m^{-2}) compared to ZIF-8. Density functional theory (DFT) calculations further demonstrate that the boosted eCO_2RR performance on ZIF-8-5% could be attributed to the improved formation of the *COOH intermediate stemming from successful DOBDC surface modification. This work opens a new path for improving the catalytic properties of MOFs *via* their surface modification.

1. Introduction

The electrochemical carbon dioxide reduction reaction (eCO_2RR) to obtain fuels and chemical feedstocks has been considered to be a promising option to mitigate the excessive emissions of CO_2 and to balance the global carbon cycle.[1–4] Among the various CO_2 RR products, carbon monoxide (CO) is one of the most promising and economically valuable candidates because it can be directly utilized as a feedstock for the preparation of value-added chemicals and complex multi-carbon products *via* the well-known Fischer–Tropsch synthesis.[5–9] Recently, metal–organic framework (MOF) materials have sparked considerable interest as novel catalysts

in the field of eCO_2RR to produce CO, as both metal ions and organic ligands could influence the catalytic performance.[10–14] More importantly, the inherent porous confinement properties of MOFs are expected to induce a local CO_2 concentration enhancement, thus, facilitating eCO_2RR catalysis.[15,16] Despite these advantages, the current density for CO, when using pure MOF catalysts in the eCO_2RR, is still limited (usually lower than 3.4 mA cm^{-2}),[12] hindering the wide utilization of MOFs in electrocatalytic reactions.[14] Therefore, there is still a grand challenge to achieve MOF-based catalysts presenting high current densities while maintaining a high faradaic efficiency (FE), both properties being essentially required for practical applications.

Two key aspects should be primarily considered to achieve high eCO_2RR performance for a catalyst: (1) increasing the number of the exposed active sites and (2) promoting the mass transport of CO_2 or relevant species during the catalytic reaction.[14,17] To achieve these two goals, surface regulation of catalysts is reported as a promising method to simultaneously increase the number of exposed active sites and improve mass transport of the reactants.[18–20] For example, the number of active sites has been increased by the surface nitrogen-decoration strategy, leading to a high formate formation rate on surface decorated Sn.[21] Moreover, due to increased mass diffusion and transport, an enhanced FE of CO can be achieved on F-doped cage-like porous carbon through engineering the pore size distributions at the surface of a F-doped carbon shell.[17] Therefore, a rational chemical modification of the catalyst's surface could be an effective strategy to obtain a

*[a]Catalan Institute of Nanoscience and Nanotechnology (ICN2), CSIC and BIST, Campus UAB, Bellaterra, 08193 Barcelona, Catalonia, Spain.
E-mail: arbiol@icrea.cat*
[b]Catalonia Institute for Energy Research (IREC), Jardins de les Dones de Negre 1, Sant Adrià del Besòs, Barcelona 08930, Catalonia, Spain
[c]School of Physical Science and Technology, ShanghaiTech University, 393 Middle Huaxia Road, Shanghai 201210, China. E-mail: yangbo1@shanghaitech.edu.cn
[d]ICREA, Pg. Lluís Companys 23, 08010 Barcelona, Catalonia, Spain
[e]Department of Physics, Universitat de Barcelona, 08028 Barcelona, Catalonia, Spain
[f]State Key Laboratory of Information Functional Materials, 2020 X-Lab, ShangHai Institute of Microsystem and Information Technology, Chinese Academy of Sciences, Shanghai 200050, China.
†Electronic supplementary information (ESI) available: SEM, TEM, EELS, XRD, Raman spectra, XPS, BET, gas calibration, *I*–*t*, LSV, and FE (H$_2$/CO), partial current densities of different samples, DFT results and ¹H-NMR results. See DOI: https://doi.org/10.1039/d3dt00185g
‡These authors contributed equally to this work.

high eCO$_2$RR performance, which would not largely change the crystal structure of the original bulk phase.[21] However, there are few reports on enhancing the eCO$_2$RR through regulating the surface of MOF catalysts. In particular, experimental and computational insights into such surface modification–performance relationship of MOF catalysts are still rare.

Here, we demonstrate that a surface modification strategy to treat ZIF-8 crystals with a polyphenolic acid such as 2,5-dihydroxyterephthalic acid (DOBDC) could bring about high-efficiency eCO$_2$RR performance. As an efficient etching and doping agent for MOFs, on the one hand, these acids can etch the surface of ZIF-8 crystals to create large surface areas and a high proportion of mesopores, potentially offering a large number of surface active sites for the eCO$_2$RR and allowing the facile diffusion of eCO$_2$RR-relevant species to the active sites.[22–24] On the other hand, DOBDC can adsorb onto the ZIF-8 surface, and then progressively replace partially the original organic linkers in ZIF-8 due to its ability to coordinate with metals,[25] thus, influencing the local environment of active sites to facilitate *COOH generation (the key intermediate for CO production).[13] Both experimental and theoretical results in this work reveal that this synergistic effect could promote the eCO$_2$RR performance on surface modified ZIF-8, realizing a dual improvement of selectivity and activity. In particular, through precisely controlling the DOBDC addition, when DOBDC is used at a concentration of 5% in weight with respect to ZIF-8 (hereafter denoted as ZIF-8-5%), ZIF-8-5% achieves a remarkable increase of the FE of CO up to 79% at −1.20 V *vs.* RHE, which is higher than that of the parent ZIF-8 (56%). More importantly, it also shows a 2.5 times higher CO current density, from −4 mA cm^{-2} on pure ZIF-8 to −10 mA cm^{-2} on ZIF-8-5%. Moreover, the selectivity can be retained over 60% in a range of working potentials from −1.0 to −1.2 V *vs.* RHE, proving that CO is still the main product on ZIF-8-5% at high overpotentials. Theoretical analyses further demonstrate that ZIF-8-5% could reduce the reaction energy for *COOH intermediate formation during the eCO$_2$RR process, thus enhancing the production efficiency of CO. We believe that this post-synthetic treatment could open a new way for boosting the catalytic performance of MOF-based catalysts with controllable surface modification.

2. Experimental section

2.1 Chemicals

If not specified, all chemical reagents were purchased from Sigma-Aldrich. Zinc nitrate hexahydrate (Zn(NO$_3$)$_2$·6H$_2$O), 2-methylimidazole (2-mim), methanol, 2,5-dihydroxyterephthalic acid (DOBDC), *N,N*-dimethylformamide (DMF), ethanol and sodium bicarbonate (NaHCO$_3$) were all of analytical grade and used as received without further purification. Meanwhile, all solutions were prepared with Milli-Q water (DI-H$_2$O, Ricca Chemical, ASTM Type I). Nafion (N-117 membrane, 0.18 mm thick) was purchased from Alfa Aesar and kept in 0.5 M NaOH solution. Carbon paper was also purchased from Alfa Aesar.

2.2 Synthesis of ZIF-8

The fabrication of ZIF-8 was similar to the method in published reports.[13] Typically, 1.115 g of Zn(NO$_3$)$_2$·6H$_2$O was dissolved in 50 mL of methanol under magnetic stirring at room temperature to form a homogeneous solution. Then, 50 mL of methanolic solution containing 1.232 g of 2-mim were added into the above mixture solution under ultrasonication until a clear solution was formed. The obtained homogeneous solution reacted at room temperature for 24 h without stirring. Then, the white powder was collected by centrifugation, washed with methanol several times to remove the organic residual. The final products were then dried in a vacuum at 60 °C overnight.

2.3 Synthesis of Zn-MOF-74

The Zn-MOF-74 sample was synthesized according to previous published protocols with minor modification.[26,27] Firstly, 60 mg of Zn(NO$_3$)$_2$·6H$_2$O and 20 mg of DOBDC were dissolved in 15 mL of mixed DMF/H$_2$O/ethanol solution (v/v/v = 1:1:1) under ultrasonication to form a homogeneous solution. Then, the obtained solution was transferred into a Teflon reactor and heated at 120 °C for 24 h, then cooled to room temperature, brown crystals were obtained by centrifugation, and washed with DMF several times. Finally, the final products were dried in a vacuum at 60 °C overnight.

2.4 Synthesis of modified ZIF-8-*x* with the DOBDC modification

In this procedure, 300 mg of as-prepared ZIF-8 powder was dispersed in 45 mL of a mixture solution containing 15 mL of DMF, 15 ml of ethanol and 15 mL of water under ultrasound for 20 min at room temperature. After forming a homogeneous solution, DOBDC with different quantities (5 mg, 15 mg, 30 mg, 50 mg and 100 mg) was added into the above solution under ultrasound for 5 min at room temperature. The weights of DOBDC added correspond to 1.7%, 5%, 10%, 17% and 33% *vs.* the ZIF-8 weight, respectively. Next, the mixed solution was left in the oven at 60 °C for 7 days. After the reaction, the powders were collected by centrifugation, washed with ethanol and DMF several times and dried in a vacuum at 60 °C overnight. The samples have been labelled depending on the percentage of the added DOBDC: ZIF-8-1.7%, ZIF-8-5%, ZIF-8-10%, ZIF-8-17% and ZIF-8-33%, respectively.

2.5 Synthesis of a physical mixture of ZIF-8-5% (labelled as ZIF-8-5%-P)

For the preparation of the ZIF-8-5%-P sample, 15 mg of DOBDC powder were directly added into 300 mg of ZIF-8 powder and mixed well.

2.6 Preparation of working electrodes

10 mg of the different synthesized samples and 50 μl of 5 wt% Nafion solutions were dissolved in ethanol (1 mL) and ultrasonicated for 1 h to form even suspensions for further electrochemical experiments. To prepare the working electrode, 500 μL of the above as-prepared inks were dropped onto the

two sides of the carbon paper electrode with 1×1 cm^2 and then dried at room temperature for a few minutes, giving a catalyst total loading mass of $\sim$2.5 mg cm^{-2}.

2.7 Electrochemical measurements and calculations

The electrocatalytic performance of different catalysts was measured at room temperature using a gas-tight H-cell with two-compartments separated by a Nafion N-117 membrane with a continuous Ar or CO_2 gas injection. Each compartment contained 70 mL of electrolyte (0.5 M NaHCO$_3$ made from deionized water). In a typical experiment, a standard three electrode setup in 0.5 M NaHCO$_3$ solution was assembled: an Ag/AgCl electrode was used as the reference electrode, a Pt sheet as the auxiliary electrode and carbon paper modified with the different samples as the working electrode (with a total surface area = 1 cm^2). The potentials were measured *versus* Ag/AgCl and converted to the reversible hydrogen electrode (RHE) according to the following equation: $E_{RHE} = E^{\circ}_{Ag/AgCl} + E_{Ag/AgCl} + 0.059 \times pH$, pH = 7.[28,29] All the electrochemical results are shown without iR-compensation and obtained using a computer-controlled BioLogic VMP3 electrochemical workstation.

Before the electrochemical CO_2 reduction experiments, an average rate of 20 mL min^{-1} Ar was injected to form an Ar-saturated solution. During electrochemical CO_2 reduction experiments, CO_2 gas was delivered at the same rate at room temperature and ambient pressure, measured downstream by a volumetric digital flowmeter. The gas phase composition was analyzed by gas chromatography (GC) during potentiostatic measurements every 20 min using a 490 Micro GC (Agilent Technologies). The calibration of peak area *vs.* gas concentration was used for the molar quantification of each gaseous effluent. The liquid products were analyzed afterwards by quantitative ^{1}H-NMR using water as the deuterated solvent. Moreover, the MOF sample was digested by HF solution overnight to completely destroy the structure. The ^{1}H-NMR of the sample was conducted using MeOD as the solvent.

Details of the calculation are shown below.

The partial current density for a given gas product was calculated as given below:[30]

$$j_i = x_i \times V \times \frac{n_i F P_0}{RT} \times (\text{electrode area})^{-1}$$

where x_i is the volume fraction of a certain product determined by online GC referenced to calibration curves from three standard gas samples, V is the flow rate, n_i is the number of electrons involved, P_0 = 101.3 kPa, F is the Faraday constant, T is temperature and R is the gas constant. The corresponding FE at each potential is calculated by

$$FE = \frac{j_i}{j} \times 100\%.$$

2.8 Characterization

X-ray diffraction patterns (XRD) were obtained using a Bruker D4 X-ray powder diffractometer using Cu Kα radiation (1.54184 Å). Field emission scanning electron microscopy

(FE-SEM) images were collected on a FEI Magellan 400 L scanning electron microscope. Transmission electron microscopy (TEM) and high angle annular dark field scanning TEM (HAADF-STEM) images were obtained in a Tecnai F20 field emission gun microscope with a 0.19 nm point-to-point resolution at 200 kV equipped with an embedded Quantum Gatan image filter for EELS analyses. Images have been analyzed by means of the Gatan Digital Micrograph software. X-ray photoelectron spectroscopy (XPS) was performed on a Phoibos 150 analyzer (SPECS GmbH, Berlin, Germany) under ultra-high vacuum conditions (base pressure 4×10^{-10} mbar) with a monochromatic aluminum Kα X-ray source. Binding energies (BE) were determined using the C 1s peak at 284.5 eV as a charge reference. Raman spectra were obtained using Senterra. Brunauer–Emmett–Teller (BET) surface areas were measured using nitrogen adsorption at 77 K (TriStar II 3020-Micromeritics). Proton nuclear magnetic resonance (^{1}H-NMR) was conducted in a Bruker Advance III 400 MHz.

2.9 DFT calculations

DFT calculations were performed using the Vienna *ab initio* simulation package (VASP) code[31] with the projector augmented wave (PAW) method.[32–35] Generalized gradient approximation (GGA) with the Perdew–Burke–Ernzerhof (PBE) exchange–correlation function was used to set the plane wave basis.[36,37] The energy cutoff was 500 eV and all structures were allowed to relax. The force convergence criteria on each configuration were below 0.05 eV Å^{-1}. In order to avoid interactions between molecules in the periodic structures, we placed the model in a 20 Å $\times$ 20 Å $\times$ 20 Å cell. $1 \times 1 \times 1$ k-point grids with the Monkhorst–Pack scheme were used for all systems. The DFT-D3 method with Becke–Jonson damping was utilised to include van der Waals interactions between molecules.[38,39]

Molecular orbital (MO) analyses were performed with the PBE function and dgdzvp2 basis sets in the Gaussian 09 program.[40] The ZIF-8 model was generated with four 2-mim ligands coordinating with the central Zn^{2+} to form a tetrahedral configuration, which is according to the approach reported previously.[13] The ZIF-8-5% structure was built with one DOBDC replacing two 2-mim of ZIF-8. The free energy of the reaction at each elementary step was estimated using the computational hydrogen electrode model,[41] and the following elementary steps were considered for the electrochemical CO_2RR to CO:

$$CO_2(g) + * + H^+(aq) + e^- \leftrightarrow COOH*$$

$$COOH* + H^+(aq) + e^- \leftrightarrow CO* + H_2O(l)$$

$$CO* \leftrightarrow CO(g) + *$$
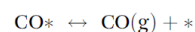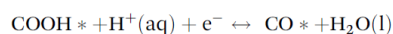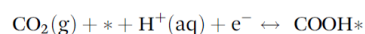
where *, COOH* and CO* represent the free site and adsorption state of COOH and CO, respectively. The free energies of the reaction were calculated according to the following formula:

$$G = E_{DFT} + E_{ZPE} - TS + E_{sol}$$

where E_{DFT} is the DFT calculated total energy, E_{ZPE} represents the zero-point energy, and S is the entropy. E_{sol} is the solvation cor-
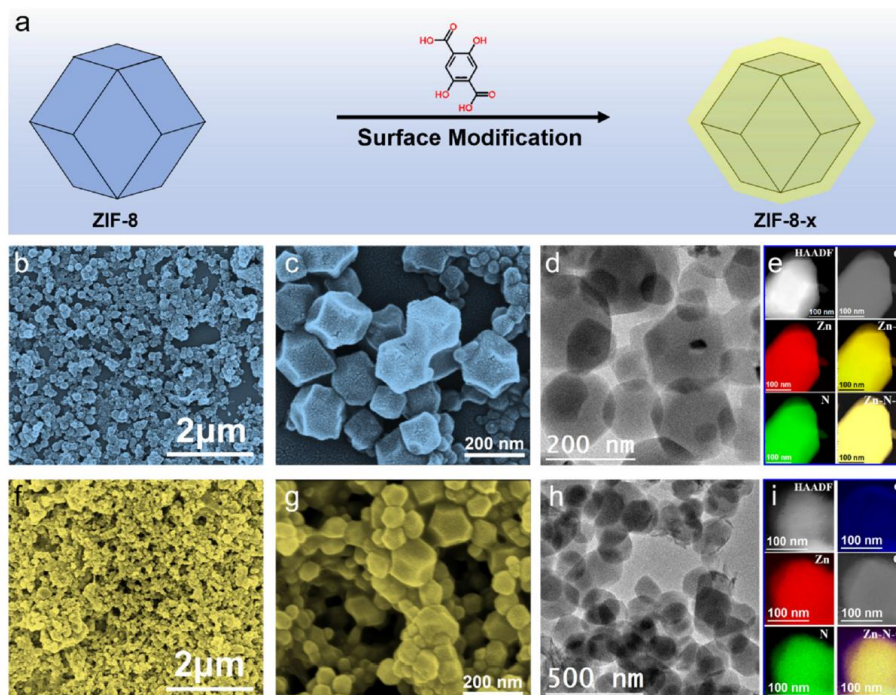
Fig. 1 (a) Schematic illustration of the formation of ZIF-8-*x* samples. (b and c) FE-SEM images, (d) BF TEM, (e) HAADF STEM and EELS chemical composition maps of ZIF-8. (f and g) FE-SEM images, (h) BF TEM, (i) HAADF STEM and EELS chemical composition maps of ZIF-8-5%. Individual Zn $L_{2,3}$-edges at 1020 eV (red), N K-edges at 401 eV (green), O K-edges at 532 eV (blue) and C K-edges at 285 eV (grey) as well as their composites.

rection and the values used for CO* was −0.1 eV and −0.25 eV for COOH*.[42]

3. Results and discussion

3.1 Structural characterization

A schematic illustration of the synthesis route followed to obtain the corresponding modified ZIF-8-*x* samples is shown in Fig. 1a. ZIF-8 is initially synthesized based on previous literature.[13] In a second step, the corresponding ZIF-8-*x* (where *x* represents the weight percentage of DOBDC with respect to ZIF-8) are prepared by incubating a dispersion of the pristine ZIF-8 crystals and different amounts of DOBDC in a mixture of DMF, ethanol and water. Following this synthetic protocol, five different samples denoted as ZIF-8-1.7%, ZIF-8-5%, ZIF-8-10%, ZIF-8-17% and ZIF-8-33% are prepared.

The surface morphology and elementary composition of the as-prepared samples are revealed by field emission scanning electron microscopy (FE-SEM) and transmission electron microscopy (TEM). As revealed by FE-SEM (Fig. 1b and c), the prepared ZIF-8 shows homogeneous crystals with the characteristic rhombic dodecahedral morphology. In addition, TEM analyses show that the ZIF-8 crystals have a size in the range of 80–200 nm (Fig. 1d). After DOBDC doping modification, various morphologies of ZIF-8-*x* samples are shown in Fig. 1f,

g and Fig. S1.† As shown in Fig. S1a† and Fig. 1f, g, the as-synthesized ZIF-8-1.7% and ZIF-8-5% samples still inherit the original rhombic dodecahedral morphology, which is similar to the one shown by the pure ZIF-8 structures, suggesting that there is not an apparent morphology damage of these crystals after exposing them to a small proportion of DOBDC. With increasing ratios of DOBDC, the ZIF-8-10% sample displays an irregular spherical shape (Fig. S1b†), indicating the surface corrosion caused by the large concentration of DOBDC. However, ZIF-8-17% and ZIF-8-33% samples are composed by some larger bulks and small spherical particles. The formation of these bulky structures could be attributed to the coordination between excess DOBDC and liberated Zn(ɪɪ) ions accompanied by further etching/dissolution of the sacrificial ZIF-8, forming other crystalline species. The chemical compositions of ZIF-8 and ZIF-8-5% crystals were further investigated by high angle annular dark filed scanning transmission electron microscopy (HAADF STEM) and electron energy loss spectroscopy (EELS) elemental maps. STEM EELS compositional maps show the homogeneous distribution of Zn, N and C in ZIF-8 and ZIF-8-5% crystals (Fig. 1e and i). It is worth noting that the presence of the element O in the ZIF-8-5% crystal indicates the successful doping DOBDC into ZIF-8.

These samples were further investigated by X-ray powder diffraction (XRD). Indeed, the XRD patterns of ZIF-8-1.7%, ZIF-8-5% and ZIF-8-10% suggest similar crystal patterns to that

of standard ZIF-8,[13] indicating that the addition of a low concentration (up to 10%) of DOBDC does not significantly change the crystal structure of ZIF-8 (Fig. 2a and Fig. S2†). However, the XRD patterns of ZIF-8-17% and ZIF-8-33% show the appearance of some additional diffraction peaks, demonstrating that introducing a high concentration of DOBDC could change the inner bulk phase of ZIF-8, which are in accordance with the results of SEM. To determine the surface area of different samples, Brunauer–Emmett–Teller (BET) measurements were performed. As shown in Fig. 2b, the measured surface area (1403 $m^2 g^{-1}$) of ZIF-8 is fully consistent with the previously reported value.[43] Obviously, when DOBDC is introduced at a low concentration (up to 10%), all the modified ZIF-8-x show an increased surface area compared to the parent ZIF-8. In addition, the porosity of the ZIF-8 and ZIF-8-5% samples was investigated by N_2 adsorption–desorption measurement, as shown in Fig. S3.† Both ZIF-8 and ZIF-8-5% show a typical type I adsorption/desorption isotherm curve in Fig. S3a,† indicating that both samples have numerous micropores.[44,45] Notably, the existence of a higher proportion of mesopores observed on ZIF-8-5% (Fig. S3b†) could facilitate mass diffusion and transport of $CO_2(aq)$ or the eCO_2RR-relevant species in solution.[17,24] The results proves that DOBDC can be used to tailor the surface of ZIF-8 to provide a large number of surface active sites for the eCO_2RR and enhance the mass diffusion.[46]

Furthermore, the chemical valence state and surface composition of the ZIF-8 and ZIF-8-5% samples have been proved by X-ray photoelectron spectroscopy (XPS). The full survey scan XPS spectrum shown in Fig. 2c indicates the presence of C, N, O and Zn in both ZIF-8 and ZIF-8-5% samples. Remarkably, the O signal in ZIF-8-5% is significantly larger than in ZIF-8. The high-resolution XPS spectra obtained on the Zn 2p shows

two main peaks in both samples at around 1020 eV and 1044 eV (Fig. 2d), corresponding to Zn $2p_{3/2}$ and Zn $2p_{1/2}$, respectively, which indicates the presence of Zn^{2+} in both samples.[47] However, for the Zn 2p XPS spectrum of ZIF-8, a slight shift toward the low binding energy for the Zn $2p_{3/2}$ and Zn $2p_{1/2}$ peaks of ZIF-8-5% is ascribed to the introduced DOBDC ligand with electron-donating ability.[48] The N 1s spectra for ZIF-8 and ZIF-8-5% are shown in Fig. 2e, which reveals that both samples mainly show three major peaks corresponding to –NH–, Zn–N and –N= at 398.0 eV, 399.2 eV and 400.3 eV, respectively.[13] The O 1s XPS core level spectra for ZIF-8-5% can be deconvoluted into three peaks at around at 532.8, 531.7 and 530.1 eV, which would be related to C–O, C=O and Zn–O, respectively (Fig. 2f).[49] These results support the successful introduction of DOBDC into the ZIF-8 crystal surface. In addition, as shown in Fig. S4,† red-shifts at *ca.* 643.5, 1147.2, 1188, 1461.5, 1503 and 1510.7 cm^{-1}, are observed in the high-resolution Raman peaks on ZIF-8 after surface modification by DOBDC doping. These shifts are attributed to the tiny torsion and stretching of the different bonds, revealing that the coordinated environment of ZIF-8 is influenced by the introduced DOBDC ligand.[50] Meanwhile, Fourier transform infrared spectrophotometry (FT-IR) of ZIF-8-5%, as shown in Fig. S5,† proves the formation of Zn–DOBDC coordination by the negligible peak from characteristic O–H vibration peaks in ZIF-8-5% compared to DOBDC.[25] Furthermore, successful introduction of DOBDC into ZIF-8 with a concentration of 5% has been directly investigated by ^1H-NMR. We digested the ZIF-8-5% sample and analysed the resulting solutions by ^1H-NMR. As shown in Fig. S6,† the ZIF-8-5% sample shows a small peak at 7.41 ppm attributed to the functional group of DOBDC, thus corroborating the successful introduction of DOBDC into ZIF-8-5%. We then calculated the DOBDC : 2-mim ratio for ZIF-8-5% by a comparison
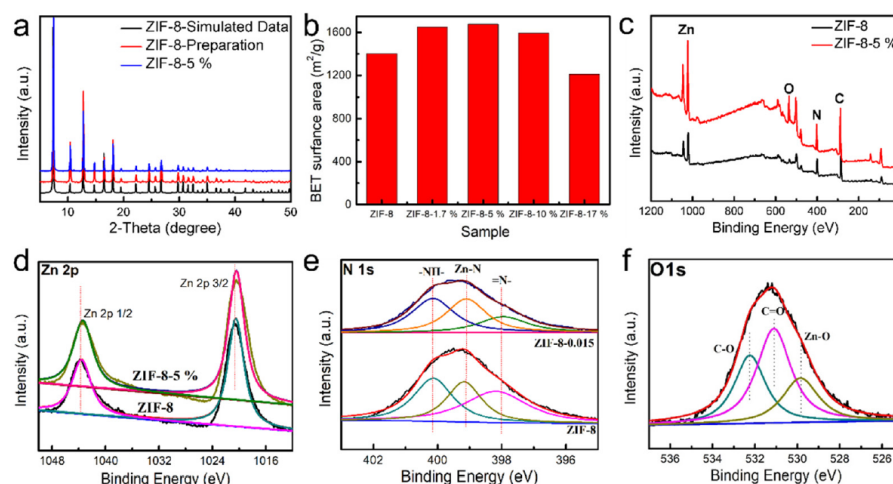
Fig. 2 (a) Simulated data from crystal structure and experimental XRD patterns of ZIF-8 and ZIF-8-5%. (b) The BET surface area of different samples. (c) XPS survey spectra, (d) high-resolution XPS spectra of Zn 2p, and (e) high resolution XPS spectra of N 1s on ZIF-8 and ZIF-8-5%. (f) High resolution XPS spectra of O 1s of ZIF-8-5%.
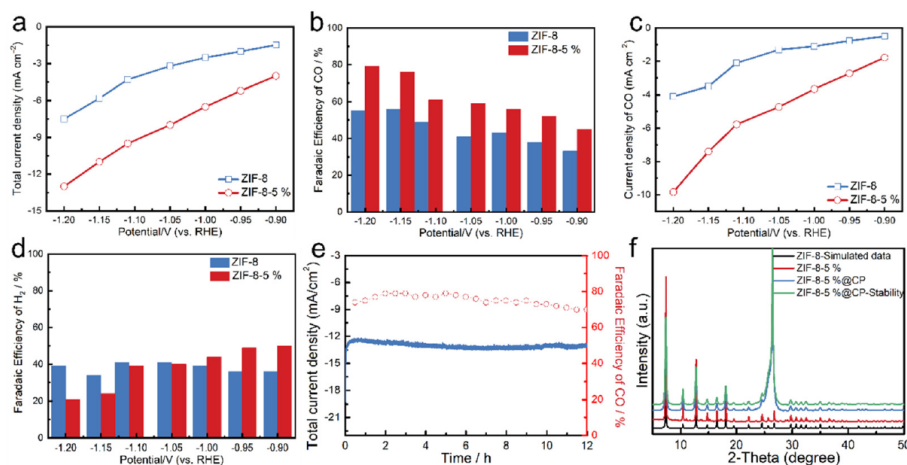
Fig. 3 (a) Total current densities, (b) corresponding FE for CO, (c) current densities of CO and (d) corresponding FE for H_2 on ZIF-8 and ZIF-8-5% coated on carbon paper in CO_2-saturated 0.5 M $NaHCO_3$ solution. (e) Current density *vs.* time (*I*−*t*) curve for ZIF-8-5% modified carbon paper at −1.20 V *vs.* RHE and (f) XRD pattern of ZIF-8-5% coated on the carbon paper before and after the stability test.

of the integration of the peak at 7.41 ppm corresponding to DOBDC and the peak at 7.17 ppm corresponding to 2-mim, indicating a DOBDC : 2-mim ratio of 0.02. All these results suggest that the surface modification with DOBDC was successful on ZIF-8-5%, which not only increases the surface area of the parent ZIF-8, but also successfully forms the Zn–DOBDC coordination.

3.2 eCO_2RR

The electrocatalytic activity of ZIF-8 and ZIF-8-5% coated on carbon paper with the same mass loading of 2.5 mg cm^{-2} was studied in Ar or CO_2-saturated 0.5 M $NaHCO_3$ solution as the electrolyte using a three-electrode H-cell. Before the eCO_2RR electrochemical tests, the prepared electrodes were pretreated at a constant potential of −0.90 V *vs.* RHE for 30 min until a stable current was reached (Fig. S7a and b†). To roughly evaluate the electroreduction ability of ZIF-8 and ZIF-8-5% samples, linear sweep voltammetry (LSV) curves under an Ar- and a CO_2-saturated atmosphere were obtained (Fig. S7c and d†). Under CO_2 purging, an enhanced current density could be observed on ZIF-8 and ZIF-8-5%, which was higher than that observed in an Ar-saturated solution, which confirmed the efficient catalytic performance of the ZIF-8 and ZIF-8-5% samples. Meanwhile, ZIF-8-5% shows a higher current density in CO_2-saturated solution than ZIF-8, delivering a higher activity toward the eCO_2RR. Fig. 3a shows the total current density plotted against the applied potential of both samples. The current density of the ZIF-8-5% sample increases to −13 mA cm^{-2} as the applied potential shifted negatively; however, a lower current density is observed at all applied potentials in the case of the ZIF-8 sample. The high current density achieved by ZIF-8-5% in comparison with that of the pristine ZIF-8 structure could be attributed to the increased active-site density caused by surface modification by DOBDC.[46,51] As

shown in Fig. 3b, the parent ZIF-8 exhibits lower FE(CO) values similar to previous reports.[11] The FE(CO) for the ZIF-8-5% sample at each applied potential is higher than that of ZIF-8, with the highest FE(CO) of 79% at −1.20 V *vs.* RHE. In addition, according to Fig. 3c, the corresponding partial current densities of CO obtained on the ZIF-8-5% sample at all applied potentials are higher than those of ZIF-8, which reveals its higher reaction rate during the eCO_2RR.[7] Furthermore, the electrochemical active surface area (ECSA) was measured to confirm the high activity of ZIF-8-5%. It is established that an increase of the electrochemical active surface area often leads to the enhancement of catalytic activity.[28,52] The ECSA can be calculated by the electrochemical double-layer capacitance (C_{dl}) of active materials, which is generally proportional to their ECSA (ECSA = C_{dl}/C_s, C_s is specific capacitance). Therefore, the C_{dl} of ZIF-8 and ZIF-8-5% was probed by cyclic voltammogram (Fig. S8†). By plotting the $\Delta J = J_a − J_c$ against the scan rate, the slope which is twice of C_{dl} can be obtained. As shown in Fig. S8c,† the C_{dl} of surface modified ZIF-8-5% is significantly larger than that of ZIF-8, indicating that ZIF-8-5% could provide more active sites to contact with the reactant to accelerate the electrocatalytic CO_2 RR.[52] The operating stability of a catalyst is a significant parameter for its practical applications. In this manner, as displayed in Fig. 3e, the *I*–*t* curve for ZIF-8-5% is obtained, showing a negligible decay of the current density (from −9.7 to −10 mA cm^{-2}) and the FE(CO) (from 79 to 70%) during continuous electrolysis under a CO_2-staturated solution at −1.20 V *vs.* RHE for 12 h, indicating good stability of the prepared ZIF-8-5%, which was further confirmed by XRD measurement before and after the *I*–*t* test (Fig. 3f), in which no appreciable difference in the crystal structure was observed after 12 h of stability test in 0.5 M $NaHCO_3$, proving that the main structure of ZIF-8-5% had been retained. Meanwhile, ^{1}H-NMR analyses are performed to

detect the absence of any liquid byproducts after the stability measurement, revealing that there is no liquid byproduct produced during the CO_2 RR process (Fig. S9†). The above results strongly support that after the rational surface modification using DOBDC ZIF-8-5% could achieve both high current density and FE(CO) at high applied potentials.

The FE for CO and H_2 on different ZIF-8-x samples are shown in Fig. S10† for comparison. Apparently, other samples show lower FE(CO) than that of ZIF-8-5%. Such decreased selectivity is attributed to the concentration of DOBDC introduced. The FE (CO and H_2) values of ZIF-8-1.7% at applied potentials are similar to that of ZIF-8 (Fig. S11†), although this sample shows an increased surface area compared to that of ZIF-8. In order to reveal this phenomenon, we also digested ZIF-8-1.7% and analysed the resulting solutions by ^{1}H-NMR, as shown in Fig. S12.† There is no signal from the functional group of DOBDC observed in the ZIF-8-1.7% sample. Therefore, its FE(CO) is limited by deficient DOBDC content, leading to only the etching process occurring on the surface of ZIF-8-1.7%, while there is negligible Zn–DOBDC coordination formation because of deficient DOBDC content. However, for ratios above 17%, the significant decrease in their catalytic activities is due to the new crystalline species formed which tend to cover up the active sites and even further change the active sites of catalysts, as found in our SEM and XRD results. In addition, we further investigated the FE(CO) of a ZIF-8-5%-P sample prepared by a physical mixture of ZIF-8 and DOBDC. As observed in Fig. S13a,† the ZIF-8-5%-P shows poor CO selectivity, lower than 40% FE(CO) at all applied potentials. Therefore, we conclude that the enhanced eCO_2RR activity on ZIF-8-5% is mainly influenced by the rational DOBDC surface modification, which changes the coordinated environment of ZIF-8, thus, boosting the catalytic performance.

DFT calculations were performed to reveal the origin of the excellent activity obtained on ZIF-8-5% upon rational DOBDC surface modification. The catalyst models of ZIF-8 and ZIF-8-5% used in the simulations are shown in Fig. 4a–d, and the optimal adsorption configurations of reaction intermediates are presented in Fig. S14 and 15.† The Gibbs free energy profiles of CO_2 reduction to CO at 0 V and -1.0 V vs. RHE are shown in Fig. 4e and f. As indicated in these two profiles, CO_2 activation to form COOH* is endergonic at 0 V vs. RHE on the two catalysts studied while the subsequent steps of CO formation and desorption are exergonic. Therefore, COOH* formation is the potential-limiting reaction step in the electrocatalytic reduction of CO_2. In addition, the Gibbs energy of the COOH* formation reaction of ZIF-8 is 0.4 eV more positive than that of ZIF-8-5% at both 0 V and -1.0 V vs. RHE, strongly suggesting that ZIF-8-5% is much more active than ZIF-8 towards electrocatalytic reduction of CO_2 to CO, which is in good agreement with the experimental results shown in the current work.

Further molecular orbital (MO) analysis is performed to elucidate the origin of distinct behaviors of ZIF-8 and ZIF-8-5% for the formation of COOH*. The HOMO and LUMO energy levels of ZIF-8 and ZIF-8-5% are shown in Fig. 4g. Interestingly, ZIF-8 and ZIF-8-5% exhibit a similar level of HOMO energy. The difference lies in the LUMO energy wherein ZIF-8-5% shows a much lower LUMO energy (-3.90 eV) than ZIF-8 (-0.50 eV), forming a narrower HOMO–LUMO energy gap for ZIF-8-5%. It is well established that a narrow HOMO–LUMO energy gap is beneficial for the charge transfer process, thus making electrocatalytic CO_2 RR more efficient as observed in recent works.[53–55]

Moreover, in order to further confirm that the increase of catalytic activity comes from the in situ DOBDC doping modification instead of the formation of new crystals of Zn-MOF-74 assembled by DOBDC and liberating Zn^{2+} on the ZIF-8 surface, a pure Zn-MOF-74 sample was prepared using the DOBDC ligand and Zn^{2+} salts (Fig. S16†). Zn–MOF-74 was also tested for the eCO_2RR and exhibited poor performance for generating CO (below 20%) at each applied potential (Fig. S17†). In addition, a control experiment was performed to verify that the obtained CO comes from the reduction of CO_2 on ZIF-8-5%, instead of the DOBDC ligand decomposition, as shown in Fig. S18.†
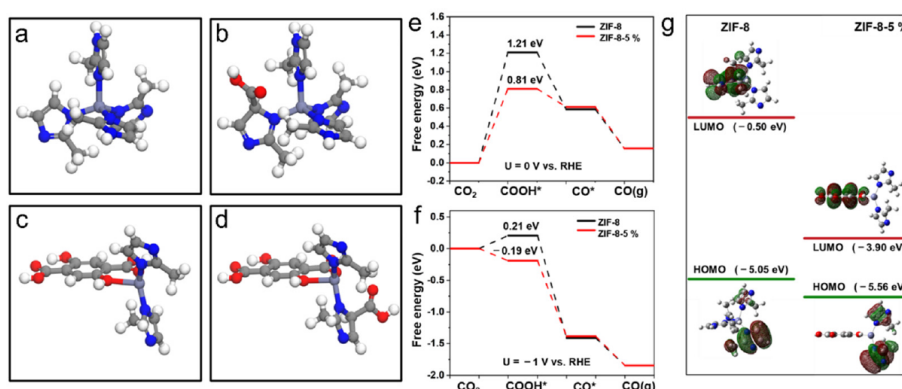
Fig. 4 The clean surface and optimized adsorption configuration on (a and b) ZIF-8 and (c and d) ZIF-8-5% surface model. (e and f) Free energy profiles for CO_2RR over ZIF-8 and ZIF-8-5% at 0 V and -1.0 V vs. RHE; (g) the HOMO and LUMO energy level of ZIF-8 and ZIF-8-5% models (Zn, C, N, O atoms are represented in purple, grey, blue, and red, respectively).

4. Conclusions

In summary, we systematically explored the surface modification strategy of ZIF-8 with DOBDC and found that it indeed influences the activity and selectivity towards CO production. In the case of the optimized ZIF-8-5% sample, an increase of selectivity towards the CO_2 RR is observed. The product selectivity to CO increased to 79%, which is higher than that of pristine ZIF-8 (56%). In addition, ZIF-8-5% also exhibited an enhanced CO partial current density of -10 mA cm^{-2} at -1.20 V vs. RHE, leading to a boosted CO production rate. The DFT calculations suggest that DOBDC modification not only maintains the active sites of ZIF-8 but also promotes the formation of COOH* during the eCO$_2$RR in the newly synthesized ZIF-8-5%. The enhanced ZIF-8-5% performance can be attributed to a decrease of the energy gap between the HOMO and LUMO. These results offer an efficient strategy to synthesize improved MOF-based materials towards CO_2 electroreduction by surface modification.

Conflicts of interest

There are no conflicts to declare.

Acknowledgements

References

1 Y. J. Sa, C. W. Lee, S. Y. Lee, J. Na, U. Lee and Y. J. Hwang, *Chem. Soc. Rev.*, 2020, **49**, 6632–6665.

2 W. Shan, R. Liu, H. Zhao, Z. He, Y. Lai, S. Li, G. He and J. Liu, *ACS Nano*, 2020, **14**, 11363–11372.

3 A. Ozden, Y. Wang, F. Li, M. Luo, J. Sisler, A. Thevenon, A. Rosas-Hernández, T. Burdyny, Y. Lum, H. Yadegari, T. Agapie, J. C. Peters, E. H. Sargent and D. Sinton, *Joule*, 2021, **5**, 706–719.

4 T. Zhang, X. Han, H. Liu, M. Biset-Peiró, X. Zhang, P. Tan, P. Tang, B. Yang, L. Zheng, J. R. Morante and J. Arbiol, *Energy Environ. Sci.*, 2021, **14**, 4847–4857.

5 D. M. Koshy, S. Chen, D. U. Lee, M. B. Stevens, A. M. Abdellah, S. M. Dull, G. Chen, D. Nordlund, A. Gallo, C. Hahn, D. C. Higgins, Z. Bao and T. F. Jaramillo, *Angew. Chem., Int. Ed.*, 2020, **59**, 4043–4050.

6 Q. He, D. Liu, J. H. Lee, Y. Liu, Z. Xie, S. Hwang, S. Kattel, L. Song and J. G. Chen, *Angew. Chem., Int. Ed.*, 2020, **59**, 3033–3037.

7 O. S. Bushuyev, P. De Luna, C. T. Dinh, L. Tao, G. Saur, J. van de Lagemaat, S. O. Kelley and E. H. Sargent, *Joule*, 2018, **2**, 825–832.

8 X. Han, T. Zhang, M. Biset-Peiró, X. Zhang, J. Li, W. Tang, P. Tang, J. R. Morante and J. Arbiol, *ACS Appl. Mater. Interfaces*, 2022, **14**, 32157–32165.

9 T. Zhang, X. Han, H. Liu, M. Biset-Peiró, J. Li, X. Zhang, P. Tang, B. Yang, L. Zheng, J. R. Morante and J. Arbiol, *Adv. Funct. Mater.*, 2022, **32**, 2111446.

10 W. Geng, W. Chen, G. Li, X. Dong, Y. Song, W. Wei and Y. Sun, *ChemSusChem*, 2020, **13**, 4035–4040.

11 Y. Wang, P. Hou, Z. Wang and P. Kang, *ChemPhysChem*, 2017, **18**, 3142–3147.

12 X. Jiang, H. Li, J. Xiao, D. Gao, R. Si, F. Yang, Y. Li, G. Wang and X. Bao, *Nano Energy*, 2018, **52**, 345–350.

13 S. Dou, J. Song, S. Xi, Y. Du, J. Wang, Z.-F. Huang, Z. J. Xu and X. Wang, *Angew. Chem., Int. Ed.*, 2019, **58**, 4041–4045.

14 S. Dou, X. Li and X. Wang, *ACS Mater. Lett.*, 2020, **2**, 1251–1267.

15 D.-H. Nam, P. De Luna, A. Rosas-Hernández, A. Thevenon, F. Li, T. Agapie, J. C. Peters, O. Shekhah, M. Eddaoudi and E. H. Sargent, *Nat. Mater.*, 2020, **19**, 266–276.

16 C. S. Diercks, Y. Liu, K. E. Cordova and O. M. Yaghi, *Nat. Mater.*, 2018, **17**, 301–307.

17 W. Ni, Y. Xue, X. Zang, C. Li, H. Wang, Z. Yang and Y.-M. Yan, *ACS Nano*, 2020, **14**, 2014–2023.

18 P. Chen, Y. Tong, C. Wu and Y. Xie, *Acc. Chem. Res.*, 2018, **51**, 2857–2866.

19 L. Cao and C. Wang, *ACS Cent. Sci.*, 2020, **6**, 2149–2158.

20 L. Jiao, J. Wang and H.-L. Jiang, *Acc. Mater. Res.*, 2021, **2**, 327–333.

21 H. Cheng, S. Liu, J. Zhang, T. Zhou, N. Zhang, X.-s. Zheng, W. Chu, Z. Hu, C. Wu and Y. Xie, *Nano Lett.*, 2020, **20**, 6097–6103.

22 X. Song, Z. Ou, X. Hu, X. Zhang, M. Lin, L. Wen and M. Li, *ACS Mater. Lett.*, 2021, **3**, 171–178.

23 M. Hu, Y. Ju, K. Liang, T. Suma, J. Cui and F. Caruso, *Adv. Funct. Mater.*, 2016, **26**, 5827–5834.

24 Y. Liu, Z. Liu, N. Lu, E. Preiss, S. Poyraz, M. J. Kim and X. Zhang, *Chem. Commun.*, 2012, **48**, 2621–2623.

25 H. Wang, W. Zhu, Y. Ping, C. Wang, N. Gao, X. Yin, C. Gu, D. Ding, C. J. Brinker and G. Li, *ACS Appl. Mater. Interfaces*, 2017, **9**, 14258–14264.

26 X. Wang, H. Xiao, A. Li, Z. Li, S. Liu, Q. Zhang, Y. Gong, L. Zheng, Y. Zhu, C. Chen, D. Wang, Q. Peng, L. Gu, X. Han, J. Li and Y. Li, *J. Am. Chem. Soc.*, 2018, **140**, 15336–15341.

27 H. Q. Wu, L. Huang, J. Q. Li, A. M. Zheng, Y. Tao, L. X. Yang, W. H. Yin and F. Luo, *Inorg. Chem.*, 2018, **57**, 12444–12447.

28 T. Zhang, J. Du, P. Xi and C. Xu, *ACS Appl. Mater. Interfaces*, 2017, **9**, 362–370.

29 J. Yin, Q. Fan, Y. Li, F. Cheng, P. Zhou, P. Xi and S. Sun, *J. Am. Chem. Soc.*, 2016, **138**, 14546–14549.

30 T. Zheng, K. Jiang, N. Ta, Y. Hu, J. Zeng, J. Liu and H. Wang, *Joule*, 2019, **3**, 265–278.

31 J. Hafner, *J. Comput. Chem.*, 2008, **29**, 2044.

32 P. E. Blöchl, *Phys. Rev. B: Condens. Matter Mater. Phys.*, 1994, **50**, 17953–17979.

33 G. Kresse and J. Furthmüller, *Phys. Rev. B: Condens. Matter Mater. Phys.*, 1996, **54**, 11169–11186.

34 G. Kresse and J. Furthmüller, *Comput. Mater. Sci.*, 1996, **6**, 15–50.

35 G. Kresse and D. Joubert, *Phys. Rev. B: Condens. Matter Mater. Phys.*, 1999, **59**, 1758–1775.

36 J. P. Perdew, K. Burke and M. Ernzerhof, *Phys. Rev. Lett.*, 1996, **77**, 3865–3868.

37 J. P. Perdew, K. Burke and M. Ernzerhof, *Phys. Rev. Lett.*, 1997, **78**, 1396–1396.

38 S. Grimme, J. Antony, S. Ehrlich and H. Krieg, *J. Chem. Phys.*, 2010, **132**, 154104.

39 S. Grimme, S. Ehrlich and L. Goerigk, *J. Comput. Chem.*, 2011, **32**, 1456–1465.

40 N. Godbout, D. R. Salahub, J. Andzelm and E. Wimmer, *Can. J. Chem.*, 1992, **70**, 560–571.

41 J. K. Nørskov, J. Rossmeisl, A. Logadottir, L. Lindqvist, J. R. Kitchin, T. Bligaard and H. Jónsson, *J. Phys. Chem. B*, 2004, **108**, 17886–17892.

42 A. A. Peterson, F. Abild-Pedersen, F. Studt, J. Rossmeisl and J. K. Nørskov, *Energy Environ. Sci.*, 2010, **3**, 1311–1315.

43 J. K. Zaręba, M. Nyk and M. Samoć, *Cryst. Growth Des.*, 2016, **16**, 6419–6425.

44 C. Wang, Q. Lai, P. Xu, D. Zheng, X. Li and H. Zhang, *Adv. Mater.*, 2017, **29**, 1605815.

45 C. Chen, H. Huang, Y. Yu, J. Shi, C. He, R. Albilali and H. Pan, *Chem. Eng. J.*, 2018, **353**, 584–594.

46 C.-W. Kung, C. O. Audu, A. W. Peters, H. Noh, O. K. Farha and J. T. Hupp, *ACS Energy Lett.*, 2017, **2**, 2394–2401.

47 K. Liu, J. Wang, M. Shi, J. Yan and Q. Jiang, *Adv. Energy Mater.*, 2019, **9**, 1900276.

48 J. Liu, S. Zou, L. Xiao and J. Fan, *Catal. Sci. Technol.*, 2014, **4**, 441–446.

49 Z. Liu, Z. Zhao, Y. Wang, S. Dou, D. Yan, D. Liu, Z. Xia and S. Wang, *Adv. Mater.*, 2017, **29**, 1606207.

50 S. Tanaka, K. Fujita, Y. Miyake, M. Miyamoto, Y. Hasegawa, T. Makino, S. Van der Perre, J. Cousin Saint Remi, T. Van Assche, G. V. Baron and J. F. M. Denayer, *J. Phys. Chem. C*, 2015, **119**, 28430–28439.

51 N. Kornienko, Y. Zhao, C. S. Kley, C. Zhu, D. Kim, S. Lin, C. J. Chang, O. M. Yaghi and P. Yang, *J. Am. Chem. Soc.*, 2015, **137**, 14129–14135.

52 Z. Xin, Y.-R. Wang, Y. Chen, W.-L. Li, L.-Z. Dong and Y.-Q. Lan, *Nano Energy*, 2020, **67**, 104233.

53 Q. Wu, M.-J. Mao, Q.-J. Wu, J. Liang, Y.-B. Huang and R. Cao, *Small*, 2021, **17**, 2004933.

54 J. Zhu and S. Mu, *Adv. Funct. Mater.*, 2020, **30**, 2001097.

55 L. Sun, Z. Huang, V. Reddu, T. Su, A. C. Fisher and X. Wang, *Angew. Chem., Int. Ed.*, 2020, **59**, 17104–17109.

Retrosynthetic Analysis Applied to Clip-off Chemistry: Synthesis of Four Rh(II)-Based Complexes as Proof-of-Concept

Anna Broto-Ribas[+], Sara Ruiz-Relaño[+], Jorge Albalad,* Yunhui Yang, Felipe Gándara, Judith Juanhuix, Inhar Imaz,* and Daniel Maspoch*

Abstract: Clip-off Chemistry is a synthetic strategy that our group previously developed to obtain new molecules and materials through selective cleavage of bonds. Herein, we report recent work to expand Clip-off Chemistry by introducing into it a retrosynthetic analysis step that, based on virtual extension of the products through cleavable bonds, enables one to define the required precursor materials. As proof-of-concept, we have validated our new approach by synthesising and characterising four aldehyde-functionalised Rh(II)-based complexes: a homoleptic cluster; a *cis*-disubstituted paddlewheel cluster; a macrocycle; and a crown.

Introduction

New molecules and materials are and will be key for our society, so that their design and synthesis will still be a vibrant challenge for chemists.[1–3] Traditionally, the way that chemists envision their synthesis is ultimately driven by bond formation steps (i.e. from simple starting materials to a complex product)[4–7] or, to a lesser extent, by bond-breaking.[8,9] We have recently developed an alternative synthetic approach, named Clip-off Chemistry, which proposes using bond breaking as the core synthetic step.[10] Clip-off Chemistry benefits from the rich repertoire of molecules and materials synthesised by traditional methods by using these as precursors that, once conferred with cleavable sites, can generate new molecules and materials upon selective bond cleavage.

In a first attempt to demonstrate the feasibility of Clip-off Chemistry, we have recently applied this concept using reticular materials as the starting precursors. We reasoned that reticular materials such as metal–organic frameworks (MOFs)[11] and metal-organic polyhedra (MOPs)[12,13] would be ideal candidates for the following three reasons. Firstly, they are all formed by periodic structures, such that their constituent organic linkers are perfectly ordered.[14,15] Secondly, they are porous, so reagents can diffuse throughout their structures to reach all cleavable sites.[16–18] Finally, Reticular Chemistry dictates that for a given structure, the constituents can be chemically functionalised pre- and/or post-synthetically, without any loss in structural connectivity.[19–21] This idea translates to the ability to encode the organic linkers of an existing reticular material with synthetic information by inserting into them cleavable groups without altering the linkers' shape or directionality, to ultimately enable the synthesis of analogous cleavable isoreticular structures.[22] In our first report, we inserted olefinic groups as cleavable bonds in MOFs/MOPs, and then selectively and quantitatively cleaved those bonds by ozonolysis. Thus, we demonstrated Clip-off Chemistry by synthesising two topologically distinct 3D MOFs (each from a distinct MOF precursor) and one metal-organic macrocycle (from a single precursor MOP).[10]

Herein, we advance on the development of Clip-off Chemistry by introducing the concept of retrosynthetic analysis. In Organic Chemistry, retrosynthesis is a crucial process that allows defining the reactants and the chemical reactions needed to form a desired product (Figure 1a).[23–25] This process starts by virtually dissecting stepwise the product into simple and easily-accessible synthons. Each synthon is later chemically translated to suitable reagent precursors, essentially building backwards the series of chemical reactions that will be followed to synthesise the product. However, in Clip-off Chemistry, we cannot apply

[*] A. Broto-Ribas,[+] S. Ruiz-Relaño,[+] Dr. J. Albalad, Y. Yang, Dr. I. Imaz, Prof. Dr. D. Maspoch
Catalan Institute of Nanoscience and Nanotechnology (ICN2), CSIC and The Barcelona Institute of Science and Technology Campus UAB, Bellaterra, 08193 Barcelona (Spain)
and
Departament de Química, Facultat de Ciències, Universitat Autònoma de Barcelona (UAB)
Cerdanyola del Vallès, 08193 Barcelona (Spain)
E-mail: jorge.albalad@icn2.cat
        inhar.imaz@icn2.cat
        daniel.maspoch@icn2.cat

Dr. F. Gándara
Materials Science Institute of Madrid (ICMM), Consejo Superior de Investigaciones Científicas (CSIC)
Calle Sor Juana Inés de la Cruz, 3, 28049 Madrid (Spain)

Dr. J. Juanhuix
Alba Synchrotron Light Facility
Cerdanyola del Vallès, 08290 Barcelona (Spain)

Prof. Dr. D. Maspoch
ICREA
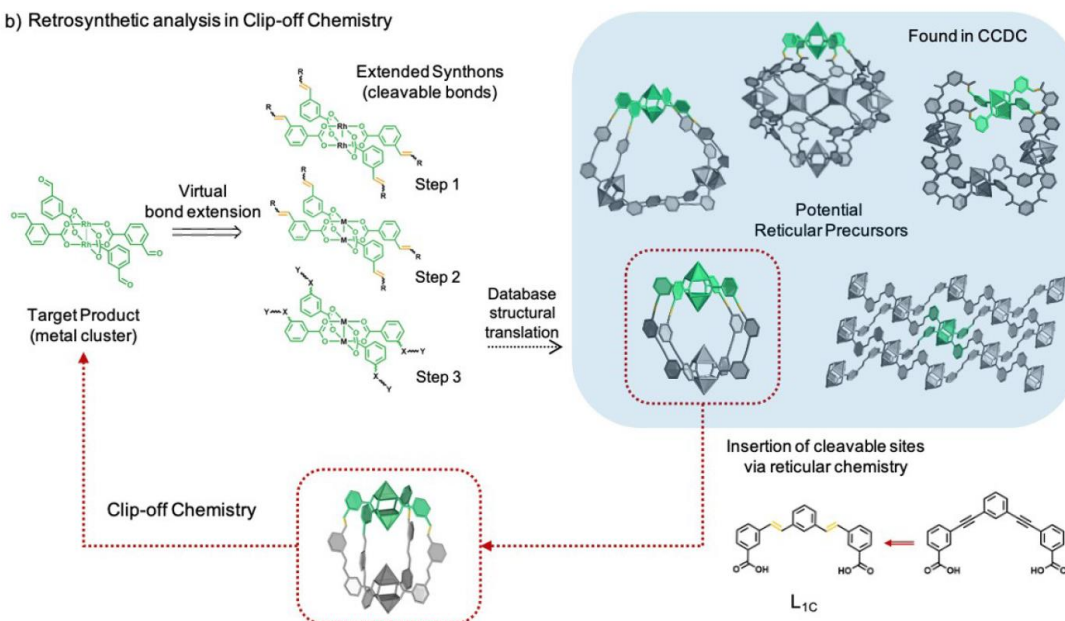Pg. Lluís Companys 23, 08010 Barcelona (Spain)

[+] These authors contributed equally to this work.
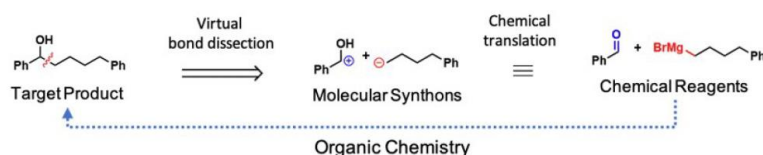
Figure 1. (a) Schematic example of the retrosynthetic analysis of bond formation steps in Organic Chemistry. A target bond is virtually dissected into molecular synthons, which later get chemically translated into logical reagent substrates. (b) Schematic of retrosynthetic analysis in Clip-off Chemistry, used here to obtain the product [Rh$_2$(3FBA)$_4$]. In it, the final product is virtually extended via cleavable bonds into a logical structure (discrete or periodic), which later is structurally translated into suitable reported lattices from several structural databases. If required, a final step consisting of isoreticular conversion of the reported linkers into an alkene-tagged analogue can be performed.

this style of retrosynthetic analysis, as it is ultimately based on bond breaking rather than bond formation steps. In fact, we should conceive it in an opposite way: retrosynthesis in Clip-off Chemistry should start by virtually connecting the target product through cleavable bonds into an initial molecule or material, which will be used as the sacrificial precursor to synthesise our target product via bond breaking reactions (Figure 1b).

As proof-of-concept, we employed our retrosynthetic approach to design and synthesise four novel, aldehyde-functionalised, Rh(II) metal-organic materials: a homoleptic paddlewheel cluster; a *cis*-disubstituted paddlewheel cluster; a triangular macrocycle; and a crown-like architecture. In each case, we followed a three-step process: firstly, retrosynthetic conversion of the target product into a suitable reticular precursor that contains olefinic bonds as future cleavage sites; secondly, synthesis of that precursor; and finally, cleavage of the olefinic bonds (by ozonolysis). We characterised all four products through a battery of

analytical techniques and single-crystal X-ray diffraction (SCXRD).

Results and Discussion

We began with the synthesis of a homoleptic Rh–Rh paddlewheel cluster, as the simplest test-case scenario. As ozonolysis enables transformation of an olefinic bond into either an aldehyde (under reductive conditions) or a carboxylic acid (under oxidative conditions),[26] we envisaged this cluster to be built up with four 3-formylbenzoate (3FBA) ligands under strict control of the reaction conditions (Figure 1b). Thus, our initial target product was a Rh–Rh paddlewheel cluster of formula [Rh$_2$(3FBA)$_4$], which is functionalised with four aldehyde groups located at the *meta* position of each phenyl ring. Once we had defined the product, we conducted the retrosynthetic analysis by the conceptual assembly of this cluster through cleavable

olefinic bonds (Figure 1b, extended synthon) into a suitable reticular material.

To facilitate identification of the desired reticular material, we searched the Cambridge Crystallographic Data Centre (CCDC) database (ConQuest v. 2022.3.0, CCDC, Cambridge, UK)[27] for structures that would contain such an extended synthon. To this end, we followed a stepwise search protocol that can be applied to retrosynthetic analysis of any metal-organic product in Clip-off Chemistry. In Step 1, one searches for structures containing the exact extended synthon (in our case, the synthon comprising a Rh(II) paddlewheel cluster extended via olefinic cleavable bonds). If that is unsuccessful, then one proceeds to Step 2: expanding the search to encompass analogous synthons made with any metal ion. Finally, if that also fails, the one can do Step 3: an even broader search, of structures containing a simplified synthon (in our case, a paddlewheel cluster of any metal, extended via any organic atom). Note here that Steps 2 and 3 involve the use of isoreticular chemistry to synthesise the suitable precursor material, converting the linkers of any successful search into alkene-based analogues, and/or substituting the identified metal ions with the desired ones. In our search for $[Rh_2(3FBA)_4]$, steps 1 and 2 failed. However, in Step 3, we found five suitable structures (Figure 1b): one Cu(II)-based double-wall triangular macrocycle;[28] one Cu(II)-based octahedral MOP;[29] one Cu(II)-based square-like MOP;[30] several lantern-type MOPs made of different metal ions [including Rh(II)];[31] and one extended two-dimensional Cu(II)-based MOF.[32] Among these structures, we selected the lantern-type MOP as our candidate precursor, as it was both the simplest and the only one containing Rh(II) ions. This inspired us to design a similar lantern-type MOP embedded with alkene bonds, by substituting the reported 3,3′-phenylenebis(ethyne-2,1-diyl)dibenzoic acid linker with one containing olefinic bonds, the (E)-3,3′-(1,3-phenylenebis(ethene-2,1-diyl))dibenzoic acid linker (L_{1C}; Figure 1b). The precursor lantern-type MOP of formula $[Rh_2(L_{1C})_2]_2$ was obtained by solvothermal synthesis in $N'N$-dimethylacetamide (DMA) at 100°C. The formation of this MOP was confirmed by MALDI-ToF spectrometry (experimental $[m/z]=1884.9$; simulated $[m/z]$ for $[Rh_4(L_{1C})_4 + H^+]^+ = 1886.2$) and ^1H NMR spectroscopy (Figures S5–S6, ESI†). Crystallisation of the green powder by vapour diffusion of diethyl ether into a DMA solution containing 4-*tert*-butylpyridine yielded parallelepiped-shaped purple crystals from which SCXRD analysis revealed the expected lantern-type structure (Figure 2a, left).

With the precursor in hand, we carried out the ozonolysis in a DMA/DMSO (1:0.7 v/v) mixture under a flow of ozone (10.4 mmol/h) at 0°C for 15 minutes in the presence of dimethyl sulphide (DMS, 0.3 mL) as reducing agent. The DMSO was required to protect the axial Rh(II) metal sites from ozone by coordination. The products were precipitated out and filtered off and crystallised from acetone/water by slow evaporation (see ESI for details). Encouragingly, SCXRD of the resulting crystals confirmed the formation of the expected $[Rh_2(3FBA)_4]$ cluster (Figure 2a, right), with a yield of 96%. Mass spectrometric
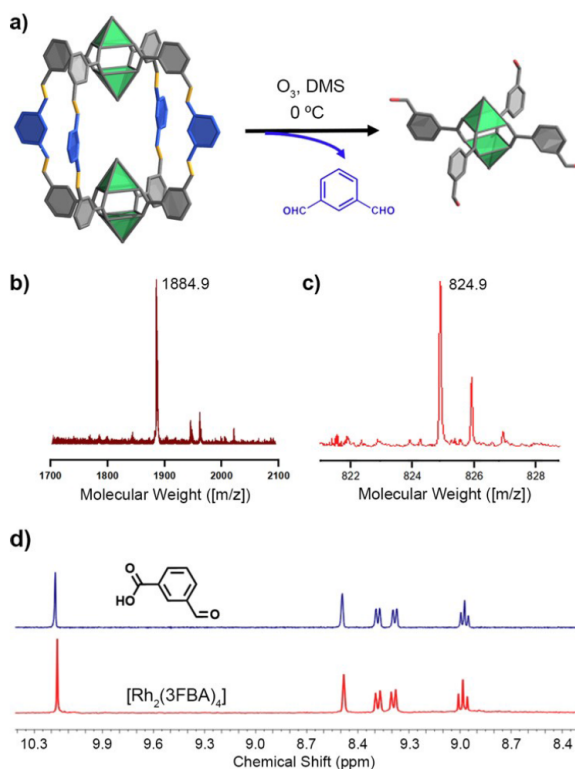
Figure 2. (a) Schematic of the Clip-off synthesis of the homoleptic paddlewheel $[Rh_2(3FBA)_4]$ cluster from $[Rh_2(L_{1C})_2]_2$. Representations of $[Rh_2(L_{1C})_2]_2$ (left) and $[Rh_2(3FBA)_4]$ (right) corresponding to their X-ray crystal structures. Axial capping agents (pyridine derivatives, solvents) and H atoms were omitted for clarity. (b) MALDI-ToF spectrum of $[Rh_2(L_{1C})_2]_2$. (c) ESI-MS spectrum of $[Rh_2(3FBA)_4]$. (d) Digested ^1H NMR spectra of $[Rh_2(3FBA)_4]$ (red) and its molecular component, 3FBA (blue).

analysis confirmed the formation of the product, with an experimental molecular weight of $[m/z]=824.9$ (simulated $[m/z]$ for $[Rh_2(3FBA)_4 + Na^+]^+ = 824.9$, Figure 2c, Figure S7). ^1H NMR analysis of the digested precipitate showed a quantitative loss of the starting L_{1C} signals in $[Rh_2(L_{1C})_2]_2$ (HC=CH δ ≈ 7.4 ppm, Figure S11), as well as a proportional formation of new signals perfectly matching those expected for 3FBA (CHO δ = 10.2 ppm, Figure 2d). Concurrently, ^1H NMR analysis of the acidic supernatant from the ozonolysis reaction revealed 1,3-benzenedicarboxaldehyde as the only side-product (Figure S11).

Having demonstrated the feasibility of retrosynthetically designing reticular precursors by connecting the products through cleavable bonds, we decided to extend our approach to the synthesis of a product that we expected to be more difficult to obtain using traditional synthetic methods. Thus, our second target was the cis-geometric isomer of the Rh–Rh paddlewheel cluster coordinated by two 3FBA ligands and two 4FBA (where 4FBA is 4-formylbenzoate) ligands. This new cluster, of formula $[Rh_2(3FBA)_2(4FBA)_2]$, is functionalised with two aldehyde groups at the *meta*

position and two at the *para* position of the phenyl rings, as shown in Figure 3a. Indeed, such a product is quite challenging to obtain through bottom-up assembly, as it would likely produce a statistical combination of homoleptic and mixed-linker Rh-paddlewheel clusters, whether mono-, di-, or tri-substituted.[33,34] Furthermore, *trans* clusters are far more common in the literature than *cis* clusters, further increasing the complexity of obtaining our target product by traditional methods.[35,36] Thus, we challenged our Clip-off Chemistry for the synthesis of this new *cis*-[Rh$_2$(3FBA)$_2$-(4FBA)$_2$] cluster in high yields and phase purity. Analysis of the target product shows that the starting precursor must contain at least two distinct cleavable linkers, with alkene groups in the *meta* positions and *para* positions, respectively, relative to the carboxylate sites. Additionally, both linkers must be connected to Rh–Rh nodes in a *cis* conformation (Figure 3a). After searching for suitable candidates, we found the perfect precursor in a family of heteroleptic MOPs (Figure 3a).[37–39] These heteroleptic MOPs are built from two different linker groups, distributed regularly into axial and equatorial positions around 6 paddlewheel nodes. Closer analysis of their structure revealed that the linkers are homogeneously distributed as two pairs of *cis*-distributed bridges in between clusters, thereby making them perfect candidates for our *cis*-cluster synthesis. Therefore, we

reasoned that if we could design suitable cleavable linkers for each position (i.e. equatorial and axial), we would be able to obtain our target product via Clip-off Chemistry. After virtually extending the product, we decided to employ the linkers (*E*)-3,3′-stilbenedicarboxylic acid (L$_{2C}$) and (*E*)-4,4′-(1,3-phenylene-*bis*(ethene-2,1-diyl))dibenzoic acid (L$_{3C}$) as the best candidates to generate the moieties 3FBA and 4FBA, respectively, through ozonolysis (Figure 3a).

We synthesised the MOP of formula [Rh$_2$(L$_{2C}$)(L$_{3C}$)]$_6$ through a solvothermal reaction of L$_{2C}$, L$_{3C}$ and rhodium acetate. Unfortunately, our attempts to obtain single crystals suitable for SCXRD were unsuccessful. Nonetheless, we were able to characterise the digested solid by ^{1}H NMR spectroscopy, which confirmed the formation of a single entity comprising a 1:1 linker ratio (Figure S12). We confirmed the formation of [Rh$_2$(L$_{2C}$)(L$_{3C}$)]$_6$ by MALDI-ToF spectrometry: the spectrum contained a broad peak centred at [m/z] = 5530.3, which agrees with the expected mass of [m/z] = 5524.6 for the targeted formula [Rh$_{12}$(L$_{2C}$)$_6$-(L$_{3C}$)$_6$ + H$^+$]$^+$·6 DMSO (Figure S13). Ozonolysis of [Rh$_2$-(L$_{2C}$)(L$_{3C}$)]$_6$ in DMA/DMSO/DMS mixture (1:0.7:0.3 v/v/v) under the same conditions at 0°C for 15 minutes resulted in quantitative alkene bond cleavage, and [Rh$_2$(3FBA)$_2$-(4FBA)$_2$] was obtained in 92% yield. Slow evaporation of a solution of the product in a mixture of MeCN/H$_2$O (1:1 v/v)
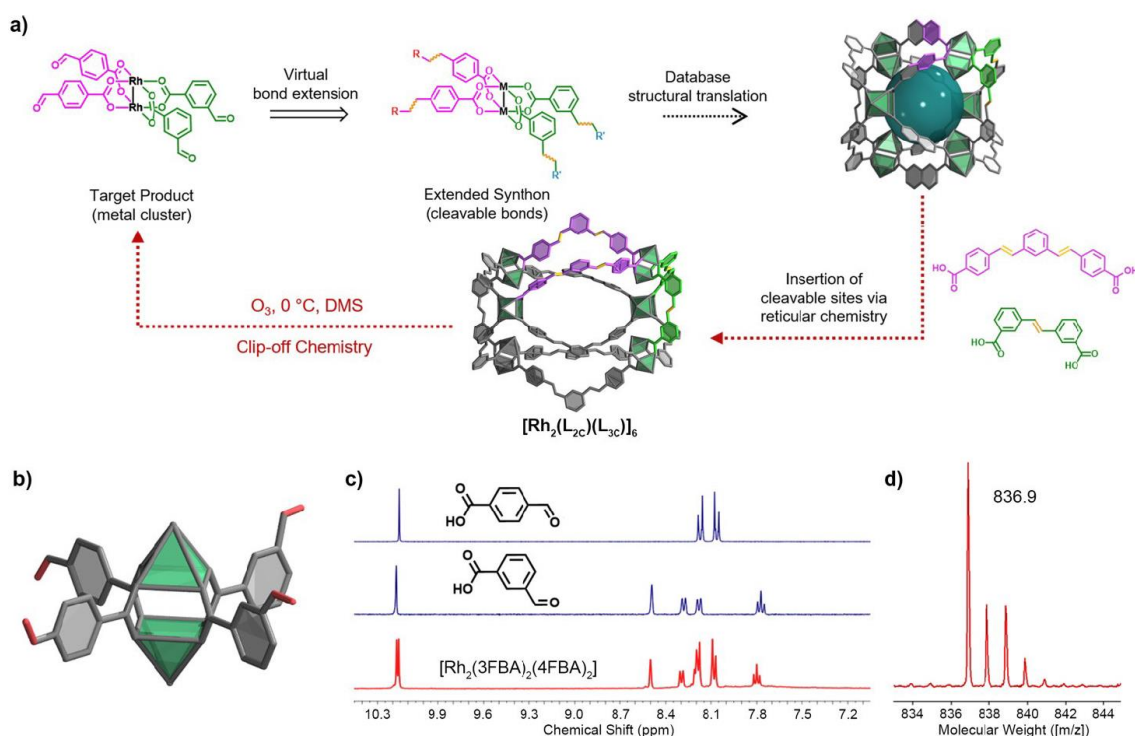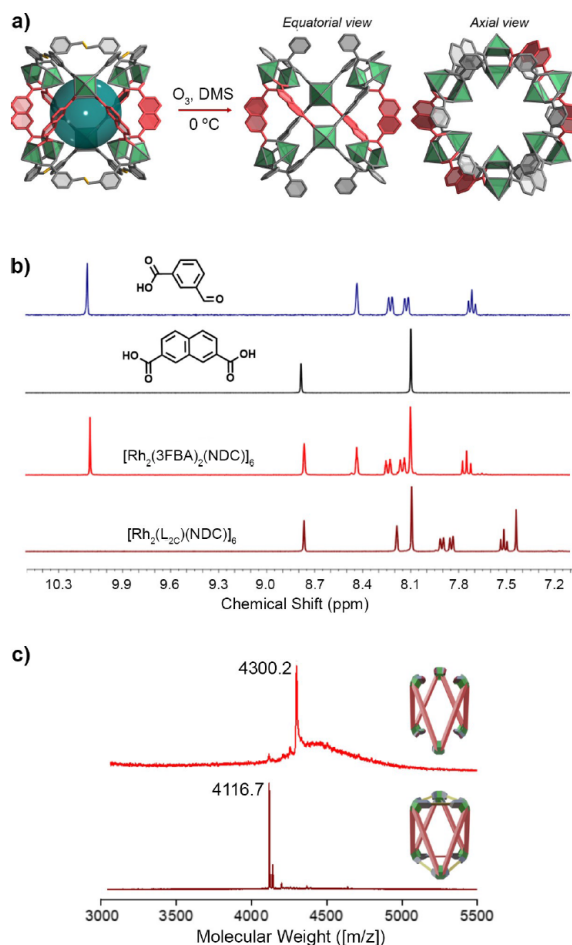

Figure 3. (a) Schematic representation of the retrosynthetic analysis conducted for the synthesis of the *cis*-disubstituted [Rh$_2$(3FBA)$_2$(4FBA)$_2$] cluster via Clip-off Chemistry, from which the precursor [Rh$_2$(L$_{2C}$)(L$_{3C}$)]$_6$ was identified. (b) Single-crystal structure of [Rh$_2$(3FBA)$_2$(4FBA)$_2$]. (c) Digested ^{1}H NMR spectra of [Rh$_2$(3FBA)$_2$(4FBA)$_2$] (red) versus those of its molecular components: 3FBA and 4FBA (blue). (d) ESI-MS spectrum of [Rh$_2$(3FBA)$_2$(4FBA)$_2$].

afforded plate-shaped crystals suitable for SCXRD (Figure 3b). Synchrotron diffraction data confirmed the integrity of Rh–Rh paddlewheel clusters after ozonolysis, and the quantitative cleavage of both linkers into the expected product. SCXRD data revealed an experimental 50:50 occupancy distribution between the 3- and 4-substituted FBA ligands, corresponding to an overlay of an average of superimposed *cis*-clusters in different orientations (Figure S14). NMR analysis of the digested product revealed a 1:1 ratio of 3FBA and 4FBA ligands (Figures 3c, S15). Likewise, ESI-MS analysis of the products showed a single entity with the expected molecular weight attributed to $[Rh_2(3FBA)_2(4FBA)_2]$ (experimental $[m/z]=836.9$, simulated $[m/z]$ for $[[Rh_2(3FBA)_2(4FBA)_2]+Cl^-]^-=836.9$; Figures 3d, S16). Analysis of the acid supernatant used to precipitate the product did not reveal any residual traces of free rhodium ions, thereby confirming the inert character of the metal cluster upon ozone exposure (Table S5). Additionally, ^1H NMR analysis of the supernatant showed exclusively the presence of 1,3-diformylbenzene (side product expected from the reductive ozonolysis of L_{3C}), thus ruling out any potential linker exchange/substitution around the Rh–Rh node (Figure S19).
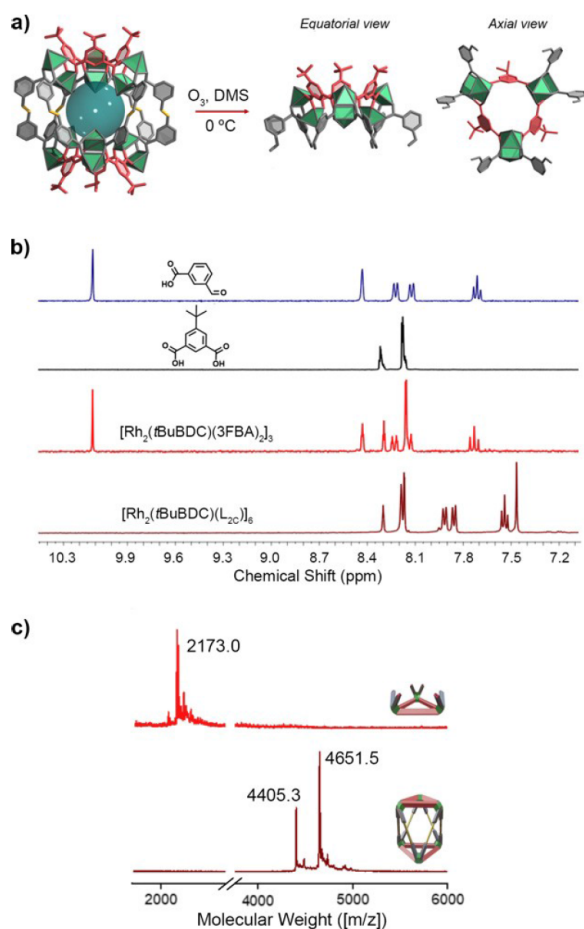
Reflecting on the aforementioned heteroleptic MOP precursor, which contains two different linkers, we envisioned that in such MOPs, we could mix cleavable linkers with inert ones. We reasoned that this combination could follow either of two distinct routes. In the first one, the inert linker would occupy the equatorial positions, such that clipping of the precursor should generate a crown-shaped product (Figure 4a). In the second case, the axial sites would be resistant to ozone and therefore, clipping should generate a macrocyclic product (Figure 5a). In both cases, we restricted our search for the suitable precursors to those reported in this family of heteroleptic MOPs, from which we identified two previously reported MOPs: $[Rh_2(L_{2C})(NDC)]_6$ (where NDC = 2,7-naphthalenedicarboxylic acid), to provide the *crown*; and $[Rh_2(tBuBDC)(L_{2C})]_6$ (where $tBuBDC = 5$-*tert*-butylisophthalic acid), to give the *macrocycle*.

We synthesised the first heteroleptic MOP precursor with inert equatorial positions from a mixture of L_{2C} and NDC. SCXRD analysis and spectroscopic characterisation of the product confirmed the formation of the targeted heteroleptic cage of formula $[Rh_2(L_{2C})(NDC)]_6$, with six cleavable axial L_{2C} linkers and six inert equatorial NDC moieties (Figure 4a, Figures S20–S21). $[Rh_2(L_{2C})(NDC)]_6$ was treated with ozone for 20 minutes under the standard reductive conditions. The product was collected by filtration after precipitation, washed with water, and obtained in 70% yield after crystallisation via ether vapour diffusion to a THF solution containing 4-*tert*-butylpyridine. The resultant crystals were characterised by SCXRD, using synchrotron diffraction data that was collected at a maximum resolution of 1.3 Å, suggesting the synthesis of the $[Rh_2(3FBA)_2(NDC)]_6$ crown (Figure 4a). The formation and phase purity of the targeted $[Rh_2(3FBA)_2(NDC)]_6$ crown functionalised with aldehyde groups was further confirmed by spectroscopic analysis, revealing the lack of all the characteristic peaks of L_{2C} (olefinic protons at $\delta=7.45$ ppm; and aromatic

Figure 4. (a) Schematic of the Clip-off Chemistry synthesis of the crown-shaped $[Rh_2(3FBA)_2(NDC)]_6$ complex, using the $[Rh_2(L_{2C})(NDC)]_6$ MOP as precursor. Representations of $[Rh_2(L_{2C})(NDC)]_6$ (left) and $[Rh_2(3FBA)_2(NDC)]_6$ (right) correspond to their X-ray crystal structures. (b) Digested ^1H NMR spectra of the $[Rh_2(L_{2C})(NDC)]_6$ precursor (dark red) and the crown (red), versus those of their molecular components: NDC (black) and 3FBA (blue). (c) MALDI-ToF spectra of the $[Rh_2(L_{2C})-(NDC)]_6$ precursor (dark red) and the synthesised crown (red).

protons at $\delta=8.19$ ppm, 7.92 ppm, 7.85 ppm and 7.52 ppm) by digestion ^1H NMR (Figure 4b). Instead, the ^1H NMR spectrum revealed the characteristic signals of NDC (phenyl protons at $\delta=8.74$ ppm and 8.08 ppm) and those of 3FBA (aldehyde proton at $\delta=10.07$ ppm; phenyl protons at $\delta=8.41$ ppm, 8.21 ppm, 8.13 ppm and 7.73 ppm). Moreover, the integrated spectrum indicated an 3FBA/NDC acid-proton ratio of 2:1, consistent with the formula expected for the crown (Figure S22). The formation of the Rh(II)-based crown was unambiguously corroborated by MALDI-TOF (Figure 4c), which showed the molecular weight increase expected for a product of formula $[Rh_{12}(3FBA)_{12}(NDC)_6+H^+]^+$ (experimental $[m/z]=4300.2$ expected $[m/z]=4306.8$, Figure S23); in comparison to the $[Rh_2(L_{2C})(NDC)]_6$ precur-

a)

Equatorial view   Axial view

O₃, DMS
0 °C

b)

[Rh₂(tBuBDC)(3FBA)₂]₃

[Rh₂(tBuBDC)(L₂C)]₆

Chemical Shift (ppm)

c)

Molecular Weight ([m/z])

Figure 5. (a) Schematic of the Clip-off Chemistry synthesis of the triangular [Rh₂(tBuBDC)(3FBA)₂]₃ macrocycle, using the MOP [Rh₂-(tBuBDC)(L₂C)]₆ as precursor. The representation of [Rh₂(tBuBDC)-(L₂C)]₆ (left) corresponds to its X-ray crystal structure, whereas those of [Rh₂(tBuBDC)(3FBA)₂]₃ (right) are graphic models. (b) Digested ¹H NMR spectra of the [Rh₂(tBuBDC)(L₂C)]₆ precursor (dark red) and the macrocycle (red) versus those of their molecular components: tBuBDC (black) and 3FBA (blue). (c) MALDI-ToF spectra of the [Rh₂(tBuBDC)(L₂C)]₆ precursor (dark red) and the synthesised macrocycle (red).

sor (experimental $[m/z] = 4116.7$; expected for $[Rh_{12}(L_{2C})_6$-$(NDC)_6 + H^+]^+$ $[m/z] = 4116.4$). Finally, analysis of the supernatant (Table S5, Figure S26) did not reveal any rhodium ions or free 3FBA moieties, thus confirming the selectivity of the method.

In our final example, we synthesised a heteroleptic MOP precursor, the one exhibiting ozone-inert axial positions, using tBuBDC and L_{2C} linkers. SCXRD analysis of the product revealed a heteroleptic MOP cage of formula $[Rh_2(tBuBDC)(L_{2C})]_6$, composed of six paddlewheel Rh–Rh SBUs connected through six axial tBuBDC linkers and six equatorial L_{2C} linkers poised for Clip-off Chemistry (Figures 5a, S27–28). Thus, a solution of $[Rh_2(tBuBDC)(L_{2C})]_6$ in DMA/DMSO/DMS (1:0.7:0.3 v/v/v) was subjected to ozo-

nolysis at 0 °C for 30 minutes under reductive conditions, which cleaved the MOP structure into two identical halves, with a yield of 65 %. Indeed, although we could not solve its crystal structure, we confirmed formation of the expected metal-organic Rh-macrocycle by comparing ¹H NMR spectra of the starting $[Rh_2(tBuBDC)(L_{2C})]_6$ with that of the ozonated product (Figure 5b). The ¹H NMR spectrum lacked all the characteristic peaks of L_{2C} (olefinic protons at $\delta = 7.45$ ppm; and phenyl protons at $\delta = 8.18$ ppm, 7.90 ppm, 7.84 ppm and 7.53 ppm). However, it revealed the characteristic signals of tBuBDC (phenyl protons at $\delta = 8.30$ ppm and 8.16 ppm; and tert-butyl protons at $\delta = 1.31$ ppm) and those of 3FBA with the expected 1:2 ratio (Figure S29). This integrated spectrum indicated the quantitative transformation into a Rh-macrocycle. This was supported by MALDI-TOF analysis (Figure 5c) where the spectrum of the reaction product showed only the macrocycle $[Rh_6(3FBA)_6$-$(tBuBDC)_3 + H^+]^+$ $[m/z] = 2173.0$ (simulated $[m/z] = 2172.9$, Figure S30) and nothing for the $[Rh_2(tBuBDC)(L_{2C})]_6$ starting material $[M + H]^+$ ($[m/z] = 4651.5$). Moreover, no shift in the low-energy UV/Vis absorption band I (λ_{max}) at 592 nm was consistent with no change in Rh(II) coordination mode and there was no significant trace of Rh in the supernatant from ICP-OES analysis, confirming a clean and chemoselective alkene cleavage (Table S5, Figure S33).

Conclusion

In summary, we have expanded our paradigm of Clip-off Chemistry to include a new step of retrosynthetic analysis. Unlike retrosynthesis in Organic Chemistry, which is based on the virtual dissection of bonds, retrosynthesis in Clip-off Chemistry entails virtually extending the product into a logical periodic material through cleavable bonds. As proof-of-concept, we employed our new retrosynthesis analysis in the Clip-off synthesis of four unprecedented, aldehyde-functionalised Rh(II)-based structures: a homoleptic cluster; a cis-disubstituted cluster; a macrocycle; and a crown-like architecture. Specifically, we used retrosynthesis to define the Rh-based MOP precursors functionalised with cleavable alkene bonds that would be required for the subsequent Clip-off synthesis of each target in high yield. We extensively characterised all four products. Considering this new retrosynthetic approach, and the fact that bond-breaking can be applied both selectively and quantitatively to precursors of different dimensionalities (from 3D to 0D), we anticipate that Clip-off Chemistry will complement existing synthetic methodologies to ultimately inform the design and synthesis of new molecules and materials.

Acknowledgements

10.13039/501100011033/ and by "ERDF A way of making Europe"; and the Catalan AGAUR (project 2017 SGR 238). It was also funded by the CERCA Programme/Generalitat de Catalunya. ICN2 is supported by the Severo Ochoa Centres of Excellence programme, Grant CEX2021-001214-S, funded by MCIN/AEI/10.13039.501100011033. F.G. acknowledges funding from the Spanish Research Agency (PID2021-123287OB-I00). Y.Y. acknowledges the China Scholarship Council for scholarship support.

Conflict of Interest

The authors declare no conflict of interest.

Data Availability Statement

The data that support the findings of this study are available from the corresponding author upon reasonable request.

[1] O. M. Yaghi, M. O'Keeffe, N. W. Ockwig, H. K. Chae, M. Eddaoudi, J. Kim, *Nature* **2003**, *423*, 705–714.

[2] S. Zhang, *Biotechnol. Adv.* **2002**, *20*, 321–339.

[3] J. E. Moses, A. D. Moorhouse, *Chem. Soc. Rev.* **2007**, *36*, 1249–1262.

[4] N. G. Schmidt, E. Eger, W. Kroutil, *ACS Catal.* **2016**, *6*, 4286–4311.

[5] K. G. Maskill, J. P. Knowles, L. D. Elliott, R. W. Alder, K. I. Booker-Milburn, *Angew. Chem. Int. Ed.* **2013**, *52*, 1499–1502.

[6] I. Alfonso, *Chem. Commun.* **2016**, *52*, 239–250.

[7] M. Hutin, D. Schultz, J. R. Nitschke, *Chimia* **2008**, *62*, 198–203.

[8] P. Shieh, M. R. Hill, W. Zhang, S. L. Kristufek, J. A. Johnson, *Chem. Rev.* **2021**, *121*, 7059–7121.

[9] L. Feng, S. Yuan, L. L. Zhang, K. Tan, J. L. Li, A. Kirchon, L. M. Liu, P. Zhang, Y. Han, Y. J. Chabal, H. C. Zhou, *J. Am. Chem. Soc.* **2018**, *140*, 2363–2372.

[10] Y. Yang, A. Broto-Ribas, B. Ortín-Rubio, I. Imaz, F. Gándara, A. Carné-Sánchez, V. Guillerm, S. Jurado, F. Busqué, J. Juanhuix, D. Maspoch, *Angew. Chem. Int. Ed.* **2022**, *61*, e202111228.

[11] H. C. Zhou, J. R. Long, O. M. Yaghi, *Chem. Rev.* **2012**, *112*, 673–674.

[12] M. Eddaoudi, J. Kim, J. B. Wachter, H. K. Chae, M. O'Keeffe, O. M. Yaghi, *J. Am. Chem. Soc.* **2001**, *123*, 4368–4369.

[13] S. Lee, H. Jeong, D. Nam, M. S. Lah, W. Choe, *Chem. Soc. Rev.* **2021**, *50*, 528–555.

[14] H. Furukawa, U. Müller, O. M. Yaghi, *Angew. Chem. Int. Ed.* **2015**, *54*, 3417–3430.

[15] J. Cho, Y. Ishida, *Adv. Mater.* **2017**, *29*, 1605974.

[16] H. Li, M. Eddaoudi, T. L. Groy, O. M. Yaghi, *J. Am. Chem. Soc.* **1998**, *120*, 8571–8572.

[17] X. Zhang, Z. Chen, X. Liu, S. L. Hanna, X. Wang, R. Taheri-Ledari, A. Maleki, P. Li, O. K. Farha, *Chem. Soc. Rev.* **2020**, *49*, 7406–7427.

[18] A. J. Gosselin, C. A. Rowland, E. D. Bloch, *Chem. Rev.* **2020**, *120*, 8987–9014.

[19] T.-Y. Luo, S. Park, T.-H. Chen, Prerna, R. Patel, X. Li, J. I. Siepmann, S. Caratzoulas, Z. Xia, M. Tsapatsis, *Angew. Chem.* **2022**, *134*, e202209034.

[20] A. M. Bumstead, I. Pakamorė, K. D. Richards, M. F. Thorne, S. S. Boyadjieva, C. Castillo-Blas, L. N. McHugh, A. F. Sapnik, D. S. Keeble, D. A. Keen, R. C. Evans, R. S. Forgan, T. D. Bennett, *Chem. Mater.* **2022**, *34*, 2187–2196.

[21] J. Albalad, H. Xu, F. Gándara, M. Haouas, C. Martineau-Corcos, R. Mas-Ballesté, S. A. Barnett, J. Juanhuix, I. Imaz, D. Maspoch, *J. Am. Chem. Soc.* **2018**, *140*, 2028–2031.

[22] V. Guillerm, H. Xu, J. Albalad, I. Imaz, D. Maspoch, *J. Am. Chem. Soc.* **2018**, *140*, 15022–15030.

[23] E. J. Corey, *Pure Appl. Chem.* **1967**, *14*, 19–38.

[24] R. O. M. A. de Souza, L. S. M. Miranda, U. T. Bornscheuer, *Chem. Eur. J.* **2017**, *23*, 12040–12063.

[25] S. V. McCowen, N. A. Doering, R. Sarpong, *Chem. Sci.* **2020**, *11*, 7538–7552.

[26] R. Criegee, *Angew. Chem. Int. Ed.* **1975**, *14*, 745–752.

[27] C. R. Groom, I. J. Bruno, M. P. Lightfoot, S. C. Ward, *Acta Crystallogr. Sect. B* **2016**, *72*, 171–179.

[28] X. Song, X. Liu, M. Oh, M. S. Lah, *Dalton Trans.* **2010**, *39*, 6178–6180.

[29] M. J. Prakash, Y. Zou, S. Hong, M. Park, M. P. N. Bui, G. H. Seong, M. S. Lah, *Inorg. Chem.* **2009**, *48*, 1281–1283.

[30] J. Park, Y. P. Chen, Z. Perry, J. R. Li, H. C. Zhou, *J. Am. Chem. Soc.* **2014**, *136*, 16895–16901.

[31] L. Chen, T. Yang, H. Cui, T. Cai, L. Zhang, C. Y. Su, *J. Mater. Chem. A* **2015**, *3*, 20201–20209.

[32] B. Ortín-Rubio, H. Ghasempour, V. Guillerm, A. Morsali, J. Juanhuix, I. Imaz, D. Maspoch, *J. Am. Chem. Soc.* **2020**, *142*, 9135–9140.

[33] E. V. Dikarev, B. Li, H. Zhang, *J. Am. Chem. Soc.* **2006**, *128*, 2814–2815.

[34] Y. Lou, T. P. Remarchuk, E. J. Corey, *J. Am. Chem. Soc.* **2005**, *127*, 14223–14230.

[35] M. Ebihara, M. Nomura, S. Sakai, T. Kawamura, *Inorg. Chim. Acta* **2007**, *360*, 2345–2352.

[36] F. A. Cotton, J. L. Thompson, *Inorg. Chim. Acta* **1984**, *81*, 193–203.

[37] S. Sudan, R.-J. Li, S. M. Jansze, A. Platzek, R. Rudolf, G. H. Clever, F. Fadaei-Tirani, R. Scopelliti, K. Severin, *J. Am. Chem. Soc.* **2021**, *143*, 1773–1778.

[38] J.-R. Li, H.-C. Zhou, *Nat. Chem.* **2010**, *2*, 893–898.

[39] A. Broto-Ribas, M. S. Gutiérrez, I. Imaz, A. Carné-Sánchez, F. Gándara, J. Juanhuix, D. Maspoch, *Chem. Commun.* **2022**, *58*, 10480–10483.

[40] Deposition numbers 2281386 (for [Rh$_2$(L$_{1C}$)$_2$]$_2$), 2281052 (for [Rh$_2$(3FBA)$_4$]), 2281054 (for [Rh$_2$(3FBA)$_2$(4FBA)$_2$]), and 2281053 (for [Rh$_2$(3FBA)$_2$(NDC)]$_6$) contain the supplementary crystallographic data for this paper. These data are provided free of charge by the joint Cambridge Crystallographic Data Centre and Fachinformationszentrum Karlsruhe Access Structures service.